

RS-8232-2/ 70199

SANDIA REPORT

SAND89-2030 • UC-721

Unlimited Release

Printed March 1990

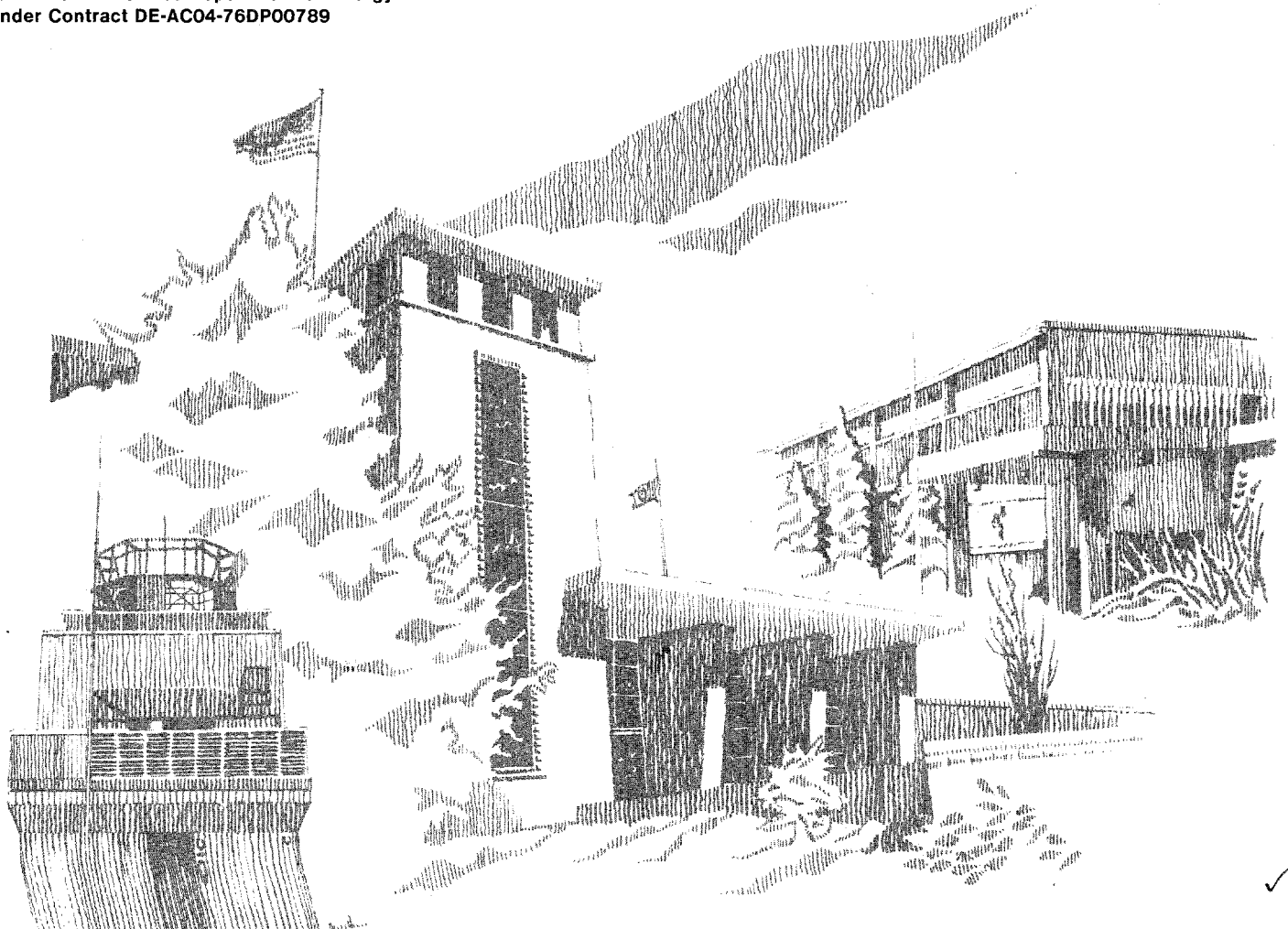
8232-2/070199

00000001 -

Parameter Sensitivity Studies of Selected Components of the Waste Isolation Pilot Plant Repository/Shaft System

Rob P. Rechard, Walt Beyeler, Ron D. McCurley,
David K. Rudeen, James E. Bean, James D. Schreiber

Prepared by
Sandia National Laboratories
Albuquerque, New Mexico 87185 and Livermore, California 94550
for the United States Department of Energy
under Contract DE-AC04-76DP00789



✓

Issued by Sandia National Laboratories, operated for the United States Department of Energy by Sandia Corporation.

NOTICE: This report was prepared as an account of work sponsored by an agency of the United States Government. Neither the United States Government nor any agency thereof, nor any of their employees, nor any of their contractors, subcontractors, or their employees, makes any warranty, express or implied, or assumes any legal liability or responsibility for the accuracy, completeness, or usefulness of any information, apparatus, product, or process disclosed, or represents that its use would not infringe privately owned rights. Reference herein to any specific commercial product, process, or service by trade name, trademark, manufacturer, or otherwise, does not necessarily constitute or imply its endorsement, recommendation, or favoring by the United States Government, any agency thereof or any of their contractors or subcontractors. The views and opinions expressed herein do not necessarily state or reflect those of the United States Government, any agency thereof or any of their contractors.

Printed in the United States of America. This report has been reproduced directly from the best available copy.

Available to DOE and DOE contractors from
Office of Scientific and Technical Information
PO Box 62
Oak Ridge, TN 37831

Prices available from (615) 576-8401, FTS 626-8401

Available to the public from
National Technical Information Service
US Department of Commerce
5285 Port Royal Rd
Springfield, VA 22161

NTIS price codes
Printed copy: A10
Microfiche copy: A01

SAND89-2030
Unlimited Release
Printed March 1990

Distribution
Category UC-721

PARAMETER SENSITIVITY STUDIES OF SELECTED COMPONENTS OF THE WASTE ISOLATION PILOT PLANT REPOSITORY/SHAFT SYSTEM

Rob P. Rechard
Walt Beyeler,* Ron D. McCurley**
David K. Rudeen,** James E. Bean**
James D. Schreiber*

Sandia National Laboratories
Albuquerque, New Mexico 87185

Abstract

This status report presents preliminary analyses of flow through the rooms, drifts, seals, and shafts of the Waste Isolation Pilot Plant (WIPP). The purpose of these analyses is to evaluate the importance of various components and parameters of the transuranic waste repository. These analyses are presented to show the current status of repository/shaft system modeling, and to provide input for evaluating proposed engineered modifications to the waste and rooms to ensure compliance with the Environmental Protection Agency's *Environmental Standards for the Management and Disposal of Spent Nuclear Fuel, High-Level and Transuranic Waste*. Detailed descriptions are given for nine computational models of the WIPP repository for either undisturbed or human intrusion conditions. Some models are refined versions of earlier models; others include rudimentary studies of an additional phenomenon, flow of generated gas. The models of an undisturbed repository substantiated the results of earlier models by showing that no waste leaves the vicinity of the disposal area in 10,000 yr. The models that studied gas flow agreed with this position; however, the models are too rudimentary to permit conclusive statements. The five models of the human intrusion event explored the importance of parameters (e.g., waste permeability and Salado Formation heterogeneity) that influence the flow of brine through the waste, establishing a base for understanding the behavior of the waste, disposal rooms, drifts, and interbeds in the host rock.

* Science Application International Corporation, Albuquerque, NM 87106

** New Mexico Engineering Research Institute, Albuquerque, NM 87131

OTHER RELATED DOCUMENTS

Bertram-Howery, S. G., M. G. Marietta, D. R. Anderson, K. F. Brinster, L. H. Brush, M. S. Y. Chu, L. S. Gomez, R. V. Guzowski, R. L. Hunter, R. P. Rechar, 1989. *Draft Forecast of the Final Report for the Comparison to 40 CFR 191, Subpart B for the Waste Isolation Pilot Plant*, SAND88-1452. Sandia National Laboratories, Albuquerque, NM.

Lappin, A. R., R. L. Hunter, D. P. Garber, and P. B. Davies, eds., 1989. *Systems Analysis Long-Term Radionuclide Transport, and Dose Assessments, Waste Isolation Pilot Plant (WIPP), Southeastern New Mexico; March 1989*, SAND89-0462. Sandia National Laboratories, Albuquerque, NM.

Marietta, M. G., S. G. Bertram-Howery, D. R. Anderson, K. F. Brinster, R. V. Guzowski, H. J. Iuzzolino, R. P. Rechar, 1989. *Performance Assessment Methodology Demonstration: Methodology Development for Purposes of Evaluating Compliance with EPA 40 CFR 191, Subpart B, for the WIPP*, SAND89-2027. Sandia National Laboratories, Albuquerque, NM.

Rechar, R. P., 1989. *Review and Discussion of Code Linkage and Data Flow in Nuclear Waste Compliance Assessments*, SAND87-2833. Sandia National Laboratories, Albuquerque, NM.

Rechar, R. P., H. J. Iuzzolino, J. S. Rath, A. P. Gilkey, R. D. McCurley, D. K. Rudeen, 1989. *User's Manual for CAMCON: Compliance Assessment Methodology Controller*, SAND88-1496. Sandia National Laboratories, Albuquerque, NM.

ACKNOWLEDGEMENTS

Most of the models for this report were started in October 1989. The models and initial draft were completed by January 1, 1990. This aggressive documentation schedule could not have been met without the help of Janet Chapman and Darcy Pulliam, Tech. Reps., Inc., Albuquerque, NM. I also appreciate the time and suggestions supplied by the technical reviewers: Mel Marietta (6342), Sharla Bertram-Howery (6342), Barry Butcher (6345), and Jim Nowak (6346).

CONTENTS

NOMENCLATURE	xv
1. INTRODUCTION	1
1.1 Purpose and Organization of Report	1
Purpose	1
Organization	1
1.2 Background on WIPP	2
Purpose of WIPP	2
SNL Role in Project	2
Location and Stratigraphy	2
Design of Repository, Backfill, and Seals	2
Description of Waste Form and Containers	9
WIPP Waste Containment System	12
1.3 Background on SNL Method to Assess Compliance	12
Five Steps of Compliance Assessment	12
The Repository/Shaft System Model	15
Background on Sensitivity and Uncertainty Analysis	17
Background on CAMCON	17
2. REPOSITORY/SHAFT SYSTEM ISSUES AND MODELS	19
2.1 Issues	19
Issues Concerning Undisturbed Performance	19
Issues Concerning Human Intrusion	20
2.2 General Modeling Description	20
Scenarios Modeled	20
Conceptual Model of Panels and Rooms in Disposal Area	21
Modeling of the Repository/Shaft System	26
2.3 Computer Modules	29
Modules Used in CAMCON	29
Code Descriptions	32
2.4 Material Property Values	33

3. UNDISTURBED REPOSITORY MODELS	35
3.1 Two-Dimensional Model of Radionuclide Migration Pathway	35
Purpose.....	35
Summary.....	36
Description of Grid and Boundary Conditions	37
Constant and Varied Parameters	49
Results.....	49
3.2 Cylindrical Model of Shaft Saturation	61
Purpose.....	61
Summary.....	61
Process Description.....	61
Description of Grid and Boundary Conditions	62
Results.....	63
Discussion.....	68
3.3 Two-Dimensional Model of Gas Flow from Disposal Area to Shaft Using SUTRA	69
Purpose.....	69
Summary.....	69
Description of Grid and Boundary Conditions	70
Varied Parameters	70
Results.....	73
3.4 One-Dimensional Model of Gas Flow from Disposal Area to Shaft Using BOAST	81
Purpose.....	81
Summary.....	81
Description of Grid and Boundary Conditions	82
Varied Parameters	83
Results.....	83
4. HUMAN INTRUSION MODELS	91
4.1 Cylindrical Model of Salado Brine Flow through Panel to Borehole	91
Purpose.....	91
Summary.....	92
Amount of Accessible Waste.....	92
Description of Grid and Boundary Conditions	94
Varied Parameters	94
Results.....	94

4.2	Cylindrical Model of Effects of Anhydrite Layers on Salado Brine Flow through Panel	102
	Purpose	102
	Summary	102
	Analytical Model Description and Results	102
	Numerical Model of Flow Diversion near Panel.....	106
	Numerical Model of Far-Field Flow from Heterogeneous Salado	107
	Possible Future Work	110
4.3	Cylindrical Model of Flow from Brine Pocket through a Room	111
	Purpose	111
	Summary	111
	Model Description.....	112
	Model Implementation.....	115
	Simplifying Approximations and Calculations Made Based on Characteristic Times	118
	Discussion.....	129
4.4	Characteristic Flow Times for the Cylindrical Models of Room and Panel	131
	Purpose	131
	Summary	131
	Description of Grid and Boundary Conditions for Numerical Model for Gas.....	131
	Analytic Model for Gas	131
	Varied and Constant Parameters	133
	Results.....	133
4.5	Two- and Three-Dimensional Models of Quarter Panel	136
	Purpose	136
	Summary	136
	Description of Grid and Boundary Conditions	137
	Results of Two-Dimensional Model.....	139
	Results of Three-Dimensional Model	144
	Differences Between Two-Dimensional SUTRA and Three-Dimensional HST3D Models.....	147
5.	SUMMARY AND CONCLUSIONS	153
5.1	Undisturbed Repository Models.....	153
	Two-Dimensional Modeling of Migration Pathway	153
	Cylindrical Modeling of Shaft Saturation	154
	Cylindrical Modeling of Gas Movement in Drift with SUTRA.....	154
	One-Dimensional Modeling of Gas and Brine Movement in Drift and MB139 with BOAST.....	155

5.2 Human Intrusion Models	155
Cylindrical Modeling of Salado Brine Flow through Panel to Borehole	157
Cylindrical Modeling of Effects of Anhydrite Layers on Brine Flow through Panel.....	157
Cylindrical Modeling of Castile Brine Pocket through a Room.....	158
Characteristic Flow Times for the Room and Panel	159
Two- and Three-Dimensional Modeling of Salado Brine Flow through Quarter Panel.....	159
GLOSSARY	161
APPENDIX A -- Material Property Values.....	167
REFERENCES	187

Figures

Figure

1-1	WIPP Location in Southeastern New Mexico	3
1-2	Level of WIPP Repository, Located in the Salado Formation	4
1-3	Stratigraphy at the Repository Horizon.....	5
1-4	Generalized Stratigraphic and Structural Cross Section of MB139.....	6
1-5	Marker Bed 139, One of Many Polyhalite Anhydrite Interbeds near the WIPP Repository Horizon	7
1-6	Proposed WIPP Repository, Showing Both TRU Disposal Areas and Experimental Areas	8
1-7	Schematic Diagram of Typical Backfilled and Sealed Access Shaft.....	10
1-8	Schematic of Typical Multicomponent Seals	11
1-9	Schematic of Typical Multicomponent Seal for Drifts and Panels	11
1-10	Subsystems and Components of WIPP Waste Containment System	13
1-11	Tasks Performed During the Five Major Steps of Assessing Regulatory Compliance of WIPP with 40 CFR 191, Subpart B.....	14
1-12	Basic Phenomena, Major Interactions, and Components of the Repository/Shaft Model.....	16
2-1	Hypothesized Episodes in Disposal Area Leading to Undisturbed Conditions.....	22
2-2	Hypothesized Episodes in Disposal Area after Human Intrusion	25
2-3	Schematic Diagram of Main Computer Modules Linked by CAMCON	30
3-1	Conceptual Model and Network for the Undisturbed Disposal System Modeled by NEFTRAN	38
3-2	Schematic and Boundary Conditions for SUTRA Simulation of Undisturbed Conditions (Set I)	39
3-3	Schematic and Boundary Conditions for Large-Scale SUTRA Calculations Used to Generate Boundary Conditions for Embedded Fine Zone (Set II)	40
3-4	Mesh of SUTRA Calculation of Undisturbed Repository/Shaft System for Sets I and II (Fine Mesh)	41
3-5	Closeup of SUTRA Mesh at Shaft-Drift Intersection for Sets I and II	42
3-6	Closeup of SUTRA Mesh at Panel Seal and Storage Room for Sets I and II.....	43
3-7	Pressure Contours for SUTRA Calculation Set I, Case IA, Showing Hydrostatic Boundary Condition Edge Effects	45

3-8	Pressure Contours for SUTRA Calculation Set I, Case IB (Degraded Properties), Showing Hydrostatic Boundary Condition Edge Effects.....	45
3-9	Pressure Contours for Large-Scale SUTRA Calculations Used to Provide Boundary Conditions for Set II, Case IA (Steady State).....	46
3-10	Pressure Contour Details for Large-Scale SUTRA Calculations Used to Provide Boundary Conditions for Set II, Case IA (Steady State).....	46
3-11	Pressure Contours for Large-Scale SUTRA Calculations Used to Provide Boundary Conditions for Set II, Case IB (Steady State).....	47
3-12	Pressure Contour Details for Large-Scale SUTRA Calculations Used to Provide Boundary Conditions for Set II, Case IB (Steady State).....	47
3-13	Comparison of Left and Right Boundary Conditions for Set II, Cases 1A, 1B with Hydrostatic Boundary Conditions for Set I (Steady State).....	48
3-14	Comparison of Top and Bottom Boundary Conditions for Set II, Cases 1A, 1B with Hydrostatic Boundary Conditions for Set I (Steady State).....	48
3-15	Solute Concentration Contours for SUTRA, Set I, Case IA, Expected Properties at 10,000 Yr.....	51
3-16	Solute Concentration Contours for SUTRA, Set I, Case IB, Degraded Properties at 10,000 Yr.....	51
3-17	Pressure Contours for SUTRA, Set II, Case IA, with Expected Properties and Boundary Conditions Interpolated from Large-Scale Simulation at 10,000 Yr.....	53
3-18	Solute Concentration Contours for SUTRA, Set II, Case IA, Expected Properties at 10,000 Yr.....	53
3-19	Pressure Contours for SUTRA, Set II, Case IB, Degraded Properties and Boundary Conditions Interpolated from Large-Scale Simulations at 10,000 Yr.....	54
3-20	Solute Concentration Contours for SUTRA, Set II, Case IB, Degraded Properties at 10,000 Yr.....	54
3-21	Pressure Contours for SUTRA, Set II, Case IC, No Shaft Seal at 10,000 Yr.....	55
3-22	Solute Concentration Contours for SUTRA, Set II, Case IC, No Shaft Seal at 10,000 Yr.....	55
3-23	Interstitial Velocities around Panel Seal, Set II, Case IA, Expected Properties at 10,000 Yr.....	56
3-24	Brine Volume Fluxes in and around the Seal and across Boundaries around a Disposal Room as Calculated by SUTRA.....	58
3-25	Schematic Diagram of Geometry and Boundary Conditions Used in the Air Intake Shaft Inflow Calculations.....	64
3-26	Mesh Used For Air Intake Shaft Simulations.....	65
3-27	Estimated Cumulative Air Intake Shaft Inflow (Q_t) vs. Time (t)	67

3-28	Plan View of Disposal Area and Finite Element Mesh Used for Gas Flow to Shafts.....	71
3-29	Time-Dependent Pressure Boundary Conditions at Center of Disposal Area (Node 152) for Gas Flow Simulation	72
3-30	Time Variation of Permeability Due to Consolidation for Disposal Area, Drift, and Seal (Calculation 4)	74
3-31	Gas Pressure Profile Using Unconsolidated Permeability for Drift, Seal, and Waste, Calculation 1, (a) 0 to 153 Yr and (b) 0 to 4.8 Yr	75
3-32	Gas Pressure Profile Using Unconsolidated Drift Permeability and Consolidated Seal and Waste Permeability, Calculation 2, (a) 142 to 1,565 Yr and (b) 1 to 153 Yr.....	76
3-33	Gas Pressure Profile Using Consolidated Permeability for Drift, Seal, and Waste, Calculation 3, (a) 142 to 1,565 Yr and (b) 1 to 153 Yr	77
3-34	Gas Pressure Profile Using Time-Dependent Permeability for Drift, Seal, and Waste, Calculation 4, (a) 142 to 1,565 Yr and (b) 1 to 153 Yr	78
3-35	Gas Pressure Profile without Seal and with Time-Dependent Drift and Waste Permeability, Calculation 5, (a) 142 to 1,565 Yr and (b) 1 to 153 Yr.....	80
3-36	Model of Disposal Area, Seal, and Drift (or Marker Bed 139) Leading to Shaft (83 Blocks).....	83
3-37	Comparison of Gas Pressure Profiles in Drift, Seal, and Waste Using SUTRA and BOAST	84
3-38	Gas Saturation Profiles in Marker Bed, Seal, and Waste, with Marker Bed Permeability Equal to 10^{-9} m ²	86
3-39	Gas Saturation Profiles in Marker Bed, Seal, and Waste, with Marker Bed Permeability Equal to 10^{-11} m ²	86
3-40	Gas Saturation Profiles in Marker Bed, Seal, and Waste, with Marker Bed Permeability Equal to 10^{-13} m ²	87
3-41	Gas Saturation Profiles in Marker Bed, Seal, and Waste, with Marker Bed Permeability Equal to 10^{-15} m ²	87
3-42	Gas Pressure Profiles in Marker Bed, Seal, and Waste, with Marker Bed Permeability Equal to 10^{-13} m ²	89
3-43	Gas Pressure Profiles in Marker Bed, Seal, and Waste, with Marker Bed Permeability Equal to 10^{-15} m ²	89
4-1	Boundary Conditions Applied in Borehole Model and Axisymmetric Mesh for SUTRA Calculations of an Intrusion Borehole through a Waste Panel.....	95
4-2	Variation of Mass Flux to a Borehole as a Function of Waste Permeability at Several Pressure Gradients Assuming Steady-State Conditions.....	96
4-3	Variation of Transient Mass Flux to a Borehole as a Function of Waste Permeability.....	97

4-4	Pressure Contours near Cylindrical Waste Panel at 10,000 Yr for a Capacitance of (a) $5.1 \times 10^{-9} \text{ Pa}^{-1}$ and (b) $7.8 \times 10^{-12} \text{ Pa}^{-1}$	99
4-5	Variation of Cumulative Flux with Permeability at a Salado Formation Capacitance of $5.1 \times 10^{-9} \text{ Pa}^{-1}$, $7.54 \times 10^{-11} \text{ Pa}^{-1}$, and $7.8 \times 10^{-12} \text{ Pa}^{-1}$	100
4-6	Variation of Fraction of Panel Accessed with Permeability at a Salado Formation Capacitance of $5.1 \times 10^{-9} \text{ Pa}^{-1}$, $7.54 \times 10^{-11} \text{ Pa}^{-1}$, and $7.8 \times 10^{-12} \text{ Pa}^{-1}$	100
4-7	Radial Distance versus Time for Neutrally Buoyant Particle in Transient Velocity Field for Capacitance of $7.8 \times 10^{-12} \text{ Pa}^{-1}$ as Calculated by TRACKER	101
4-8	Schematic Diagram of Stratigraphy Surrounding Repository Showing Potential Discharge Paths to an Exploratory Borehole.....	103
4-9	Simple Analytical Model for Potential Discharge Paths to an Exploratory Borehole	104
4-10	Analytical Estimates of Diversion Fraction as a Function of Relative Anhydrite Permeability for Three Values of Relative Halite Permeability	105
4-11	Geometry and Boundary Conditions for Diversion Fraction Finite-Element Model Assuming Steady-State Conditions.....	106
4-12	Conceptual Model of Repository Flow Field Considered in Calculation of Access Fraction from Brine Pocket Flow	113
4-13	Schematic Diagram of the Geometry Used for Calculating Access Fraction from Brine Pocket Flow	114
4-14	Estimated Characteristic Response Time in Seconds of Each Model Component to Stress Changes at the Region Boundary for Flow from a Brine Pocket.....	119
4-15	Model Grid and Boundary Condition Locations for Brine Pocket Calculation.	123
4-16	Steady-State Diversion Fraction versus Borehole/Waste Permeability Ratio	124
4-17	Schematic Diagram Illustrating the Region from which Soluble Species Will Be Removed by Brine Pocket Flow in Specified Time, t_r	126
4-18	Estimated Number of Pore Volumes Circulated as a Function of Flow Radius at the Center of Repository for Three Values of $k_{\text{borehole}}/k_{\text{waste}}$	128
4-19	Schematic Diagram Showing Repository Region and Boundary Conditions for Evaluating Characteristic Depressurization Times.	132
4-20	Mesh for Cylindrical Model of Room with Gas for Evaluating Characteristic Depressurization Times.....	132
4-21	Quarter Panel Mesh and Boundary Conditions for Two-Dimensional SUTRA Calculation.....	138
4-22	Vertical Mass Flux as a Function of Time as Calculated by Cylindrical SUTRA Model	139
4-23	Mesh for HST3D Flow Simulation of WIPP Quarter Panel.....	140

4-24	Fraction of Waste Accessed in 10,000 Yr with Waste Permeabilities of 10^{-13} and 10^{-19} m^2 , and Capacitances of 7.8×10^{-12} Pa^{-1} and 7.54×10^{-11} Pa^{-1}	141
4-25	Fraction of Waste Accessed in 10,000 Yr with Waste Permeabilities of 10^{-13} and 10^{-19} m^2 and Capacitance of 5.1×10^{-9} Pa^{-1}	142
4-26	Comparison of Access Fraction versus Waste Permeability for Cylindrical and Actual Panel Geometry	143
4-27	Comparison of Salado Formation Inflow Rates from SUTRA and One-Dimensional Model for Base-Case Parameter Values	145
4-28	Pressure Contours Showing Very Little Pressure Disturbance about WIPP Quarter Panel after 10,000 Yr with Capacitance Equal to 5.1×10^{-9} Pa^{-1}	146
4-29	Comparison of Vertical Flux into a Waste Panel as Calculated by SUTRA and HST3D.....	146
4-30	Schematic Diagram of Salado Formation Pressure Development Due to Depressurization of Two Parallel Room Excavations	148
4-31	Radial and One-Dimensional Estimates of Flow Rate per Unit Length of Room Excavation	149
4-32	Two-Dimensional Flow Rates to Three Different Fixed-Pressure Boundaries	151
A-1	Excavated and Enclosed Areas in the WIPP Repository.....	184
A-2	Planned Dimensions of WIPP Repository and Access Drifts	185

Tables

Table

3-1	Material Properties for SUTRA Model of Radionuclide Migration Pathway	50
3-2	Comparison of Volume Flux Between SUTRA and NEFTRAN	60
3-3	Hydrologic Properties and Boundary Conditions Used in Air Intake Shaft Saturation Simulations	66
3-4	Estimated Inflow Volumes and Rates for the Various Salado Formation Permeabilities and Boundary Conditions	66
3-5	Pertinent Material Properties for Gas Flow through Drift to Shaft	72
3-6	Gas Pressure in Waste Room Obtained Using SUTRA and BOAST	85
4-1	Maximum Repository Volume Accessed by Brine and Cumulative Mass Flux in 10,000 Yr under Steady-State Conditions	97
4-2	Maximum Repository Volume Accessed by Brine and Cumulative Mass Flux in 10,000 Yr under Transient Conditions For Salado Capacitance of 5.1×10^{-9} Pa ⁻¹	101
4-3	Parameter Descriptions and Corresponding Fluxes and Diversion Fractions for the Steady-State Local Numerical Model	108
4-4	Maximum Range of Characteristic Times and Intermediate Parameter Values for Components of the Cylindrical Model of Flow from a Brine Pocket	117
4-5	Flow Rates and Associated Diversion Fractions Estimated with SUTRA for Five Borehole/Waste Permeability Ratios	124
4-6	Volume of Flow Diverted through Repository for Selected Combinations of Diversion Fraction and Brine Pocket Discharge Volume	125
4-7	Access Radius, Access Volume, and Volumetric Access Fraction for Selected Combinations of Borehole/Waste Permeability Ratio and Brine Pocket Discharge Volume	130
4-8	Estimated Access Volumes and Repository Flow Volumes Associated with the Three Repository Flow Field Components Created by Exploratory Borehole Plug Degradation in 10,000 Yr	130
4-9	Estimated Gas Depressurization Time Constants for Selected Values of Waste Permeability	134
4-10	Estimated Brine Depressurization Time Constants for Selected Values of Waste Permeability	135
A-1	Parameter Values for Salado Formation	170
A-2	Parameter Values for Marker Bed 139	171
A-3	Parameter Values for Culebra Dolomite Member of Rustler Formation	172

A-4	Parameter Values for Castile Formation Brine Pocket	173
A-5	Relative Permeabilities for Typical Salt.....	174
A-6	Parameter Values for Engineered Materials.....	175
A-7	Parameter Values for Unmodified Average Waste.....	176
A-8	Parameter Values for Specific Materials.....	177
A-9	Fluid Properties	180
A-10	Salado Brine Compressibility.....	181
A-11	Climate Variability and Intrusion Characteristics	182
A-12	Summary of Excavated and Enclosed Areas and Initial Volumes of Excavated Regions within the WIPP Repository, not Considering Closure.....	183
A-13	Depths of Stratigraphic Layers around Waste, Exhaust, and C&SH Shafts.....	186

NOMENCLATURE

MATHEMATICAL SYMBOLS

A	- cross-sectional area (m^2)
a	- constant
a_{mix}	- mixture constant for gas in Redlich-Kwong gas equation of state
b	- aquifer thickness (m)
b_{mix}	- mixture constant for gas in Redlich-Kwong gas equation of state
C	- concentration (kg/m^3)
\hat{C}	- mass fraction (kg/kg)
C_m	- constants required by the initial/boundary conditions
C_s	- specific heat (J/kg/K)
c	- capacitance (S_s/γ) (Pa^{-1})
D°	- molecular diffusion in fluid (m^2/s)
D^*	- molecular dispersivity in porous media (m^2/s) ($D^* = a \tau D^\circ$)
d	- hydraulic diffusivity ($K/S_s = \frac{k}{\mu c}$)
E	- Young's modulus (Pa)
e	- fracture aperture (m)
F_ℓ	- function representing ℓ^{th} consequence module of CAM
g	- gravity constant, $9.79 m/s^2$ at repository level
H	- hydraulic head (m)
i	- hydraulic gradient, $\Delta H/\Delta z$
K	- hydraulic conductivity (m/s)
K_d	- distribution (or partition) coefficient (m^3/kg)
k	- permeability (m^2)
ℓ	- length (m)
M	- total mass (kg)

- m - mass flux rate (kg/s)
- $P(\hat{R}_k > R)$ - probability of $\hat{R}_k > R$
- $P(\hat{R}_k > R | S_j)$ - conditional probability of $\hat{R}_k > R$ given scenario S_j occurs
- p - pressure (Pa)
- p_{ci} - critical pressure of species i (Pa)
- Q - total fluid discharge (m^3)
- q - fluid discharge rate (m^3/s)
- R - resistance
- \bar{R} - universal gas constant $8.31434 \frac{Pa \cdot m^3}{gmole \cdot K}$
- \hat{R} - calculated summed normalized releases (EPA sum)
- r - radius (m)
- S - solubility (kg chemical/ m^3 fluid)
- S_s - specific storage [m^{-1}]
- T - transmissivity (Kb) (m^2/s)
- \bar{T} - temperature (K)
- \bar{T}_{ci} - critical temperature of species i (K)
- t, t_c, t_r, t_s - time, characteristic time, travel time, and reference volume time, respectively (s)
- $t_{1/2}$ - radionuclide half-life (s)
- v - velocity (m/s)
- w_{i_k} - predicted release at time t for radionuclide i for run k
- x, y, z - variable
- y_i - mole fraction of species i
- Z - gas compressibility factor
- α_L, α_T - dispersivity, longitudinal and transverse, respectively (m)
- β_s, β_f - material compressibility of solids and fluid, respectively (Pa^{-1})

χ	- eigenvalue
ϕ	- porosity
Ω	- total volume (m ³)
ρ	- density (kg/m ³)
$\dot{\rho}$	- mass source density (kg/[m ³ -s])
γ	- specific weight/unit area (kN/m ³) = ρg
$\psi_m(\chi)$	- eigenfunctions appropriate for the given geometry and boundary conditions
μ	- fluid viscosity (Pa-s)
\bar{v}	- molar specific volume (m ³ /gmole)
ν	- Poisson's ratio
τ	- tortuosity in porous media (ℓ/ℓ_{path}) ²
ω	- molecular weight

ACRONYMS AND INITIALISMS

ALGEBRA	- support program module for manipulating data in CAMDAT
BLOT	- a mesh and curve plot support program for CAMDAT data
BOAST II	- Black Oil Applied Simulation Tool, a program to simulate simultaneous flow of three immiscible fluids (oil, water, and gas) in a three-dimensional porous medium
CAM	- Compliance Assessment Methodology
CAMCON	- Compliance Assessment Methodology CONtroller--controller (driver) for compliance evaluations developed for WIPP
CAMDAT	- Compliance Assessment Methodology DATa--computational data base developed for WIPP
CCDF	- Complementary Cumulative Distribution Function
CH	- Contact Handled (TRU waste)
C2FINTRP	- support program to interpolate boundary conditions from a coarse to embedded fine mesh

C&SH - Construction and Salt Handling Shaft

DOE - U.S. Department of Energy

DRZ - Disturbed Rock Zone

EPA - U.S. Environmental Protection Agency

FD - Finite Difference numerical analysis

FE - Finite Element numerical analysis

GENMESH - rectilinear three-dimensional FD mesh generator (main program)

HLW - High-Level Waste

HST3D - Heat and Solute Transport Code in 3-Dimensions, a main program to simulate heat and solute transport in three-dimensional groundwater flow system

MATSET - a support program to insert user-selected parameter or material values into the computational data base

MB139 - Marker Bed 139

NEFTRAN - NEtwork Flow and TRANsport code (main program)

PREHST - pre-processor (translator) for input to HST3D

PRENEF - pre-processor (translator) for input to NEFTRAN

PRESUTRA - pre-processor (translator) for input to SUTRA

POSTHST - post-processor (translator) of output from HST3D to CAMDAT

POSTSUTRA - post-processor (translator) of output from SUTRA to CAMDAT

QA - Quality Assurance

RCRA - Resource, Conservation, and Recovery Act of 1976 (Public Law 94-580) and subsequent amendments (e.g., HSWA--Hazardous and Solid Waste Amendments of 1984); codified as *40 CFR 260-280*.

RH - Remote Handled (TRU waste)

SNL - Sandia National Laboratories, Albuquerque, NM

SUTRA - Saturated-Unsaturated TRANsport code (main program)

TRACKER - a support program to estimate the pathway of a neutrally buoyant particle released in a fluid velocity field

TRU - TRansUranic
WIPP - Waste Isolation Pilot Plant
40 CFR 191 - Code of Federal Regulations, Title 40, Part 191

1. INTRODUCTION

1.1 PURPOSE AND ORGANIZATION OF REPORT

PURPOSE

This report presents preliminary analyses of brine and gas flow through the rooms, drifts, seals, and shafts that make up the repository/shaft system of the Waste Isolation Pilot Plant (WIPP), assuming various conditions and using several different models. The analyses primarily examine brine and gas transport. Mechanical phenomena, such as creep closure of the repository, or chemical phenomena, such as solubility of radionuclides within the room environment, are not included. The purpose of these analyses is to evaluate the importance of various phenomena and components to the performance of this transuranic (TRU) waste repository.

Preliminary calculations of the repository/shaft system are being reported now to help evaluate various engineered modifications to the waste, backfill, and room design that are being proposed to ensure compliance with Subpart B of the Environmental Protection Agency's (EPA) *Environmental Standards for the Management and Disposal of Spent Nuclear Fuel, High-Level and Transuranic Waste* (hereafter referred to as either "the Standard" or *40 CFR 191, Subpart B*). The Standard regulates disposal of TRU waste from U.S. Department of Energy (DOE) weapon facilities.

Although care was taken in developing models for the calculations presented here, the calculations must be considered preliminary in nature; further development is ongoing. As refinements continue and model assumptions become more accurate, results and conclusions may change.

ORGANIZATION

The report is composed of five chapters. This Introduction provides some background on the WIPP, on sensitivity analysis, and on the capabilities of the software developed to assess regulatory compliance of the WIPP with *40 CFR 191, Subpart B*. The material covered in this chapter is general knowledge to readers familiar with the WIPP; such readers may want to skip to Chapter 2 after glancing at the Chapter 1 figures. However, readers who are not familiar with either the WIPP or the compliance assessment process should find the rest of this chapter helpful. Also, a glossary of terms can be found at the end of the report.

Chapter 2 summarizes the immediate technical issues of the WIPP that must be resolved, the types of conceptual models developed for these analyses, and the computer programs used to develop computational models of the conceptual models. Chapter 3 describes in detail the computational models and results of modeling brine flow through the WIPP repository assuming undisturbed conditions (e.g., no human intrusion). Chapter 4 describes the computational models and results assuming human intrusion into the TRU waste disposal area. The results and conclusions of these preliminary calculations are summarized in Chapter 5. Appendix A contains a listing of the material properties used for the models described in Chapters 3 and 4. Variables, acronyms, and initialisms used throughout are defined in the Nomenclature at the front of the document.

1.2 BACKGROUND ON WIPP

PURPOSE OF WIPP

The WIPP was authorized by Congress in 1979 as a research and development facility to demonstrate the safe management, storage, and eventual disposal of TRU waste generated by defense programs (Public Law 96-164, 1980). Only after demonstrating compliance with *40 CFR 191, Subpart B* and the Resource, Conservation, and Recovery Act of 1976 (RCRA) will the DOE dispose of TRU waste at the WIPP repository.

SNL ROLE IN PROJECT

Besides the DOE project office in Carlsbad, NM, which oversees the project, the WIPP currently has two major participants: Sandia National Laboratories (SNL) in Albuquerque, NM, which functions as scientific investigator; and Westinghouse Electric Company, which is responsible for the management of WIPP operations. The specific tasks of SNL are (1) characterizing the disposal system and responding to specific concerns of the State of New Mexico, (2) carrying out performance assessment (i.e., ensuring regulatory compliance with *40 CFR 191, Subpart B*, except the Assurance Requirements), (3) performing analytic, laboratory, field experiments, and applied research to support disposal system characterization and performance assessment relevant to nuclear waste disposal in salt, and (4) providing ad hoc scientific and engineering support (e.g., supporting environmental assessments). This report helps fulfill the performance assessment task.

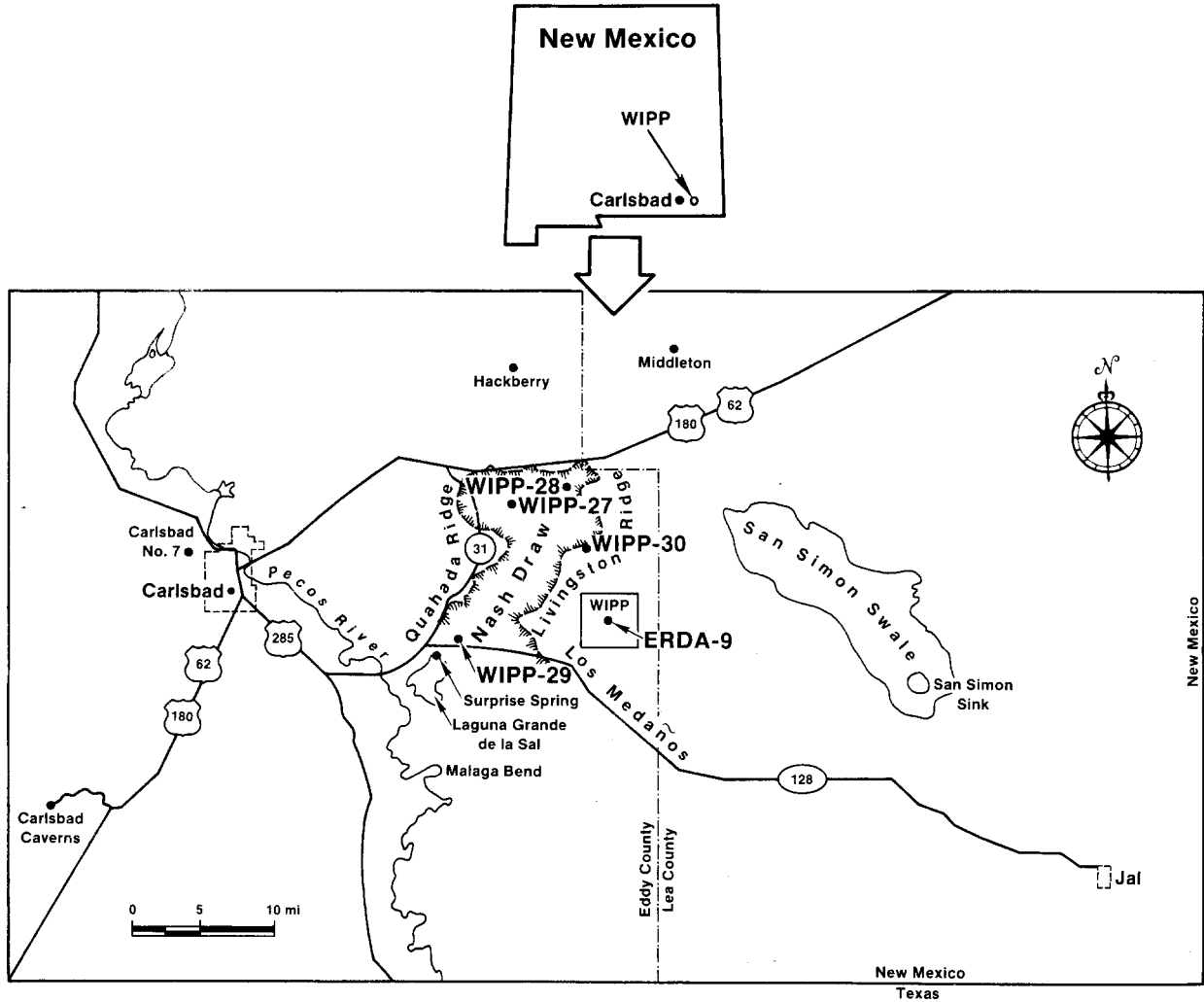
LOCATION AND STRATIGRAPHY

The WIPP is located in southeastern New Mexico, approximately 38 km (24 mi) east of Carlsbad, an area of low population density (Figure 1-1). Fewer than 30 permanent residents live within a 16-km (10-mi) radius. The location was chosen because of the underlying 600-m (2,000-ft)-thick Salado Formation and 300-m (1,000-ft)-thick Castile Formation marine evaporites, which are a desirable medium for nuclear waste disposal. The repository level is located within these bedded salts about 657 m (2,155 ft) below the surface and 390 m (1,300 ft) above sea level (Figure 1-2). The bedded salts consist of thick halite and interbeds of minerals such as clay and anhydrites of the late Permian period (Ochoan series) (approximately 255 million yr old*) that do not support flowing water (Figure 1-3). One interbed of interest to this report, Marker Bed 139 (MB139), is located about 1 m (3.3 ft) below the repository interval (Figure 1-3), is about 1 m (3.3 ft) thick (Figure 1-4), and is one of about 45 siliceous or sulfatic units within the Salado Formation consisting of polyhalitic anhydrite (Figure 1-5) (Lappin, 1988; Tyler et al., 1988).

DESIGN OF REPOSITORY, BACKFILL, AND SEALS

The WIPP repository is composed of a single underground disposal level connected to the surface by four shafts (Figure 1-6). The repository level consists of an experimental area at the north end and a disposal area at the south end. The 100-acre disposal area contains all of the underground facilities for waste handling, waste disposal, operations, and maintenance.

* This time period reflects the revised 1983 geological timescale.



TRI-6334-53-1

Figure 1-1. WIPP Location in Southeastern New Mexico (after Rechar, 1989).

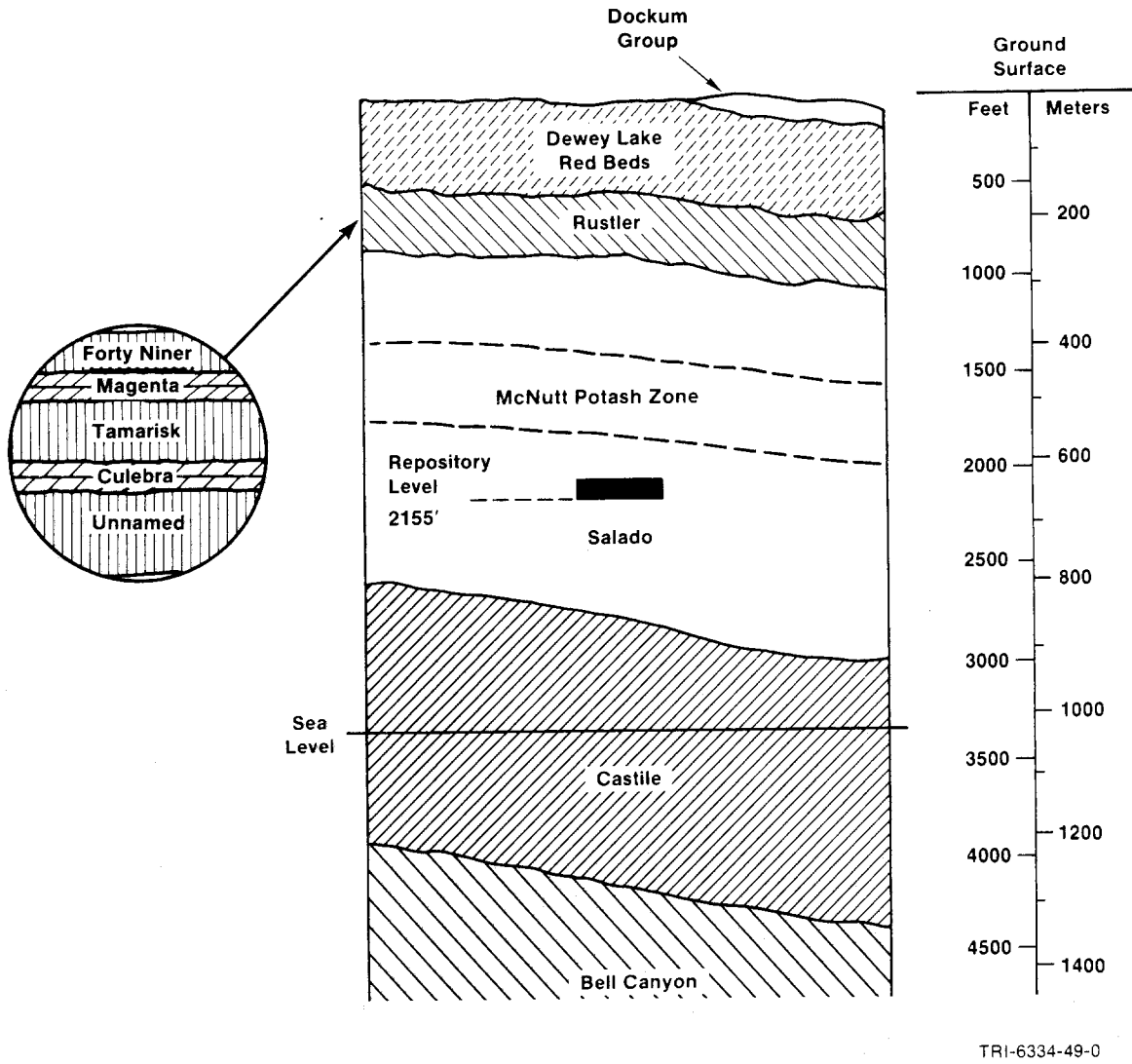


Figure 1-2. Level of WIPP Repository, Located in the Salado Formation. The Salado Formation is composed of thick halite with thin interbeds of clay and anhydrite deposited as marine evaporites about 255 million years ago (Permian period) (Rechard, 1989).

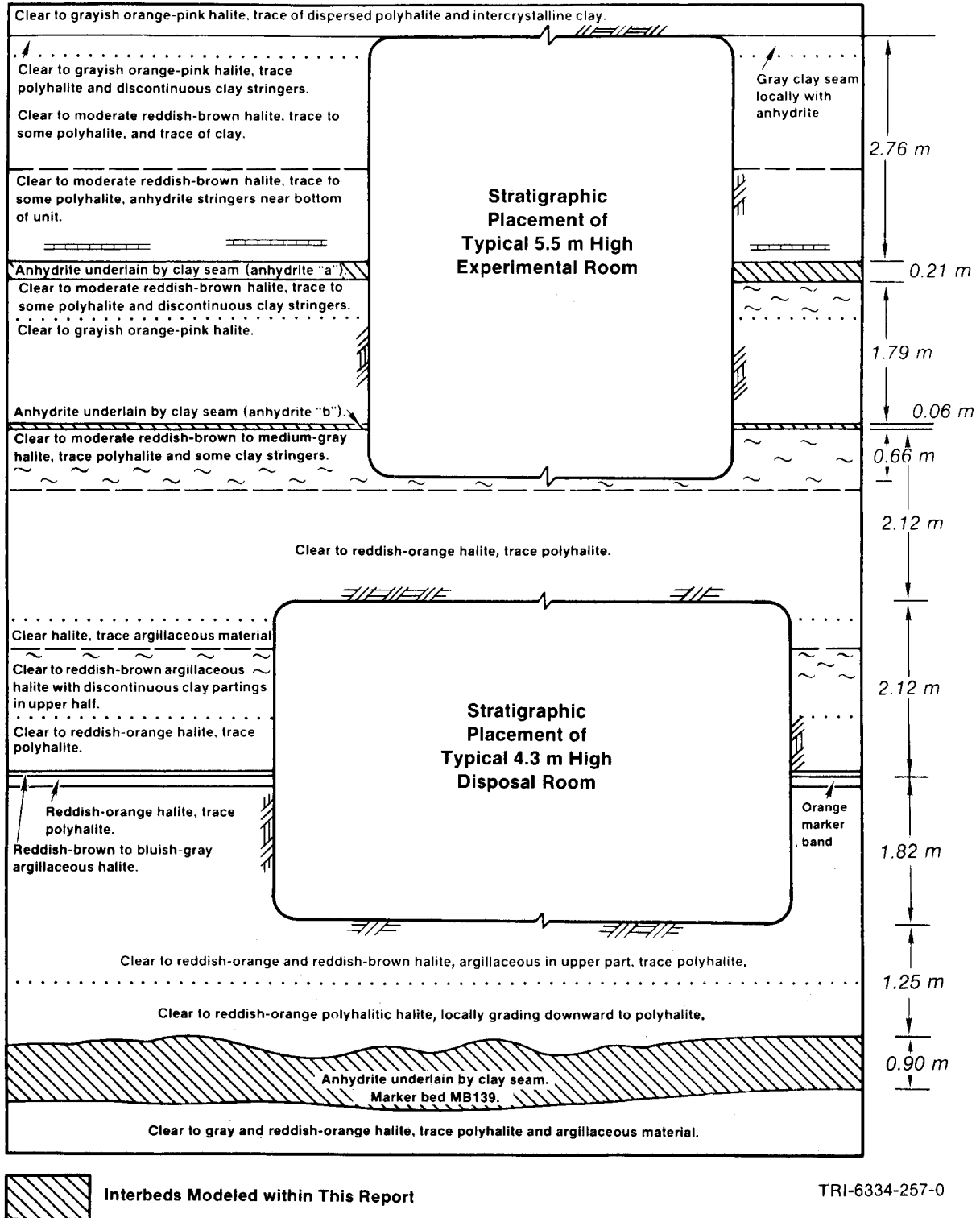
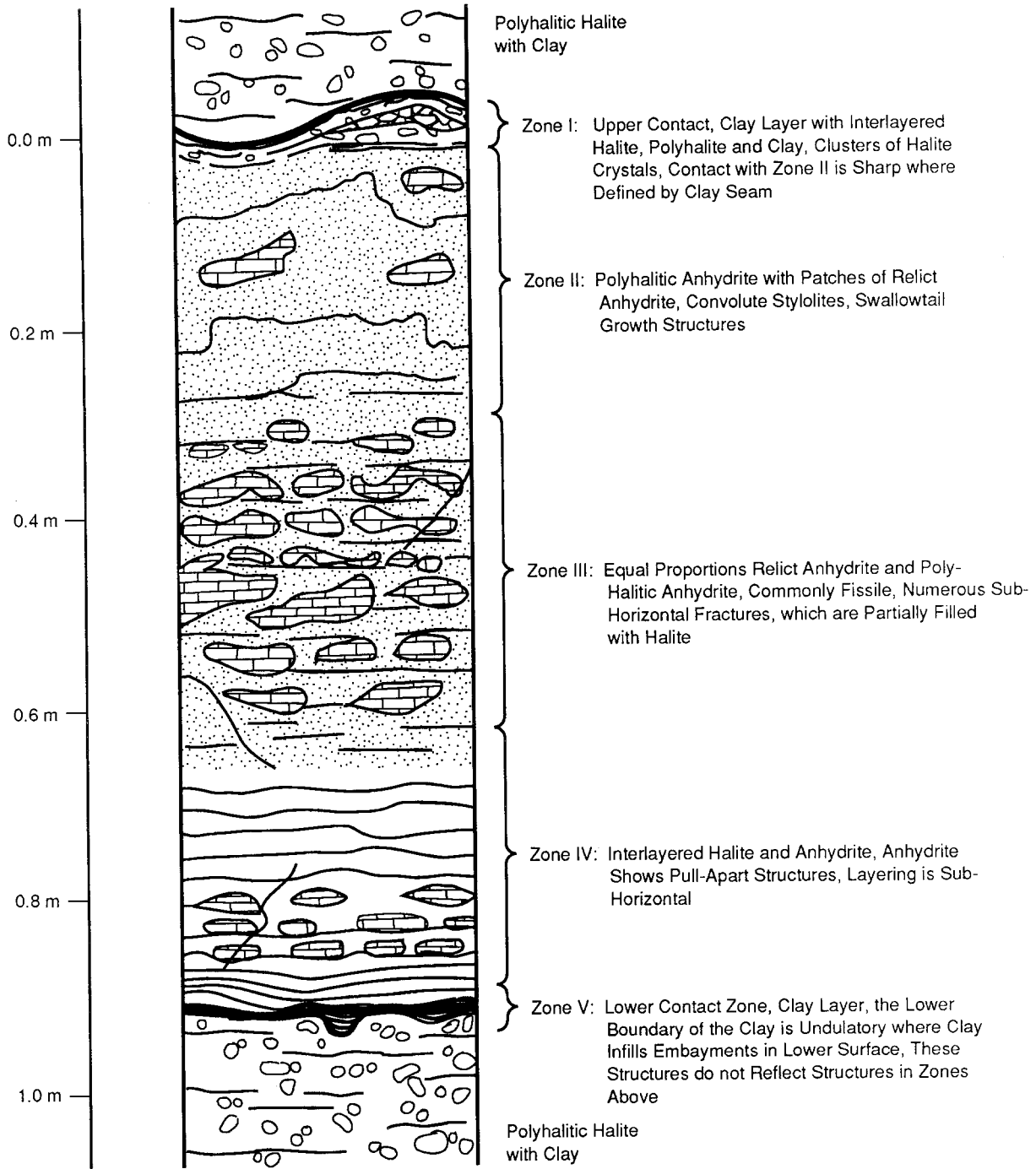
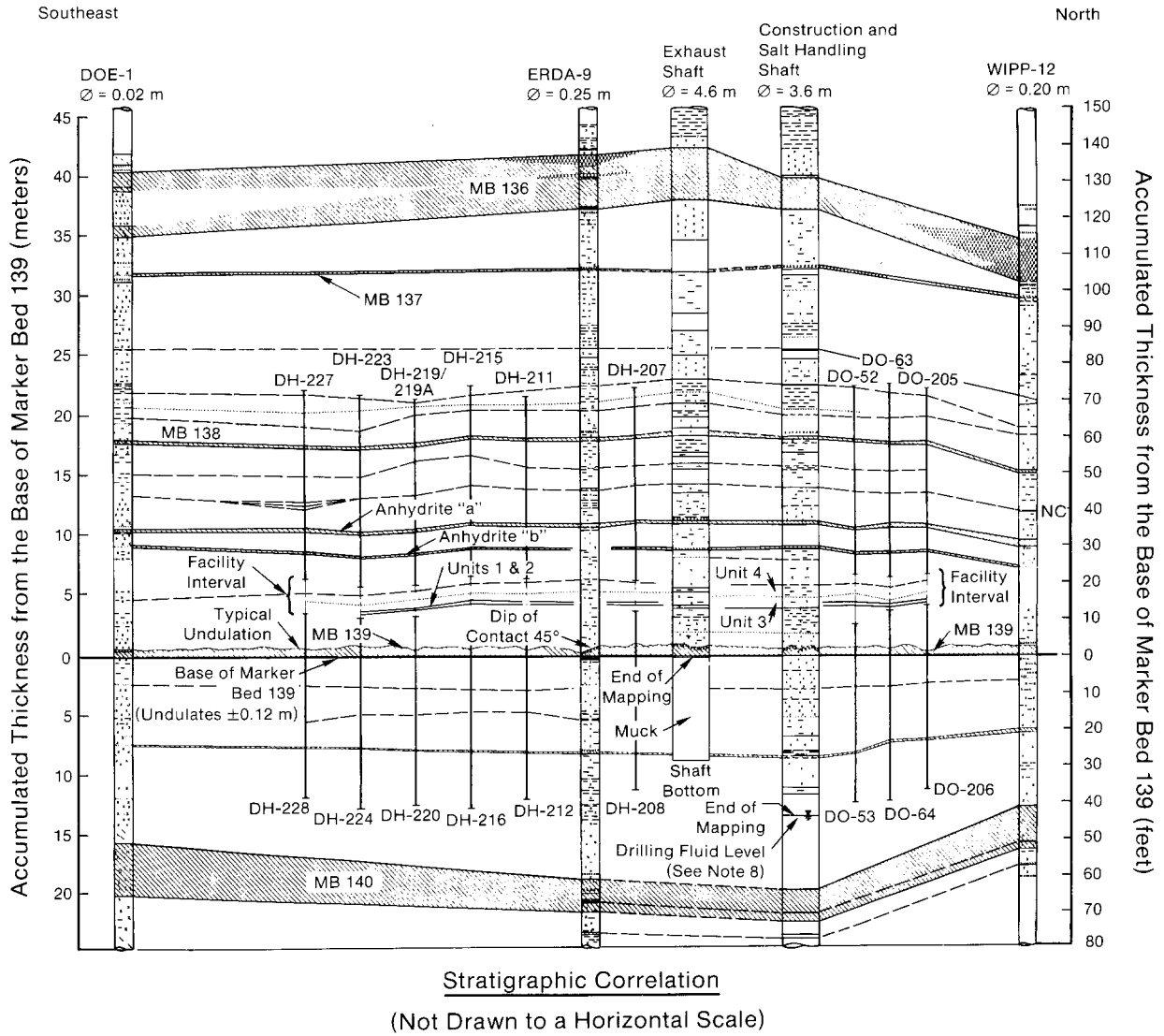


Figure 1-3. Stratigraphy at the Repository Horizon (after Lappin et al., 1989). Units in disposal area dip slightly to the south, but disposal excavations are always centered about the orange marker band (reddish-orange halite).



TRI-6334-220-0

Figure 1-4. Generalized Stratigraphic and Structural Cross Section of MB139. The figure demonstrates the internal variability of the unit and the character of both the upper and lower contacts (after Borns, 1985).



TRI-6334-240-0

Figure 1-5. Marker Bed 139, One of Many Polyhalite Anhydrite Interbeds near the WIPP Repository Horizon.

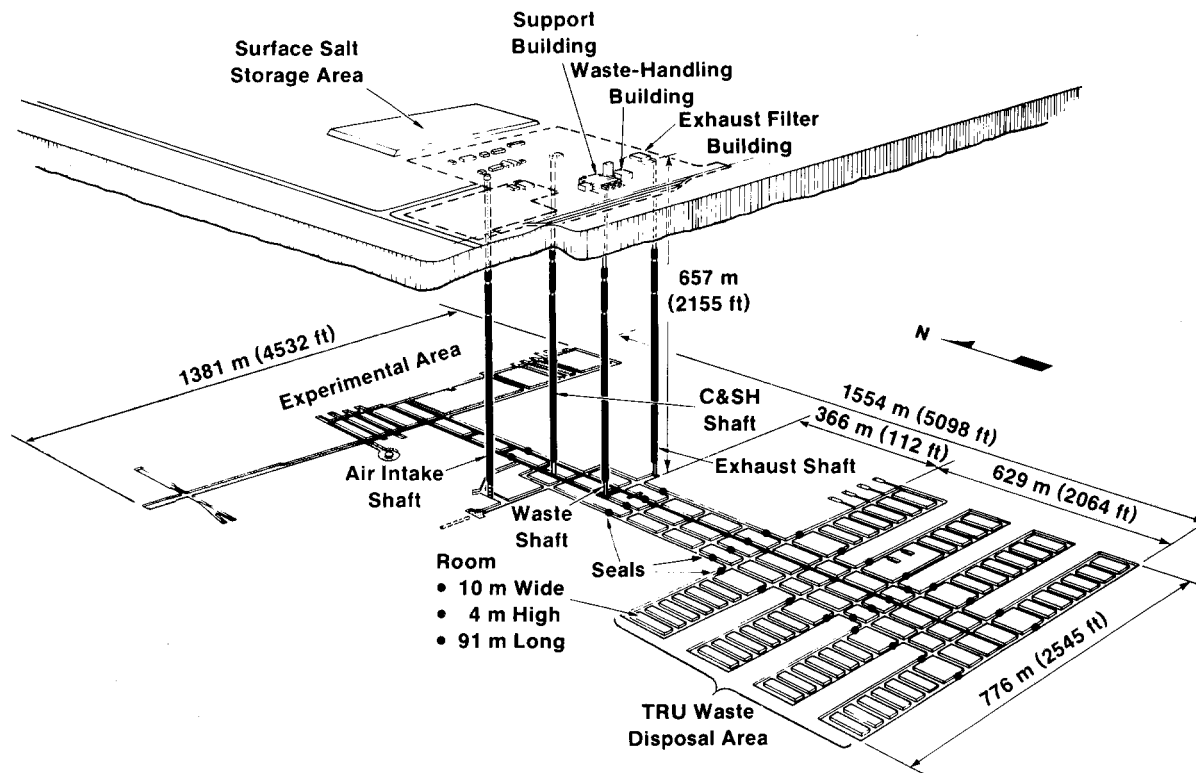


Figure 1-6. Proposed WIPP Repository, Showing Both TRU Disposal Areas and Experimental Areas (after Nowak et al., 1990).

The four shafts are (1) the Air Intake Shaft, 5 m (16 ft) in diameter; (2) the Exhaust Shaft, 4 m (14 ft) in diameter, (3) the Construction and Salt Handling (C&SH) Shaft, 3 m (10 ft) in diameter, and (4) the Waste Shaft, 6 m (19 ft) in diameter. The Waste Shaft is designed to permit the transport of radioactive waste between the surface waste-handling facilities and the underground disposal area and also provides access for personnel, materials, large equipment, and diesel fuel. The shafts will be sealed upon decommissioning of the WIPP (Figures 1-7 and 1-8) (Nowak et al., 1990).

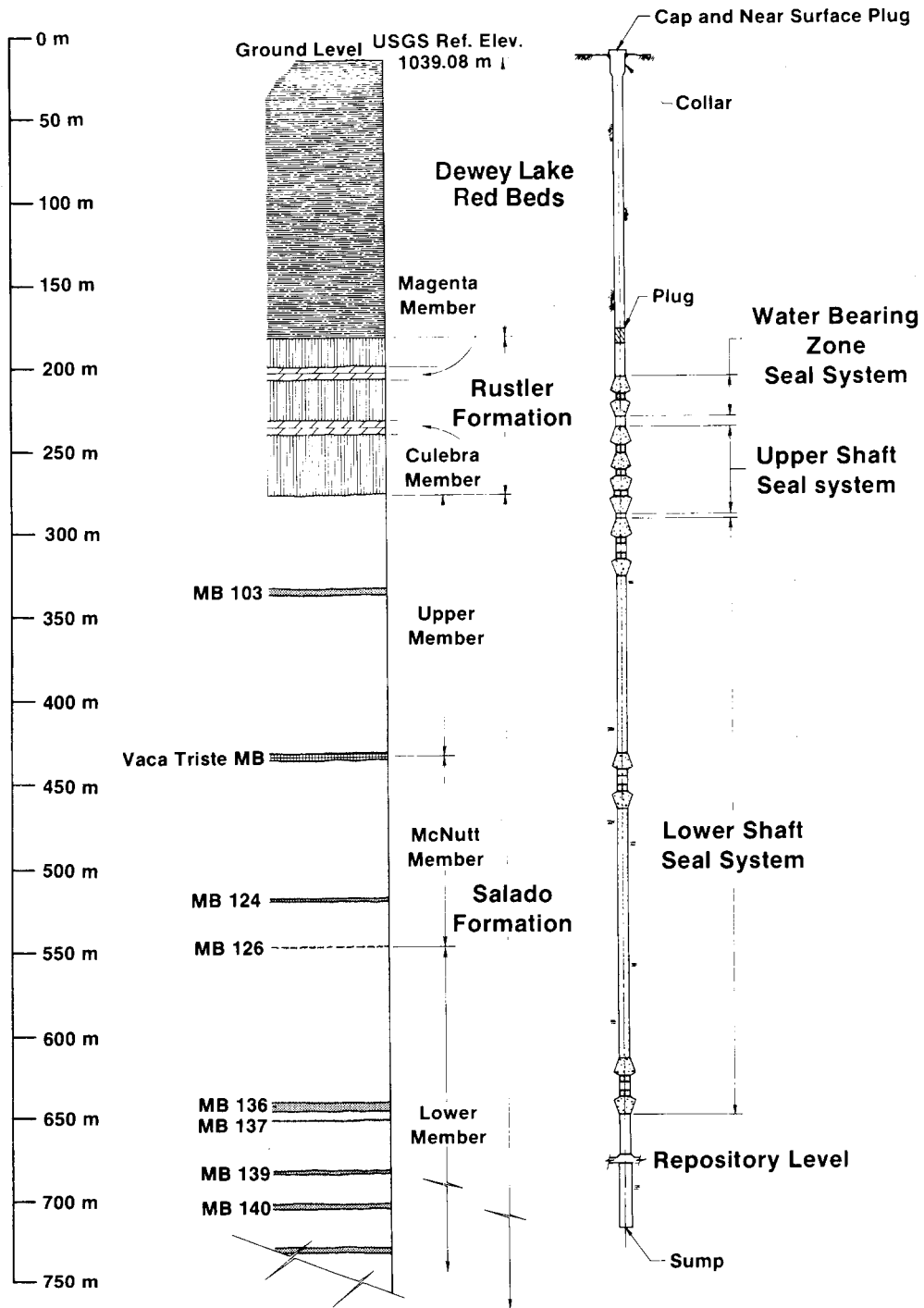
All of the underground openings are in the same stratigraphic interval, which dips slightly to the south, and rectangular in cross section. The disposal area drifts are generally 4 m (13 ft) high by 8 m (25 ft) wide; the disposal rooms are 4 m (13 ft) high, 10 m (33 ft) wide, and 91 m (300 ft) long. Other drifts range from about 2 to 4 m (8 to 12 ft) high and 4 to 8 m (14 to 25 ft) wide. The width of the pillars between rooms is 30 m (100 ft). (Specific dimensions can be found in Appendix A.) The drift entries to the disposal areas will be sealed to isolate the disposal panels. The reference design uses a multiple-component seal approximately 40 m (131 ft) long (Figure 1-9) (Nowak et al., 1990). The conceptual design for sealing the MB139 envisions a salt-based grout, if sealing is necessary (Nowak and Tyler, 1989) (Figure 1-9).

DESCRIPTION OF WASTE FORM AND CONTAINERS

The TRU waste, generated at defense-program facilities, consists of laboratory and production trash such as glassware, metal pipes, solvents, disposable laboratory clothing, cleaning rags, and solidified sludges, contaminated by alpha-emitting transuranic elements with atomic numbers greater than uranium-92, half-lives greater than 20 yr, and curie contents greater than 100 nCi/g. Approximately 60 percent of the waste may also be co-contaminated with waste considered hazardous under the RCRA, e.g., lead (WEC, 1989). Current plans specify that most of the TRU waste generated since 1970 will be placed in the WIPP repository, with the remainder to be disposed of at other DOE facilities.

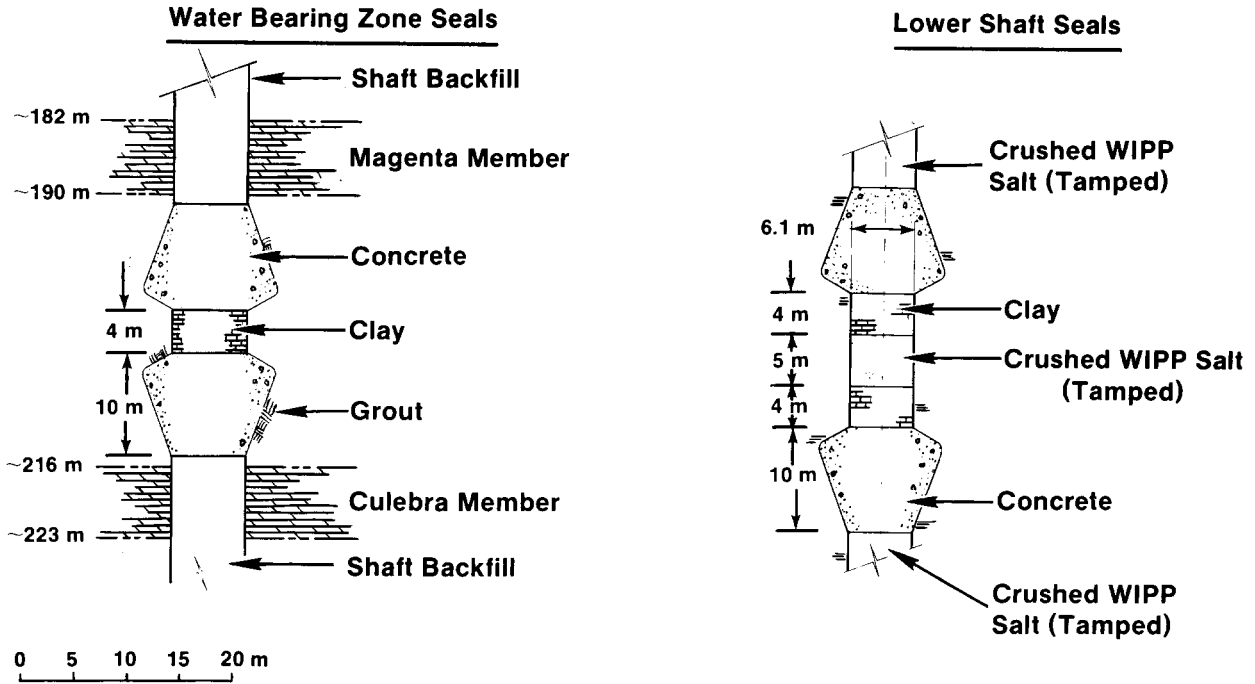
Although only about one-third of the waste currently exists, the WIPP, if licensed, will ultimately dispose of about $1.2 \times 10^5 \text{ m}^3$ ($4 \times 10^6 \text{ ft}^3$) of TRU waste. Radioactive waste emitting alpha radiation, although dangerous if inhaled or ingested, is not hazardous externally, and can be safely handled if confined in a sealed container (i.e., contact-handled [CH]). The projected CH-TRU waste consists of about 380,000 0.21-m^3 (55-gal) steel drums, 6,000 3.2-m^3 (113-ft^3) steel and plywood boxes, and 13,500 1.8-m^3 (64-ft^3) steel boxes (Lappin et al., 1989). The total curie content of the CH-TRU waste is about $9.4 \times 10^6 \text{ Ci}$. Although a room can ideally store 6,800 noncompacted drums stacked three deep, each of the 56 rooms and associated access drifts (about 56 room equivalents) will contain a repository average of 5,200 drum-equivalents.

A small portion of the TRU waste must be transported and handled in shielded casks (remotely handled [RH]). The total curie content is being determined but must be less than $5.1 \times 10^6 \text{ Ci}$ according to the agreement between DOE and the State of New Mexico (DOE/NM, 1984). The RH-TRU containers will be stored horizontally in the walls of the rooms. All CH- and RH-TRU waste must meet the WIPP Waste Acceptance Criteria (WEC, 1985) and be certified for shipment to the WIPP.



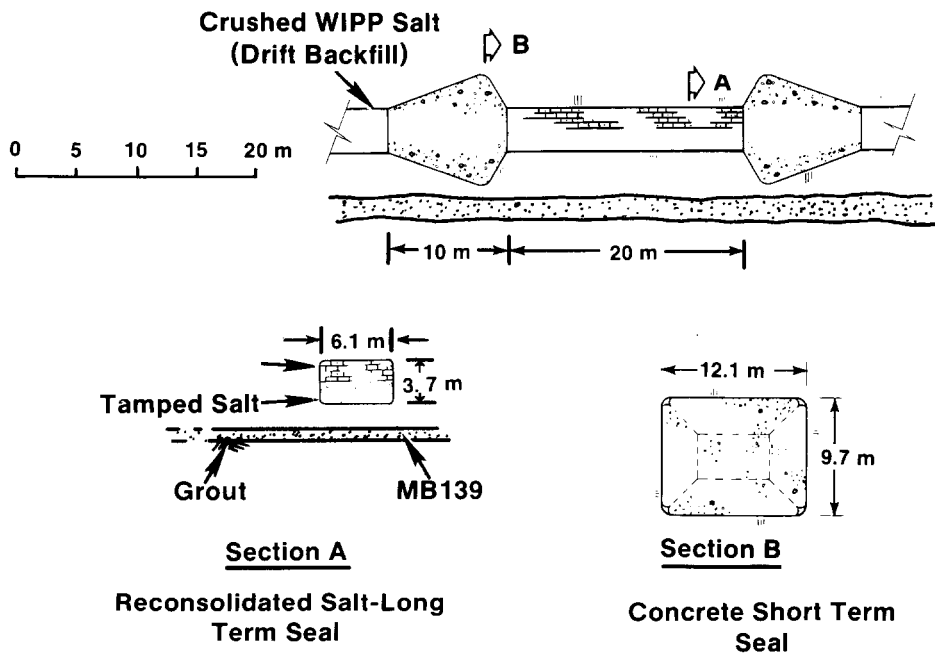
TRI-6342-311-0

Figure 1-7. Schematic Diagram of Typical Backfilled and Sealed Access Shaft (after Nowak et al., 1990).



TRI-6342-309-0

Figure 1-8. Schematic of Typical Multicomponent Seals. The drawing shows a seal between water-bearing units (e.g., Culebra Dolomite) (upper left) and part of the Lower Shaft Short-Term Seal (e.g., at Vaca Triste) for Waste Shaft (upper right) (after Nowak et al., 1990).



TRI-6342-308-0

Figure 1-9. Schematic of Typical Multicomponent Seal for Drifts and Panels (after Nowak et al., 1990).

WIPP WASTE CONTAINMENT SYSTEM

Figure 1-10 depicts the entire WIPP waste containment system including its three subsystems (institutional controls, engineered barriers, and geologic barriers) and its major components. The physical features of the repository that were described in the previous sections (e.g., stratigraphy, design of repository, waste form) are components of the engineered and geologic barrier subsystems. The disposal system defined in *40 CFR 191, Subpart B*, consists of the engineered barrier and geologic barrier subsystems. The third subsystem, institutional controls, consists of many parts, e.g., the legal ownership and regulations of the land and resources by the U.S. Government, the fencing and signs around the property, permanent markers, public records and archives, and other methods of preserving knowledge about the disposal system.

As part of the compliance assessment (i.e., determining whether the WIPP complies with *40 CFR 191, Subpart B*), analysts investigate how the disposal system behaves under specific scenarios, i.e., combinations of events and processes that represent possible future conditions at the repository. Depending on the scenario, different pieces of the engineered and geologic barrier subsystems are assembled into a system that can be modeled. In this report, the repository/shaft subsystem* is modeled with the backfill component, seal component, and a portion of the Salado Formation (Figure 1-10).

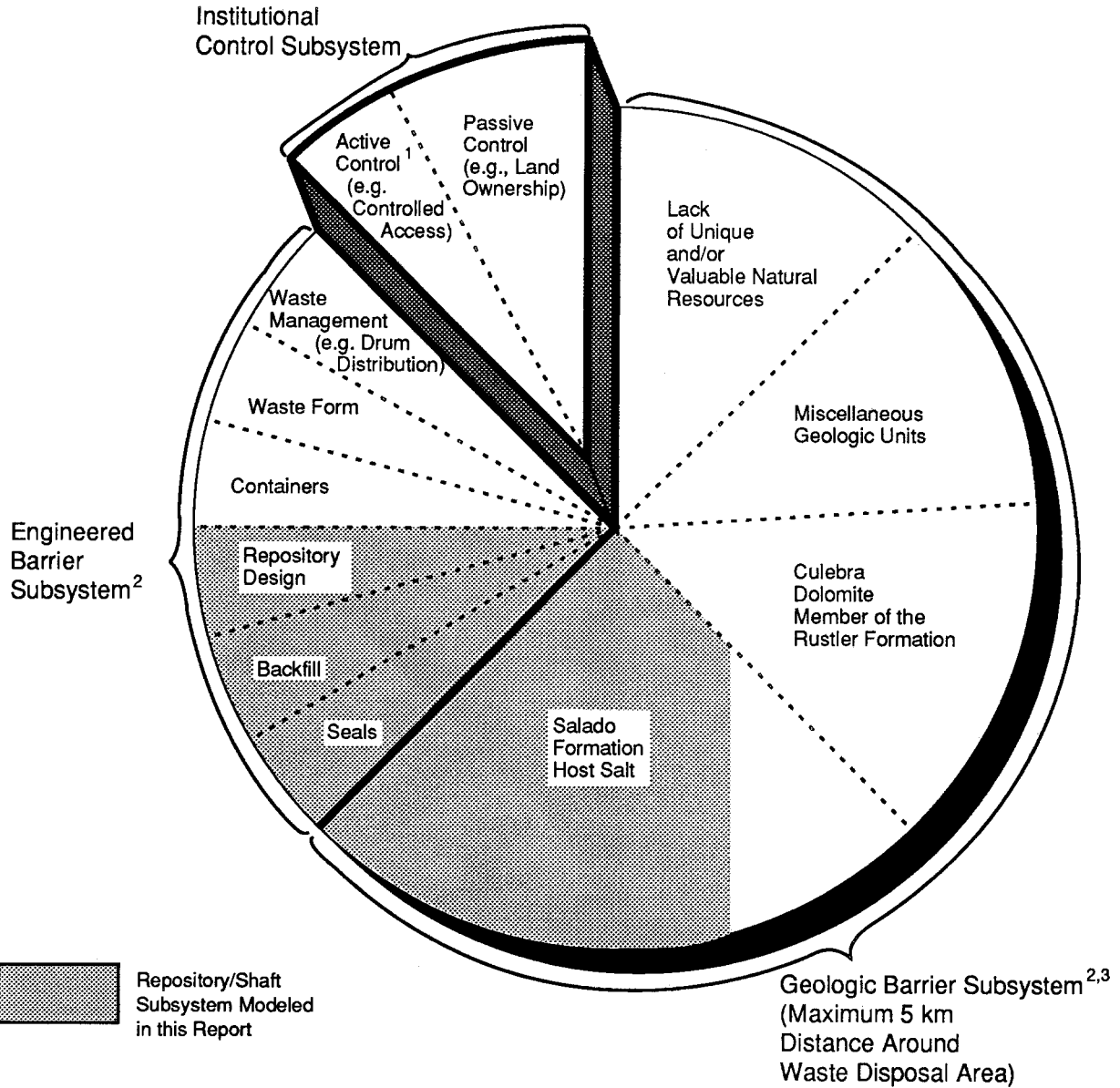
1.3 BACKGROUND ON SNL METHOD TO ASSESS COMPLIANCE

FIVE STEPS OF COMPLIANCE ASSESSMENT

Assessing compliance with the cumulative release limits for 10,000 yr (i.e., the Containment Requirement of *40 CFR 191, Subpart B*) requires extensive calculations that, in turn, require a well-defined procedure. (Refer to Rechar, 1989, and Bertram-Howery et al., 1989, for a description of *40 CFR 191, Subpart B*.)

Similar to other risk assessments, SNL's compliance assessment methodology (CAM) consists of five steps (Rechar, 1989; Bertram-Howery et al., 1989) (Figure 1-11): (1) Collecting data on waste properties, site and regional geology and hydrology, and preliminary facility design to characterize the disposal system (disposal-system characterization) (e.g., see Lappin, 1988; Tyler et al., 1988); (2) identifying the events and processes whereby radionuclides might be released outside the disposal system (scenario development) (e.g., see Guzowski, 1990; Hunter, 1989); (3) predicting the amount of these releases through modeling (consequence analysis) (a portion of this task is reported here); (4) evaluating the uncertainties associated with these predictions and the most important variables that influence these uncertainties (sensitivity/uncertainty analysis) (a portion of this task is reported here); and (5) combining the product of scenario probability and release consequence into a complementary cumulative distribution function (CCDF) and comparing with the Containment Requirements of the Standard (compliance evaluation) (e.g., see Marietta et al., 1989; Bertram-Howery et al., 1989). The Individual Protection Requirements are treated as a special case of the Containment Requirements.

* Hereafter referred to as the repository/shaft system, since it is the only WIPP disposal subsystem that is examined in this report.



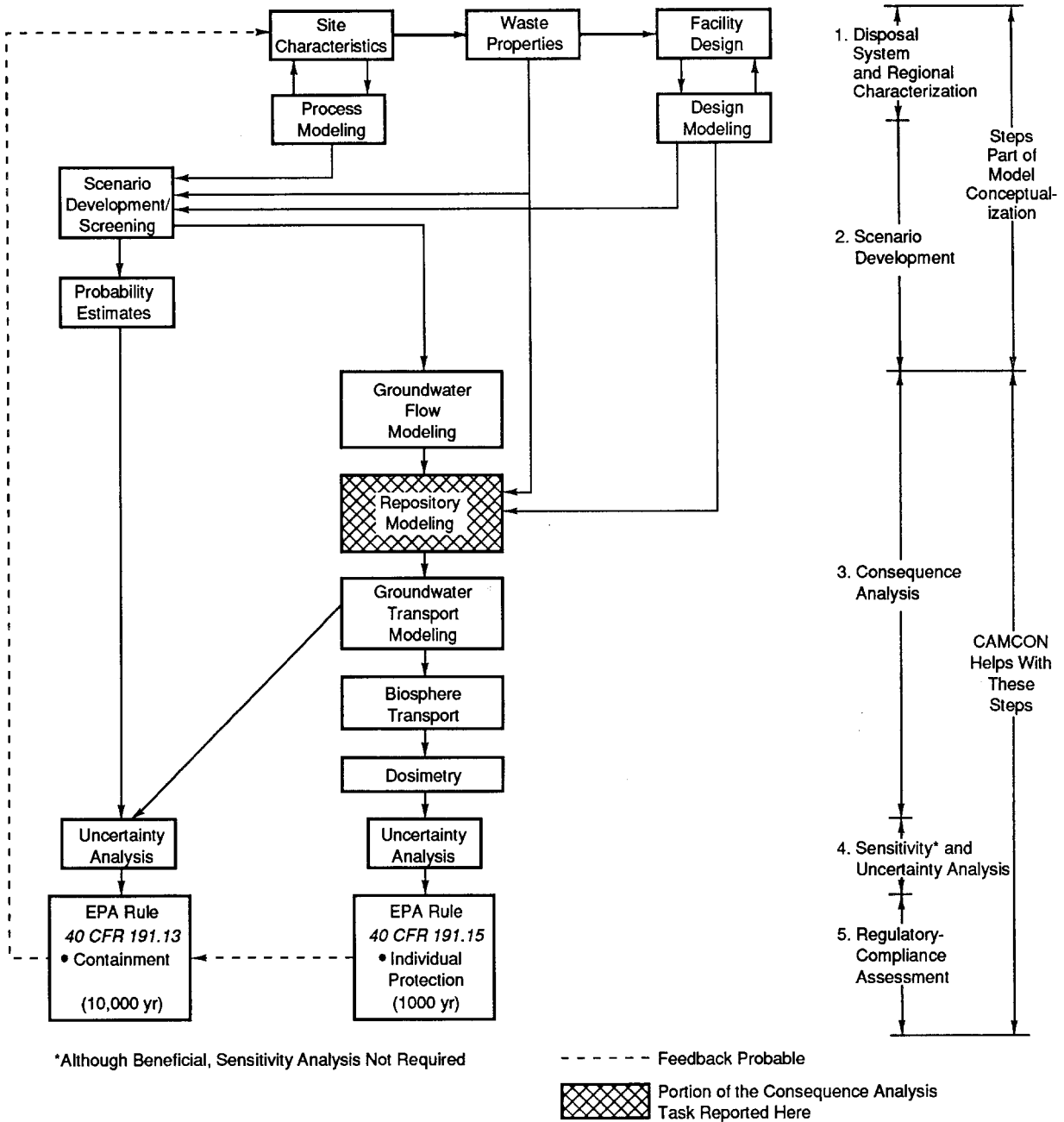
¹ 40 CFR 191 does not allow the DOE to depend upon the enforcement of active institutional controls after 100 yr, for performance assessments.

² The disposal system defined in 40 CFR 191 comprises the engineered and geologic barrier subsystems.

³ The requirement in 40 CFR 191 to consider human intrusion implies that parts or all of the geologic barrier can be effectively removed. For example, a borehole penetrating the repository would at least temporarily negate the Salado Formation's function as a barrier.

TRI-6334-250-0

Figure 1-10. Subsystems and Components of WIPP Waste Containment System.



TRI-6330-32-0

Figure 1-11. Tasks Performed During the Five Major Steps of Assessing Regulatory Compliance of WIPP with 40 CFR 191, Subpart B (after Rechard, 1989).

The first two steps establish the conceptual model (or models) of the disposal system and surrounding region for each significant scenario. (Chapter 2 discusses pertinent processes of the conceptual model.)

Step 3 mathematically simulates the conceptual model (for this report, the model of the repository/shaft, which is discussed in the next section) using CAMCON (discussed in a later section).

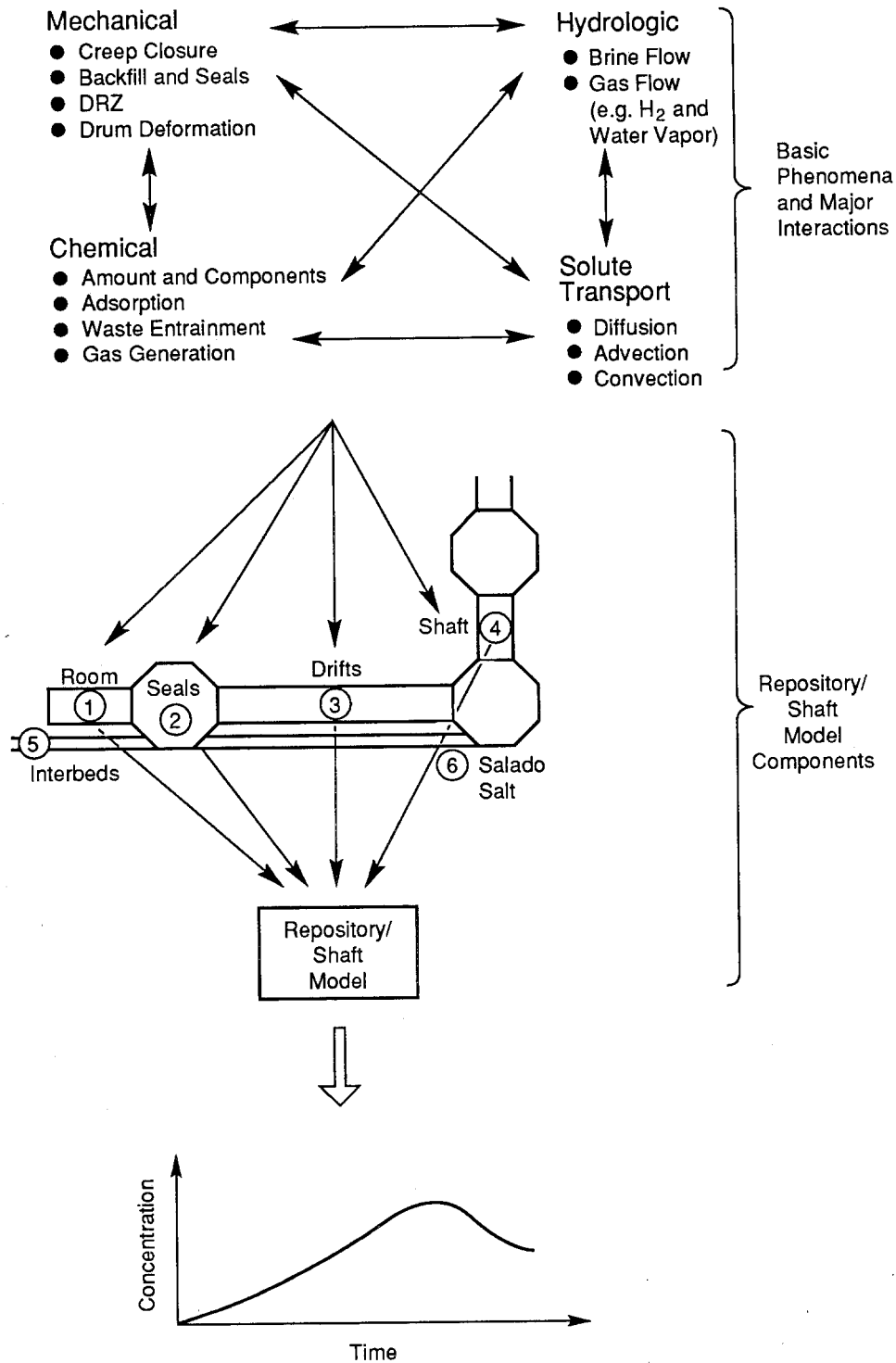
THE REPOSITORY/SHAFT SYSTEM MODEL

In general, the repository/shaft system is described by a model (or models), representing the major features of the entire underground repository, which is used to predict the migration of radionuclides (or other hazardous waste) from the consolidated waste-disposal rooms through the seals, drifts, and shafts. The time versus radionuclide concentration curves that are predicted by this repository scale model at its boundary are then used as a source term to evaluate transport to the accessible environment within a larger, local scale model, e.g., the Culebra Dolomite (Rechard, 1989).

For the WIPP, the repository scale model is as complicated as that of the overall system. Because the physical processes that affect the repository/shaft system are so complex, a great effort is required to explore the importance of the various phenomena that affect the repository and to develop a consequence module that will be appropriate for use in the overall compliance assessment. Specifically, the relative importance of four phenomena must be determined (Figure 1-12):

1. **Mechanical phenomena**, including (a) creep closure and consolidation of disposal rooms, (b) consolidation behavior of backfill and seals, (c) characteristics of the disturbed rock zone (DRZ), and (d) deformation of waste drums (not modeled in this report)
2. **Hydrologic phenomena**, including saturating brine and gas flow into and out of rooms (major phenomena modeled in this report)
3. **"Chemical" phenomena**, including (a) amounts of radioactive, organic, and inorganic components, (b) adsorption of radionuclides in backfill and host salt, (c) dissolution and entrainment of radionuclides, and (d) generation of gases from corrosion and biological decomposition (not modeled in this report)
4. **Solute Transport phenomena**, including (a) diffusion and (b) porous or fracture media fluid flow (one model in this report evaluates transport for undisturbed conditions)

The repository/shaft system model includes six modeling components (Figure 1-12). They are (1) a room component, (2) a panel seal component, (3) a drift-backfill component, (4) a shaft backfill and seal component, (5) interbed components, and (6) Salado Formation salt. These modeling components include parts of the major component categories as shown for the engineered and natural barriers in Figure 1-10. Depending on the component in question, the relative importance of the four phenomena described above varies. Therefore, the tasks in establishing the behavior of the repository/shaft system are to (a) determine the relative importance of the phenomena for each modeling component and then (b) link the four modeling



TRI-6334-26-0

Figure 1-12. Basic Phenomena, Major Interactions, and Components of the Repository/Shaft Model (after Rechard, 1989).

components so that the repository/shaft system can be viewed in the context of the whole system. An important step in accomplishing these two tasks is to perform a sensitivity analysis to determine the relative importance of two or more phenomena and components, e.g., the repository's panel seals and shaft seals. This report describes the work currently in progress in which the importance of the modeling components is being investigated by modeling only hydrologic phenomena, such as gas and brine flow.

BACKGROUND ON SENSITIVITY AND UNCERTAINTY ANALYSIS

Step 4 of the CAM requires uncertainty and sensitivity analysis on the disposal system as a whole and on individual parts. With uncertainty analysis, an analyst evaluates the level of confidence to place on a calculation. It is useful throughout the assessment.

With sensitivity analysis, on the other hand, an analyst identifies parameters that, when varied, can significantly affect the results. Thus, sensitivity analysis is a technique to gain insight about a system. Its primary usefulness then is in the early phases of an assessment to help produce understanding, identify data needs, set priorities, allocate resources, and help direct development or selection of a conceptual model of the disposal system or its parts.

Although not completed in this report, the authors examine, through phenomenological models, the repository/shaft system to provide an understanding that will help others evaluate proposed modifications to this system (e.g., the form of the TRU waste) and help the authors develop simplified models (if possible) of this system for later compliance assessments. This process continues until either compliance with the Standard can be shown, or modeling identifies engineered modifications (to the waste, backfill, room design, or waste management) that can be implemented to achieve compliance.

Uncertainty/sensitivity analysis is more precisely explained as follows. A consequence module, such as a groundwater flow model used in Step 3 (Figure 1-11), is a function, $F_1(x_1, \dots, x_n)$, of parameters x_1, \dots, x_n . Because x_1, \dots, x_n have ranges and distributions, $F_1(x_1, \dots, x_n)$ will also have a range and distribution. Uncertainty analysis involves determining properties of the distribution of F_1 . These properties include the distribution shape, expected value, and variance of F_1 . Sensitivity analysis involves determining the importance of an individual parameter, x_n , in influencing the distribution of F_1 (e.g., shape, expected value, or variance).

This report is concerned with sensitivity analysis on the repository/shaft system. The major phenomenon evaluated in the system was hydrologic, specifically, brine and gas flow. The three parameters of interest are the permeability of the media, compressibility of the media, and the pressure (or flux) boundary conditions.

BACKGROUND ON CAMCON

The compliance assessment methodology (Figure 1-11) (Rechard, 1989) places two general requirements on computational tools that are developed to assist the analyst: flexibility and adequate quality assurance (QA). In the compliance assessment procedure, the variety of scenarios analyzed, the varying complexity of the models used, and the desire to switch codes when cycling through the procedure all require flexible and versatile computational tools. Likewise, the number of repetitive computer simulations, the need to properly identify simulations, and the potential need to recreate simulations all require QA in the executive package.

Two important computational tools developed for assessing WIPP compliance with the Standard are CAMDAT (Compliance Assessment Methodology DATa) and CAMCON (Compliance Assessment Methodology CONtroller). CAMDAT is a computational data base (sometimes referred to as a neutral file) containing code output and used as the link between codes required in the compliance assessment. The computational data base, CAMDAT, has two main features: (1) it provides a trail for QA by recording the code names that have written data to the data base, and (2) it is versatile enough to handle data from different types of codes (e.g., finite-difference or finite-element codes).

CAMCON, the controller for compliance calculations, consists of a series of procedural files that allow an analyst to properly build and execute all of a compliance assessment or portions of a consequence analysis (e.g., the repository/shaft model).

The complexity and data requirements of the codes (either analytical or numerical) that comprise the analysis determine the difficulty of applying CAMCON. However, CAMCON is composed of several computer modules (e.g., mesh generation codes and groundwater codes) that can be readily assembled to analyze models, such as the repository/shaft system. It was this versatility of CAMCON that allowed the authors of this report to compute the detailed analysis in a timely manner.

The computer modules pertinent to this report are briefly described in Chapter 2.

2. REPOSITORY/SHAFT SYSTEM ISSUES AND MODELS

2.1 ISSUES

As described in the Introduction, this report presents a preliminary analysis of the repository/shaft system using several different models to evaluate the behavior of the system's components (i.e., rooms, drifts, seals, and shafts).^{*} The computational models developed were used to examine the behavior of these components for both an undisturbed performance scenario (Chapter 3) and a human intrusion scenario (Chapter 4). Briefly, the undisturbed performance scenario implies that the repository is not disrupted by human intrusion or unlikely natural events. The human intrusion scenarios consider the possibility of a borehole penetrating the repository. (Both scenarios are described more fully in a later section.) Issues concerning mechanical phenomena such as creep closure or chemical phenomena such as radionuclide adsorption or solubility are not covered in this report.

ISSUES CONCERNING UNDISTURBED PERFORMANCE

For models simulating the undisturbed scenario (Chapter 3), the major issue is to develop performance measures, both short and long term, for the shaft, panel, drift and interbed seals, and the backfill to answer questions of repository design concerning the required permeability, location, and redundancy of these components. Modeling the undisturbed scenario with a one-dimensional model, two major earlier works (Marietta et al., 1989; Lappin et al., 1989) showed no radionuclide releases (even with degraded properties) beyond the immediate vicinity of the repository over 10,000 yr. Based on these earlier works, the current seal and backfill design specifications greatly exceed (by orders of magnitude) the required undisturbed performance over the long term. However, the earlier modeling did not include gas generated from anoxic corrosion of the steel drums or microbiological degradation of the combustible waste or radiolysis. Consequently, the immediate issues that were examined for the undisturbed scenario were

- Verification of the previous bounding calculations on species transport without gas for the long term with a two-dimensional model (Sections 3.1 and 3.2)
- Evaluation of the redundancy of seals (Section 3.1)
- Estimation of gas transport (Sections 3.3 and 3.4)
- Exploration of the need for effective seals and backfill in the short term (Sections 3.3 through 3.4).

* The behavior characterization and model development of the repository/shaft system is one of the major issues described by Bertram-Howery and Hunter (1989) in Preliminary Plan for Disposal-System Characterization and Long-Term Performance Evaluation of the Waste Isolation Pilot Plant.

ISSUES CONCERNING HUMAN INTRUSION

For models simulating the human intrusion scenario (Chapter 4), the major issues are behavior of the panel and drift seals and the backfill, and performance of the waste form and transport within the Culebra Dolomite (the latter will be discussed in a later report). Behavior of the waste form was added because the requirement imposed by *40 CFR 191, Subpart B*, demands a study of a scenario in which a waste repository is hypothetically intruded by humans. In this scenario, the primary component of the geologic barrier (the Salado Formation) has been removed, leaving only the waste form or, possibly, intervening panel seals and the Culebra Dolomite as barriers. Thus, characterizing the behavior of the waste is much more important under these conditions than for the undisturbed scenario. The immediate issue explored in Chapter 4 for human intrusion scenarios was the examination of basic phenomena, including

- Evaluation of the range of expected brine inflow from the Salado Formation (Section 4.1) and underlying brine pocket (Section 4.4) to determine (1) how much waste is accessible to brine and gas transport and (2) the corresponding discharge
- The potential impact of heterogeneity within the Salado Formation on brine inflow (Section 4.2)
- The characteristic response times for room and panel depressurization and brine flow (Section 4.3)
- The potential impact of geometrical effects on the quantity of waste that is accessible to brine transport (Section 4.5).

2.2 GENERAL MODELING DESCRIPTION

SCENARIOS MODELED

Currently, two main scenarios are being examined: the undisturbed performance (or base-case) scenario and a human intrusion scenario.

Undisturbed Performance Scenario. Undisturbed performance is the base case for scenario development (Guzowski, 1990). As defined in the Standard, "undisturbed performance" means the predicted behavior of a disposal system, including the consideration of the uncertainties in predicted behavior, if the disposal system is not disrupted by human intrusion or the occurrence of unlikely natural events. For the undisturbed scenario, four simple numerical models have been developed and are described in Chapter 3.

Human Intrusion Scenarios. In addition to the undisturbed performance, the Standard also requires an analysis of the consequences of humans intruding into the repository (e.g., drilling an exploratory borehole through the repository). For the WIPP disposal system, screening has reduced the initial list of events and processes for scenario development to four (Hunter, 1989; Guzowski, 1990): (1) conventional or solution mining of potash beyond the disposal system resulting in areas of subsidence that act as areas of recharge to underlying aquifers (designated as Transport/Subsidence or TS); (2) intrusion of a borehole through a disposal room or drift and into a pressurized brine pocket (also referred to as a brine reservoir) in the Castile Formation (designated as Event 1, or E1); (3) intrusion of a borehole into a disposal room or drift (Event 2

or E2); and (4) drilling a withdrawal well downgradient from the repository (Event 3 or E3). The models reported here use either event E1 in which a borehole has been drilled through a disposal room or drift and into pressurized brine in the Castile Formation, or E2 in which a borehole has been drilled into a disposal room or drift but no further. Marietta et al. (1989) discusses the E1 and E2 scenarios in greater detail. Five numerical models were developed for this scenario and are described in Chapter 4.

CONCEPTUAL MODEL OF PANELS AND ROOMS IN DISPOSAL AREA

In an earlier study, very conservative assumptions were selected to evaluate the two scenarios listed above (Lappin et al., 1989). Furthermore, boundary conditions for the models were sometimes selected so that release would be maximized; consistency in phenomenological conditions among the problems was not maintained. For example, some models assumed lithostatic pressure in the room and hydrostatic pressure elsewhere for undisturbed conditions, while for disturbed conditions, the models assumed lithostatic pressure in the far field (i.e., Salado Formation) and hydrostatic pressure in the room.

In this report, some models are an extension of these earlier calculations, using primarily two-dimensional numerical models. Often the conservative approach in the original problem is carried over. However, many of the models here are an attempt to begin to develop realistic models that can estimate repository conditions over the 10,000-yr regulatory period. Furthermore, some models here include a phenomenon not modeled in the earlier studies: flow of gas generated by the waste.

Hypothesized Episodes for Closure of Disposal System. The assumptions for the models in this report are based on the hypothesized episodes (sequence of events in rooms) described below. (For a more detailed description of events, refer to Guzowski, 1990; Marietta et al., 1989; Lappin et al., 1989; and the "No Migration Petition Addendum" [DOE, 1989].) Although the authors thought the following hypothesis was valid at the time that work for this report was begun, current calculations being performed at SNL -- including the results of some models described here -- may render this hypothesis obsolete. Nevertheless, the hypothesis is presented to provide a framework by which to understand the models.

The following is the proposed sequence of events.* Initially, panels are filled with waste and backfill and no free brine is present. All access drifts and the experimental area are backfilled, and the drifts and shafts are sealed (Lappin et al., 1989). Grout seals are in place in Marker Bed 139 (MB139) directly under panel seals. MB139 is fractured as a result of excavation of the drifts and panels, and in response to later salt creep into these excavations. These new fractures occur directly under all excavations, but not under the intact salt pillars and concrete components of the seals. During the operational life of the repository, the fractures in MB139 have filled with brine from Salado Formation seepage (Figure 2-1a).

* The operational life of the repository is about 25 yr, which means that each panel of rooms is at a slightly different state in terms of time. This hypothesis describes episodes for the final panels and rooms.

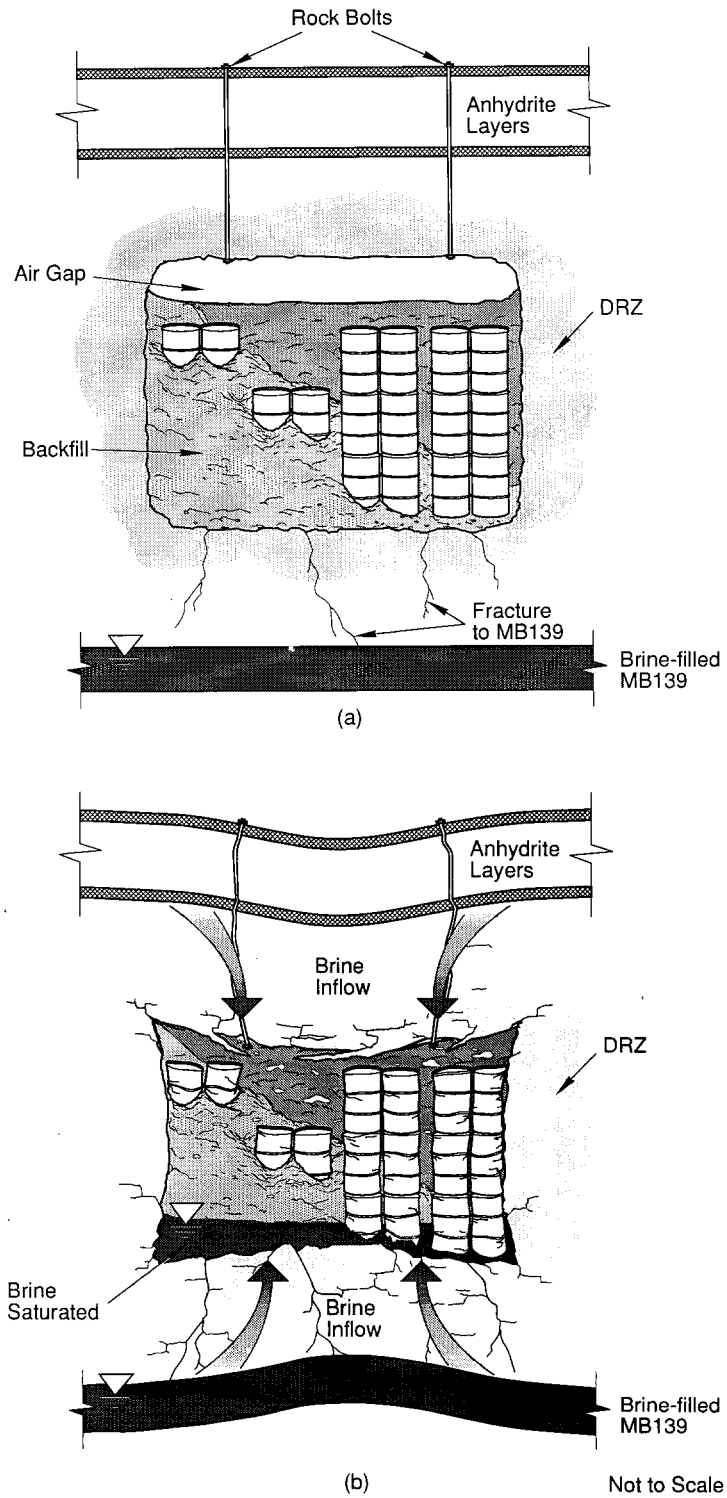


Figure 2-1. Hypothesized Episodes in Disposal Area Leading to Undisturbed Conditions. This drawing shows (a) initial conditions after decommissioning and (b) room creep closure and brine inflow.

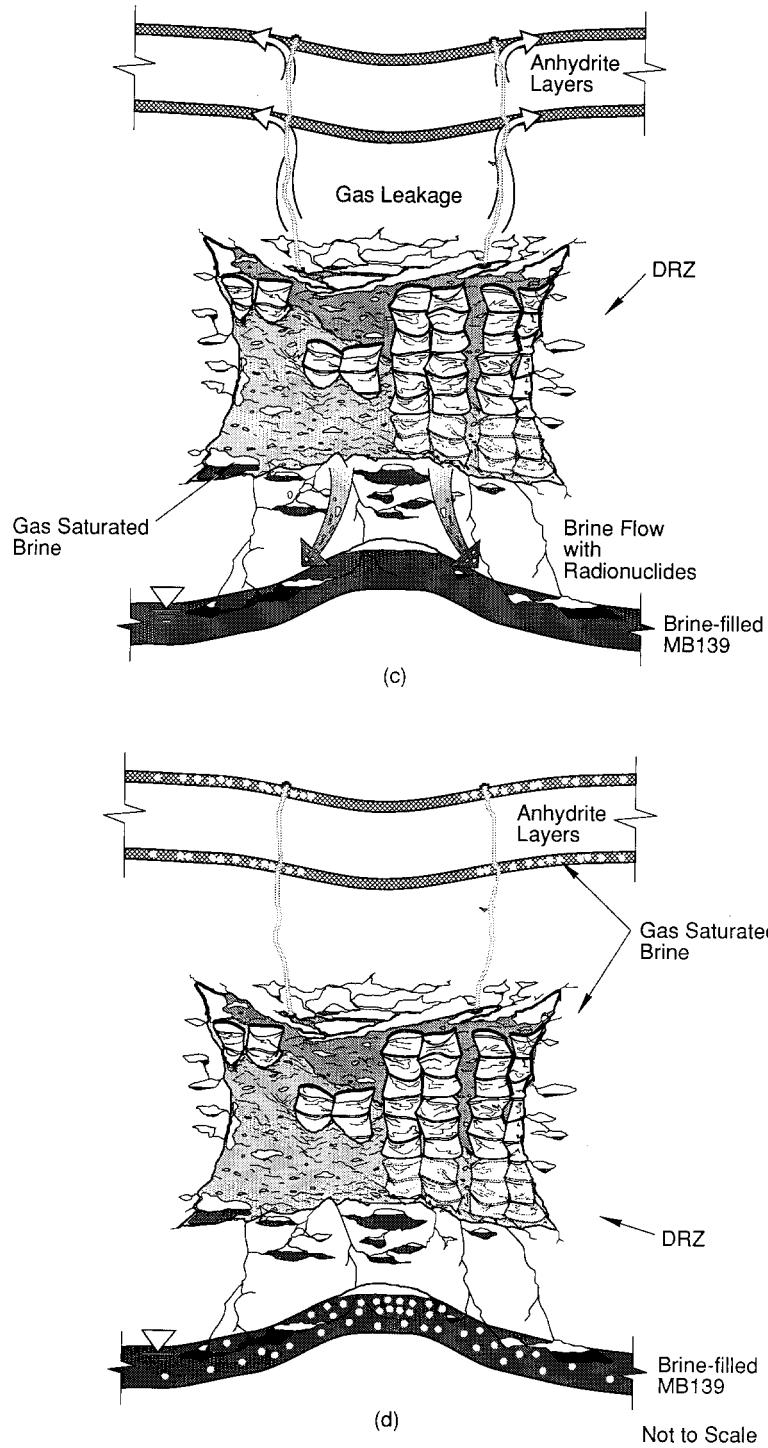


Figure 2-1. Hypothesized Episodes in Disposal Area Leading to Undisturbed Conditions. (Continued) This drawing shows (c) gas generation, brine outflow, and room expansion, and (d) undisturbed conditions with gas-filled room surrounded by gas-saturated brine.

As closure occurs, the rooms and drifts approach a very dense state. Brine flows into the remaining disturbed rock zone (DRZ) and then into the remaining voids in the rooms and drifts (Figure 2-1b). Gas generates slowly, so that the consolidation process is nearly complete before anoxic corrosion of the containers begins. Microbiological degradation of the organic material may begin earlier, but its rate is hypothesized to be very slow. The lower shaft seal is assumed to be well consolidated; the upper seal is less well consolidated. Gas generates in the room, filling any voids in the DRZ and leaking into the clay and anhydrite layers above the repository and the consolidated room. The gas generation reverses the flow of brine, driving it primarily out of the bottom of the room. As the pressure approaches lithostatic, the room above the waste begins to expand, which keeps the pressure less than about 20 MPa (Figure 2-1c).

Although these conditions are thought to be reasonable, a conservative modification is to assume that gas generates faster than represented above, and impedes complete consolidation. This conservative case was examined in an earlier report (Lappin et al., 1989), and a few models in this report continue to study these conditions. In this conservative version of the hypothesis, however, the faster rate of gas generation might result in much less brine inflow and, therefore, less radionuclide leaching and migration (unless disturbed by human intrusion).

Undisturbed Conditions -- In the undisturbed performance scenario, the room remains in this stable, gas-filled state. Any brine that initially filled the voids in the room is expelled because the direction of brine flow has been reversed by gas generation. The brine has been driven from the room primarily through the floor (down into MB139) (Figure 2-1d).

Conditions as the Result of Human Intrusion -- In the human intrusion scenario, E1, a hole is drilled through a disposal room or drift and into pressurized brine in the Castile Formation. During drilling the room quickly depressurizes, but the entire panel does not (Figure 2-2a). According to the Standard, the intruders "soon" detect that the hole has penetrated the repository and that the area is "incompatible" with their activities. ("Soon" is a term used in the guidance for 40 CFR 191, Subpart B, but its time limit is not specifically defined. The authors assume it means less than one month.) The drillers seal and then abandon the borehole. When the borehole is abandoned, the room repressurizes from continued gas generation (Figure 2-2b). Degradation of the borehole plug, which is emplaced using technology currently used today,* is assumed to occur after about 75 yr (Lappin et al., 1989).

After the borehole plug degrades, any remaining gas moves out of the panel, and the waste consolidates, followed by brine saturation. Depending on the pressure differences, whether borehole plugs above or below the repository degrade first, and the depth of drilling, brine could flow down from the repository into underpressurized formations below the repository. However, the case considered here is brine flow up the borehole to the accessible environment. Brine inflow from the Salado Formation through the room and into the borehole is assumed to be the primary carrier of radionuclides (Figure 2-2c).

* A subtle contradiction exists in the guidance to the 1985 Standard in that although we can assume that the intruders soon detect that the area is incompatible with their activities, we cannot assume that they take special precautions to seal the borehole.

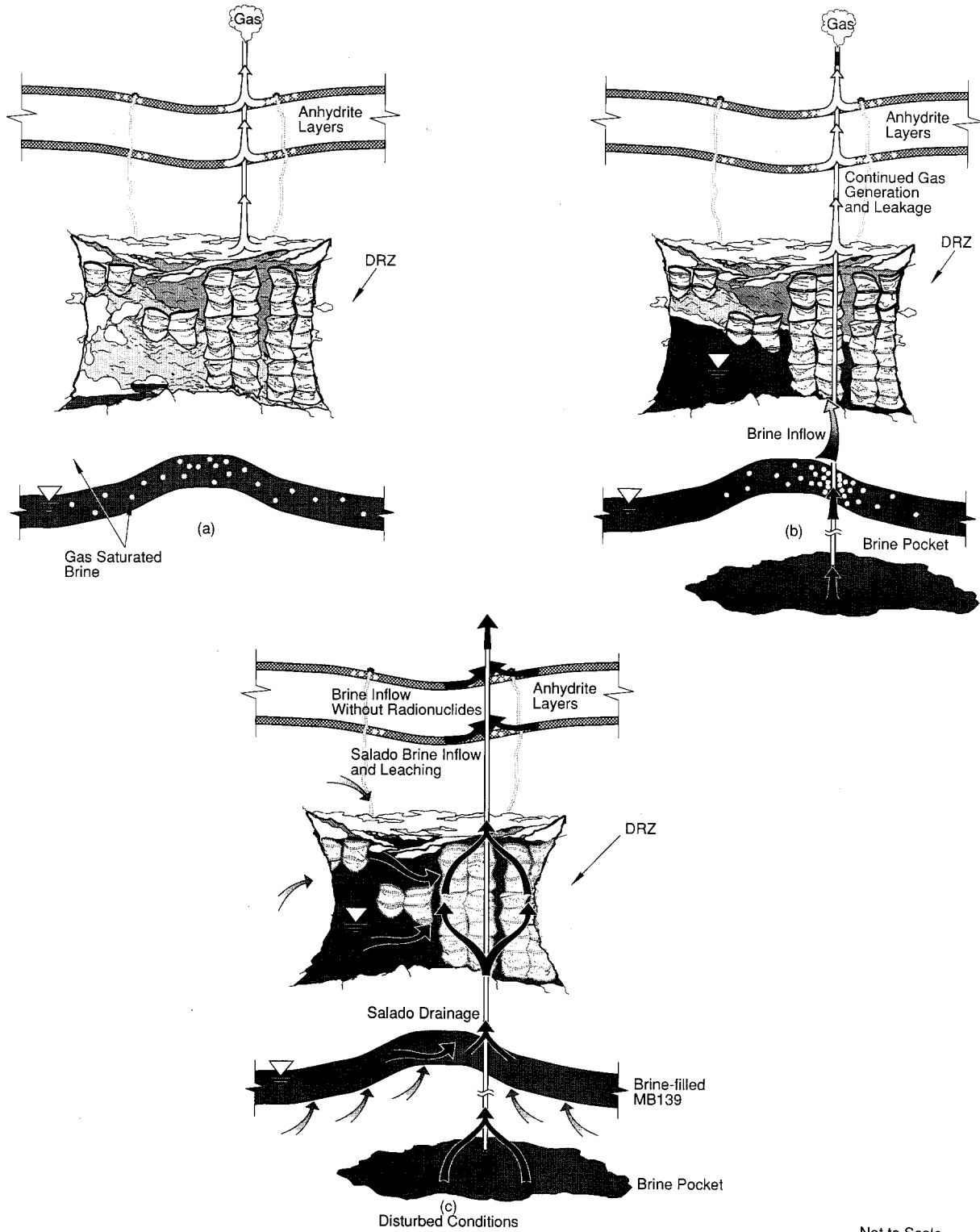


Figure 2-2. Hypothesized Episodes in Disposal Area After Human Intrusion. This drawing shows (a) initial room gas depressurization when penetrated by exploratory borehole, (b) final gas and brine depressurization as borehole seals degrade, and (c) brine flow through borehole to Culebra Dolomite.

Again, although this hypothesized sequence for the human intrusion scenario is considered to be reasonable, a wide range of responses of the system from borehole plug degradation can be expected to occur. For example, changes in the rate and timing of gas generation, the timing of human intrusion, and the rates of gas leakage through the borehole could affect the system. Some mechanisms might operate only immediately after plug degradation, such as depressurization within the repository. Others, such as circulated fluid from the brine pocket and brine inflow through the Salado Formation, might be active over much longer time periods.

MODELING OF THE REPOSITORY/SHAFT SYSTEM

Generally, the repository/shaft system models described in Chapters 3 and 4 consist of at most seven components (or features): (1) a room or disposal region; (2) a panel or drift seal; (3) drift backfill; (4) shaft backfill and seal; (5) Salado Formation salt; (6) anhydrite interbeds; and (7) brine pocket. Except for one model, the only phenomenon examined was hydrologic, such as brine or gas flow (i.e., brine or gas flow was the performance measure [F₁]). Mechanical, chemical, and solute transport and the complex interactions alluded to in the hypothesized episodes described above were neglected.

Brine Flow Equation. The governing partial differential equation describing conservation of fluid mass in a saturated porous medium is given by (Voss, 1984)

$$\rho c \frac{\partial p}{\partial t} - \nabla \cdot \left[\frac{k_p}{\mu} (\nabla p - \rho \mathbf{g}) \right] = \dot{\rho}_0 \quad (2-1)$$

where

- c = capacitance (Pa⁻¹)
- \mathbf{g} = g • elevation (m/s²)
- g = magnitude of gravity constant (m/s²)
- \underline{k} = permeability tensor (m²)
- p = fluid pressure (Pa)
- μ = fluid viscosity (Pa-s)
- ρ = density of fluid (kg/m³)
- $\dot{\rho}_0$ = fluid mass source density (kg/[m³-s]).

The capacitance (c) is defined as the volume of fluid released from pore storage due to a unit drop in fluid pressure per total matrix and pore volume. It is the combined compressibility of the porous matrix and fluid within the pores and defined in SUTRA as

$$c = (1-\phi)\beta_s + \phi\beta_f \quad (2-2)$$

where

- β_f = fluid compressibility (Pa⁻¹)
- β_s = porous matrix compressibility (Pa⁻¹)
- ϕ = porosity.

Fluid compressibility (β_f) is defined by

$$\beta_f = \frac{1}{\rho} \frac{\delta \rho}{\delta p} \quad (2-3)$$

In all the models, the varied parameters were permeability, capacitance, and pressure (or flux) boundary conditions. All the models varied permeability. In several of the models, capacitance and the pressure boundary conditions were varied also, but in a few models capacitance and the pressure boundary conditions were set at maximum values to evaluate whether flow was adverse enough to require varying them in future calculations.

The major compliance issues surrounding these parameters were discussed earlier in this chapter. The major sensitivity issues were: (1) whether within the range of values specific to the WIPP, one parameter was most important; (2) whether permeabilities of the repository/shaft model components (e.g., shaft seals or anhydrite interbeds) dominated the flow response; and (3) whether shapes of repository features (e.g., panel shape) greatly influenced the flow response. Although these sensitivity issues are not always explicitly discussed, the sensitivity of the brine or gas inflow to parameter changes are graphically presented for each model.

Gas Flow Equation. For pure gas flow, Eq. 2-1 governs except that the density and fluid compressibility are variable and must be described by an equation of state. For completeness, this section describes the equations and the modification made to SUTRA. Although several new parameters were added (most notably, the composition of the gas) only permeability was varied in the models described in Chapters 3 and 4. Consequently, the reader may wish to defer reading this section until later.

In SUTRA, the fluid compressibility is considered to be constant. In adapting SUTRA to handle gas as the fluid, it was necessary to introduce an equation of state for the gas such that given the pressure, the gas density and compressibility could be computed. To accomplish this task a subroutine was added to SUTRA to evaluate the Redlich-Kwong gas equation of state (Prausnitz, 1969). The gas density and compressibility are computed from

$$Z = \frac{p\bar{v}}{\bar{R}T} = \frac{\bar{v}}{\bar{v} - b_{\text{mix}}} - \frac{a_{\text{mix}}}{\bar{R}T^{3/2}(\bar{v} + b_{\text{mix}})} \quad (2-4)$$

where

$$a_{\text{mix}} = \text{mixture constant for gas } \frac{\text{Pa} \cdot \text{m}^6 \cdot \text{K}^{1/2}}{\text{gmole}^2}$$

$$b_{\text{mix}} = \text{mixture constant for gas } \text{m}^3/\text{gmole}$$

$$p = \text{pressure (Pa)}$$

$$\bar{R} = \text{universal gas constant} = 8.31434 \frac{\text{Pa} \cdot \text{m}^3}{\text{gmole} \cdot \text{K}}$$

$$T = \text{temperature}$$

$$Z = \text{gas compressibility factor (1 for ideal gas).}$$

$$\bar{v} = \text{molal specific volume} = \text{m}^3/\text{gmole}$$

For a gas mixture of n species, the mixture constants a_{mix} and b_{mix} are evaluated as follows

$$a_{\text{mix}} = \sum_{i=1}^n \sum_{j=1}^n y_i y_j a_{ij} \quad (2-5)$$

$$a_{ij} = (a_i a_j)^{1/2} \quad (2-6)$$

$$b_{\text{mix}} = \sum_{i=1}^n y_i b_i \quad (2-7)$$

where

$$a_i = 0.42748 \frac{R \bar{T}_{ci}^{2.5}}{P_{ci}} \quad (2-8)$$

$$b_i = 0.0867 \frac{R \bar{T}_{ci}}{P_{ci}} \quad (2-9)$$

and

P_{ci} = critical pressure of species i (Pa)

\bar{T}_{ci} = critical temperature of species i (K)

y_i = mole fraction of species i .

To obtain gas density as a function of gas pressure, Eq. 2-4 was solved for \bar{v} , the specific volume. Density is then computed from

$$P = \frac{\omega}{\bar{v}} \quad (2-10)$$

where ω = molecular weight of gas mixture (g/gmole)

$$\omega = \sum_{i=1}^n \omega_i y_i \quad (2-11)$$

where ω_i = molecular weight of species i .

The fluid (gas) compressibility β_f was evaluated numerically as follows

$$\beta_f(p) = \frac{1}{\frac{\rho(p) + \rho(p+\varepsilon)}{2}} \cdot \left(\frac{\rho(p+\varepsilon) - \rho(p)}{\varepsilon} \right) \quad (2-12)$$

for ε a small number.

Because the density and compressibility depend on the unknown gas pressure, an iterative procedure was used to solve the nonlinear problem. Convergence was measured in terms of a relative error criterion. Because SUTRA was already capable of treating nonlinearities resulting from unsaturated flow, it was not necessary to alter SUTRA to handle nonlinearities resulting from gas flow.

Multiphase Flow. The multiphase equations describing the brine and gas interaction within the disposal area are not described here but may be found in the documentation of the BOAST code (Fanchi et al., 1987). Even though the multiphase equations add several new parameters that could be varied, none was varied except matrix permeability.

For the gas phase, density was calculated by the Redlich-Kwong equation of state at several values of pressure over the full range of pressures expected. The results were then input into BOAST as tabular values from which BOAST linearly interpolated to obtain necessary density values when solving the mass balance equations.

Similarly, relative permeabilities and capillary pressures were input as tabular functions of gas and brine saturation (see Appendix A). Although viscosities of the brine and gas, the solubility of gas in the brine, and the compressibility of the salt can also be input as tabular data as functions of pressure, the viscosities and compressibilities were assumed constant and the gas assumed insoluble in the brine for calculations done in this report.

2.3 COMPUTER MODULES

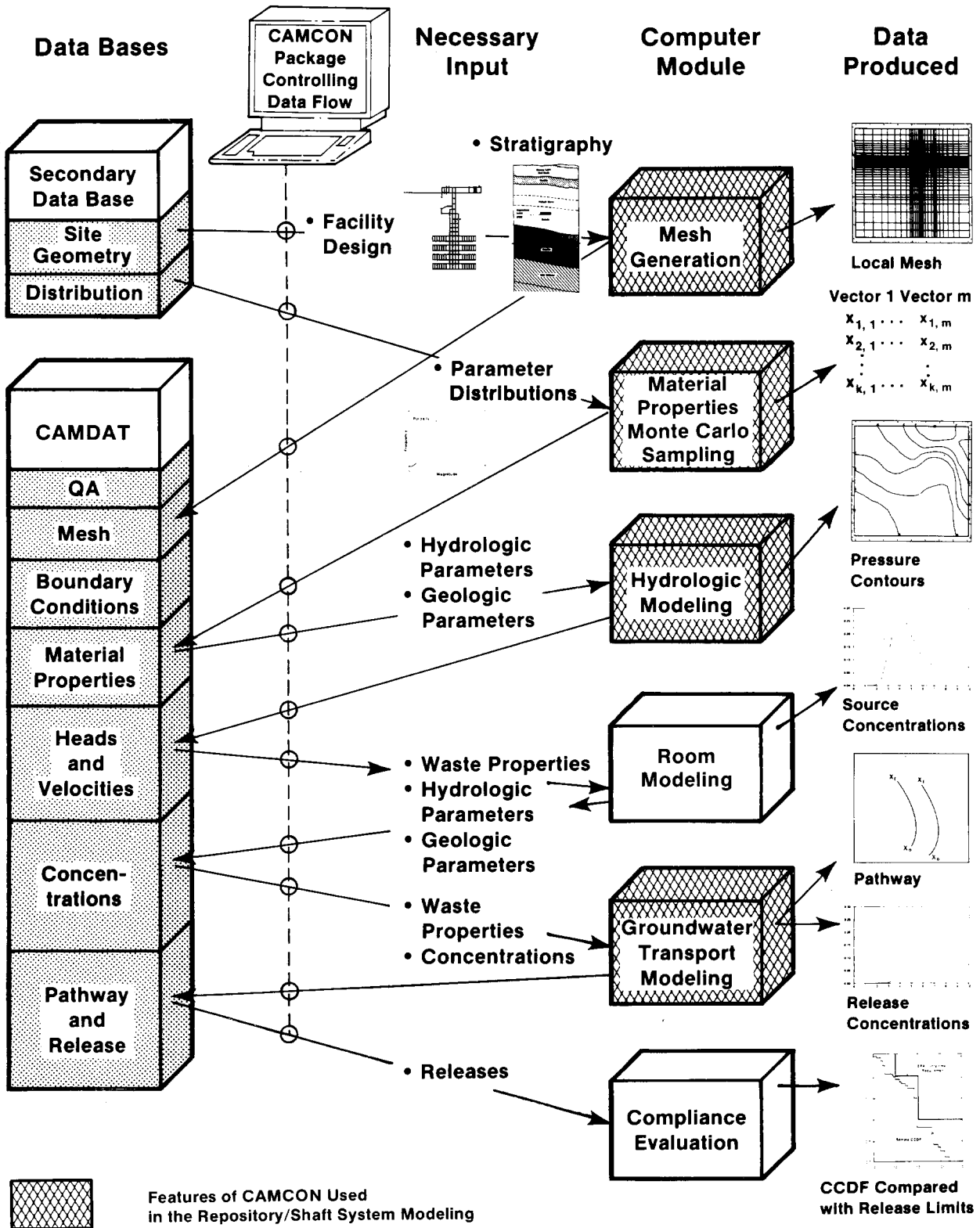
MODULES USED IN CAMCON

Figure 2-3 shows a schematic representation of the main computer modules linked by CAMCON. The numerous modules within CAMCON have been described in detail in earlier reports (Rechard, 1989; Rechard et al., 1989). A summary of each module and a list of the specific codes used in this report are provided below. The versions of code correspond to the versions reported in Rechard et al. (1989).

1. Mesh generation module

The mesh generation module discretizes the models needed for assessing consequences of one scenario.

- GENMESH: Three-dimensional finite-difference mesh generator code



TRI-6334-258-0

Figure 2-3. Schematic Diagram of Main Computer Modules Linked by CAMCON (after Rechar et al., 1989).

2. Material properties and Monte Carlo sampling module (Monte Carlo sampling not done in this report)

The material properties module selects geologic, mechanical, and hydrologic properties that are needed in subsequent calculations from the secondary data base. This module can also sample from distributions of the material properties, which are needed for uncertainty and statistical sensitivity calculations.

- MATSET: Code to set material properties in CAMDAT

3. Regional and local hydrologic modules

The groundwater flow module establishes flow conditions within the controlled area of the repository.

- SUTRA: Finite-element simulation code for saturated-unsaturated, fluid-density-dependent groundwater flow with energy transport or chemically reactive single-species solute transport (Voss, 1984). For one model in this report, SUTRA was modified to simulate compressible gas flow. A verification of this modification is contained in this report.
 - PRESUTRA: Pre-processor (translator) for SUTRA
 - POSTSUTRA: Post-processor (translator) for SUTRA
- HST3D: Computer code for simulation of heat and single-species solute transport in three-dimensional groundwater systems (Kipp, 1987)
 - PREHST: Pre-processor (translator) for HST3D
 - POSTHST: Post-processor (translator) for HST3D
- BOAST II: Black Oil Applied Simulation Tool for simulating three immiscible fluids (oil, water, and gas) in a three-dimensional porous medium. (The pre- and post-processors for BOAST have not yet been written.)

4. Room module (not used in this report)

The room module develops a source term for transport calculations by incorporating the complex processes in the waste storage room.

5. Transport module

The transport module predicts radionuclide migration from the repository source to the controlled area boundary.

- NEFTRAN: Network flow and transport code (Longsine et al., 1987)
 - PRENEF: Pre-processor (translator) for NEFTRAN
- See also SUTRA, SWIFT II, and HST3D

6. Compliance evaluation module (not used in this report)

The compliance evaluation module constructs the CCDF from simulations on all scenarios to assess compliance with the containment section of the Standard. For evaluating compliance with the Individual Protection (or safety assessments), this module is replaced with two modules, a biosphere transport module and a dosimetry/human effects module.

7. Statistical module (not used in this report)

The statistical module correlates results with input to evaluate parameter sensitivity.

8. Support modules (not shown in Figure 2-3)

Several codes are used to support the main modules listed above.

- ALGEBRA: Code that algebraically manipulates data in CAMDAT (Gilkey, 1988)
- BLOT: Mesh and curve plot code (Gilkey and Glick, 1989)
- C2FINTRP: Code to interpolate boundary conditions from a coarse to fine mesh
- TRACKER: Code to track neutrally buoyant particles

CODE DESCRIPTIONS

Following are brief descriptions of the computer codes used for the models presented in Chapters 3 and 4.

SUTRA. *SUTRA* (Saturated-Unsaturated TRANsport) evaluates density-dependent saturated or unsaturated groundwater flow in rigid, porous media with either (1) transport of a single-species solute subject to nonlinear equilibrium adsorption and zero- and first-order production or decay or (2) transport of thermal energy in the groundwater and solid matrix of an aquifer. *SUTRA* employs a two-dimensional hybrid finite-element and integrated-finite-difference method to approximate the governing equations. The primary results are fluid pressures and velocities and either solute concentrations or temperatures as they vary with time (Voss, 1984).

HST3D. *HST3D* (Heat and Solute Transport in 3-Dimensional Systems) simulates Darcy flow of saturated groundwater in three-dimensional systems, and the associated heat and single-species solute transport. The three governing equations for this model -- (1) conservation of total fluid mass combined with Darcy's laws, (2) conservation of enthalpy for the fluid and porous medium, and (3) conservation of mass of a single-solute species that may decay and may adsorb onto the porous medium -- are solved numerically. A finite-difference technique using a point-distribution grid is used to discretize the governing equations in time and space. Two techniques are available for solving the finite-difference matrix equations: a direct elimination solver and an iterative solver that uses two-line successive overrelaxation. Boundary condition types include specified value, specified flux, leakage, heat conduction, approximate free surface, and two types of aquifer-influence functions. All boundary conditions can be functions of time. Time-dependent solutions are obtained at each grid node for each of the dependent variables: pressure, temperature, and mass fraction (solute concentration). Average Darcy velocities can also be obtained at each computational cell (Kipp, 1987).

BOAST. BOAST II (Black Oil Appplied Simulation Tool, enhanced version) is a petroleum reservoir model that simulates isothermal Darcy flow in three dimensions. BOAST II assumes that reservoir fluids can be described by three fluid phases (oil, gas, and water) of constant composition with physical properties that depend only on pressure. In this report, BOAST II is used to simulate flow of brine and gas and the effects of gas generation in the waste. BOAST II uses a finite-difference, implicit pressure, explicit saturation (IMPES) numerical technique for solving the three differential equations that describe the simultaneous flow of the three phases. Both direct and iterative techniques are available to solve the resulting system of algebraic equations. Except for flow boundaries, boundary conditions must be specified by wells. The well model in BOAST II allows rate or pressure constraints on well performance to be specified, so that gas generation and brine sinks can be simulated in a variety of realistic ways. Output from the model includes time-dependent pressures and saturations of each phase in each grid block of the model region (Fanchi et al., 1987).

*NEFTRAN.** NEFTRAN (Network Flow and TRANsport) simulates radionuclide transport through porous or fractured media. The model assumes that all significant flow and radionuclide transport take place along discrete one-dimensional legs or paths. These legs are assembled to form a multidimensional network representing the flow field. Using specified pressure boundary conditions, NEFTRAN solves the flow equations. The source term within NEFTRAN contains both leach-limited and solubility-limited models and can also account for dilution of contaminants with a mixing-cell model. Each leg in the radionuclide migration path serves as a source to the next leg, and the user has the option of selecting each leg as either porous (single porosity) or fractured (dual porosity). A Distributed Velocity Method is used to calculate travel times of each radionuclide in each leg of the path. An important feature of NEFTRAN is that it allows transport of multiple radionuclide chains in a single run. The results include the rates of discharge and concentrations of each radionuclide in each chain at the end of the migration path as a function of time. In addition, integrated discharges and concentrations over the problem time, peak concentration, and concentration at a specified time can be obtained. Because of the speed of the computations, repeated trials from Monte Carlo sampling are possible, which allow parametric sensitivity to be examined (Longsine et al., 1987).

2.4 MATERIAL PROPERTY VALUES

Appendix A tabulates the material properties that are used in the calculations described in this report. Any exceptions to these values are specifically noted in the descriptions of the model simulations (Chapters 3 and 4). The sources of the data are also noted in the appendix. The primary source is a deterministic analysis of the WIPP disposal system (Lappin et al., 1989). However, important additions to these data are the expanded range for the capacitance (i.e., specific storativity divided by specific weight) for the Salado Formation (McTigue, 1989) and two-phase properties for waste-generated gas. The expanded range for the capacitance may be reduced in the future, but the calculations in this report explore the implications of the current upper bound on capacitance. Also included are data for two-phase properties to account for waste-generated gas. These latter parameter values are rough estimates, and significant revisions are expected in the future.

* Although NEFTRAN was not used in the models described in this report, several SUTRA calculations were compared to NEFTRAN calculations (Lappin et al., 1989). Hence, its description is included here.

3. UNDISTURBED REPOSITORY MODELS

The models in this chapter examine the relative importance of various phenomena and system components for an undisturbed performance scenario. As defined in the Standard, "undisturbed performance" means the predicted behavior of a disposal system, including gradual processes and the consideration of the uncertainties in predicted behavior, if the disposal system is not disrupted by human intrusion or the occurrence of unlikely or disruptive natural events.

Assumptions for the models described here are based on the hypothesized sequence described in Section 2.2 and represent pieces of that sequence. Not every aspect of the hypothesized sequence is discussed here; furthermore, development of the models that are discussed must be considered as ongoing and not complete.

The first two models discussed consider only brine flow (i.e., gas flow is not addressed). The first analysis is a two-dimensional model of brine flow from a room into MB139. The second is a cylindrical model of brine flow into a shaft. The third and fourth models discussed in this chapter include gas flow. One analysis is a two-dimensional model that evaluates only gas flow through the drifts (i.e., brine flow is not addressed). The other analysis is a one-dimensional model of both gas and fluid flow through MB139.

Each description of the four models in this chapter begins with the purpose of the model and a summary of the results. Subsequent sections describe in detail the model technique and results, which the reader may wish to defer reading until later.

3.1 TWO-DIMENSIONAL MODEL OF RADIONUCLIDE MIGRATION PATHWAY

PURPOSE

The simulations in the model described here are designed to study the effect of repressurization of the room as the result of gas generation. The hypothesized episodes described in Section 2.2 assume that under undisturbed conditions, the room remains in a gas-filled state after brine is expelled. Brine is expelled from the room by the gas, which is generated from anoxic corrosion of the containers and microbiological degradation of the waste. Because SUTRA models groundwater flow instead of gas, fluid replaces the gas in these simulations and the repository is assumed to be completely saturated. The fluid generation at pressure nodes is small and constant for the entire simulation (steady-state flow). The effect of substituting a fluid source for the gas drive is that the fluid leaves the storage area in all directions; a gas-driven fluid would be expected to leave primarily through the floor and then circle outward and up within the DRZ and host rock.

These two-dimensional SUTRA simulations of undisturbed performance are compared with NEFTRAN results (Lappin et al., 1989, Appendix D, Case I). NEFTRAN models the response of the repository/shaft system in terms of a series of discrete one-dimensional paths. SUTRA calculates two-dimensional flow and solute transport in a region around the repository shaft system. This comparison has two objectives: (1) to determine whether one or many important migration pathways exist and to consider any attendant difficulties, and (2) to confirm that fluid

fluxes resulting from a difference between lithostatic pressure in the room and hydrostatic pressure in the Culebra Dolomite, calculated by NEFTRAN along this pathway, are reasonable compared to a two-dimensional SUTRA simulation of the same conditions.

SUMMARY

In the SUTRA model, two sets of simulations were performed. The first set, Set I, was initially run so that results could be directly compared with NEFTRAN results to confirm that the fluid fluxes were reasonable (see the second objective in the Purpose) (Lappin et al., 1989). The results of Set I were also included in an earlier report (Marietta et al., 1989). The second set, Set II, was devised after analysis of Set I and provided better simulations of the problem. Set II also estimates parameter sensitivity, the effectiveness of the panel seal over the long term, and solute distributions.

In both Sets I and II, the nomenclature to describe the simulations was maintained from previous work (Lappin et al., 1989). The letter "I" indicates undisturbed, "A" indicates expected values, and "B" indicates degraded values. Thus, the first simulation, Case IA, used expected values of material parameters; the second simulation, Case IB, used unrealistic, degraded permeabilities for the MB139 seal, lower shaft, and drift. The purpose of employing the degraded properties was to investigate the response of the system to an extreme situation. In addition, a third case was added to Set II -- Case IC -- in which properties for the lower shaft were further degraded to show the effect of not having the shaft seal system.

The two-dimensional model (SUTRA) shows that over the 10,000-yr regulatory period, the brine generally moves out of the disposal area and marker bed region in all directions without a significant preference to travel up the access shaft. A somewhat localized migration pathway exists in both cases from the room, into MB139, through the MB139 seal, and then again into MB139. The path is more evident with degraded properties. However, the shaft does not serve as the dominant migration path to the near-surface environment; only the local distribution of solute is affected. In general, for expected permeabilities, flow is radially away from the disposal area; for degraded properties, flow moves down MB139 and then is radial away from both the disposal area and MB139.

The fluid generation (influx at pressure nodes) required to maintain the pressure in the room ranged from 0.07 to 0.35 m³/yr (2.5 to 12.4 ft³/yr) for Set I and 0.04 to 0.2 m³/yr (1.4 to 7.1 ft³/yr) for Set II. It is important to note that the flux decreased in the improved simulations (Set II) and is smaller for both sets than the brine inflow during saturation (1.3 m³/yr [46 ft³/yr]) that was estimated earlier (Lappin et al., 1989). Also, the third calculation for Set II (Case IC), in which upper shaft properties were used for the lower shaft seal and drift, did not influence repository performance under undisturbed conditions over the long term. Furthermore, even with permeabilities similar to sand (10⁻¹² m² [10³ mD]), very little fluid flux moves up the shaft (0.05 m³/yr [1.8 ft³/yr]). Because of the minor movement of fluid and solute, NEFTRAN provides an adequate approximation. More importantly, this long-term repository isolation under undisturbed conditions confirms the early project choices of repository design and location, for a gas-free repository. The full effect of gas or MB139 on long-term performance is yet to be determined, but if other gas effects (e.g., gas-saturated fluid) or MB139 horizontal permeability do not change this conclusion, then the undisturbed scenario will not be analyzed further. (This conclusion was also reached in Marietta et al., 1989.)

DESCRIPTION OF GRID AND BOUNDARY CONDITIONS

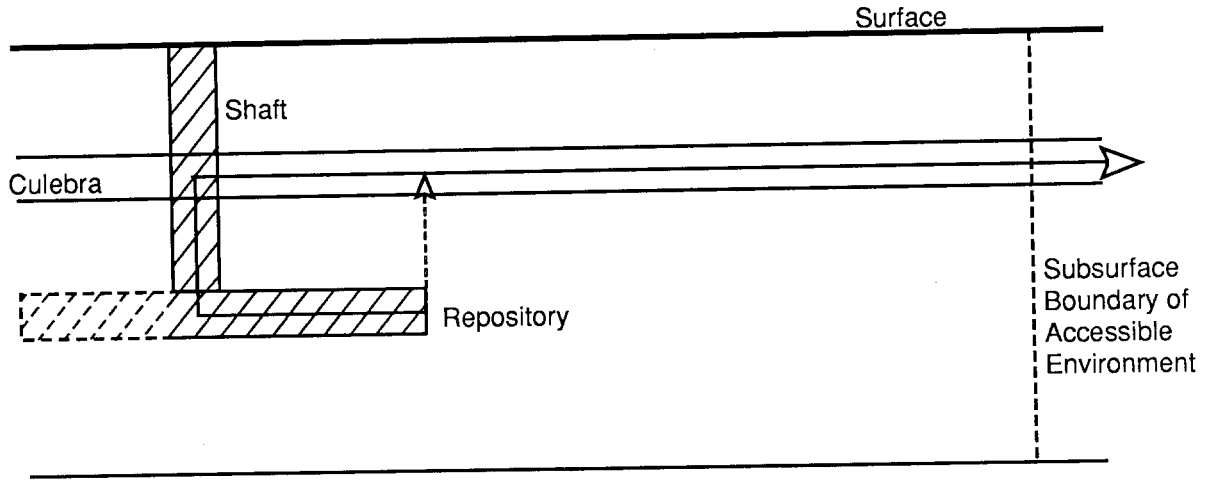
As described above, NEFTRAN was used to model the repository/shaft system's response in terms of a series of discrete one-dimensional paths (Figure 3-1). SUTRA was used to calculate two-dimensional flow and solute transport in a region around the repository/shaft system. Two sets of SUTRA simulations were performed; the simulations used steady-state flow of fluids and transient transport of a single species (i.e., ten times the estimated initial lead concentration). The reference data for the permeabilities and porosities used in SUTRA are provided in Appendix A.

The SUTRA simulations were set up to match NEFTRAN leg lengths and cross-sectional areas. However, because NEFTRAN did not model the drift, panel seal, or storage room, nominal drift dimensions were used in SUTRA. MB139 was modeled only under the drift and disposal area so that the model would match the NEFTRAN simulations and maximize the flow up the shaft. The length of one room, 90 m (300 ft), was modeled behind the drift seal (Figure 3-2). Calculated fluxes in and around the seal and storage area were so small that scaling them to full panel values is not expected to change the conclusions presented here.

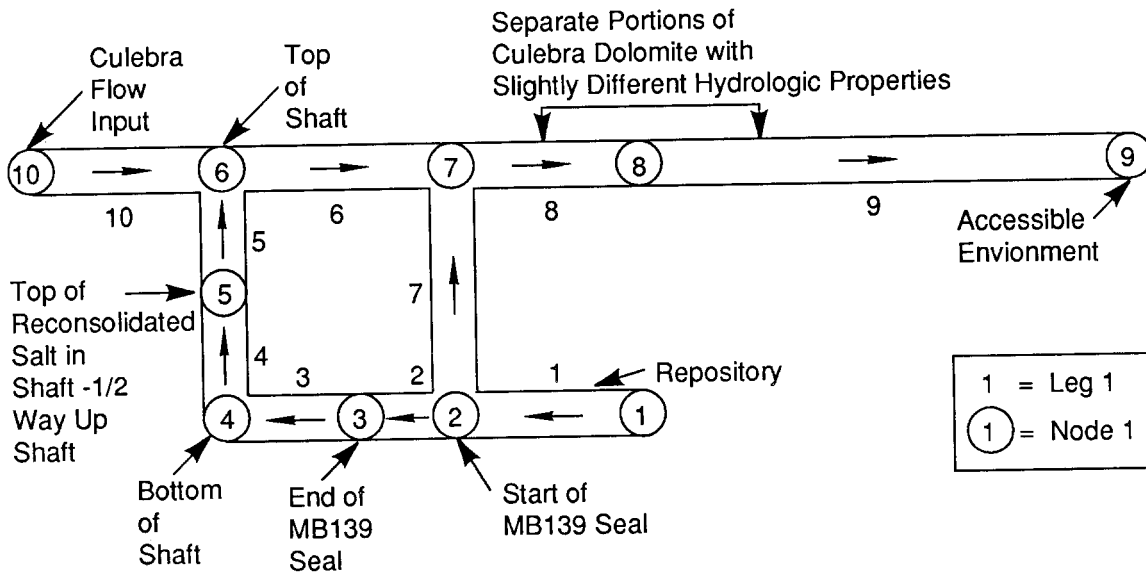
For the SUTRA model, the in-plane thickness for the Salado Formation was calculated from the cross-sectional area ($\sim 9000 \text{ m}^2$ [$\sim 97,000 \text{ ft}^2$]) and the room length ($\sim 90 \text{ m}$ [$\sim 300 \text{ ft}$]) given in the NEFTRAN model. This 100-m (330-ft) in-plane thickness was consistent with the Culebra Dolomite layer thickness in NEFTRAN. Some plume expansion was accounted for by tapering from the ceiling in-plane thickness to the Salado Formation thickness.

The first set of SUTRA simulations, Set I, used hydrostatic boundary conditions (Figure 3-2) and a highly discontinuous out-of-plane thickness. Analysis of the results of Set I led to the second, and more appropriate, set of simulations designated as Set II. In Set II, boundary conditions were interpolated from corresponding large-scale, more coarsely defined simulations (Figure 3-3), and in-plane thicknesses were smoothed over three zones surrounding the shaft, drift, and seal system. The first simulation in each set, Case IA, used expected values of material parameters. The second simulation, Case IB, used degraded permeabilities for the MB139 seal, lower shaft, and drift. In addition, a third calculation, Case IC, was run for Set II in which properties for the upper shaft were used for the lower shaft to represent an extreme case where no shaft seals are used.

A two-dimensional, finite-element mesh (Figure 3-4) that is finer around the shaft-drift intersection (Figure 3-5) and the seal-drift-MB139 interfaces (Figure 3-6) is used for Sets I and II. The mesh starts 150 m (500 ft) below the Culebra Dolomite at a depth of 400 m (1,320 ft) with the drift located at a depth of 657 m (2,155 ft). Horizontal distances are measured from the shaft (Figures 3-4 through 3-6). The shaft and MB139 are modeled with three elements of constant thickness. The thickness of the drift, room, and seal are modeled with six elements, which increase geometrically away from MB139. The seal has three elements along its length and the room has ten. The mesh along the drift is variable, extending from fine near the shaft to coarse near the seal. The in-plane thickness (third dimension) is 5 m (16 ft) for the shaft, drift, and seal, and 1 m (3.3 ft) for the MB139; the remaining Salado Formation material is 100 m (330 ft) thick.



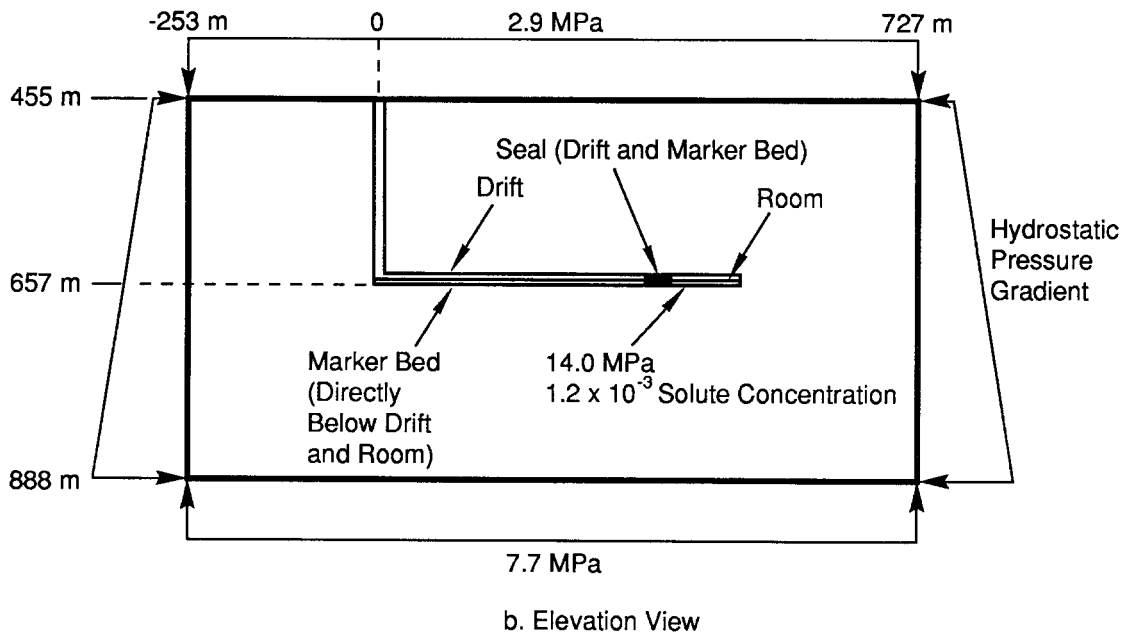
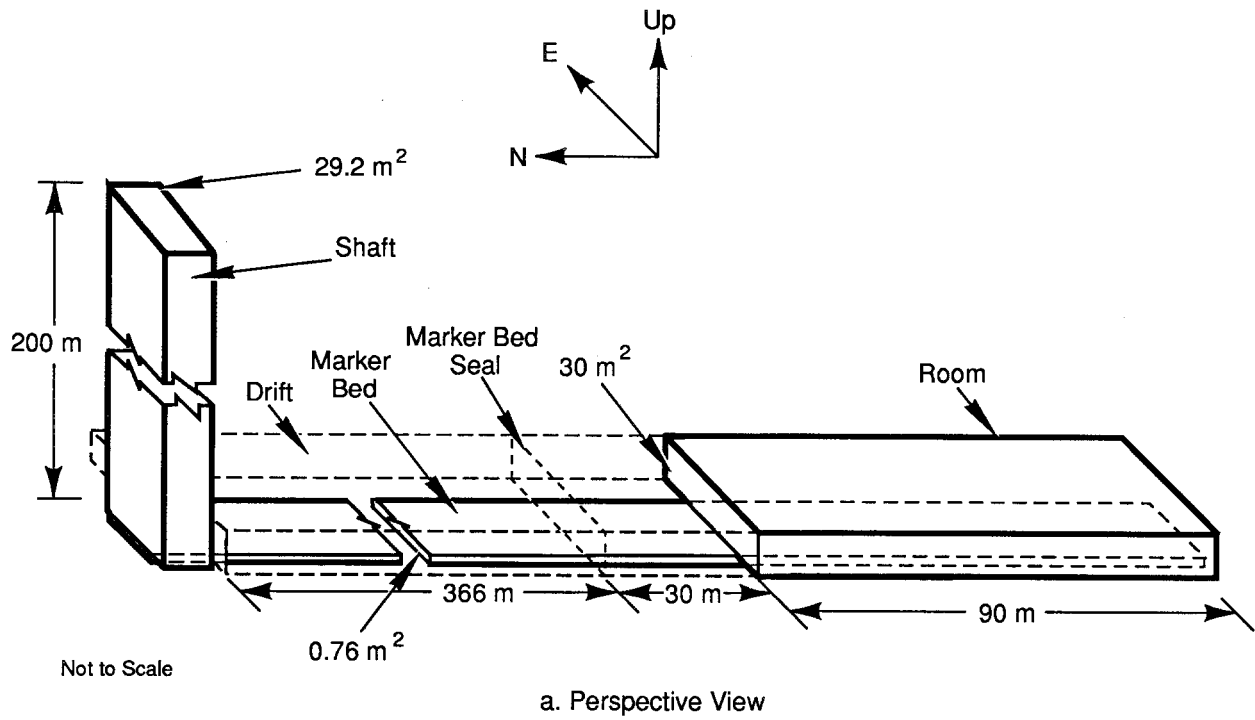
a. Conceptual Model for NEFTRAN Simulation



b. Flow Network

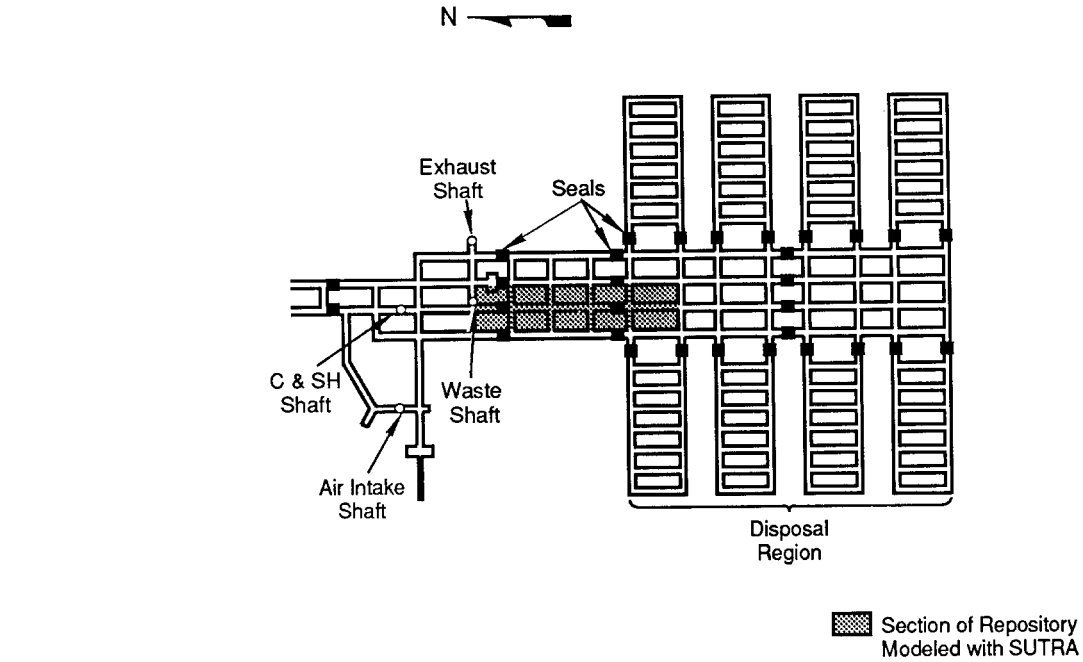
TRI-6342-199-1

Figure 3-1. Conceptual Model and Network for the Undisturbed Disposal System Modeled by NEFTRAN (after Lappin et al., 1989).

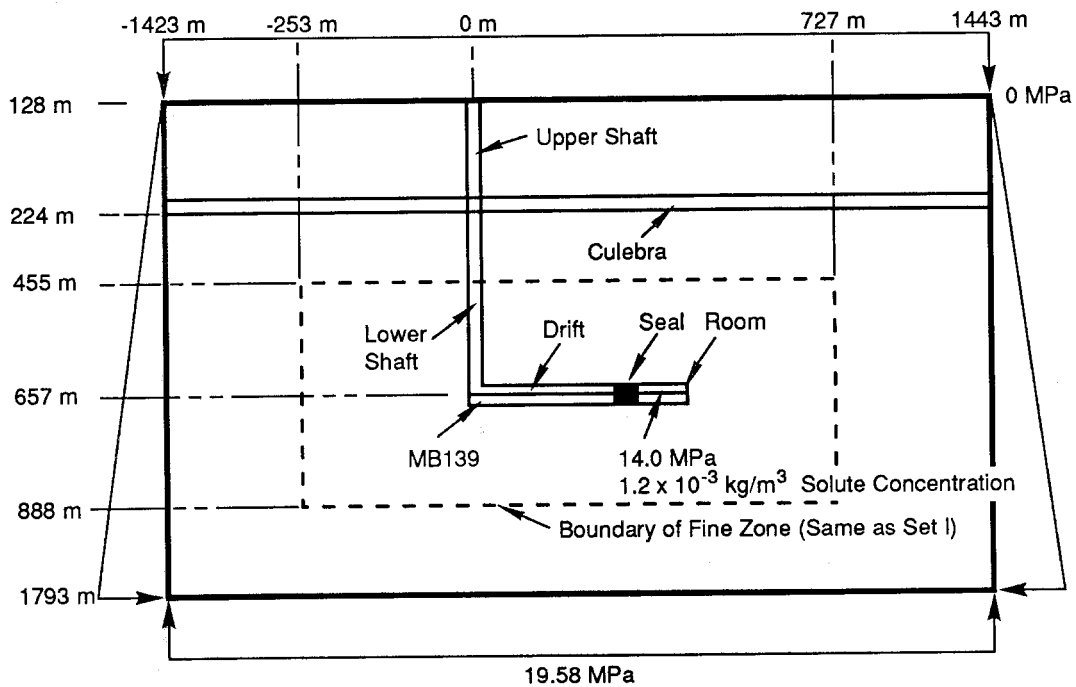


TRI-6334-176-0

Figure 3-2. Schematic and Boundary Conditions for SUTRA Simulation of Undisturbed Conditions (Set I).



a. Plan View

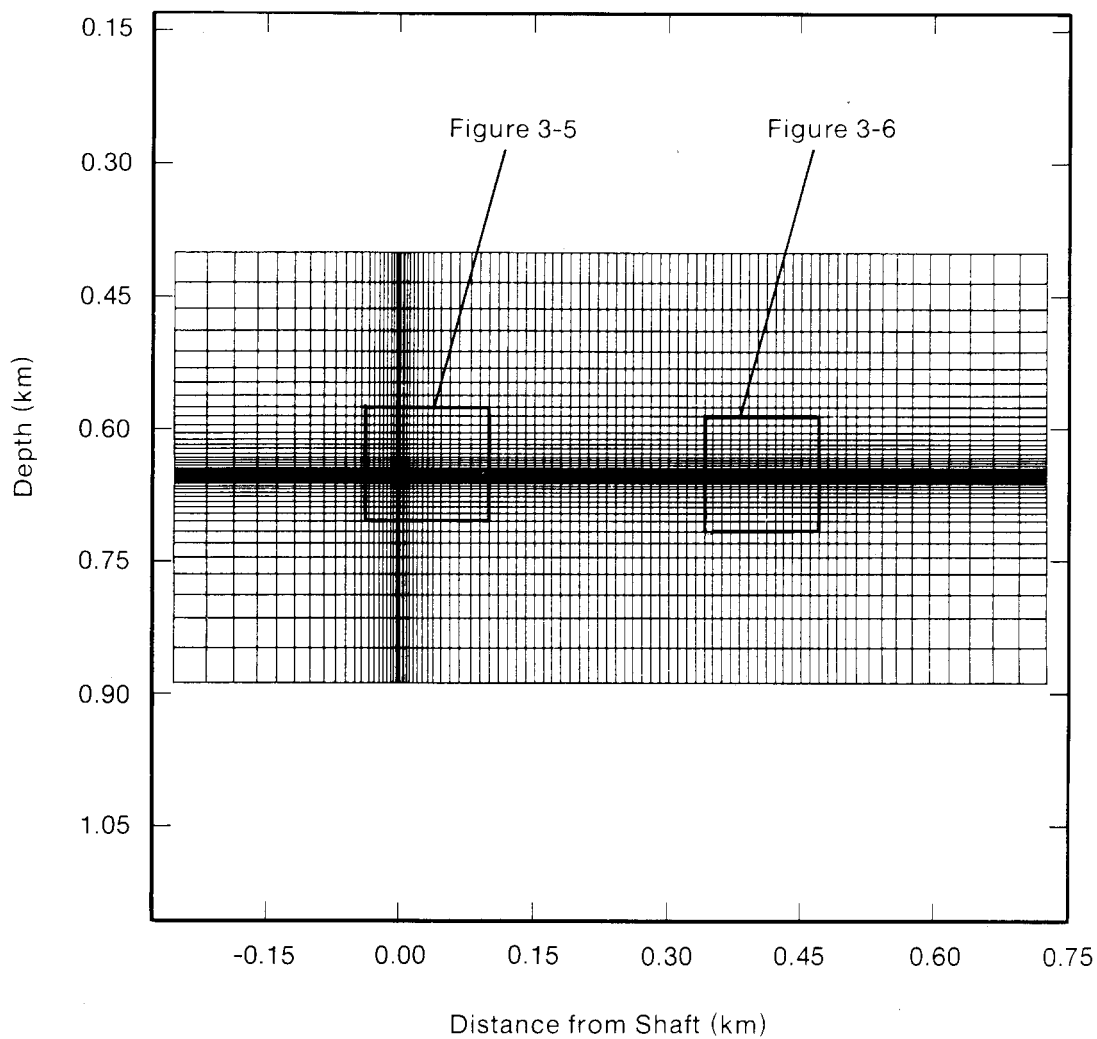


b. Elevation View

Not to Scale

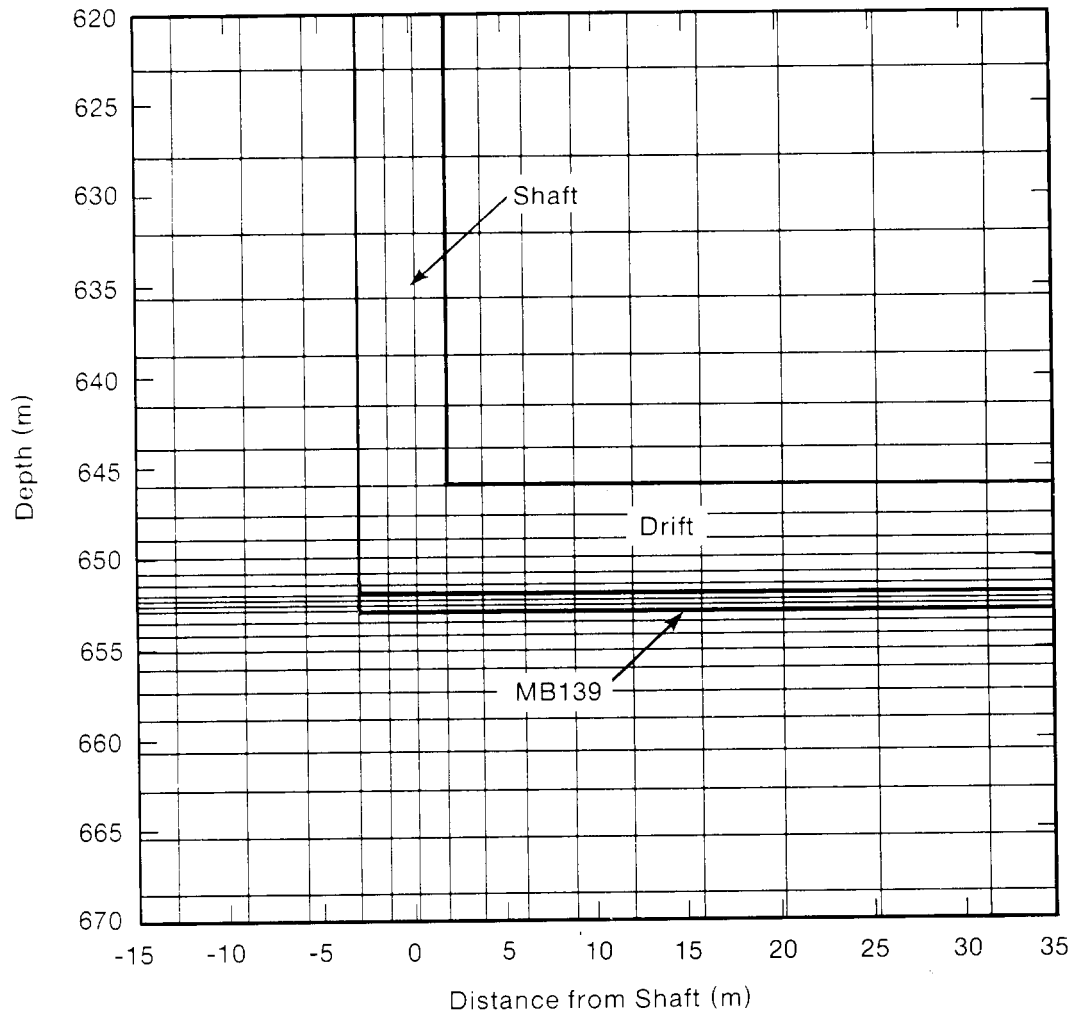
TRI-6334-177-0

Figure 3-3. Schematic and Boundary Conditions for Large-Scale SUTRA Calculations Used to Generate Boundary Conditions for Embedded Fine Zone (Set II).



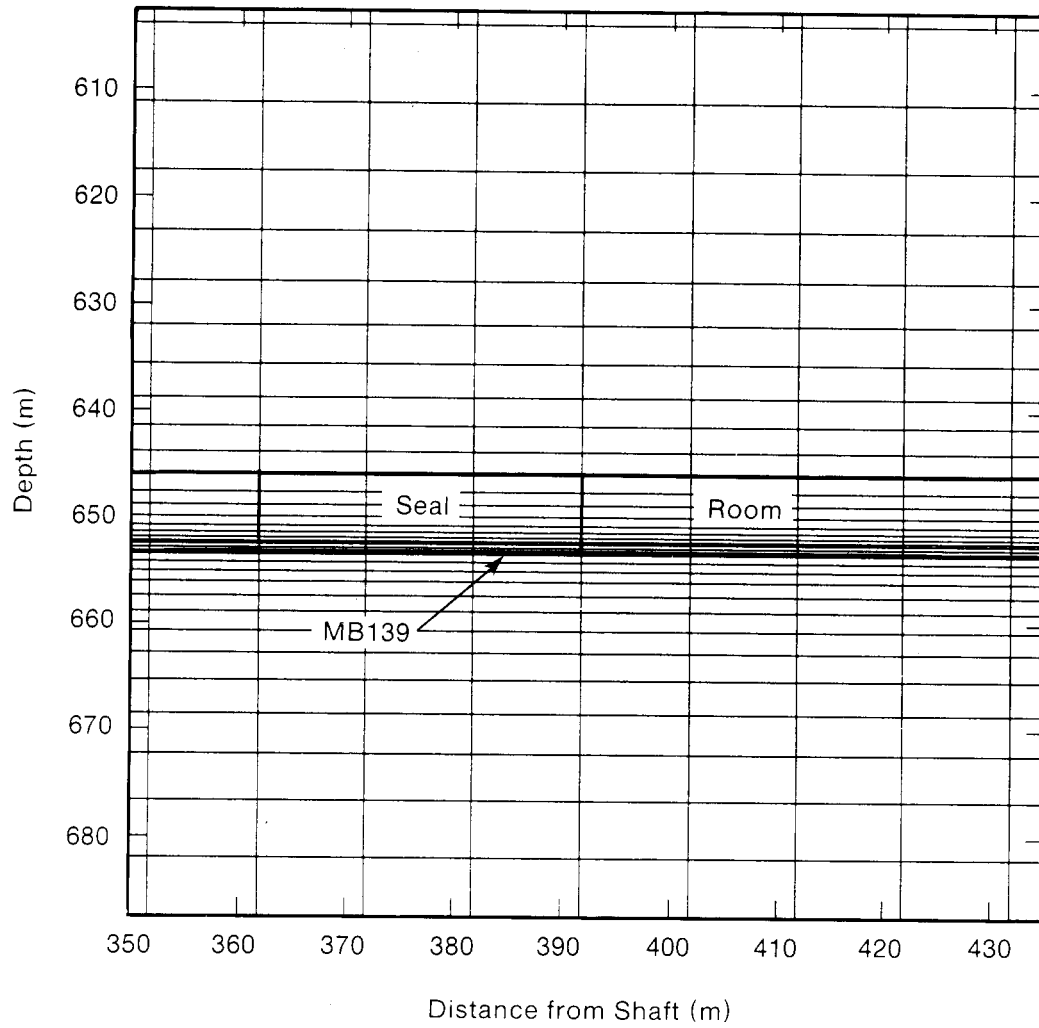
TRI-6342-201-1

Figure 3-4. Mesh of SUTRA Calculation of Undisturbed Repository/Shaft System for Sets I and II (Fine Mesh). Regions illustrated in Figures 3-5 and 3-6 are shown.



TRI-6342-202-1

Figure 3-5. Closeup of SUTRA Mesh at Shaft-Drift Intersection for Sets I and II.



TRI-6342-203-1

Figure 3-6. Closeup of SUTRA Mesh at Panel Seal and Storage Room for Sets I and II.

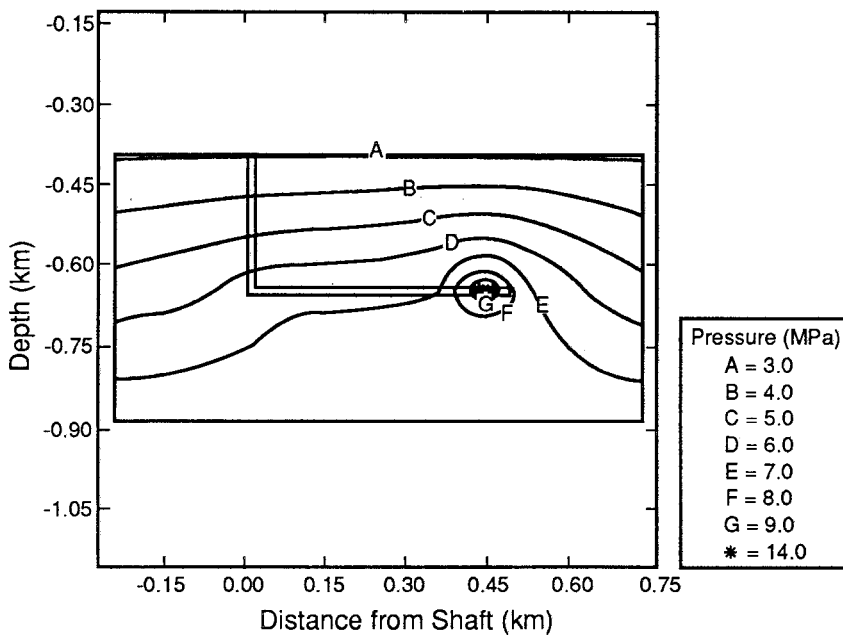
The two-dimensional mesh for Set II is identical to the mesh for Set I. However, the in-plane thickness (Δz) of the Salado Formation near the shaft, drift, seal, and room was modified. In SUTRA, thickness is a nodal variable that equals the average thickness of elements surrounding the node. Thus, the estimated fluxes near the boundaries are affected by the average zone thickness. To minimize the effect on fluxes in the room, drift, seal, and MB139, the in-plane thickness was tapered away from those regions over three zones, from 5 m to 100 m (16 ft to 330 ft).

The boundary conditions for Set I (Figure 3-2) are hydrostatic and based on a water table at a depth of 100 m (330 ft) and fluid density of $1,000 \text{ kg/m}^3$ (62 lb/ft^3) (water density was used in Set I, brine density in Set II). Hydrostatic conditions result in a pressure of 1.2 MPa at the Culebra Dolomite Member (not modeled) and 5.4 MPa at the repository horizon in the Salado Formation. Similarly, the boundary condition at 400 m and 888 m (1,310 ft and 2,910 ft) depths are 2.9 and 7.7 MPa, respectively.

The fluid flow was driven by setting a pressure of 14.8 MPa at four nodes in the center of the room, based on an assumption of a lithostatic maximum pressure (Lappin et al., 1989). This pressure implies a fluid source in the room. The assumption is required to simulate the same conditions modeled by NEFTRAN. The fluid sources and the steady-state assumptions actually provide an upper bound to the expected flow rates. The fluid source has a solute concentration of $1.16 \times 10^{-3} \text{ kg/m}^3$ ($7.24 \times 10^{-5} \text{ lb/ft}^3$) (10 times maximum lead concentration). Because the solute transport occurs over a much greater time period than that required to establish the flow field, and because the solute has little effect on the density, the calculations were run with steady-state flow and transient transport. Calculations for transient flow show that steady-state flow is effectively established within 2,500 yr, and solute has not traveled through the panel and MB139 seals in that time.

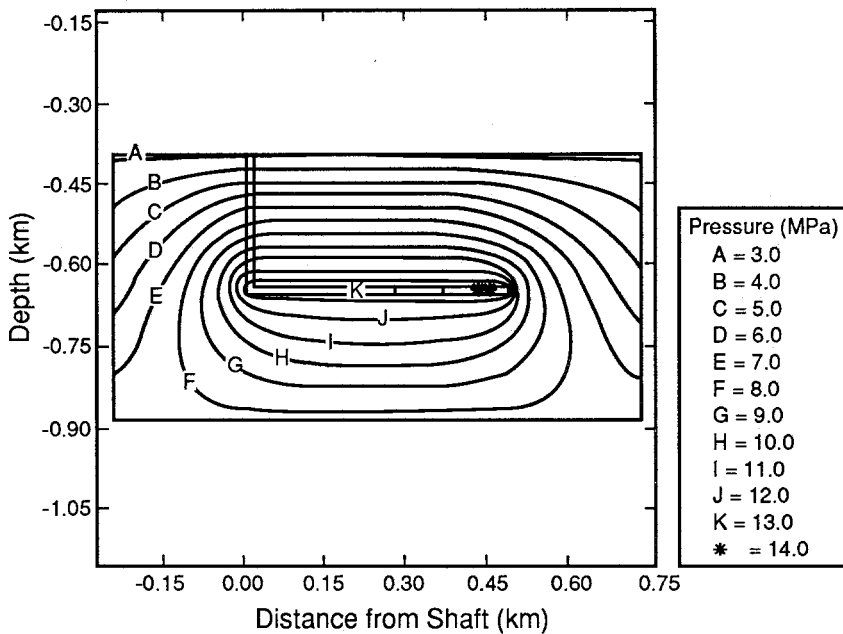
Pressure contours from the calculations for Set I revealed that the hydrostatic boundary conditions were too close to the area of interest and affected the results, i.e., the region affected by the pressurized room was much larger than the region modeled (Figures 3-7 and 3-8). Because expanding the grid would have made the calculations too large to efficiently compute, another set of calculations with properties corresponding to Cases IA, IB, and IC were run solely to generate boundary conditions for the Set II simulations. The large-scale steady-state simulations covered a region that was large enough so that hydrodynamic boundary conditions would not be affected by the pressurized room; however, the mesh was too coarse to model the details of the flow in and around the repository (Figure 3-3). The large-scale simulations included the Culebra Dolomite Member as well as the upper shaft. The top of the mesh was located at the water table (128 m [420 ft] depth). The Culebra Dolomite, MB139, shaft, and MB139 seal were modeled as one element thick. The drift, seal, and room were calculated as three elements thick. All in-plane thicknesses remained the same as in Set I. Hydrostatic boundary conditions were calculated using brine density of $1,200 \text{ kg/m}^3$ (75 lb/ft^3) and a water table at 128 m (420 ft).

The boundary conditions for Set II were defined by interpolating the pressures in the large-scale calculations along lines that corresponded to the boundaries of the smaller simulations (Figures 3-9 through 3-12). The pressure boundary conditions of Set II are shown and compared to the hydrostatic pressures used in Set I in Figures 3-13 and 3-14. The third simulation performed in



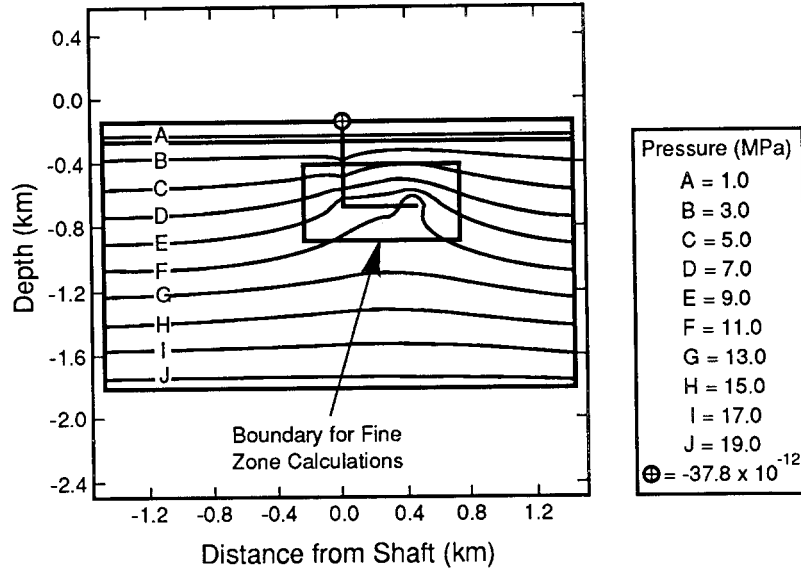
TRI-6334-223-0

Figure 3-7. Pressure Contours for SUTRA Calculation Set I, Case IA, Showing Hydrostatic Boundary Condition Edge Effects.



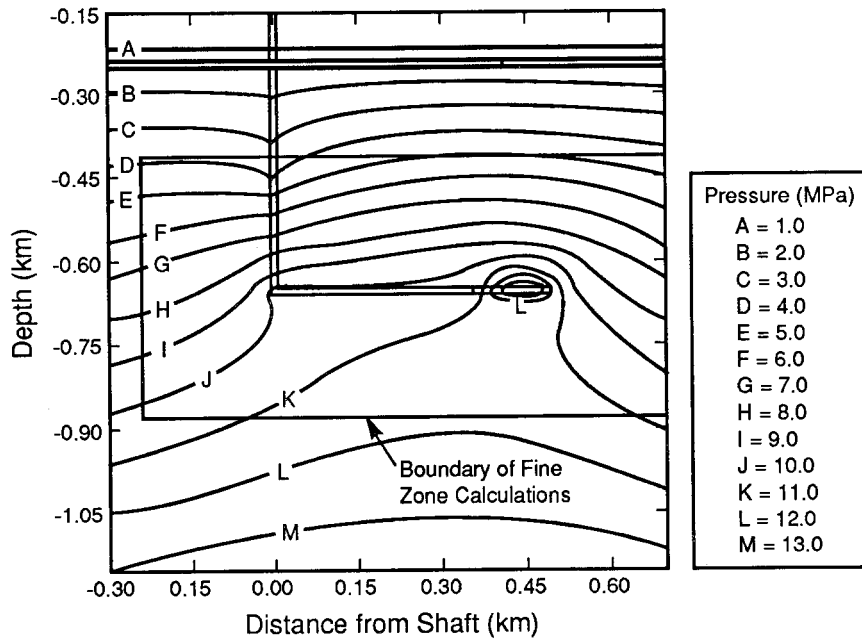
TRI-6334-224-0

Figure 3-8. Pressure Contours for SUTRA Calculation Set I, Case IB (Degraded Properties), Showing Hydrostatic Boundary Condition Edge Effects.



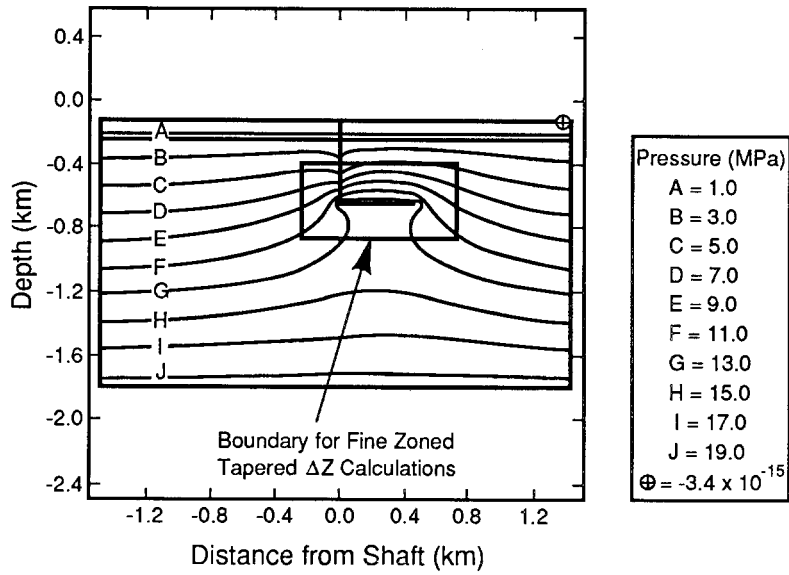
TRI-6334-225-0

Figure 3-9. Pressure Contours for Large-Scale SUTRA Calculations Used to Provide Boundary Conditions for Set II, Case IA (Steady State).



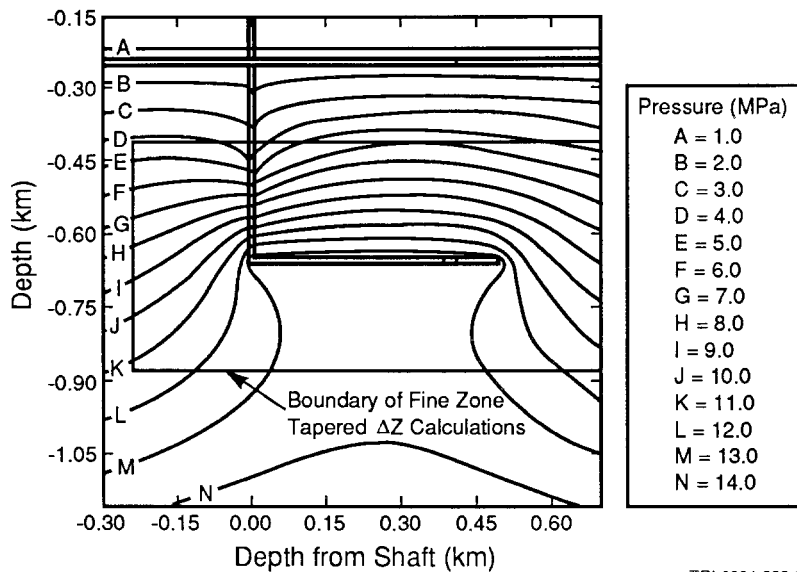
TRI-6334-226-0

Figure 3-10. Pressure Contour Details for Large-Scale SUTRA Calculations Used to Provide Boundary Conditions for Set II, Case IA (Steady State).



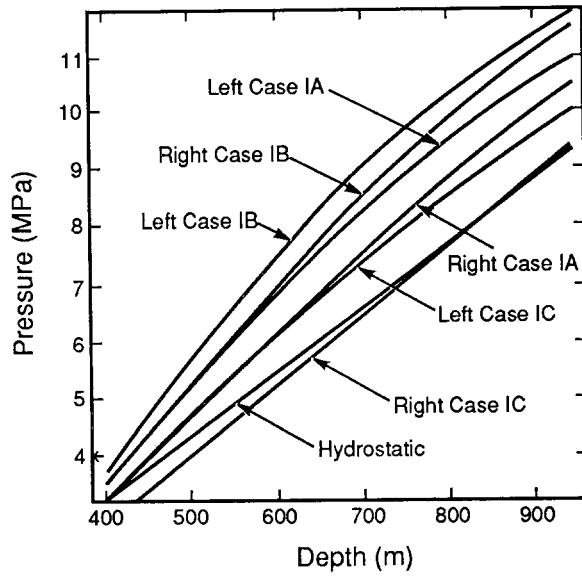
TRI-6334-227-0

Figure 3-11. Pressure Contours for Large-Scale SUTRA Calculations Used to Provide Boundary Conditions for Set II, Case IB (Steady State).



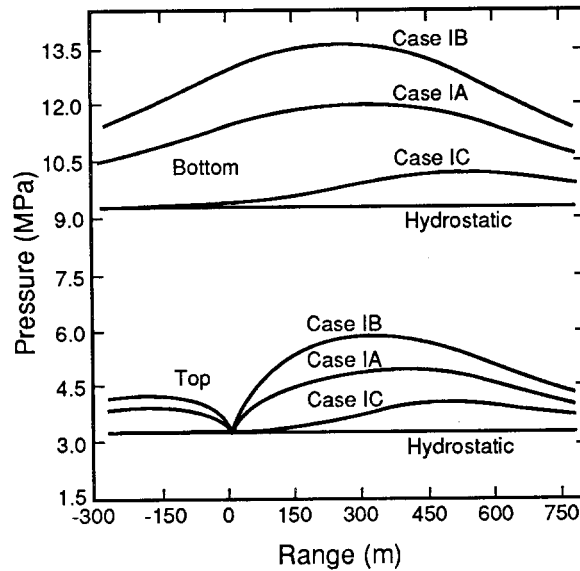
TRI-6334-228-0

Figure 3-12. Pressure Contour Details for Large-Scale SUTRA Calculations Used to Provide Boundary Conditions for Set II, Case IB (Steady State).



TRI-6334-229-0

Figure 3-13. Comparison of Left and Right Boundary Conditions for Set II, Cases IA, IB with Hydrostatic Boundary Conditions for Set I (Steady State).



TRI-6334-230-0

Figure 3-14. Comparison of Top and Bottom Boundary Conditions for Set II, Cases IA, IB with Hydrostatic Boundary Conditions for Set I (Steady State).

Set II is labeled Case IC. Case IC calculations were designed to illustrate whether the panel seal is effective over the long term. The Case IC simulation used the same geometry as Cases IA and IB (Set II), and the boundary conditions were interpolated from corresponding large-scale calculations, as described above. To demonstrate the extreme case, properties for the upper shaft were used for the lower shaft and drift in Case IC, representing a six order-of-magnitude increase in permeability and a factor of four increase in porosity. The area behind the seal was modeled with degraded drift properties in Case IB, and with expected drift properties in Case IC.

CONSTANT AND VARIED PARAMETERS

Several parameters were varied to assess each parameter's influence on flow and transport within the repository, lower shaft, and surrounding host rock. Those parameters include numerical parameters, such as size of material zones and time step, and material properties, such as porosity, permeability, and in-plane thickness of MB139. The results reported here are for variations in permeabilities for the lower shaft, drift, and seal (Table 3-1).

There are two categories of material properties (Table 3-1): (1) constant parameter values for the fluid and solid matrix and (2) parameter values that change between materials. Porosities and out-of-plane thicknesses shown by material are actually stored in the calculation at nodes because of the hybrid (integrated finite-difference/finite-element) numerical technique in SUTRA. At material boundaries, porosities and thickness are the averages of the element values around the nodes. Because of the SUTRA's modeling techniques, in-plane thickness is treated as a property.

Although the permeability of MB139 used in NEFTRAN calculations corresponds to coarse gravel ($3 \times 10^{-7} \text{ m}^2$ [$3 \times 10^8 \text{ mD}$]), a value corresponding to silty sand ($3 \times 10^{-13} \text{ m}^2$ [$3 \times 10^2 \text{ mD}$]) was used in SUTRA. The value used in NEFTRAN, 12 to 14 orders of magnitude larger than permeabilities for other materials such as rock salt, caused roundoff errors in SUTRA. The largest permeability value ($3 \times 10^{-13} \text{ m}^2$ [$3 \times 10^2 \text{ mD}$]) giving accurate results in a separate hydrostatic equilibrium calculation was selected for the Set I simulations. Values between 3×10^{-11} and $3 \times 10^{-13} \text{ m}^2$ (3×10^4 and $3 \times 10^2 \text{ mD}$) resulted in relatively small variations in flux along MB139 during the sensitivity analysis because this flux is controlled not only by MB139 properties but also by surrounding rock permeability, which is 8 to 10 orders of magnitude smaller.

The simulations in Set II used a permeability of $3 \times 10^{-9} \text{ m}^2$ ($3 \times 10^6 \text{ mD}$). The value was increased from Set I so that it would be closer to the value used by NEFTRAN. This permeability gave reasonable results in a separate hydrostatic equilibrium calculation, but not as accurate as the results obtained using $3 \times 10^{-13} \text{ m}^2$ ($3 \times 10^2 \text{ mD}$). However, the change in fluxes that results from the change in permeability is small, because the flow is controlled by the surrounding material and its value is still 10 to 11 orders of magnitude larger than the surrounding material.

RESULTS

The solute concentration contours at 10,000 yr for Set I, Cases IA and IB are shown in Figures 3-15 and 3-16; they correspond to the steady-state pressure contours field defined in Figures 3-7 and 3-8. (Note that the top of the grid is 400 m [1,320 ft] below the ground surface and 150 m [500 ft] below the Culebra Dolomite layer.) Case IA (expected properties) shows radial

TABLE 3-1. MATERIAL PROPERTIES FOR SUTRA MODEL OF RADIONUCLIDE MIGRATION PATHWAY^a

Material	Permeability, k (m^2)	Porosity, ϕ	Dispersivity, α (m)	Thickness (m)
Upper Shaft	1.0×10^{-12}	0.20	15.2	5.0
Drift/Shaft	1.0×10^{-20} 1.0×10^{-18} b	0.05	15.2	5.0
MB139	3.0×10^{-13} to 3.3×10^{-7} c 3.0×10^{-9} d	1.0	15.2	1.0
Salado Formation	3.0×10^{-21}	0.001	15.2	100.0
Seal	4.0×10^{-19} 4.0×10^{-17} b	0.03	15.2	5.0

Fluid and Solid Matrix Constants

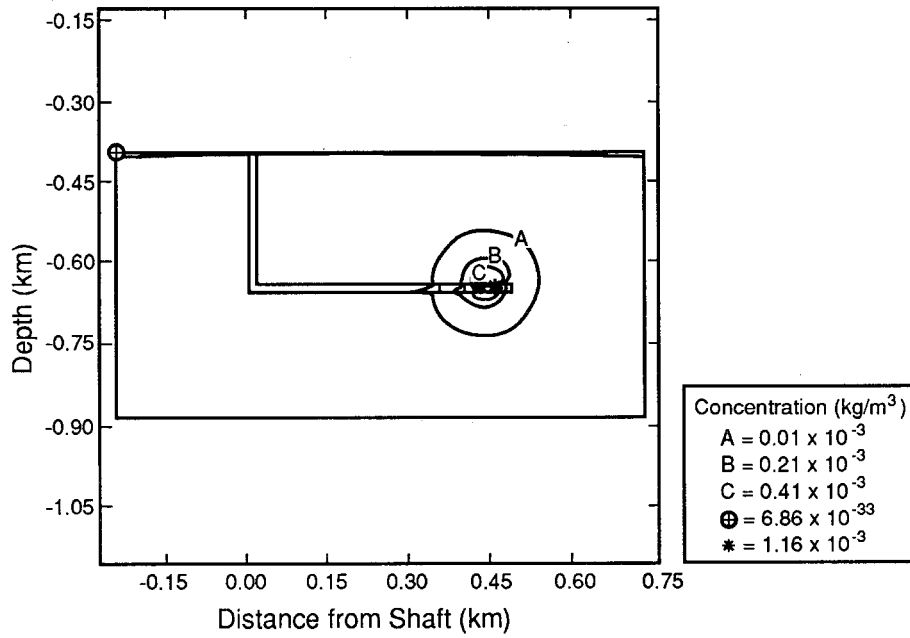
Compressibility of Fluid, β_f (water)	4.53×10^{-10} Pa ⁻¹
Compressibility of Matrix, β_s	7.54×10^{-11} Pa ⁻¹
Fluid Viscosity, μ	0.0016 Pa-s
Density of Solid, ρ_b	2300 kg/m ³
Fluid Base Density, ρ_f	1000 to 1200 kg/m ³
Molecular Diffusivity, D°	1.0×10^{-11} m ² /s

^a See Appendix A for the complete materials properties tables.

^b Degraded properties used in Case IB

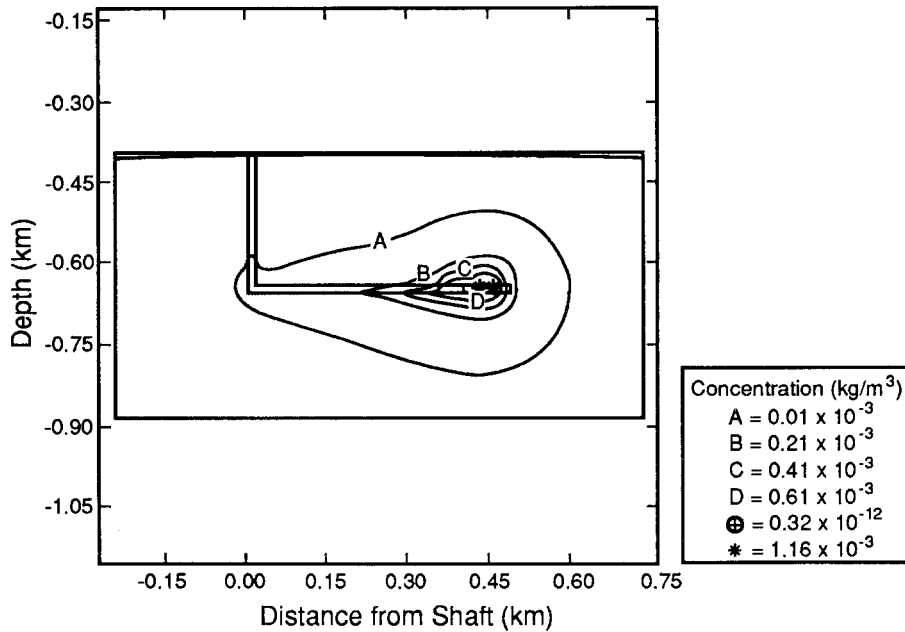
^c An effective permeability was derived for the fractures in MB139 using $k = e^2/12$ where e is fracture aperture. A fracture aperture of 2 mm was used, and to be consistent with the treatment of flow through fractures in NEFTRAN, a porosity of 1.0 was used (from Table D-2, Lappin et al., 1989).

^d Used in Set II



TRI-6334-231-0

Figure 3-15. Solute Concentration Contours for SUTRA, Set I, Case IA, Expected Properties at 10,000 Yr.



TRI-6334-232-0

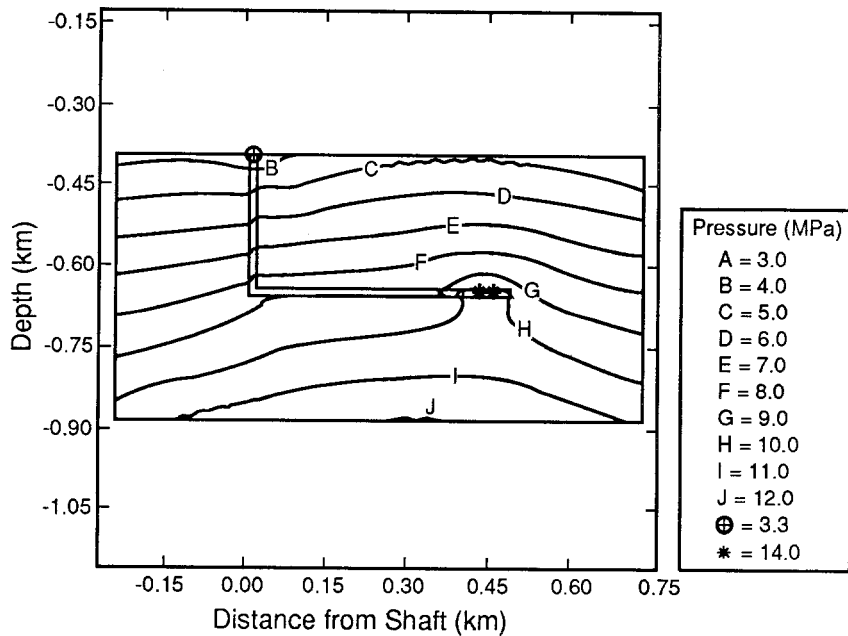
Figure 3-16. Solute Concentration Contours for SUTRA, Set I, Case IB, Degraded Properties at 10,000 Yr.

flow; Case IB (degraded properties) shows flow away from the room and MB139. Solute concentrations downstream from the seal are overestimated in Case IB, because of a larger fluid source. The larger fluid source is the result of the degraded properties behind the seal. More fluid influx is required at the pressure node to maintain the pressure at 14.8 MPa.

Pressure and solute concentration contours for Set II, with modified boundary conditions and in-plane thicknesses, are shown in Figures 3-17 to 3-22. Although solute travels slightly farther down MB139 and does not travel as far into the Salado Formation in Set II, the solute contours are quite similar to those for Set I, even though the pressure contours are quite different because of the change in boundary conditions. The pressure contours from the smaller, fine-zoned calculations of Set II (Figures 3-17 and 3-19) compare favorably with the contours in the large-scale calculations, shown in Figures 3-10 and 3-12, from which the Set II boundary conditions were derived. The differences between the contours are due to the much greater modeling detail in the Set II simulations. For example, the pressure contours for Cases IA and IB (Figures 3-17 and 3-19) indicate a difference in pressure for MB139; in Case IB, MB139 is near room pressure.

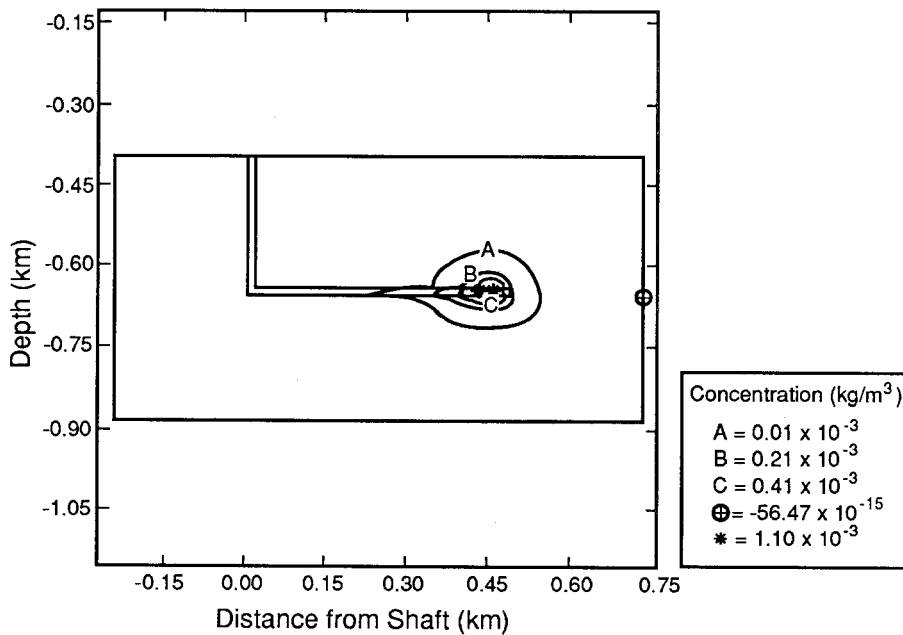
The highly degraded properties used for the lower shaft and drift in Case IC result in essentially hydrostatic pressure conditions in and around the shaft (Figure 3-21) and in a large gradient through the seal. In Case IC, higher concentrations of solute flow down MB139 than in Case IB. Also, there is very little solute in the Salado Formation downstream from the seal. In Case IC, solute flows largely into, rather than out of, the drift, indicating much more flow around the seal than in either Case IA or IB. Both Cases IC and IA have competent panel seals (Figures 3-23 and 3-18, respectively). Case IC has a much more permeable material downstream of the seal, yet the solute concentrations are similar enough to indicate that the seal is effective in retarding solute flow. Comparing Case IC with Case IB (Figure 3-20), however, indicates that very little solute reaches the base of the shaft even with a highly degraded seal and is no closer to the accessible environment than in the Salado Formation. Thus, the modeling shows that the drift seal is effective by itself, and thus a redundant component of the disposal system (possibly desirable characteristic) for undisturbed performance for a 10,000-yr evaluation period.

As an example, the interstitial-velocity vectors for Set II, Case IA, are shown in Figure 3-23; the velocity vector field for Case IB (not shown) is similar to that for Case IA, but has smaller velocities in the Salado Formation, larger velocities in MB139, and no flow around the seal. The velocity behaves differently above and below the room. Above the room, flow is away from the pressure nodes in the center of the room (only the left half of the room is shown in the figure). Though not clearly visible in the figure, there is flow around the top of the seal. In fact, slightly more fluid re-enters the drift around the top than around the bottom. Below the room the flow is into and along MB139, through and around the seal, and along MB139 toward the shaft. Because of the large permeability difference between the seal and MB139, some flow is diverted beneath the seal. However, very little fluid returns to MB139 in Case IA and none returns in Case IB because of the degraded properties. All along MB139 (except near the seal in Case IA) fluid flows away (up and down) from MB139.



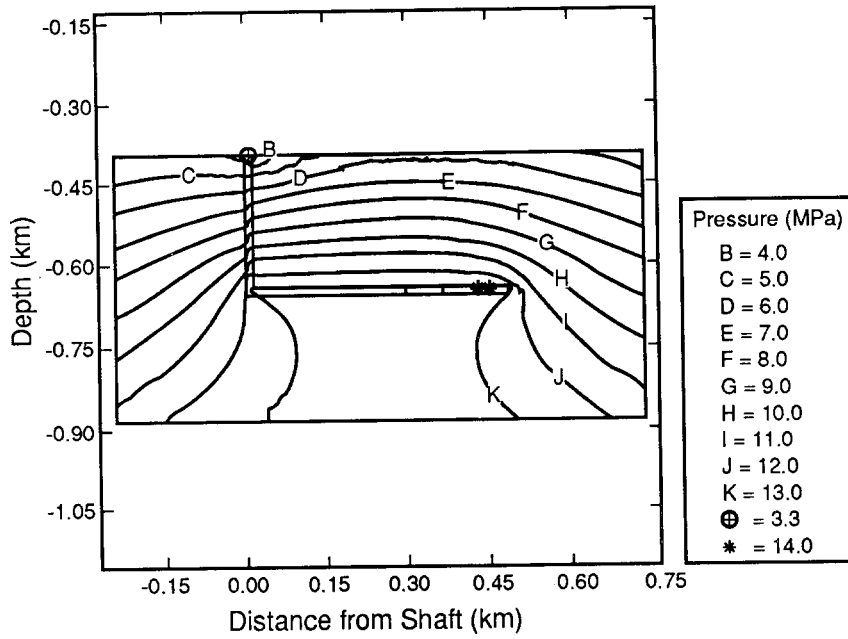
TRI-6334-234-0

Figure 3-17. Pressure Contours for SUTRA, Set II, Case IA, with Expected Properties and Boundary Conditions Interpolated from Large-Scale Simulation at 10,000 Yr. (Figure 3-10 shows the corresponding large-scale simulation.)



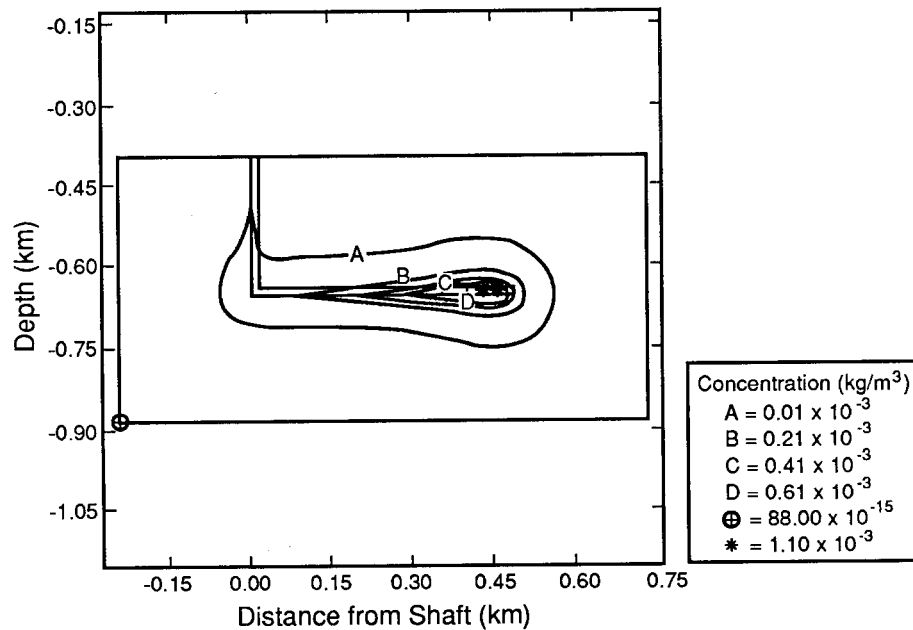
TRI-6334-235-0

Figure 3-18. Solute Concentration Contours for SUTRA, Set II, Case IA, Expected Properties at 10,000 Yr.



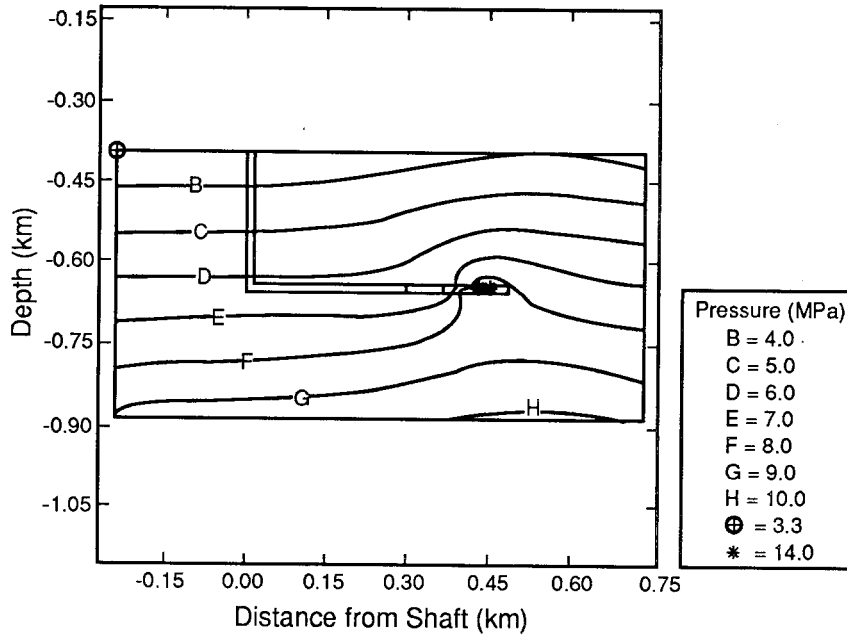
TRI-6334-236-0

Figure 3-19. Pressure Contours for SUTRA, Set II, Case IB, Degraded Properties and Boundary Conditions Interpolated from Large-Scale Simulations at 10,000 Yr. (Figure 3-12 shows corresponding, large-scale simulations.)



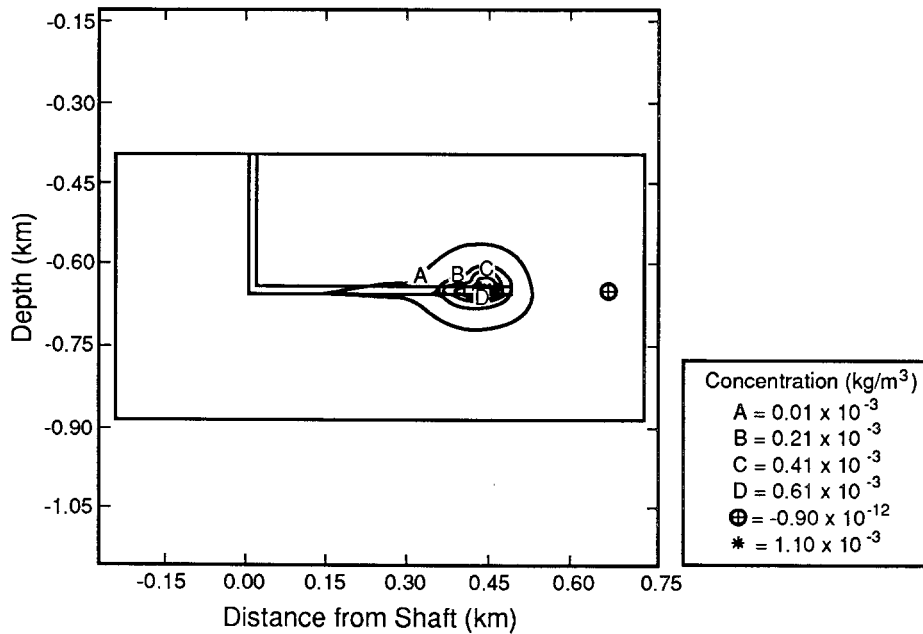
TRI-6334-237-0

Figure 3-20. Solute Concentration Contours for SUTRA, Set II, Case IB, Degraded Properties at 10,000 Yr.



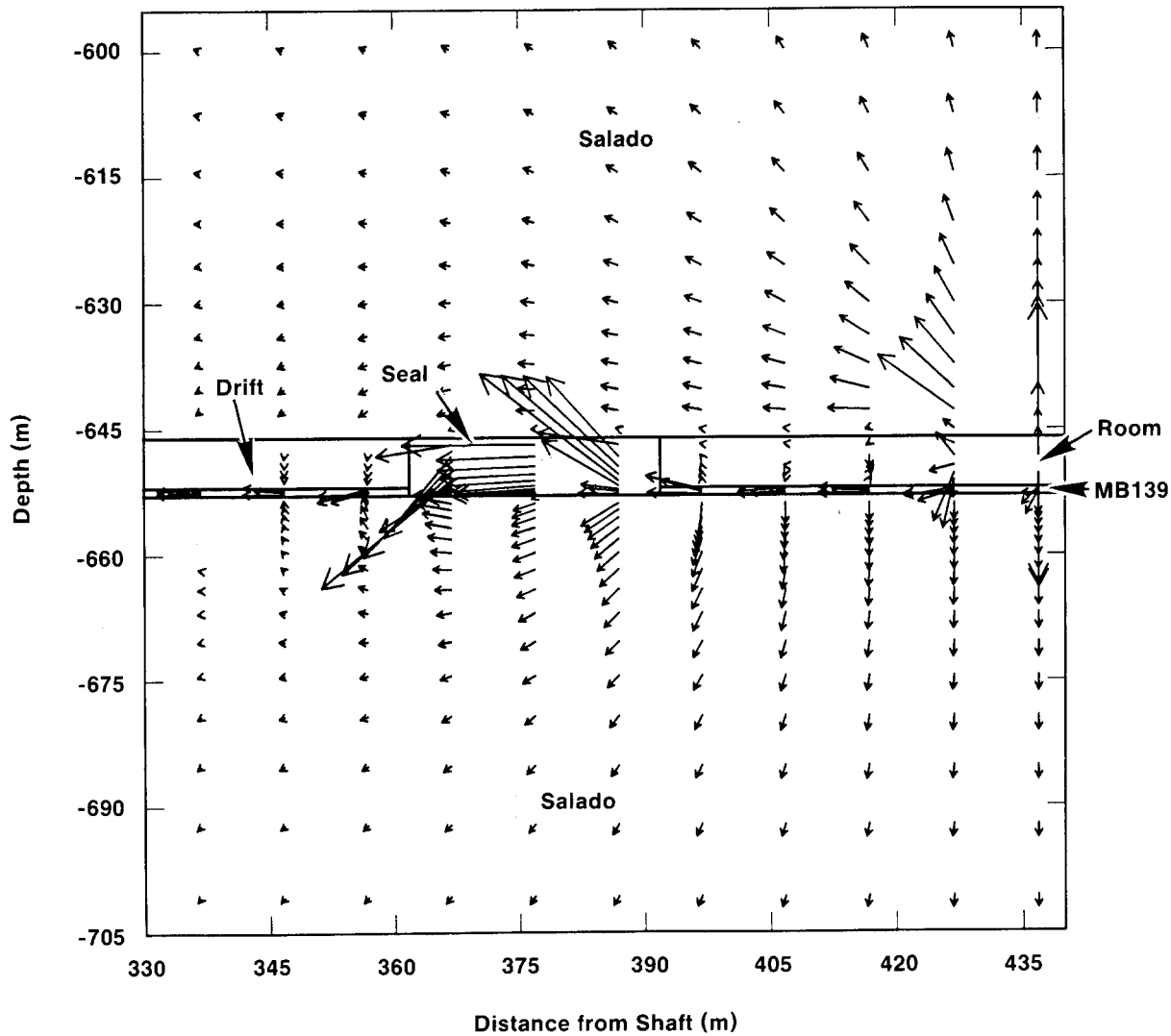
TRI-6334-238-0

Figure 3-21. Pressure Contours for SUTRA, Set II, Case IC, No Shaft Seal at 10,000 Yr.



TRI-6334-239-0

Figure 3-22. Solute Concentration Contours for SUTRA, Set II, Case IC, No Shaft Seal at 10,000 Yr.



TRI-6334-233-0

Figure 3-23. Interstitial Velocities around Panel Seal, Set II, Case IA, Expected Properties at 10,000 Yr. Relative size and direction of vectors denotes magnitude and direction of interstitial velocity at vector tail. They do not necessarily indicate that flux crosses boundaries of materials.

Volume flow rates (discharges) around the room, MB139, and the seal for Sets I and II are shown in Figure 3-24. The discharges are not output by SUTRA; rather they are estimated using interstitial velocities, porosities, and zone dimensions as follows:

$$q_x = \phi V_x \Delta y \Delta z \quad (3-1)$$

where

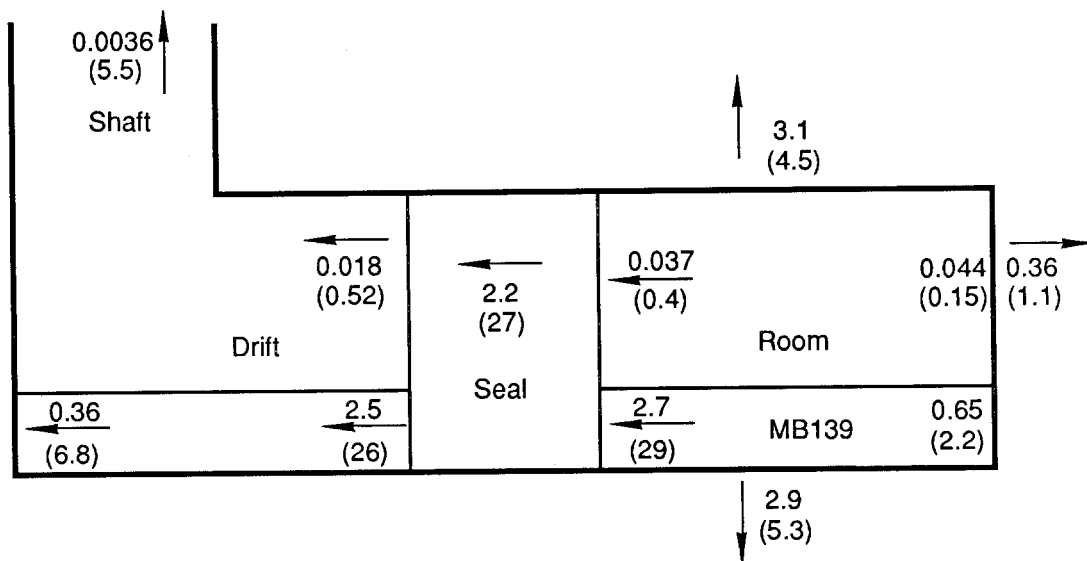
- q_x = x-component of discharge for element i (m^3/s)
- V_x = x-component of interstitial velocity in element i (m/s)
- Δy = y dimension of element i (m)
- Δz = element thickness = the average of the thickness at the nodes surrounding element i (m)
- ϕ = porosity of element i = the average of the porosities at the nodes surrounding the element.

Corresponding mass flow rates (m) can be found by multiplying by density ($1,200 \text{ kg}/m^3$ [$75 \text{ lb}/ft^3$]); solute flux is found by multiplying mass flux by concentration.

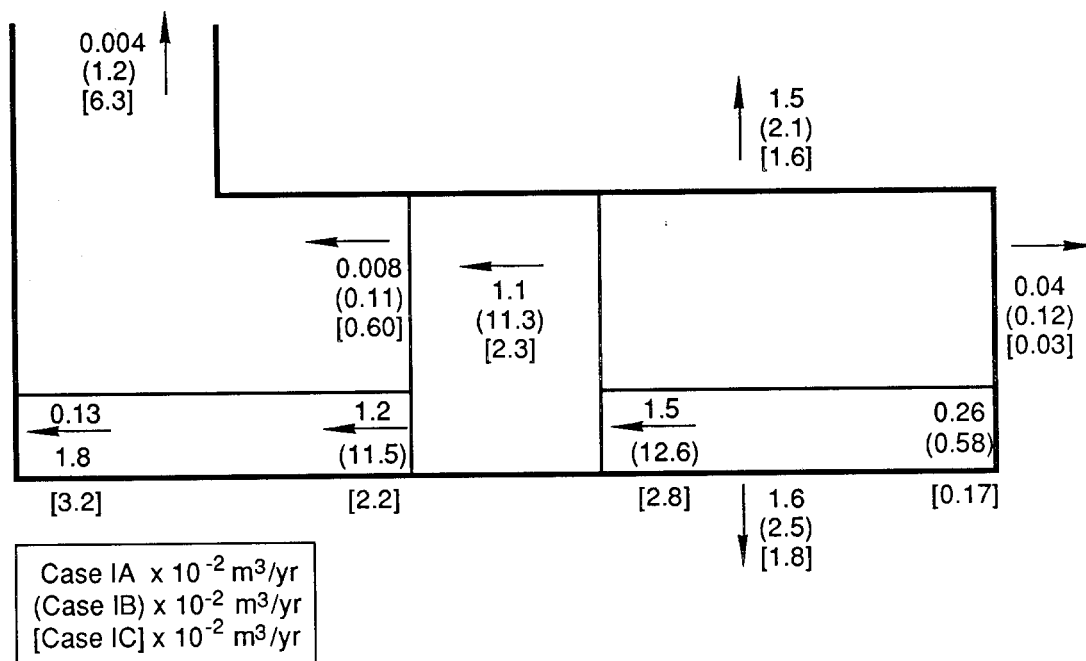
In Set I, approximately 28 percent of the fluid flow for Case IA occurs along MB139, 34 percent through the top of the room, and 32 percent through the bottom of the room. For the degraded properties, Case IB, approximately 70 percent occurs along MB139, 12 percent through the top of the room, and 8 percent through the bottom of the room. From the seal to an access shaft, flux drops by 85 percent for expected values (Case IA) and 75 percent for degraded (Case IB) along MB139. Flux through MB139 is two orders of magnitude larger than through the drift, which justifies the removal of the drift in the NEFTRAN calculations. In Set II, the fluid flow partitions are nearly the same, but the magnitudes are approximately one-half those in Set I.

The apparent imbalance of fluxes into, through, and out of the seal has two causes. One, the SUTRA code performs flux-balance calculations at nodes and does not actually generate flux as an output. Reported fluxes are calculated from element velocities that are averages of four Gauss-point velocities and areas calculated from zone dimensions and out-of-plane thicknesses with the additional problem of averaged properties at interfaces. The second cause is that only specific components of flux are shown; flow is not one-dimensional as illustrated. In a real seal, fluid flows in and out the top and bottom, thus contributing to horizontal flux (see the velocities in Figure 3-23).

When the fluxes are summed out of the room, the fluid source at the pressure nodes can be estimated. For Case IA, the influx required to maintain the pressure is about $0.088 \text{ m}^3/\text{yr}$ ($3 \text{ ft}^3/\text{yr}$); for Case IB, it is about $0.37 \text{ m}^3/\text{yr}$ ($13 \text{ ft}^3/\text{yr}$). Case IB is four times larger because of the degraded room properties. Despite the fact that the values were calculated for distinctly different problems, inflow versus outflow, the fluxes are similar to those calculated in Chapter 4, but smaller than the brine inflow of $1.3 \text{ m}^3/\text{yr}$ ($46 \text{ ft}^3/\text{yr}$) estimated in Lappin et al. (1989).



(a) Set I



(b) Set II

TRI-6334-187-0

Figure 3-24. Brine Volume Fluxes in and around the Seal and across Boundaries around a Disposal Room as Calculated by SUTRA.

The volume flux for Case IC (No Shaft Seal) from the room into the Salado Formation is very similar to Case IA because the room properties were the same. However, much of the fluid entering the Salado Formation flows around the seal and back into the drift and MB139, as indicated by the increase in flux at the shaft end of MB139. Flux up the shaft is significantly increased over fluxes calculated in Cases IA and IB, which again demonstrates the inability of the panel seal to retard long-term flow in the absence or failure of the lower shaft seal.

In Table 3-2, the mass flow rates from Figure 3-24 are compared to the NEFTRAN results. Although the agreement is not exceptional, nor the solute movement in all directions completely modeled, the simple NEFTRAN results were adequate as a first approximation. Flux into the Salado Formation has two sources: the first originates from the room and MB139 and behind the seal (a); the second comes out of MB139 downstream from the seal (b). This second source is not modeled in NEFTRAN. The difference is caused by different modeling techniques between SUTRA and NEFTRAN. NEFTRAN models MB139 as a one-dimensional pipe. SUTRA is two-dimensional so flow into surrounding host rock and along MB139 are both included, accounting for the larger fluxes at the seal-MB139 interface. NEFTRAN does not include fluid flow out the top or bottom of MB139 into surrounding host rock.

For these reasons, comparison between NEFTRAN and SUTRA is difficult. The best comparison between NEFTRAN and SUTRA simulations is made between the flux into the Salado Formation from the room plus MB139. The fluxes into the Salado Formation compare favorably for Set I, 8.5 versus 12.1; they are a factor of 3 lower for Set II, 4.2 versus 12.1. In the MB139, the SUTRA-estimated fluxes are higher (2 to 10 times) than NEFTRAN's in all cases except Set II, Case IB. The SUTRA fluxes up the shaft are much lower for the expected properties, but roughly similar for degraded properties.

In conclusion, for undisturbed conditions with an assumed pressure difference between hydrostatic in the far field and lithostatic in the room (with an implied fluid source within the room to maintain pressure), fluid migration occurs in all directions from the repository; no primary pathway exists. A localized path along MB139 does exist, but for expected properties its influence is minor. Only for degraded properties does the pathway along MB139 and up the shaft become primary.

TABLE 3-2. COMPARISON OF VOLUME FLUX BETWEEN SUTRA AND NEFTRAN

	CASE 1A (Expected) (10^{-2} m ³ /yr)			CASE 1B (Degraded) (10^{-2} m ³ /yr)			CASE 1C (No Shaft Seal) (10^{-2} m ³ /yr)
	Set I	Set II	NEFTRAN	Set I	Set II	NEFTRAN	Set II
Flux into Salado Formation							
(a) from room	6.4	3.1	12.1	10.9	4.7	12.1	3.4
(b) plus MB139	8.5	4.2	--	30.1	14.4	--	2.3
Flux down MB139							
(c) at seal	2.5	1.2	0.03	26.0	11.5	2.6	2.2
(d) at shaft	0.36	0.13	--	6.8	1.8	--	3.2
Flux up shaft	0.004	0.004	0.03	5.5	1.2	2.6	6.3

3.2 CYLINDRICAL MODEL OF SHAFT SATURATION

PURPOSE

The sensitivity of brine flow into WIPP access shafts to Salado Formation permeability was evaluated using a cylindrical model to provide input for shaft seal design. In the model, the capacitance was set at an upper bounding value suggested by McTigue (1989), and the permeability varied. Different horizontal and vertical permeabilities were chosen to test sensitivity to the presence of horizontal interbeds with high permeabilities.

Long-term permeability of the shaft seal depends on the final density of the crushed salt component following creep closure of the shaft. Fluid inflow during shaft closure may influence the final density if brine saturation inhibits consolidation of the crushed salt and, therefore, seal permeability (Nowak and Stormont, 1987). Currently, no evidence exists that initial brine contents greater than the final available pore space would prevent consolidation (Nowak et al., 1990), because excess brine, if present, could migrate out of the column, for example, up the shaft into less consolidated, more permeable zones.

SUMMARY

The SUTRA code was used to simulate brine flow from the Salado Formation into the Air Intake Shaft. SUTRA simulates Darcy flow in an elastic porous medium; creep closure, and any attendant variations in properties, were not modeled. Calculations were carried out to 200 yr, a period that includes consolidation of crushed salt in the shafts (Nowak and Stormont, 1987).

Cumulative inflow volumes vary between 200 and 1,000 m³ (7,000 and 35,000 ft³) in 200 yr for Salado Formation permeabilities ranging between 10⁻²¹ and 10⁻²⁰ m² (10⁻⁶ and 10⁻⁵ mD) and a capacitance of 5.1 x 10⁻⁹ Pa⁻¹. These results bracket the estimated range of pore volume available in the shaft at the desired minimum backfill density of 95 percent relative to the WIPP intact salt. (The range in available shaft pore volume results from an assumed range in initial placement volume.)

The effect of preferential flow through anhydrite interbeds was approximated by increasing horizontal permeability within the Salado Formation to 10⁻¹⁹ m² (10⁻⁴ mD). Little sensitivity of cumulative inflow to horizontal permeability was noted. Although substituting an average horizontal permeability applies to steady-state conditions, the substitution is not necessarily applicable for transient conditions. Therefore, this result should be verified for transient conditions using a model that explicitly includes layers with different permeabilities.

PROCESS DESCRIPTION

The shaft seal system is shown in Figure 1-7 of the Introduction. The lower shaft seal consists of: (1) a long-term seal comprised of crushed salt in two continuous columns approximately 325 and 625 m (1,070 and 2,060 ft) below the ground surface, and (2) short-term seals comprised of concrete, clay, and short-term crushed salt components. These short-term seals are located above the long-term seal, near the middle of the seal (just below the Vaca Triste marker bed), and below it (at the repository level).

Following placement of shaft seals and backfill, brine from the Salado Formation is expected to seep into the Air Intake Shaft at a rate established by pressure distributions in the Salado Formation, pressure within the shaft, and the hydrologic properties of the Salado Formation. Concurrent closure by salt creep of that portion of the shaft within the Salado Formation is expected to occur (Nowak and Stormont, 1987; Stormont, 1988). Eventually, closure and inflow will eliminate the free pore space.

Nowak and Stormont (1987) discussed the relationship between brine inflow and shaft closure in reporting the range of final backfill densities expected. In addition to influencing the final backfill pore volume (and consequently the total inflow), closure may alter the hydrologic characteristics of the salt near the shaft, thereby influencing the rate of inflow. Although the processes of closure and inflow may be closely interrelated, the model presented here focuses exclusively on flow. Some possible effects of this limitation are discussed in the Results section.

After installing the shaft seals and backfill inflow into the shaft is assumed to occur in the following stages: (a) inflow from the Salado Formation in response to the initial atmospheric pressure in the shaft; (b) reduced inflow rate as pressure develops in the shaft as the result of compression of entrapped gas and accumulation of free fluid at the base of the shaft; and (c) reduced inflow rate as free pore space is eliminated by closure and inflow, and pore fluid is pressurized to ambient Salado Formation fluid pressure. The approximations of these processes are described in the next section.

The following considerations may be important in estimating inflow volume accurately. First, the parts of the shaft above and below the short-term seal may pass through the stages described at different times, depending on the vertical distribution of Salado Formation permeabilities, relative permeabilities of the seal and Salado Formation, and vertical variability in closure rate. Second, as the Salado Formation fluid drains into the shaft, gas stored in the shaft may move into the Salado Formation, occupying pore spaces previously filled with fluid. The shaft wall might in this case be thought of as a seepage face. Finally, rather than acting as a homogeneous fluid source, Salado Formation inflow might be localized in anhydrite beds, clay seams, or lithologic interfaces.

DESCRIPTION OF GRID AND BOUNDARY CONDITIONS

Inflow during the 200 yr between short-term seal placement and closure was simulated with SUTRA. Because all fluids are assumed to be salt saturated, SUTRA's transport capability was not used. Uncertainties in mechanisms and parameters controlling flow preclude an accurate simulation of inflow; the objective of the numerical model was to estimate a reasonable upper bound for inflow. With this in mind, the following approximations were employed.

First, the possibility of partially saturated flow in the Salado Formation was ignored. The effect of partial saturation would be a reduction in net inflow by a reduction of the shaft face area available for flow. Accurate simulation of this process would require data on capillary retention characteristics and relative permeability as a function of saturation for the Salado Formation, as well as simulation of coupled fluid and gas flow.

Second, gas compression, localized saturation, and development of a fluid-filled zone in the shaft were neglected. These processes, by contributing to the evolution of backpressure in the shaft, would thereby reduce inflow rate. Ignoring the effects of fluid redistribution in the shaft allows inflow to be estimated in terms of Salado Formation properties and shaft wall boundary conditions alone. The shaft wall is assumed to impose a fixed-pressure boundary in the Salado Formation. Two fixed-pressure distributions were used: atmospheric, providing a conservatively low pressure during shaft saturation; and hydrostatic, corresponding to a fluid-filled shaft. The hydrostatic fixed-pressure boundary allows the impact of shaft backpressure on inflow rates to be gauged.

Third, preferential flow through anhydrite beds, clay seams, or anhydrite/halite contacts was not explicitly represented. The effect of high relative permeabilities in these horizontal features was approximated by raising the bulk horizontal conductivity in the Salado Formation.

Fourth, a cylindrical geometry was used, with the Air Intake Shaft at the axis. Other shafts at the WIPP can be expected to drain the Salado Formation to the same degree as the Air Intake Shaft, making the assumption of radial symmetry around the shaft only locally accurate. Reduction in Salado Formation pressure by drainage at other locations will reduce flow rates to the Air Intake Shaft below the rates expected for drainage into the Air Intake Shaft alone. Neglecting drainage at other locations therefore produces an overestimate of inflow rate.

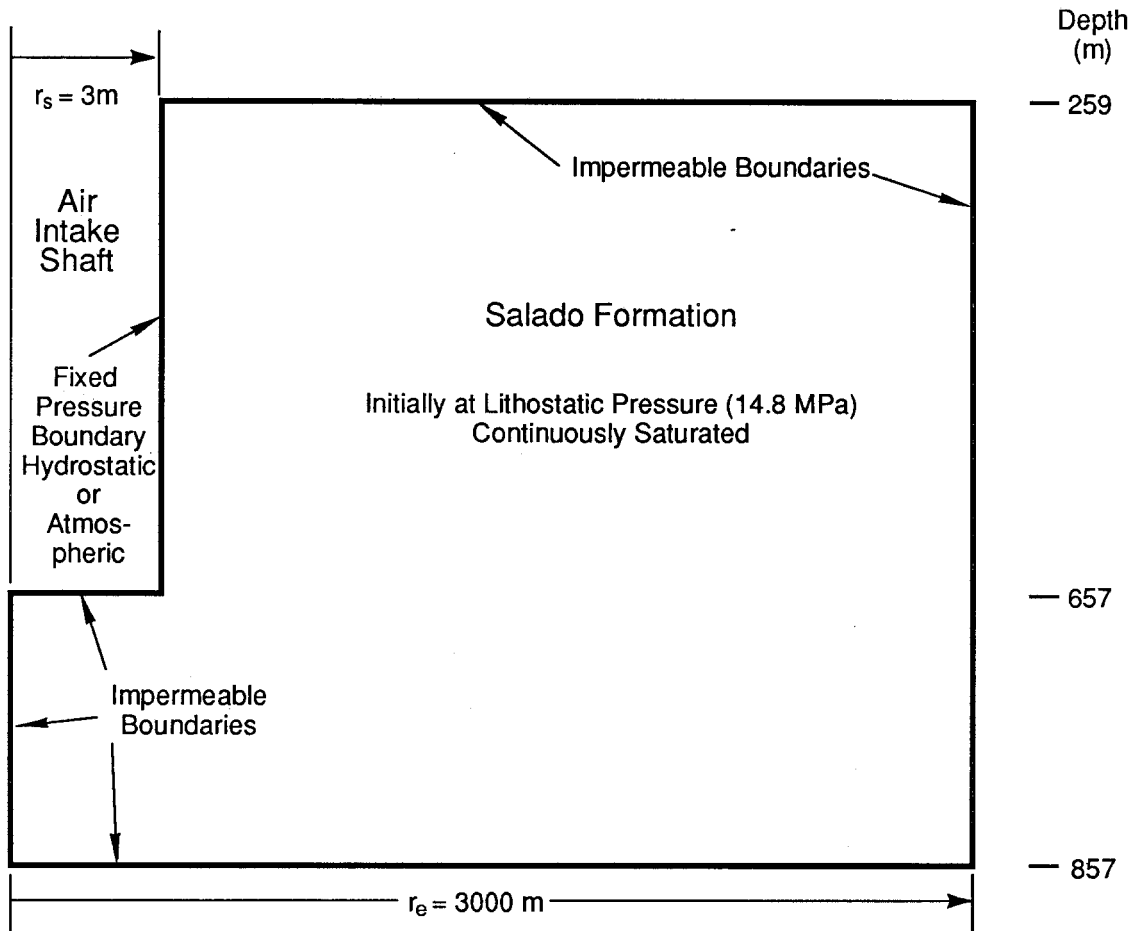
Figure 3-25 shows a schematic of the model geometry and boundary conditions. Figure 3-26 shows the model grid. (In anticipation of future model features, such as MB139, a fine grid was used near the base of the shaft, causing the dark, horizontal band seen in Figure 3-26.) The Salado Formation is assumed to be initially at lithostatic pressure. Four values of Salado Formation permeability were used in combination with the two boundary pressures discussed above. Table 3-3 presents the parameter values used in the simulations. Salado Formation capacitance was selected from the interpretation of the recent brine inflow experiments in Room D and is larger than values used previously (Lappin et al., 1989; McTigue, 1989). The effect of increasing capacitance is to increase the characteristic time of inflow rate decay, and consequently to increase inflow.

RESULTS

SUTRA output lists the flow rate at fixed-pressure boundaries for each simulated timestep. Total flow volume was calculated by integrating these rates assuming exponential variation of rates between timesteps.

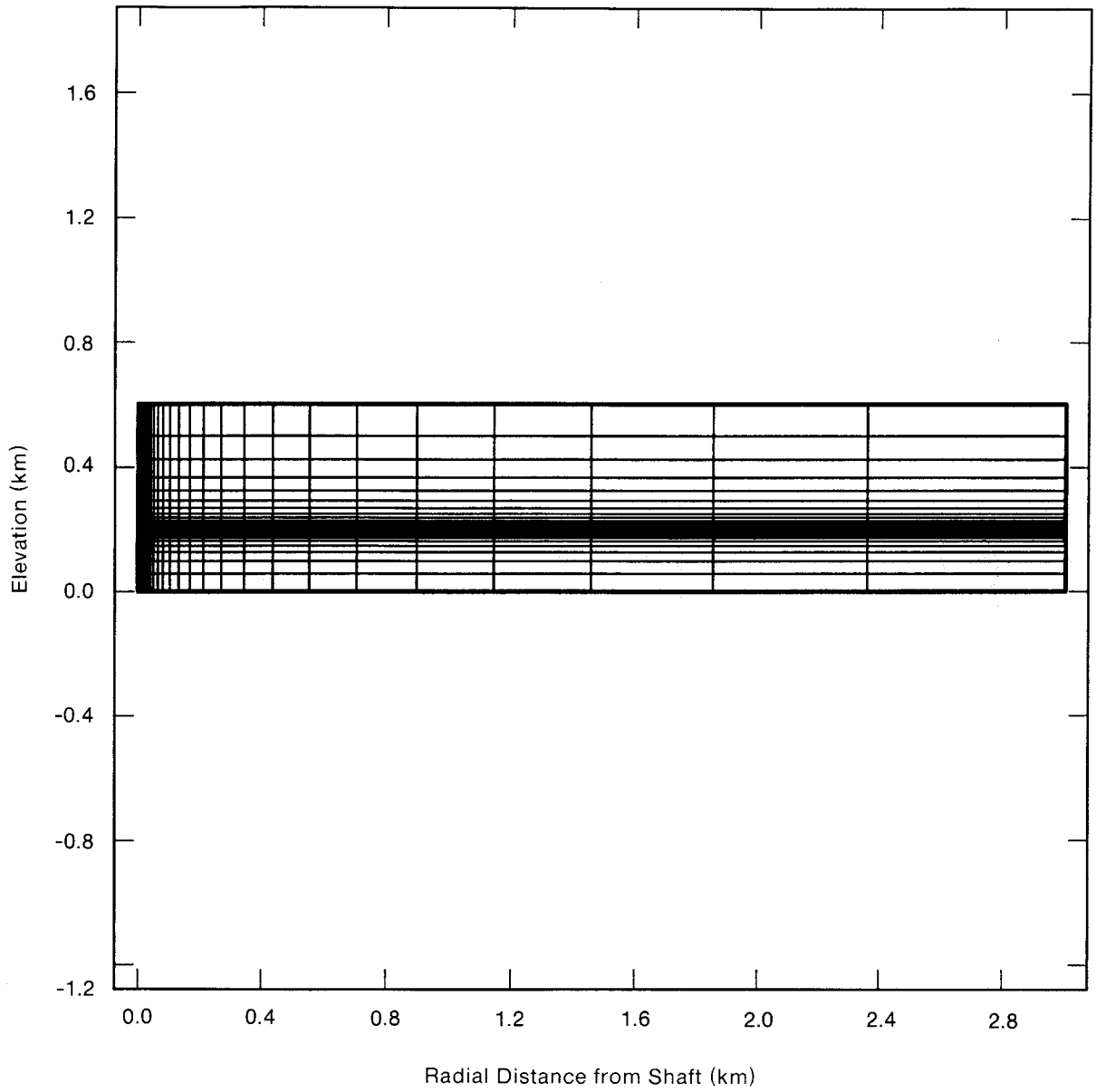
Table 3-4 presents the estimated total inflow after 200 yr for each parameter combination considered.

Figure 3-27 shows cumulative inflow along the shaft wall as a function of time for the combinations of Salado Formation permeabilities and shaft wall boundary conditions explored. The effect of boundary condition variation on total inflow is less than the uncertainty in estimated inflow resulting from uncertainty in Salado Formation permeability. Inflow in the case of anisotropic permeability (not shown in Figure 3-27) is marginally larger than estimated inflow for the expected value of permeability.



TRI-6334-180-0

Figure 3-25. Schematic Diagram of Geometry and Boundary Conditions Used in the Air Intake Shaft Inflow Calculations.



TRI-6334-246-0

Figure 3-26. Mesh Used for Air Intake Shaft Simulations.

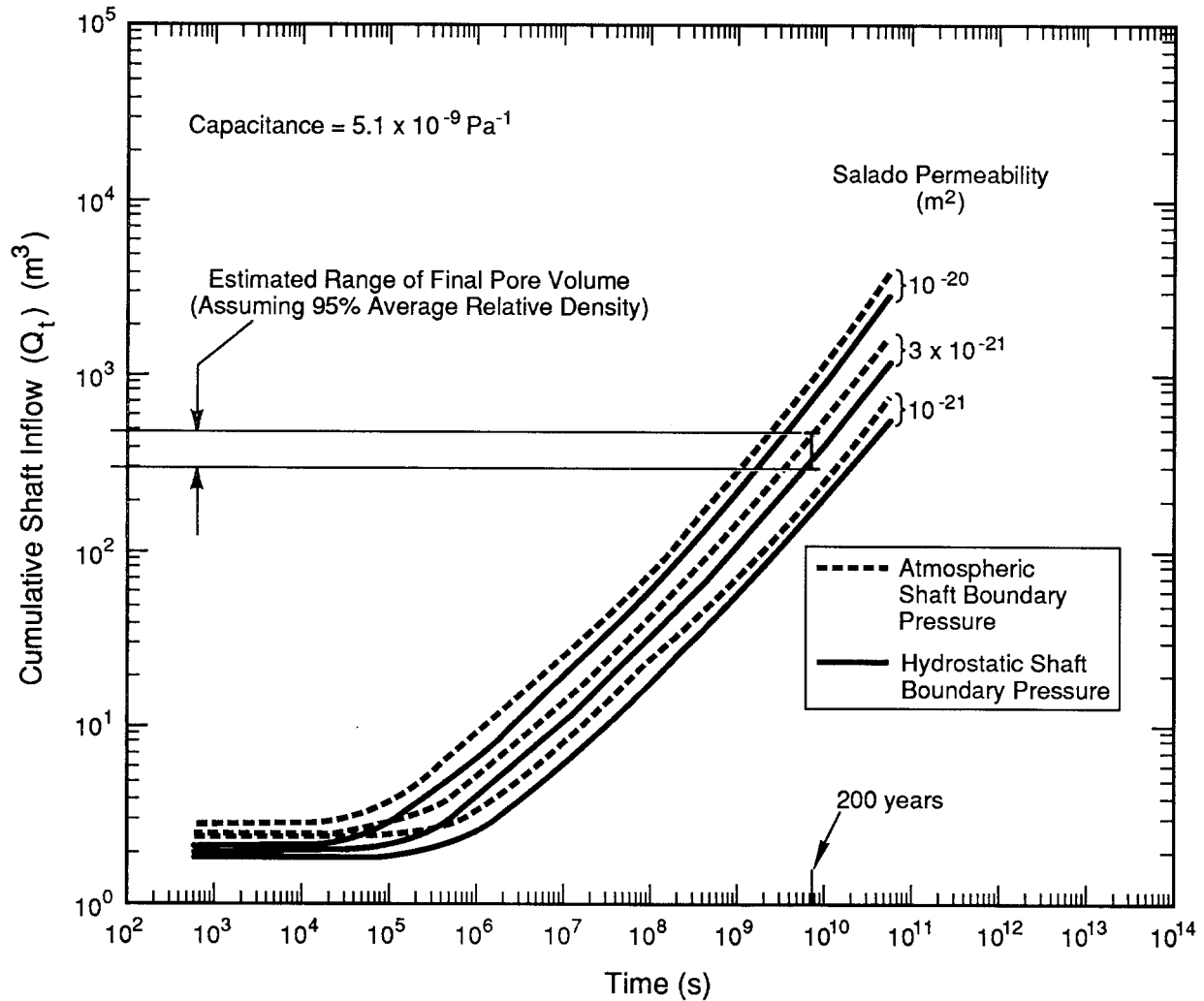
TABLE 3-3. HYDROLOGIC PROPERTIES AND BOUNDARY CONDITIONS USED IN AIR INTAKE SHAFT SATURATION SIMULATIONS

<u>Salado Formation Permeability (m²)</u>	
<u>Horizontal</u>	<u>Vertical</u>
1. 1 x 10 ⁻²¹	1 x 10 ⁻²¹
2. 3 x 10⁻²¹	3 x 10⁻²¹
3. 1 x 10 ⁻²⁰	1 x 10 ⁻²⁰
4. 1 x 10 ⁻¹⁹	3 x 10 ⁻²¹
 <u>Shaft Wall Boundary Conditions</u> Atmospheric, Hydrostatic	
 <u>Salado Formation Capacitance (c)</u> 5.1 x 10 ⁻⁹ Pa ⁻¹	

TABLE 3-4. ESTIMATED INFLOW VOLUMES AND RATES FOR THE VARIOUS SALADO FORMATION PERMEABILITIES AND BOUNDARY CONDITIONS

<u>Salado Formation Permeability (m²)</u>		Shaft Wall Boundary Condition	Cumulative Flow at 200 yr (m ³)	Average Flow Rate (m ³ /yr)
Horizontal	Vertical			
1 x 10 ⁻²¹	1 x 10 ⁻²¹	hydrostatic	185	0.93
		atmospheric	242	1.21
3 x 10⁻²¹	3 x 10⁻²¹	hydrostatic	362	1.81
		atmospheric	474	2.37
1 x 10 ⁻²⁰	1 x 10 ⁻²⁰	hydrostatic	800	4.00
		atmospheric	1050	5.25
1 x 10 ⁻¹⁹	3 x 10 ⁻²¹	hydrostatic	367	1.84
		atmospheric	481	2.40

Boldface = Expected Value



TRI-6334-181-0

Figure 3-27. Estimated Cumulative Air Intake Shaft Inflow (Q_t) vs. Time (t).

Figure 3-27 also shows the estimated range of shaft backfill pore volume corresponding to 95 percent average backfill density relative to the in-situ host salt. Previous calculations (Arguello and Torres, 1987) show that a relative backfill density of 95 percent achieves a backfill permeability approximately equal to the permeability of intact WIPP salt. The range in available pore volume in the Air Intake Shaft results from the range in initial placement density. At a final relative density of 95 percent, the available pore volume (Ω_p) occupies a volume of

$$\Omega_p = 0.05\Omega_m = \frac{M}{0.95\rho_s} \rightarrow 360 \text{ to } 510 \text{ m}^3 \quad (3-2)$$

where

- D_r = relative density
- h = shaft height
- M = total salt mass = $D_r\rho_s\Omega_i$
- r_s = shaft radius
- ρ_s = grain density

Ω_i = initial volume of Air Intake Shaft = $\pi r_s h = 11,400 \text{ m}^3$

Ω_m = volume of mass.

The design-specified initial relative density of the crushed salt within the shaft (D_r) is 80 percent (Nowak et al., 1990). The upper bound was set at 85 percent. Although not applicable to the shaft, the initial relative density of the crushed salt within the drift backfill is 60 percent (Nowak et al., 1990) and was used as a lower bound.

This range brackets the estimated inflow volume for expected Salado Formation permeability, and is bounded by estimated inflow volume for the bounding values of Salado Formation permeability considered here. Excessive inflow does not preclude optimal compaction of some portion of the backfill. Greater stresses at the bottom of the shaft are expected to result in more rapid closure at depth.

Nowak and Stormont (1987) discusses the relationship of final backfill density to overall seal system performance, and the influence of brine inflow from overlying units on the final density of shaft backfill. By simulating shaft closure in the presence of uniform inflow from the top of the shaft, Nowak and Stormont identified an acceptable average inflow rate of approximately $1 \text{ m}^3/\text{year}$ ($40 \text{ ft}^3/\text{yr}$), resulting in optimal compaction of the lower 100 m (330 ft) of the shaft (Stormont, 1988, Fig. 7-7). The effective average inflow rate estimated here ranges from approximately 1 to $5 \text{ m}^3/\text{yr}$ (40 to $200 \text{ ft}^3/\text{yr}$).

DISCUSSION

The present model suggests other effects that might be useful to consider in subsequent models, such as coupled effects of closure and fluid flow. Closure of the shaft may influence shaft wall permeability (Rechard and Schuler, 1982), and might possibly reduce far-field mechanical stress in the Salado Formation, consequently reducing pore fluid pressure. In addition, the model did not account for upward flow of shaft fluid as a result of progressive closure from the bottom to the top of the shaft. A coupled mechanical-hydrological model would help to assess the importance of these processes.

Another future consideration might be backpressure in the shaft resulting from gas compression. The results presented here using a hydrostatic shaft wall pressure suggest that accumulation of free fluid in the shaft does not significantly retard inflow.

Other influences that might be considered include simultaneous drainage of the Salado Formation into all repository/shaft excavations, and assumptions governing flow through the Salado Formation, particularly the ambient pressure and flow mechanism.

The present model has not been used to assess the effects of uncertainty in long-term capacitance. Because inflow rates are expected to be sensitive to this parameter, uncertainty in capacitance should be included in any related, future work.

3.3 TWO-DIMENSIONAL MODEL OF GAS FLOW FROM DISPOSAL AREA TO SHAFT USING SUTRA

PURPOSE

This two-dimensional model simulates the flow of hydrogen gas in the disposal area, drift seal, and drift backfill materials leading to a shaft. In the model, it is assumed that the surrounding Salado Formation is impermeable to gas flow. (This is initially true, relative to the drift, because the drift is initially unsaturated.) The intent of the model is to evaluate (1) whether gas from the disposal area will reach the bottom of the shaft before shaft consolidation is complete and (2) the sensitivity of gas flow to the permeability of the seal and drift material.

The model also investigates the rate at which the gas pressures that are generated in the room influence the gas pressures in the drift. Because of these limited purposes, gas flow up the shafts was not modeled in this rudimentary simulation. Although the hypothesized episodes described in Section 2.2 assume that consolidation will occur before a significant amount of gas is generated from anoxic corrosion of the containers and microbiological degradation of the waste, this model investigates whether the drift seals will retard gas flow if the waste produces high gas pressures before complete consolidation of drift seals.

The analysis examines the influence of the permeability of the seals and drift material on the flow of gas to the base of the shaft.

SUMMARY

This analysis was performed using a modified version of SUTRA that models compressible fluid flow (e.g., gas). Modifications to the code allow fluid density to depend on pressure and account for nonconstant fluid compressibility. Isothermal, transient flow from an initial uniform gas pressure was considered. Solute transport was not addressed in these calculations.

This model of gas flow demonstrates the influence of the seal and drift backfill properties (permeabilities) on gas pressurization at the base of the shaft. Only one set of drift seals is modeled, and the seal does not contain a concrete component. Because of hypothesized predominance of hydrogen and its low viscosity, these studies used only hydrogen gas rather than a mixture.

Assuming initial permeability in the drift and disposal area, the entire disposal area and drift were uniformly pressurized in less than 5 yr. Assuming final permeabilities at final drift consolidation, the pressure at the base of the shaft had not changed from the initial state even after 1,565 yr. Additional calculations assuming a time-dependent decrease in permeability for the disposal area and drift backfill materials showed that without drift seals, the pressure at the base of the shaft increased to about 10 MPa after about 71 yr, but did not significantly increase beyond that level even to times as great as 1,565 yr. For calculations including the drift seals, but without the concrete component, pressures at the base of the shaft rose to about 2.5 MPa after 24 yr, but remained at that level to at least 1,565 yr.

Thus, the calculations indicate that the slowly consolidating salt in the drift seal can be quite effective in retarding gas flow to the shaft. Whether such an impermeable barrier to gas is

required, however, demands a more detailed model that would simulate flow up the shaft to examine the possibility of any adverse effects.

DESCRIPTION OF GRID AND BOUNDARY CONDITIONS

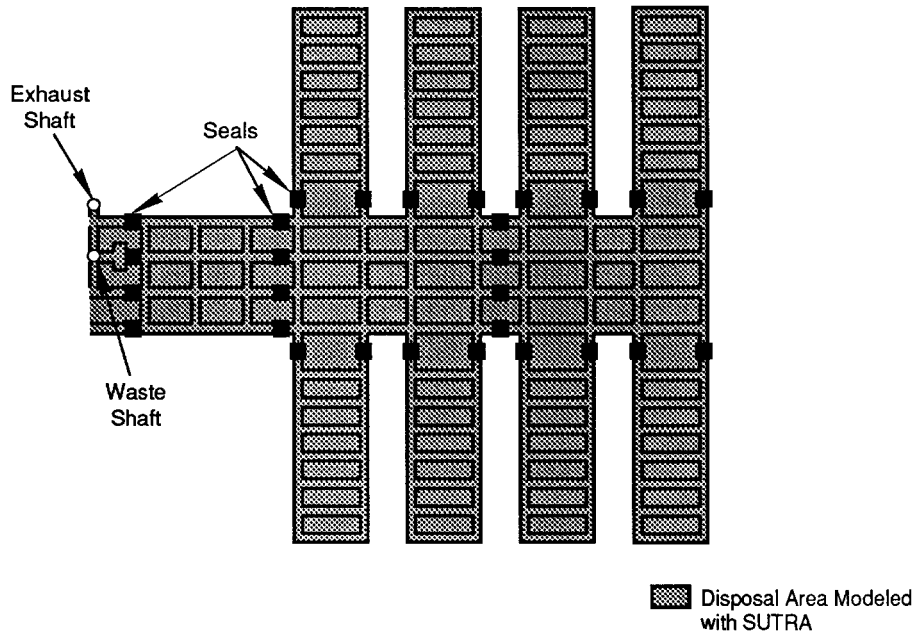
The calculations described in this section treat the flow domain as two dimensional (plane geometry) with appropriate out-of-plane thickness specified to account for the actual volume of each region under consideration. The plan view of the region under consideration is shown in Figure 3-28a. Although the disposal region contains many rooms, it was not practical to model each room individually. Therefore, the approach adopted for this model was to group the excavated volume of the disposal region into a single region, 630 m (2,060 ft) long. This length was the approximate distance from the access drift seals to the southern edge of the disposal region. The total excavated area of the disposal region was $1.1 \times 10^5 \text{ m}^2$ ($1.1 \times 10^4 \text{ ft}^2$); therefore, an out-of-plane thickness of 175 m (570 ft) was specified for the disposal region. Likewise, there were four drifts leading into the disposal area. These were grouped in a single region with an equivalent out-of-plane thickness of 19 m (60 ft). Only one set of drift seals was modeled. The seals were modeled as 30-m (100-ft) long sections* with the same out-of-plane thickness as the access drifts (19 m [60 ft]). The modeled height of all regions was 4 m (13 ft), which was the preconsolidated thickness. Figure 3-28b gives some of the computational dimensions of the mesh. Three hundred elements and 453 nodes were used in these calculations to resolve flow gradients. While the physical dimensions are approximate, they are sufficient to provide gross characterization of the overall flow and pressurization process.

The boundary conditions assumed in the analysis were based on the assumption that the Salado Formation was impermeable, i.e., the boundary of the domain was treated as a no-flux boundary. To provide a gradient for gas flow, the pressure in the center of the disposal area (node 152) was assumed to increase from 0.101 MPa (1 atm) at time equal to 0.0 to 14.8 MPa in 100 yr, and then hold constant for the remainder of the simulation, as shown in Figure 3-29.

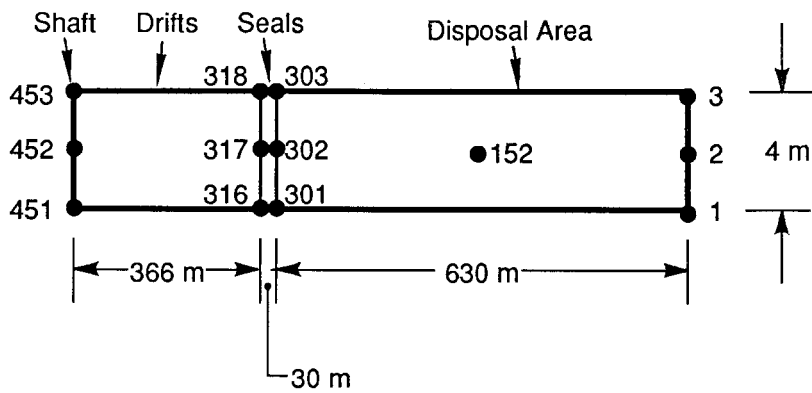
VARIED PARAMETERS

The parameters that were varied in the calculations were permeabilities of the seal, drift backfill, and disposal area waste. Five calculations are discussed in this section; the simulations progress from extreme worst-case conditions to more realistic conditions. Calculation 1 corresponds to gas flow in the unconsolidated materials. (The term unconsolidated is used to describe material that is at its initial placement density.) Calculation 2 corresponds to gas flow in unconsolidated drift and consolidated seal and disposal area material; Calculation 3 corresponds to fully consolidated materials. The final two calculations represent the time-dependent decrease in permeability during consolidation of the seal, drift, and disposal area. Calculation 4 studies the effect of including the seal, and Calculation 5 eliminates the seal. Together, these five calculations provide qualitative comparisons of the influence of material permeabilities on the gas pressures in the shaft region of the drift.

* This length was chosen before the reference design was completed. The current reference design uses a 20-m (66-ft) crushed salt section with 10-m (33-ft) concrete components at each end (Figure 1-9).



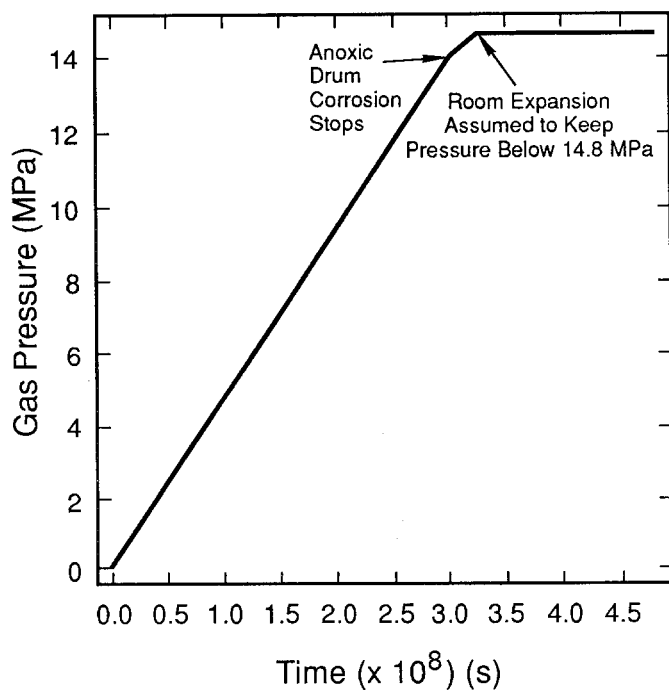
a. Plan View



TRI-6334-182-0

b. Finite Element Model

Figure 3-28. Plan View of Disposal Area and Finite Element Mesh Used for Gas Flow to Shafts (300 Elements; 453 Nodes).



TRI-6334-202-0

Figure 3-29. Time-Dependent Pressure Boundary Conditions at Center of Disposal Area (Node 152) for Gas Flow Simulation.

The material properties for the first three calculations are shown in Table 3-5. Calculation 1 uses the unconsolidated material constants (Run 1, Table 3-5).

TABLE 3-5. PERTINENT MATERIAL PROPERTIES FOR GAS FLOW THROUGH DRIFT TO SHAFT

Region	Thickness (m)	Porosity	Permeability (m ²)		
			Run 1	Run 2	Run 3
Drift	19	0.05	1 x 10 ⁻¹⁰	1 x 10 ⁻¹⁰	1 x 10 ⁻²⁰
Seal	19	0.03	1 x 10 ⁻¹⁴	1 x 10 ⁻²⁰	1 x 10 ⁻²⁰
Disposal Area	175	0.18	1 x 10 ⁻⁸	1 x 10 ⁻¹⁵	1 x 10 ⁻¹⁵

In Calculation 2, the seal and disposal area permeabilities were decreased to correspond to the consolidated values (Run 2, Table 3-5). This calculation roughly corresponds to the use of initially compacted waste and a multicomponent seal since the seal contains a concrete component, which has a low permeability initially. In Calculation 3, the drift, seal, and disposal area permeabilities correspond to consolidated values (Run 3, Table 3-5).

In Calculations 1 through 3, the time-dependent decrease in permeability as the result of consolidation was not simulated. These effects were examined in Calculations 4 and 5.

Figure 3-30 illustrates the permeability-time functions used in Calculations 4 and 5. These functions describe permeability decreases that result from the time-dependent consolidation of the crushed-salt backfill and waste materials, assuming creep closure results in consolidation in about 100 yr (Sjaardema and Krieg, 1987). Creep closure of the drift is assumed to consolidate the crushed salt until it reaches 95 percent of the intact WIPP salt density. As noted for Calculation 2, the concrete component of the seal, which was not modeled, has an initial permeability that is lower than shown for the crushed-salt component.

The permeability-time function used for the drift seal was based on a combination of laboratory consolidation data and numerical analysis of creep closure effects on seal density (Arguello and Torres, 1987; Holcomb and Hannum, 1982; Nowak and Tyler, 1989). The laboratory data provided permeability as a function of relative density (compared to intact Salado Formation salt density); the numerical model provided an estimate of the relative density as a function of time. From these two relations, it was possible to estimate the drift seal permeability during consolidation using the following additional assumptions.

The drift and seal backfill materials are assumed to be identical, except that the initial relative density of the seal is 0.80 compared to 0.60 for the drift backfill. Because the initial density of the drift backfill was lower, it was assumed that the permeability decreased linearly from 10^{-10} to 10^{-14} m² (10^5 to 10 mD) in the first 50 yr. Since the drift permeability at 50 yr is the same as the seal permeability at the start of the calculation, it was assumed that the permeability followed the same relation as the first 50 yr for the seal.

The permeability of the waste material was assumed to decrease linearly from 10^{-8} m² (10^7 mD) to 10^{-15} m² (1 mD) in the first 100 yr, and then remain constant.

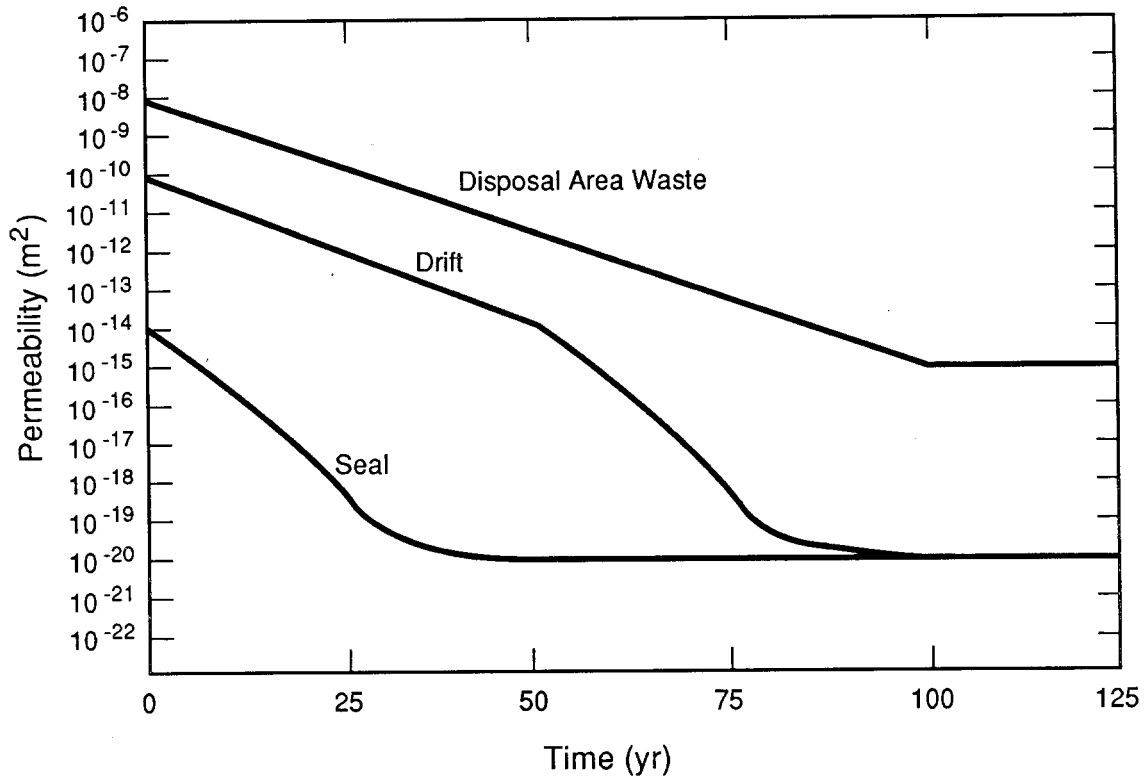
To study the effects of eliminating the seal, Calculation 5 simply replaced the seal material with drift backfill material.

In all calculations, the gas density was evaluated using the Redlich-Kwong equation of state for a gas mixture (Prausnitz, 1969). However, the only gas species treated in the analysis was hydrogen because of its predominance and low viscosity. The viscosity of the hydrogen gas was assumed to be 9.7×10^{-6} Pa-s at 30°C.

RESULTS

Figures 3-31 through 3-33 are the gas pressure profiles computed along the center of the finite element grid. Multiple curves on single plots indicate different times during the simulation. Distance on the horizontal axis is measured from the shaft area towards the seal and disposal area.

Figure 3-31 illustrates the pressures generated within the disposal area, seal and drift materials for Calculation 1 (unconsolidated material). Because of the high permeability, the gas pressures in the entire region become uniform in a short time (< 5 yr).



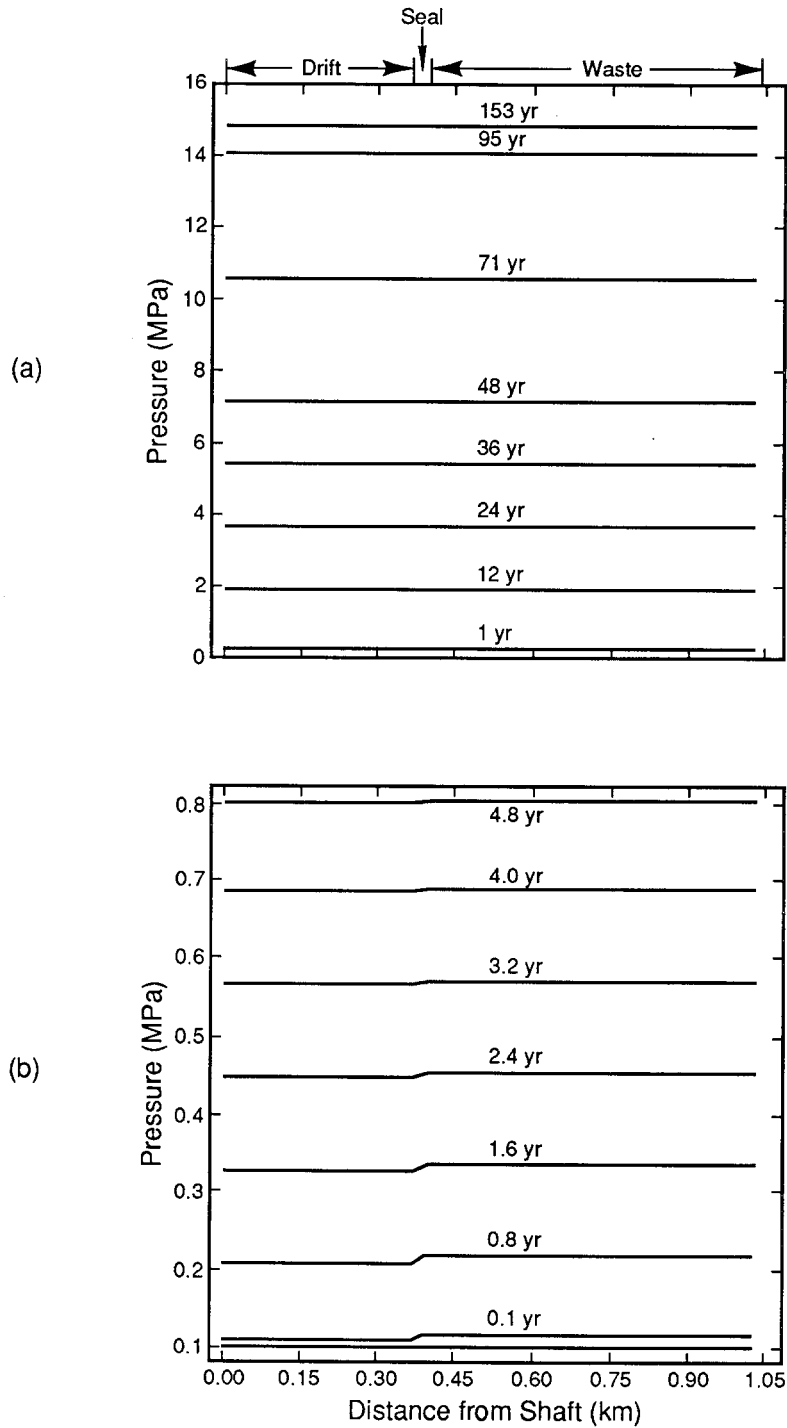
TRI-6334-183-0

Figure 3-30. Time Variation of Permeability Due to Consolidation for Disposal Area, Drift, and Seal (Calculation 4). Seal permeability does not include the concrete component.

Figure 3-32, from Calculation 2, shows the influence of decreasing the seal and waste area permeability to consolidated values, while leaving the drift backfill permeability at the initial, unconsolidated value. As shown in Figure 3-32b, the waste area pressurizes but the pressure in the drift area is less because of the low permeability of the seal and waste area. After 1,565 yr (Figure 3-32a), the drift gradually pressurizes to a level of 8.4 MPa. Because of the relatively high permeability of the drift backfill material, the drift pressurizes uniformly.

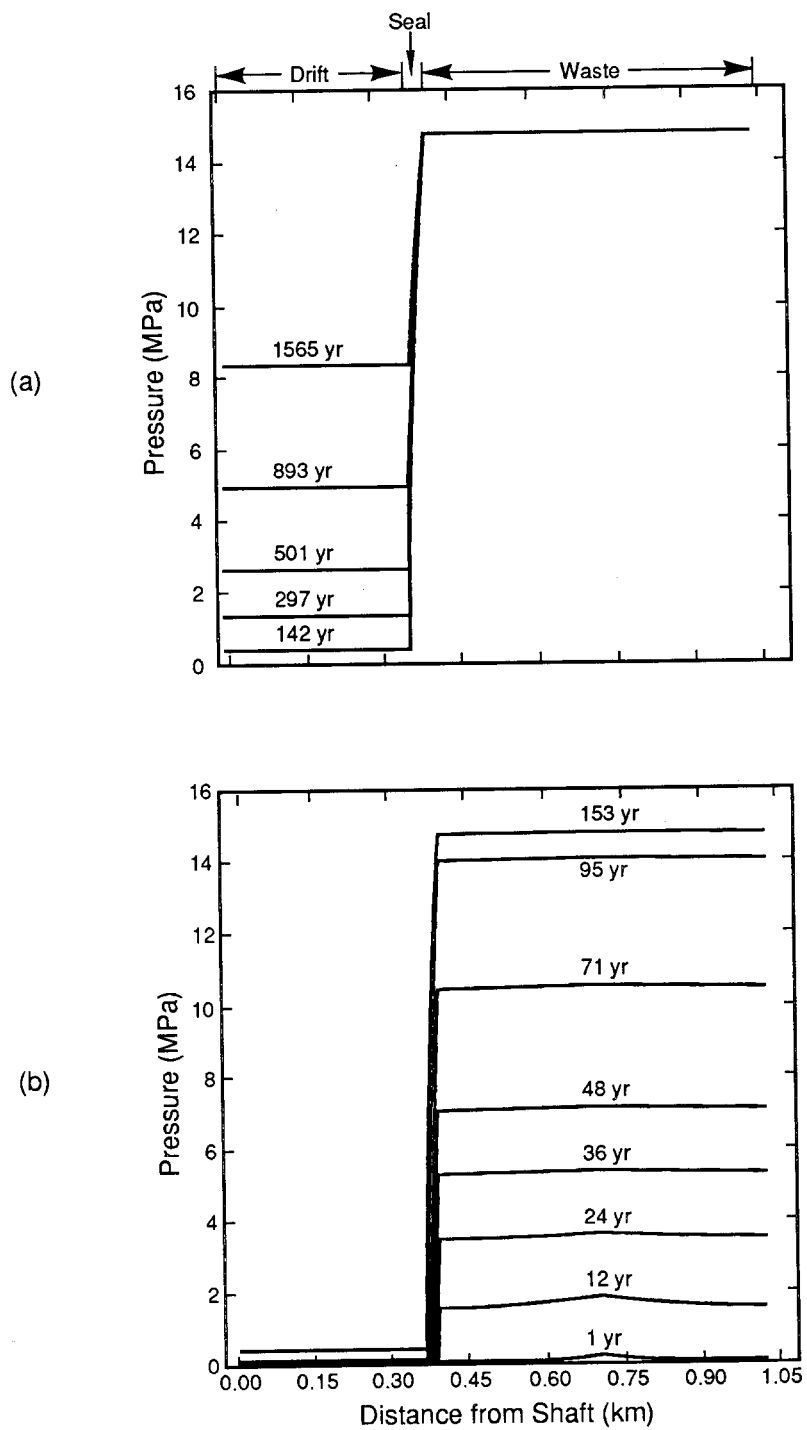
Calculation 3 shows the effect of assuming permeability for fully consolidated material (Figure 3-33). Although the first 24 yr is nearly identical to the values for Calculation 2 (Figure 3-33b), later times indicate the effect of the lower drift permeability. Figure 3-33a shows that the pressure within a region 200 m (654 ft) from the shaft has not changed from its initial pressure, even after 1,565 yr.

Calculation 4 shows effects of time-dependent changes in permeability (Figure 3-34). Initially, the high permeability causes a somewhat uniform pressurization of the entire area. After 24 yr, the seal permeability is approximately six orders of magnitude smaller than the drift permeability. The difference causes the disposal area to pressurize at a faster rate than the drift. At 1,565 yr, a region about 120 m (392 ft) from the shaft area is still at a pressure of 2.5 MPa, the same pressure reached during the first 24 yr.



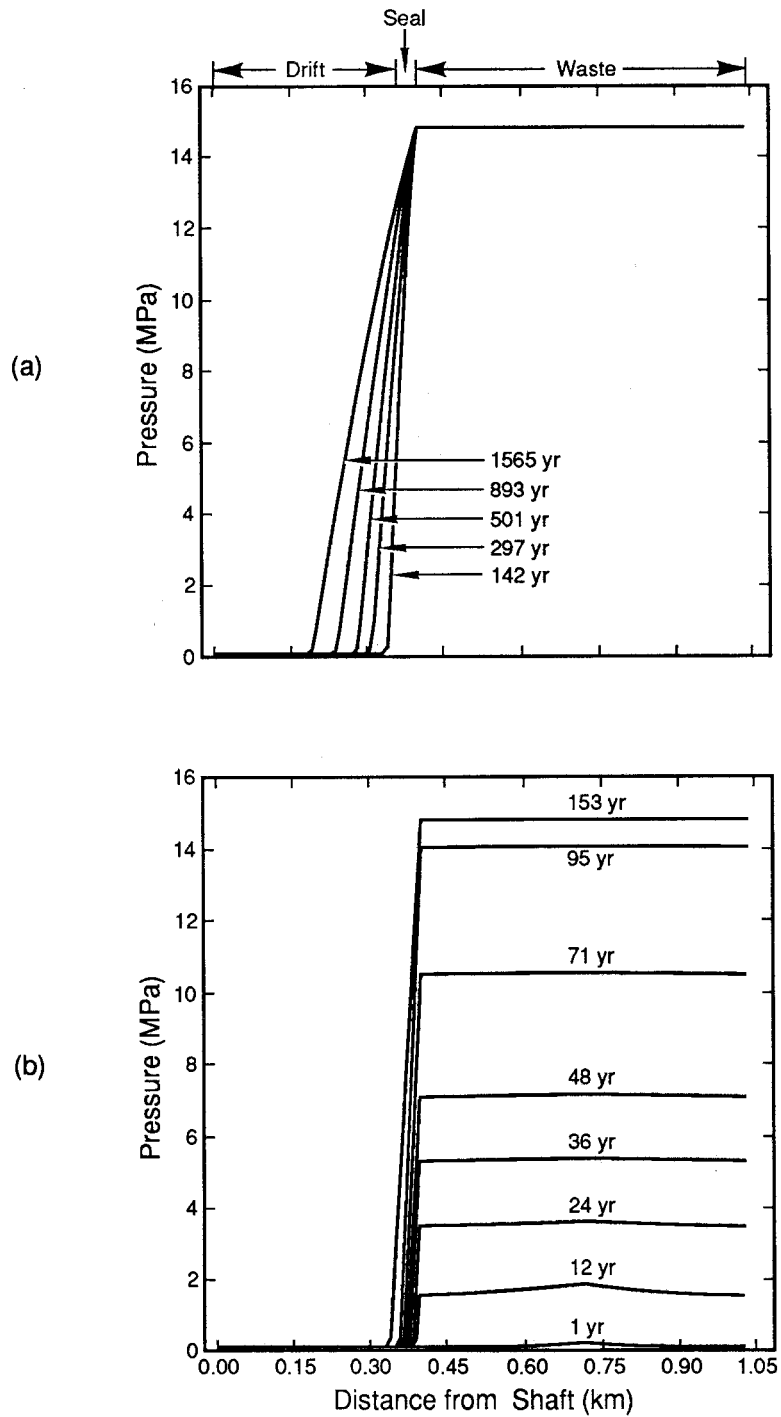
TRI-6334-192-0

Figure 3-31. Gas Pressure Profile Using Unconsolidated Permeability for Drift, Seal, and Waste, Calculation 1, (a) 0 to 153 Yr and (b) 0 to 4.8 Yr.



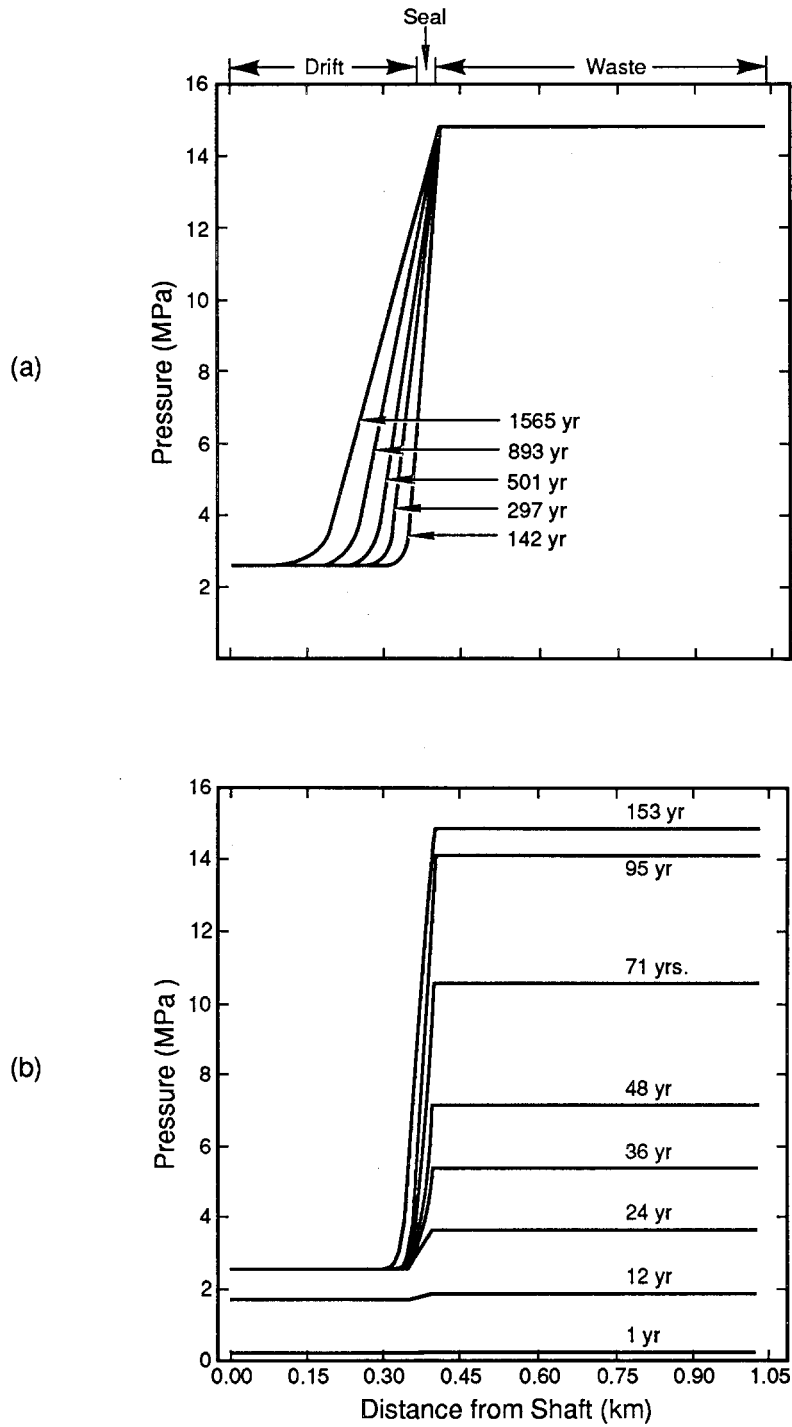
TRI-6334-193-0

Figure 3-32. Gas Pressure Profile Using Unconsolidated Drift Permeability and Consolidated Seal and Waste Permeability, Calculation 2, (a) 142 to 1,565 Yr and (b) 1 to 153 Yr.



TRI-6334-195-0

Figure 3-33. Gas Pressure Profile Using Consolidated Permeability for Drift, Seal, and Waste, Calculation 3, (a) 142 to 1,565 Yr and (b) 1 to 153 Yr.



TRI-6334-197-0

Figure 3-34. Gas Pressure Profile Using Time-Dependent Permeability for Drift, Seal, and Waste, Calculation 4, (a) 142 to 1,565 Yr and (b) 1 to 153 Yr.

The effect of excluding the seal is illustrated in Calculation 5 (Figure 3-35). Before 48 yr, the entire region uniformly pressurizes to about 7.2 MPa (Figure 3-35b). The pressure increase in the drift is retarded, however, when the permeability of the drift begins to decrease at a higher rate (Figure 3-30). Comparing Calculation 5 to Calculation 4 shows that the pressure at the shaft area is approximately four times higher without the seal (i.e., 10 MPa for Calculation 5 and 2.5 MPa for Calculation 4).

In conclusion, these calculations demonstrate the influence of the seal and assumptions of time-dependent changes in permeability on pressurization of the shaft region. This rudimentary simulation indicates that the drift seals will likely be effective in retarding gas flow to the shafts, even when the salt is unsaturated. Evaluating the implications and desirability of these results will require more detailed modeling.

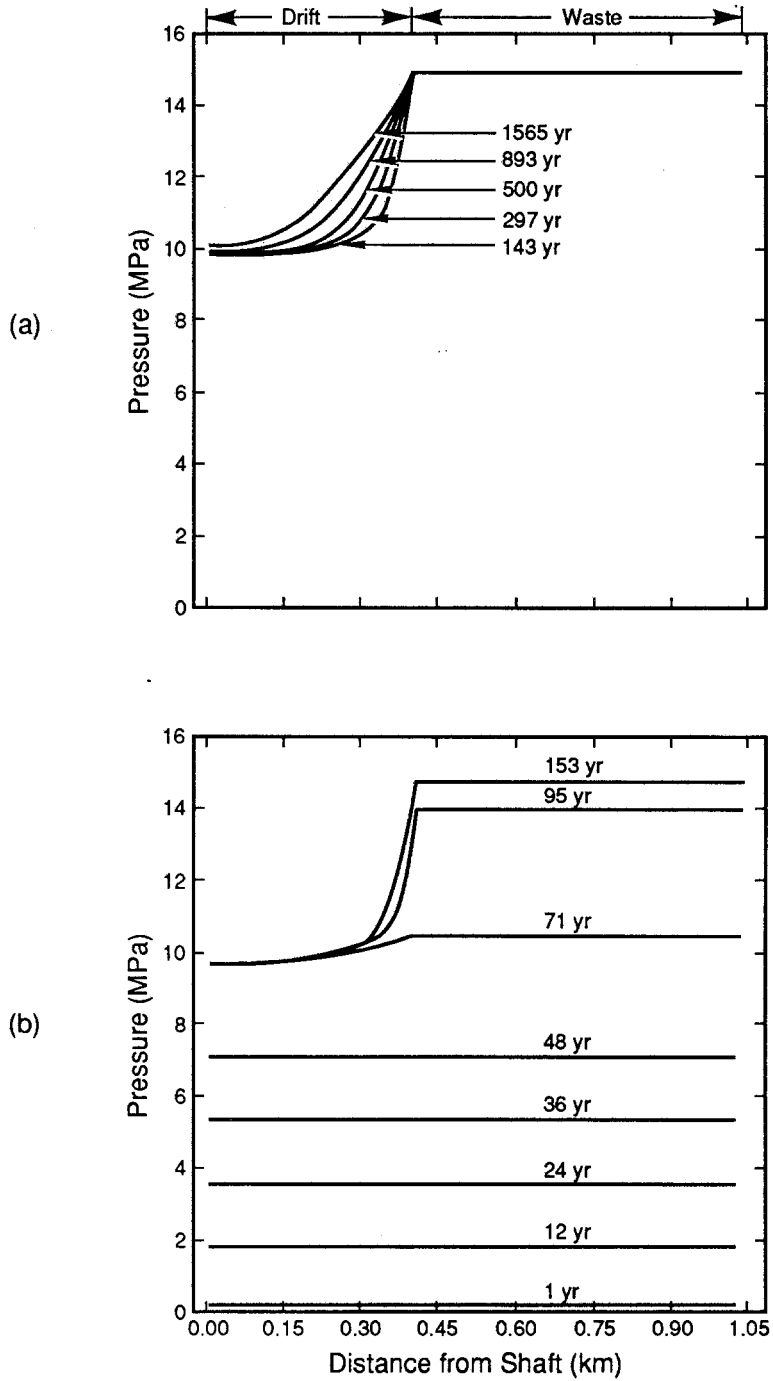


Figure 3-35. Gas Pressure Profile Without Seal and With Time-Dependent Drift and Waste Permeability, Calculation 5, (a) 142 to 1,565 Yr and (b) 1 to 153 Yr.

3.4 ONE-DIMENSIONAL MODEL OF GAS FLOW FROM DISPOSAL AREA TO SHAFT USING BOAST

PURPOSE

The objectives of this model were twofold: First, the model was intended to verify (by a model-model comparison) the modifications made to SUTRA in the previous section (Section 3.3); second, the model studied the effects of brine saturation on gas movement from the waste disposal rooms to the shafts for the undisturbed scenario. As discussed in Chapter 2, BOAST is a three-dimensional, three-phase petroleum reservoir model that is designed to simulate compressible multiphase flow through porous media.

The first set of calculations checked the accuracy of results using a modified version of SUTRA to confirm that the models were being used and interpreted properly. Specifically, in Section 3.3, a modified version of SUTRA was used to model hydrogen generation and flow from the waste repository assuming that the rooms, seals, and drifts were fully saturated with gas. Calculation 3 of the SUTRA model, in which the permeability of the seals and drifts was examined under consolidated conditions, was repeated here using BOAST.

It was assumed that hydrogen (and no other gas) was generated by anoxic corrosion of drums and metallic wastes, and that this gas could flow through the rooms, seals, and drifts to the nearest shaft, which provides direct communication to the surface. The surrounding Salado Formation was assumed to be impermeable to gas and brine (although this assumption is self-conflicting, since the Salado Formation is the source of the brine). To match the SUTRA model, the geometry of the repository is simplified to a one-dimensional conceptual model, although BOAST actually numerically models the problem in three dimensions.

The second set of calculations was intended to probe the behavior of the repository when the seals, drifts, and marker bed were initially saturated with brine. Hypothetically, gas generation in the waste under these conditions could produce a number of complex interactions. For example, gas pressurization of the rooms may prevent further influx of brine, thereby precluding continued gas generation. The presence of brine in the pore space retards flow of gas (and vice versa), possibly to an extent that obviates the need for seals in the access drifts. The calculations reported here are an initial examination of these complex interactions between brine and gas in the WIPP repository.

SUMMARY

Calculations using BOAST to verify the modifications made to SUTRA in the previous section (Section 3.3) showed excellent agreement between the two models. During a simulation of 200 yr, the difference in gas pressure in the waste between the models was never more than 8 percent; at 200 yr, it differed by 5 percent.

Under conditions of complete brine saturation, gas generation in the waste resulted in pressures in the waste exceeding lithostatic very rapidly (i.e., in less than 2 yr). This result was expected because of the overly simplified model. In the model, the gas could move only through the seals and drifts; with no free volume into which it could expand, the gas had to increase the pressure very rapidly. These results prompted an examination of slightly more realistic

conditions, still using the one-dimensional grid. The drifts and seals were reinterpreted as MB139 and its seals, which allowed substantially greater flow than could be realized in the drifts leading to the shaft. Marker Bed 139 and the seals were again assumed to be initially saturated with brine, but the waste was modeled as initially saturated with gas.

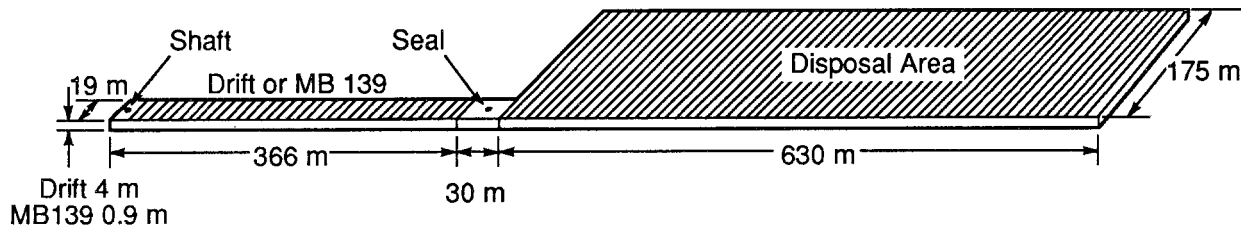
For the MB139 model, hydrogen generated continuously over 600 yr forced its way through to the shaft (where hydrostatic pressure was maintained) in about 3 to 300 yr, depending on the permeability of MB139 and the seals (between 10^{-9} and 10^{-15} m² [10^6 and 1 mD]). At the higher permeability (10^{-9} m² [10^6 mD], i.e., an essentially open channel), there was so little resistance to flow that pressures throughout the grid were very nearly uniform. When the marker bed and seals were assigned a moderate permeability (10^{-15} m² [1 mD]), pressures in the waste exceeded lithostatic pressure in less than 500 yr, but at later times, as gas saturation throughout MB139 increased, the pressure rapidly dropped.

DESCRIPTION OF GRID AND BOUNDARY CONDITIONS

The approach in modeling the rooms, seals, and drifts is essentially the same as that used in Section 3.3. The excavated volume of the disposal region was grouped into a single region with a length equal to the approximate distance from the drift seals to the southern end of the disposal region (630 m [2,060 ft]). The height used was the preconsolidated initial height of 4 m (13 ft). To give a volume equivalent to the excavated disposal volume, a width of 175 m (574 ft) was used. Similarly, the four access drifts and seals were grouped into a single region 396 m (1,300 ft) long, 19 m (60 ft) wide, and 4 m (13 ft) high. In the second set of calculations, in which MB139 was the flow path, the height was 0.9 m (3 ft), while the other dimensions were unchanged. BOAST uses a three-dimensional block-centered grid. Therefore, each region was divided into blocks that were of uniform length in each region (Figure 3-36). The drift was modeled as 30 contiguous blocks, each 12.2 m (40 ft) long. The seal was divided into 5 blocks, each 5.97 m (20 ft) in length. The disposal "room" consisted of 48 blocks, each 13.1 m (43 ft) long.

The porosity of the waste was 0.18 in all the calculations reported in this section. The value of porosity for the drift was 0.05; for the drift seals, 0.03. In the calculations involving MB139, both the marker bed and its seals were assigned a porosity of 1.0 to represent open fractures; a finite permeability was used to reflect the size of the fractures (see Table 3-1).

The Salado Formation was assumed to be impermeable. Thus, there was no flow of brine or gas beyond the region modeled. Pressure was maintained at a constant value at the north end of the drift where the access shafts are located. In the first case examined, in which the room and drifts were assumed to be fully saturated with gas, the pressure at the north end was fixed at 0.101 MPa (1 atm). In the second set of calculations, the pressure was fixed at hydrostatic at the level of the repository, or 6.3 MPa. In BOAST, this type of boundary condition is specified by means of a gas or water production well located at the center of the block and held at constant bottom-hole flowing pressure. A "productivity index" must also be specified, which is a largely empirical function of the permeability of the porous medium comprising the block, the dimensions of the block, and the diameter of the well. An arbitrarily large value of 4.6×10^{-5} m³/s (25 stock tank barrels per day) was used to preclude any resistance to flow from the well to the formation, in effect fixing the pressure of the entire block to equal that of the wellbore.



TRI-6334-205-0

Figure 3-36. Model of Disposal Area, Seal, and Drift (or Marker Bed 139) Leading to Shaft (83 Blocks).

Gas generation in the waste region was simulated by rate-controlled gas-injection wells. One well was located in each waste region block so that gas generation would be distributed uniformly over the entire region. Each well had an injection rate of $7.49 \text{ m}^3/\text{s}$ (0.048 MCF/D) at atmospheric pressure and 30°C , which corresponds to the expected hydrogen production rate of $9.5 \times 10^5 \text{ mol/yr}$ as a result of anoxic corrosion of drums and metallic waste. This rate was continued for 600 yr, the maximum duration of the calculations presented here. This time period is just slightly longer than the period in which hydrogen production from iron corrosion is expected to be completed (527 yr).

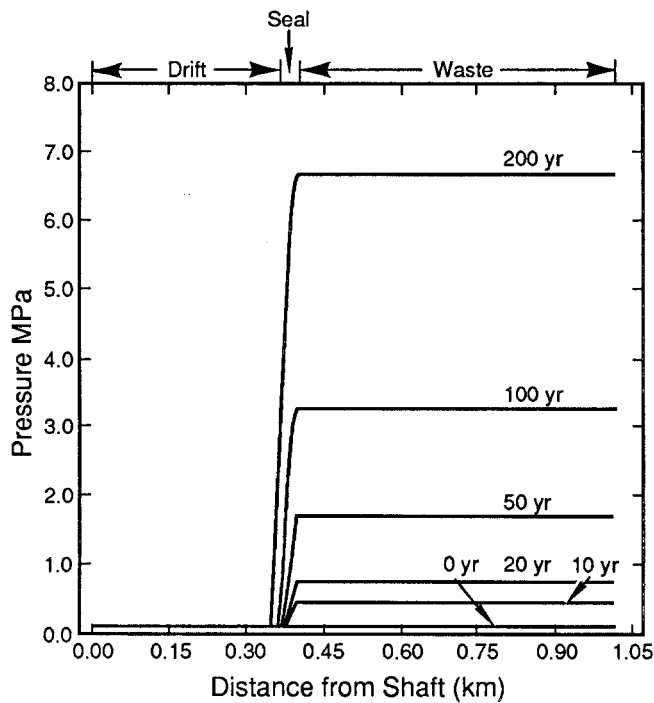
VARIED PARAMETERS

No parameters were varied in the model-to-model comparison of the first two-phase calculations. The permeabilities of MB139 and its seals were varied in the second calculations. The MB139 and its seals were given the same permeabilities, ranging from 10^{-15} to 10^{-9} m^2 (10 to 10^6 mD). The range examined is fairly large, because the permeability of MB139 has not been accurately determined. If MB139 is widely fractured and the apertures are propped open, it could have extremely high permeability. Less severe fracturing would result in a moderate permeability, perhaps less than that of the consolidated waste.

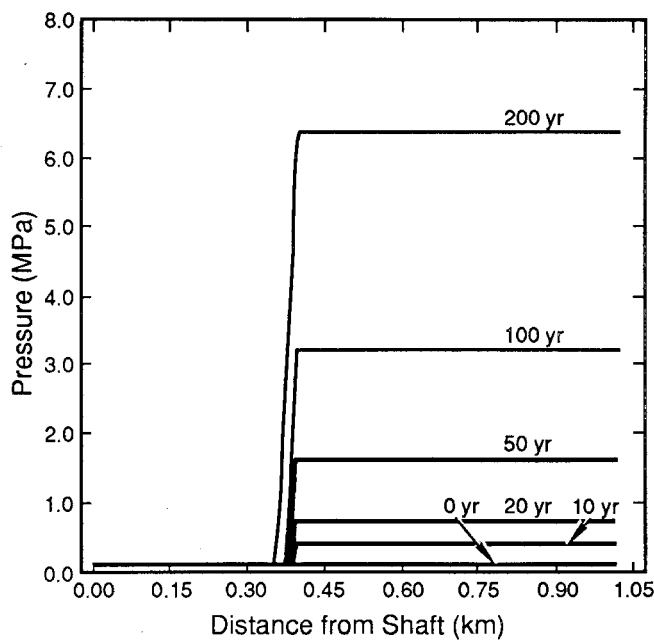
In the second calculations, the degree of brine saturation of the waste was also varied. Only the extreme values, 1.0 and 0.0, were considered.

RESULTS

In the model-to-model comparison calculation, the waste, seals, and drifts were assumed to be saturated with hydrogen, and atmospheric pressure was maintained at the north (shaft) end of the drift. The permeability of the waste was assigned a value of 10^{-15} m^2 (1 mD), while that of the drifts and seals was assumed to be 10^{-19} m^2 (10^{-4} mD). Pressure profiles at various times during the 200-yr BOAST simulation are shown in Figure 3-37a and can be compared with results obtained using the modified version of SUTRA (Figure 3-37b). The calculated pressure in the room for each model is shown in Table 3-6. The agreement between the two models is excellent. The small differences can be attributed to differences in model formulation (SUTRA is a finite-element model, whereas BOAST is a finite-difference model) and to differences in solution convergence criteria. In addition, the models calculate the compressibility of hydrogen differently. SUTRA calculates a new value from the Redlich-Kwong equation of state (Prausnitz, 1969) at each node for each iteration and time step, which is an accurate but relatively time-consuming procedure. BOAST uses the same equation of



a. BOAST



b. SUTRA

TRI-6334-208-0

Figure 3-37. Comparison of Gas Pressure Profiles in Drift, Seal, and Waste Using SUTRA and BOAST (no brines present).

TABLE 3-6. GAS PRESSURE IN WASTE ROOM OBTAINED USING SUTRA AND BOAST*

Time (yr)	Gas Pressure (MPa)		Difference (%)
	BOAST	SUTRA	
10	0.438	0.404	7.8
20	0.746	0.710	4.8
50	1.68	1.63	3.1
100	3.28	3.18	3.2
200	6.69	6.36	4.9

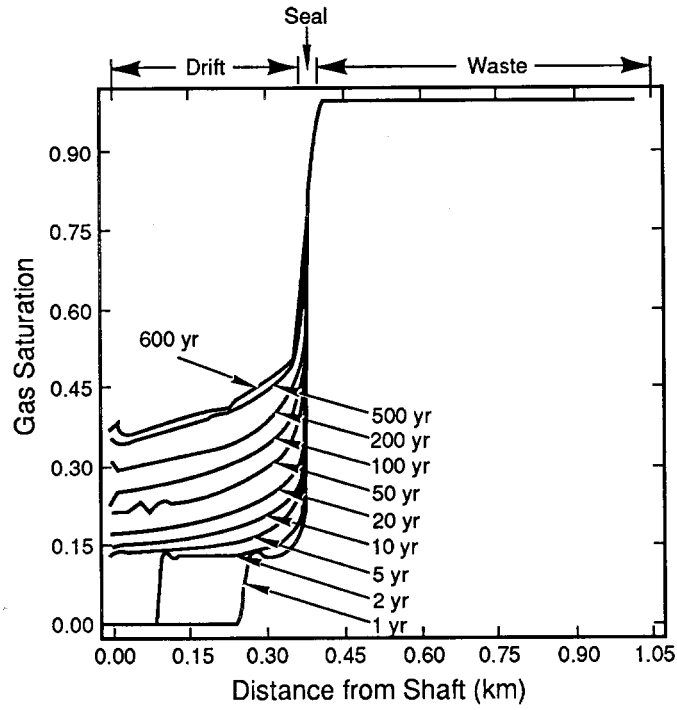
*Time step = 1 yr.

state, but interpolates linearly in a lookup table when a new value is required. This technique is faster computationally, but can be inaccurate if the table values are not closely spaced where the compressibility changes rapidly. The relatively coarse table values used by BOAST in these calculations could account for the differences between the models.

The first two-phase calculation modeled hydrogen production in the waste when the drifts, seals, and waste were all initially saturated with brine. The same porosities and permeabilities were used as in the previous calculation. The results were as expected. They showed that because of the low permeabilities, neither gas nor brine could move anywhere rapidly enough to dissipate the large pressure increase from gas generation. In less than 2 yr after injecting gas into the disposal area, gas pressures exceeded lithostatic pressure. While useful as a limiting case, this model is not realistic because air that has initially been trapped in the disposal rooms and in the backfilled drifts is assumed to dissipate before any gas can be generated by corrosion of containers and waste.

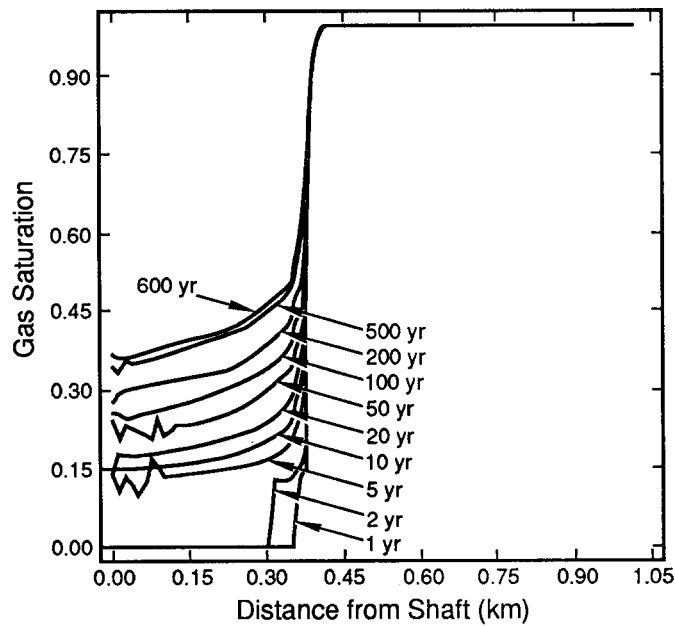
In the second two-phase calculations, four assumptions were changed from the previous model. First, the flow path from the room to the shaft was changed to MB139. Although the length of the path is the same, the change to MB139 provided a rationale for considering higher permeabilities than could reasonably be expected in the drifts, and at the same time allowed an analysis of a more probable flow path to the access shafts. Second, the waste was now assumed to be completely saturated with gas initially. Third, a slightly higher waste permeability of 10^{-13} m² (10² mD) was used. The final difference from the previous calculations is that the porosity of MB139 was set to 1.0 to simulate an open fracture. The height of this flow path was reduced to 0.9 m (3 ft), but the volume of brine in this model of MB139 is clearly much greater than the pore volume of the drift. Since a greater amount of brine must be displaced for gas to flow through, the time frame for significant events would be expected to increase.

Figures 3-38 to 3-41 show gas saturation profiles at various times during the 600-yr simulations, with the permeability of MB139 and seals assigned as 10^{-9} , 10^{-11} , 10^{-13} , and 10^{-15} m² (10⁶, 10⁴, 10², and 1 mD), respectively. The lowest permeability delays the flow of hydrogen into MB139 and into the shaft. However, except for the lowest permeability, the saturation profiles are nearly identical at 600 yr, indicating that a steady state is reached just when hydrogen production from corrosion is expected to cease.



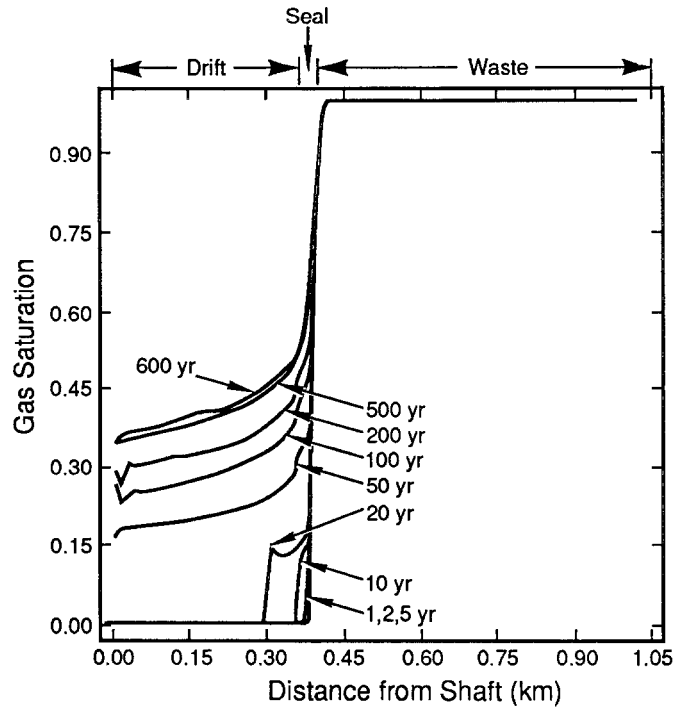
TRI-6334-209-0

Figure 3-38. Gas Saturation Profiles in Marker Bed, Seal, and Waste, with Marker Bed Permeability Equal to 10^{-9} m^2 . Marker bed and seal initially saturated with brine.



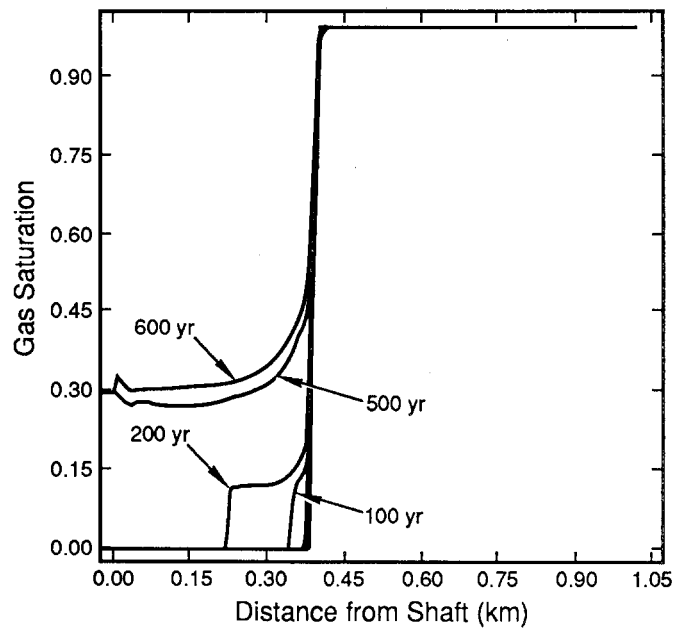
TRI-6334-210-0

Figure 3-39. Gas Saturation Profiles in Marker Bed, Seal, and Waste, with Marker Bed Permeability Equal to 10^{-11} m^2 . Marker bed and seal initially saturated with brine.



TRI-6334-211-0

Figure 3-40. Gas Saturation Profiles in Marker Bed, Seal, and Waste, with Marker Bed Permeability Equal to 10^{-13} m^2 . Marker bed and seal initially saturated with brine.



TRI-6334-212-0

Figure 3-41. Gas Saturation Profiles in Marker Bed, Seal, and Waste, with Marker Bed Permeability Equal to 10^{-15} m^2 . Marker bed and seal initially saturated with brine.

Using a marker bed permeability of 10^{-9} m^2 (10^6 mD), the calculations show that gas reaches the shaft in less than 5 yr (Figure 3-38). (Such a high permeability represents an essentially open channel.) Pressures throughout the waste and marker bed are nearly uniform at hydrostatic pressure, 6.3 MPa.

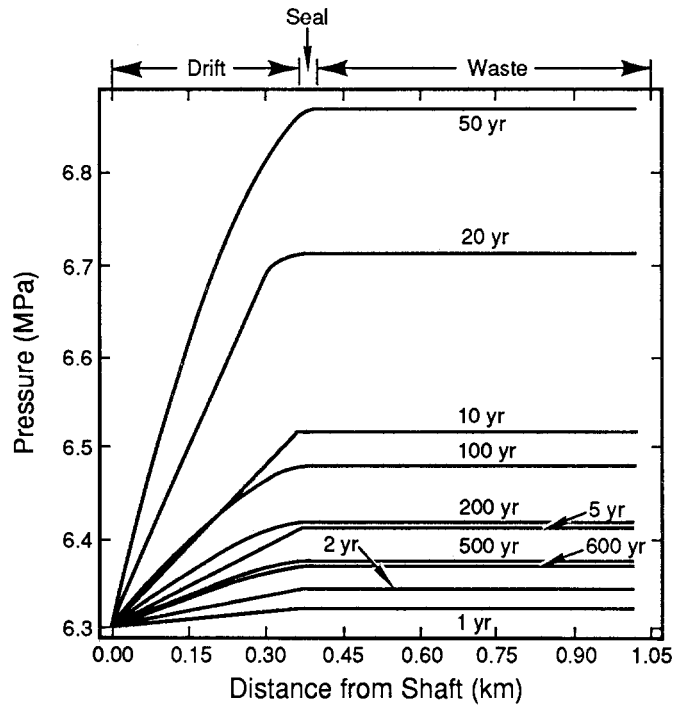
Decreasing the marker bed permeability by two orders of magnitude initially slows the displacement of brine by hydrogen, but breakthrough still occurs in less than 5 yr (Figure 3-39). Pressures in this case are also nearly uniform everywhere.

With the permeability of MB139 reduced to 10^{-13} m^2 (10^2 mD) gas flow is significantly retarded; gas reaches the shaft between 10 and 20 years (Figure 3-40). Gas pressure in the waste shows a maximum increase of about 9 percent over hydrostatic at 50 yr (Figure 3-42), after which gas saturation throughout the marker bed provides an easy conduit for gas flow, and the pressure in the room drops. At 600 yr, the pressure is almost as low as at 2 yr. The permeability of the marker bed in this case is the same as that of the waste.

At the lowest marker bed permeability considered, 10^{-15} m^2 (1 mD), hydrogen does not reach the shaft until after 200 yr (Figure 3-41). A very substantial increase in pressure in the room occurs, reaching a peak in 500 yr slightly in excess of lithostatic pressure before decreasing (Figure 3-43).

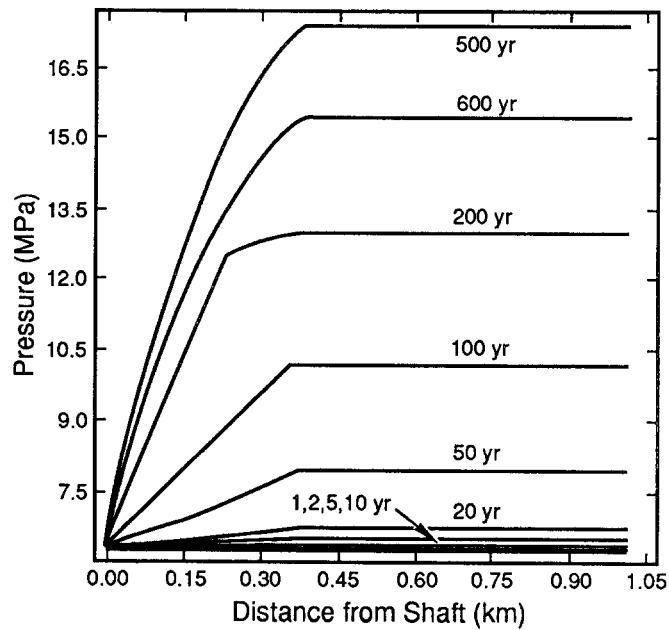
These calculations confirm one's intuition that the presence of brine can significantly retard the flow of gas in a porous medium of low permeability. If the path of least resistance is a fully brine-saturated drift under consolidated conditions, where the absolute permeability is low, gas generated by anoxic corrosion of the waste drums and metallic components cannot travel through the brine, and pressures in excess of lithostatic will result leading to expansion of the room by salt creep. If some free gas initially exists in the waste, gas pressures will build more slowly. If, at the same time, a much higher permeability path exists, such as a well-fractured marker bed, brine and gas can be driven to a sink (located near the shaft in this analysis) without excessive pressure being generated in the waste.

3.4 One-Dimensional Model of Gas Flow from Disposal Area to Shaft Using BOAST



TRI-6334-213-0

Figure 3-42. Gas Pressure Profiles in Marker Bed, Seal, and Waste, with Marker Bed Permeability Equal to 10^{-13} m^2 .



TRI-6334-214-0

Figure 3-43. Gas Pressure Profiles in Marker Bed, Seal, and Waste, with Marker Bed Permeability Equal to 10^{-15} m^2 .

4. HUMAN INTRUSION MODELS

The five models discussed in this chapter examine the relative importance of system components for a human intrusion scenario considering only brine and gas flow. Under the scenario designated as E1, an exploratory borehole is assumed to penetrate both the repository and an underlying pressurized Castile Formation brine pocket as part of future natural resource exploration. The exploratory borehole is assumed to be subsequently plugged in accordance with state regulations effective in 1990.

The assumptions for the models described here are based on the hypothesized sequence described in Section 2.2 and represent pieces of that sequence. Not every aspect of the hypothesized sequence is discussed here; furthermore, the models that are discussed must be considered as under development and not complete.

The first four models in this chapter are cylindrical approximations of a panel with a borehole. The first model examines brine inflow from the Salado Formation; the second, brine flow from a brine pocket through one room; the third, the effect of the anhydrite layers on brine flow from a brine pocket; and the fourth, gas and brine flow from waste. The fifth model also explores brine inflow using a two-dimensional model and a simple three-dimensional model.

Like Chapter 3, each major section begins with the model's purpose and a summary of results. Subsequent sections discuss in detail the modeling technique and present the numerical results.

4.1 CYLINDRICAL MODEL OF SALADO BRINE FLOW THROUGH PANEL TO BOREHOLE

PURPOSE

The purpose of this axisymmetric simulation is to calculate the access fraction (i.e., the ratio of the volume of waste through which brine can pass and still reach the borehole to the total volume of waste). This access fraction can then be used as a performance metric for evaluating engineered modifications of the waste (see, for example, Butcher, 1990).

Earlier analyses (Lappin et al., 1989) assumed that the radionuclide source is solubility-limited until the radionuclide is depleted. The time of depletion depends upon the volume of waste accessed. As a conservative assumption, those analyses assumed that an entire panel could be accessed. This model explores the validity of this conservative assumption. Determining realistic values for the calculations is important because if engineered modifications are required, they must be designed using values that are realistic and not inflated. (See also Section 4.5, which is a more accurate, two-dimensional model that was also designed to refine the access fraction.)

The current hypothesis assumes that any gas will leave through the exploratory borehole followed by further consolidation of the disposal area, slowing brine inflow. The current set of calculations begins after this final escape of gas and the consolidation and saturation of the

waste. Minor transport of radionuclides during saturation was not modeled here. Also, complications that could result from gas in other panels was not considered in these simulations. Gas depressurization and brine saturation would likely leave the pore pressure in the panel near hydrostatic. However, all but one of the simulations assumed the pore pressures in the waste were lithostatic. This condition represents a slightly more conservative case.

SUMMARY

The results from these axisymmetric models show that under steady-state conditions, mass flux to an exploratory borehole varies with permeability when the permeability of the waste is less than three orders of magnitude above the permeability of the Salado Formation. Under transient conditions, mass flux varies when the permeability difference is less than four orders of magnitude. Similar to strictly radial flow, flow to the borehole varies linearly with the changes in pressure gradient, Δp .

Varying the capacitance of the Salado Formation has a significant effect on the amount of brine seeping from the formation. Because of the large variation in fluxes, the amount of waste accessed in these axisymmetric models varies greatly, also. At the upper bound of capacitance ($5.1 \times 10^{-9} \text{ Pa}^{-1}$), essentially the entire panel is accessed. At the lower calculated bound ($7.8 \times 10^{-12} \text{ Pa}^{-1}$), a maximum of only 54 percent of the panel is accessed.

In conclusion, if the pressure gradients specified for this simulation are valid (pressure gradient reversed from the Two-Dimensional Model of Brine Flow to Shaft, Section 3.1), modifications that reduce the waste permeability to within four orders of magnitude (and preferably three orders) of the Salado Formation permeability can reduce the potential brine flux into an intrusion borehole.

AMOUNT OF ACCESSIBLE WASTE

The amount of radionuclides transported from a repository region compared to the region's total inventory is referred to as the access fraction. Access fraction is a convenient metric for evaluating various scenarios or identifying important parameters. Although the amount of radionuclides transported by a given flow field depends on chemical interactions of the waste, fluid, and rock matrix, the assumption that contaminants are transported by advection and are not retarded by interaction with the rock matrix allows access fraction to be estimated in terms of the flow field alone. The influence of hydrologic parameters, and the impact of various scenarios, can then be gauged without recourse to geochemical models. However, the appropriate measure of access fraction, in terms of a Darcy flow field, does depend on the gross nature of source geochemistry. (The above simplifying assumption will be removed in future studies.)

Two idealizations of source behavior lead to two methods of calculating access fraction as a function of the flow field.

Consider a flow field created in some region of the repository, operating for a given time, Δt . If the species is assumed to have infinite solubility, the amount of waste accessed in time Δt

depends on the volume of the waste region that discharges fluid in time Δt . The access fraction (Γ_A) is then limited by

$$\Gamma_A \leq \frac{\text{mass removed}}{\text{initial mass } (m_0)} = \frac{\rho_s \Omega_{\Delta t}}{\rho_s \Omega_R} = \frac{\Omega_{\Delta t}}{\Omega_R} \quad (4-1)$$

where

- ρ_s = Density of the waste
- Ω_R = Region volume
- $\Omega_{\Delta t}$ = Volume of the sub-region having an advective travel time to a discharge boundary less than or equal to Δt .

If, however, the species has limited solubility, then the access fraction is much reduced from that estimated by Eq. 4-1. Considering the repository as a well-mixed chemical reactor with a fixed waste inventory, the mass release rate at a given time is then (substituting the solubility limit, S_i , for the starting concentration)

$$m = \frac{dM}{dt} = C_o q(t) = S_i q(t) \quad (4-2)$$

where

- C_o = starting concentration
- m = mass flux rate
- M = cumulative mass
- $q(t)$ = fluid flow rate through waste as a function of time
- S_i = solubility limit of species i
- t = time after start of release.

Integrating Eq. 4-2, assuming S_i is time independent, yields a conservative expression for the mass removed, from which the access fraction (Γ_B) can be expressed as

$$\Gamma_B = \frac{S_i \int q(t) dt}{M_o} = \frac{S_i Q}{M_o} \quad (4-3)$$

Eq. 4-3 assumes that outflow occurs continuously at the solubility limit, i.e., the source is not depleted. Note that the access fraction varies for each containment. If

$$S_i Q < \rho_s i \Omega_{\Delta t} \quad (4-4)$$

then the access fraction calculated by Eq. 4-3 is less than Eq. 4-2. If interested, the reader can calculate Γ_B using the discharges reported in each section and the solubility limits of Appendix A.

Currently, however, the upper limit of solubility for each isotope (10^{-3} mole/l) is set such that $S_i Q > \rho_s i \Omega_{\Delta t}$, as a very conservative assumption. For example, using the inventories, panel

volume, and solubilities of Appendix A, only if $S < 10^{-4}$ mole/l for plutonium, $S < 10^{-5}$ mole/l for americium and uranium, and $S < 10^{-6}$ mole/l for neptunium isotopes, does Eq. 4-3 determine the access fraction. (The above limits for Eq. 4-3 are only approximate; actual calculations may be lower. For example, in Marietta et al. [1989], some plutonium isotopes depleted even when $S = 10^{-6}$ mole/l.) At higher solubilities, only the access volume, $\Omega_{\Delta t}$, evaluated from flow properties alone, determines the access fraction (neglecting adsorption as initially stated).

Because Eq. 4-1, which involves flow properties alone, is easy to use and provides a convenient upper bound, it is used for the access fraction in this and the following sections.

DESCRIPTION OF GRID AND BOUNDARY CONDITIONS

For this axisymmetric simulation, one WIPP waste panel was modeled as a disk 2.0 m (6.5 ft) high (thickness after consolidation) and 60.6 m (200 ft) in radius centered about the borehole. This radius preserves the exterior surface area of an actual panel of 11,530 m² (124,000 ft²). The boundaries are 200 m (660 ft) above and below the disk and 500 m (1,600 ft) out from the axis of symmetry (Figure 4-1). A variable mesh was used, proceeding from fine to coarse in both the vertical and radial directions (Figure 4-1).

VARIED PARAMETERS

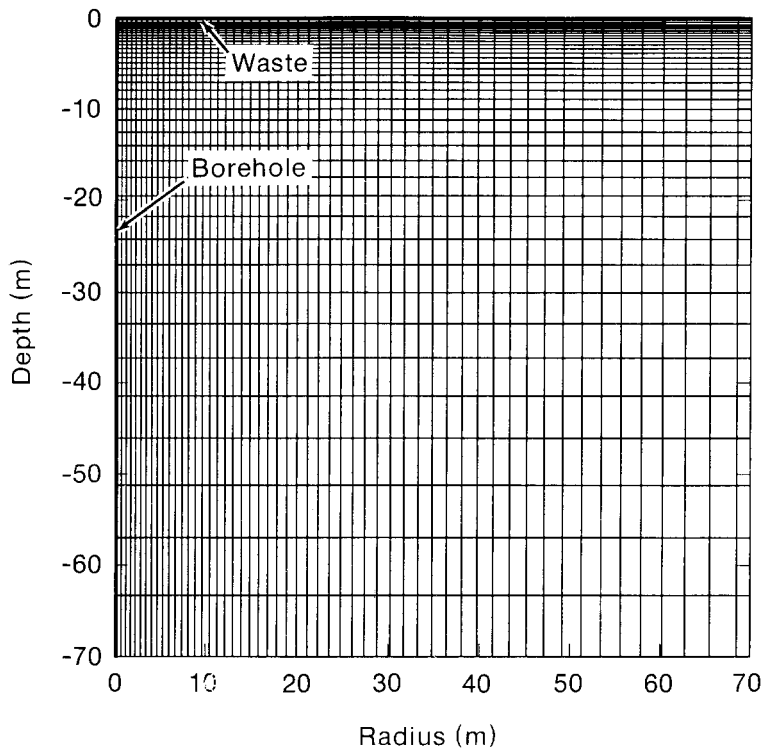
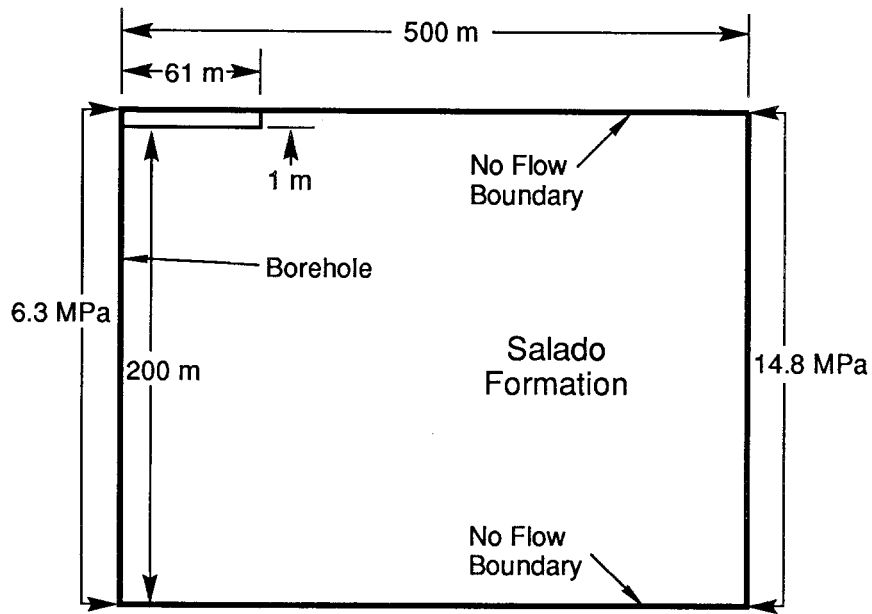
The varied parameters were pressure (p), permeability (k), and capacitance (c). Specifically, the assumed conditions were the following: (1) initial and far-field boundary pressures (p) of 14.8 MPa (lithostatic), and 10.5 and 8.4 MPa (steady-state conditions); and (2) 6.3 MPa (~hydrostatic for water) in the borehole within the panel (Figure 4-1).

Waste permeability was varied between 10^{-21} and 10^{-13} m² (10^{-6} and 10^2 mD). Although porosity varies directly with permeability, it was kept constant at 0.18 for the waste and 0.001 for the Salado Formation (expected conditions). For transient simulations, the Salado Formation capacitance (c) was varied between 7.8×10^{-12} Pa⁻¹ and 5.1×10^{-9} Pa⁻¹.

RESULTS

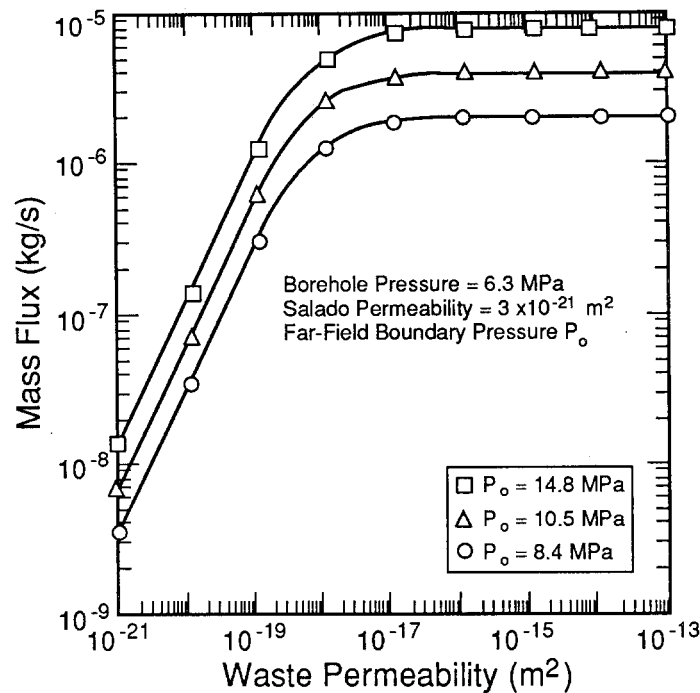
Results from both steady-state and transient simulations are reported. The steady-state results are discussed first. (A few of these steady-state results were summarized in Marietta et al. [1989].) Note that only the relative changes in the results (not absolute values) are meaningful for the steady-state simulations, since mass flux (or any other flow parameter) depends uniquely on the geometry and boundary conditions (e.g., distances to boundaries and specified pressures). However, the relative changes in parameters are still useful for evaluating engineered modifications to the waste; furthermore, steady-state results are very easy to obtain. Refer to Butcher (1990) for examples of how the results reported here were used to rank engineered modifications.

Steady-State Results. Using the cylindrical approximation to the panel, mass flux to the borehole varies with changes in permeability of the waste when the waste permeability is less than three orders of magnitude above the permeability of the Salado Formation (Figure 4-2). At waste permeabilities greater than three orders of magnitude, the flow resistance provided by the waste is negligible in relation to the low permeability of the Salado Formation. Figure 4-2 also shows that similar to a strictly radial flow problem, mass flux to the borehole varies linearly with the changes in pressure gradient (Δp).



TRI-6334-221-0

Figure 4-1. Boundary Conditions Applied in Borehole Model and Axisymmetric Mesh for SUTRA Calculations of an Intrusion Borehole through a Waste Panel.



TRI-6334-203-0

Figure 4-2. Variation of Mass Flux to a Borehole as a Function of Waste Permeability at Several Pressure Gradients Assuming Steady-State Conditions. Because mass flux is dependent upon pressure and distance to boundary, only relative changes (not absolute values) are meaningful.

The volume of waste accessed in 10,000 yr for these steady-state simulations was estimated from the radial distance traveled by a neutrally buoyant particle using TRACKER (Rechard et al., 1989). The maximum volume of unmodified waste ($k = 10^{-13} \text{ m}^2$ [10^{-12} ft^2]) through which brine will flow and still reach the exploratory borehole within 10,000 yr is about 47 percent of one panel (Table 4-1). The more meaningful results, however, are the reductions in this access fraction as the pressure gradient between the far-field boundary and the borehole are reduced. For the radial distances examined, the access fraction decreases roughly linearly with the pressure gradient (Δp) (Table 4-1).

Table 4-1 also tabulates the ratio of cumulative flux out of the borehole in 10,000 yr to the cumulative flux in the base case. This flux can also be compared to the mass of brine in the panel as follows. The volume of pores in the panel is $2.1 \times 10^3 \text{ m}^3$ ($7.4 \times 10^4 \text{ ft}^3$), assuming a porosity of 0.18. Using this pore volume and a brine density of $1.2 \times 10^3 \text{ kg/m}^3$ (75 lb/ft^3), simple arithmetic yields a total mass of brine in the panel of $5.0 \times 10^6 \text{ kg}$ ($1.1 \times 10^7 \text{ lb}$).

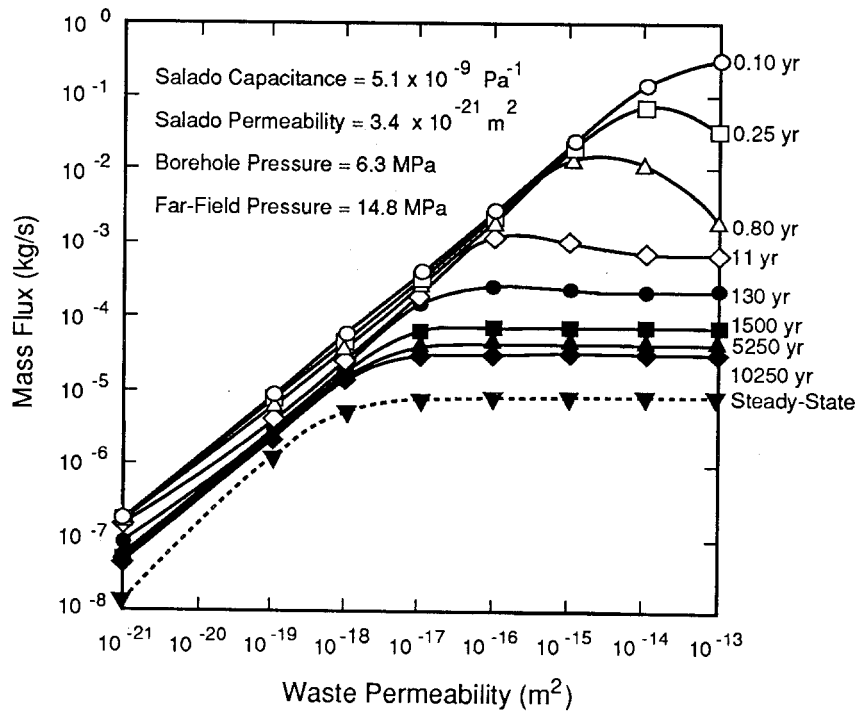
Transient Results. Under transient conditions, permeability changes in the waste panel influence mass flux to an exploratory borehole when the difference in permeability between the waste and Salado Formation is less than about four or five orders of magnitude (Figure 4-3).

TABLE 4-1. MAXIMUM REPOSITORY VOLUME ACCESSED BY BRINE AND CUMULATIVE MASS FLUX IN 10,000 YR UNDER STEADY-STATE CONDITIONS

Pressure Gradient Δp (MPa)	Waste Permeability k/k_{base}	Access Fraction ^{a,b} Γ/Γ_{base}	Cumulative Brine Flux ^a M/M_{base}
4.1	1	0.55	0.49
1.9	1	0.26	0.25
8.5	10^{-3}	0.98	1.00
8.5	10^{-4}	0.94	0.95
8.5	10^{-5}	0.66	0.64
8.5	10^{-6}	0.19	0.15

^a Base case is $k_{base} = 10^{-13} \text{ m}^2$, $\Gamma_{base} = 0.47$, $M_{base} = 2.59 \times 10^6 \text{ kg}$

^b Estimated by TRACKER



TRI-6334-244-0

Figure 4-3. Variation of Transient Mass Flux to a Borehole as a Function of Waste Permeability.

Although not affecting the relative importance of permeability changes discussed above, the Salado Formation capacitance was varied between 7.8×10^{-12} and $5.1 \times 10^{-9} \text{ Pa}^{-1}$ for transient simulations in addition to varying waste permeability. With a smaller capacitance (smaller compressibility), the pressure changes from initial conditions of 14.8 MPa move substantially farther into the Salado Formation (Figure 4-4). This is analogous to sound (a pressure wave) traveling much faster through steel (low compressibility) than air (high compressibility).

Varying capacitance has a profound effect on the amount of brine seeping from the Salado Formation, through the waste, and into an exploratory borehole (Figure 4-5). The cumulative fluxes over 10,000 yr plotted in Figure 4-5 were evaluated using a trapezoidal rule.

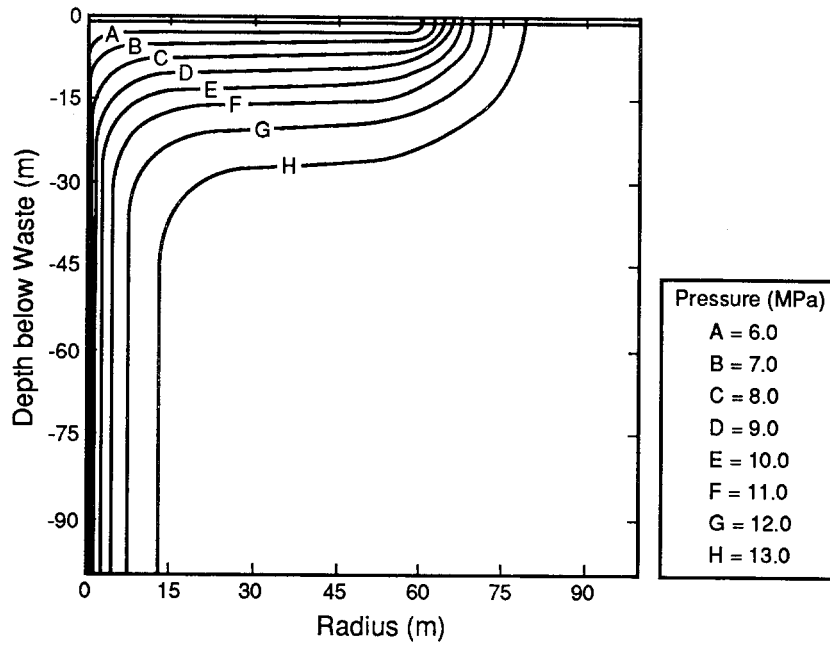
Because of the large variation in fluxes to the borehole when capacitance is varied, the amount of waste accessed in these axisymmetric models varied greatly, also (Figure 4-6).

At the upper bound of capacitance ($5.1 \times 10^{-9} \text{ Pa}^{-1}$) essentially the entire panel was accessed (Table 4-2), while at the lower theoretical bound of capacitance ($7.8 \times 10^{-12} \text{ Pa}^{-1}$) a maximum of only 54 percent of the waste was accessed using a cylindrical approximation of the waste panel (Figure 4-6). (Calculations in Section 4.5 explore the influence of the panel shape upon the access fraction.) As for the steady-state velocity fields, TRACKER was used to evaluate these access fractions in the transient velocity fields. A neutrally buoyant particle in the transient velocity had a typical exponential velocity increase as it approached the borehole (Figure 4-7).

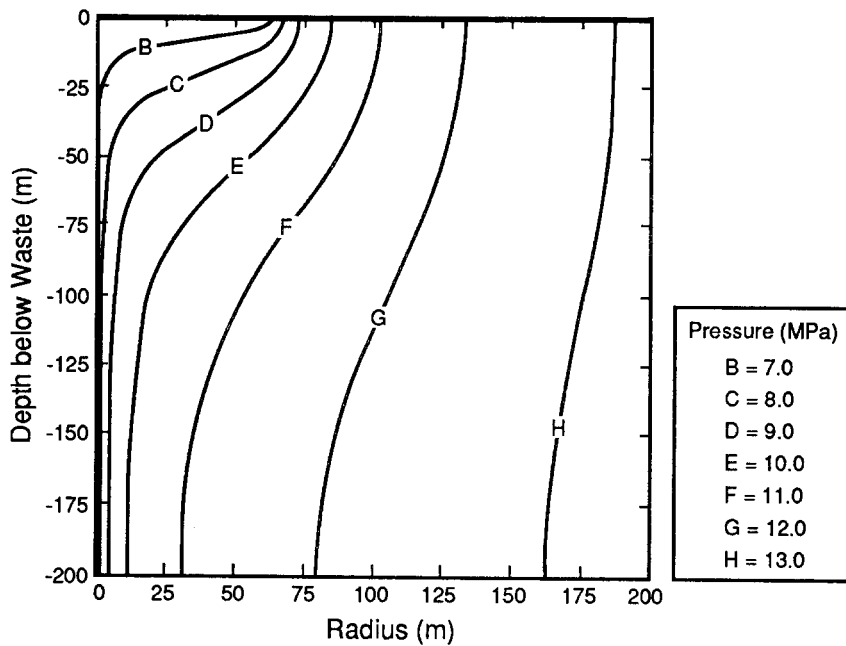
Table 4-2 tabulates several values from Figure 4-6. It also shows the minor influence of the initial pressure within the waste on access times and the cumulative flux (Q). As discussed further in Section 4.3, provided the waste permeability is high, the time for the waste to equilibrate with the borehole is very short and has only a small effect on the cumulative flux.

Figure 4-6 clearly shows that if engineered modifications to the waste are required, they must reduce the permeability to within four orders of magnitude of the Salado Formation before reducing brine passing through the waste. (However, reducing permeability is not the only purpose of an engineered modification. For example, engineered modifications that reduce the solubilities and leach rates of contaminants in the waste can greatly reduce contaminant movement from the disposal area without reducing permeabilities to such low values.)

In summary, if the pressure gradients specified for this simulation are valid (14.8 MPa in the far field and 6.3 MPa at the borehole) (pressure gradient reversed from the Two-Dimensional Model of Brine Flow to Shaft, Section 3.1), modifications that reduce the waste permeability to within four orders of magnitude (and preferably three orders) of the Salado Formation permeability can significantly reduce the potential brine flux into an intrusion borehole.



(a) $c = 5.1 \times 10^{-9} \text{ Pa}^{-1}$



(b) $c = 7.8 \times 10^{-12} \text{ Pa}^{-1}$

TRI-6334-242-0

Figure 4-4. Pressure Contours near Cylindrical Waste Panel at 10,000 Yr for a Capacitance of (a) $5.1 \times 10^{-9} \text{ Pa}^{-1}$ and (b) $7.8 \times 10^{-12} \text{ Pa}^{-1}$.

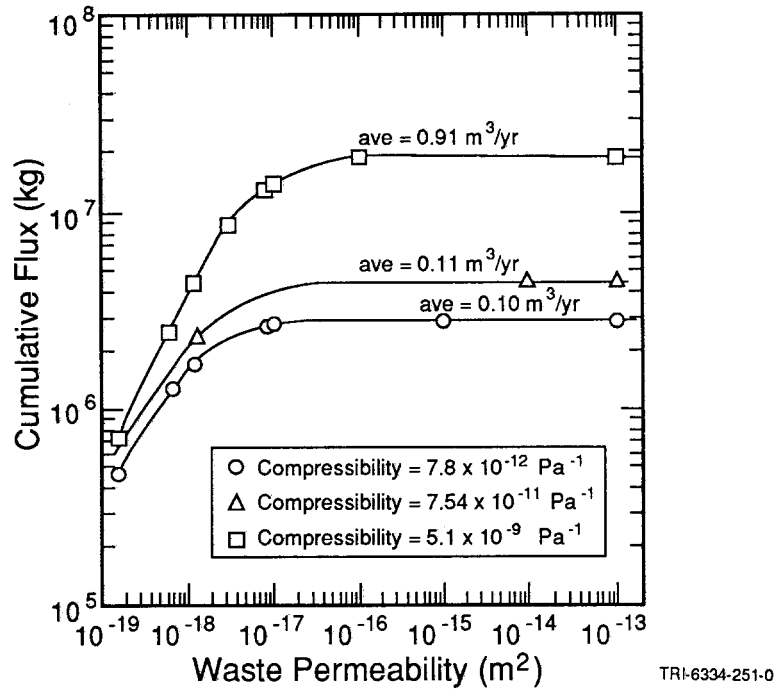


Figure 4-5. Variation of Cumulative Flux with Permeability at a Salado Formation Capacitance of $5.1 \times 10^{-9} Pa^{-1}$, $7.54 \times 10^{-11} Pa^{-1}$, and $7.8 \times 10^{-12} Pa^{-1}$.

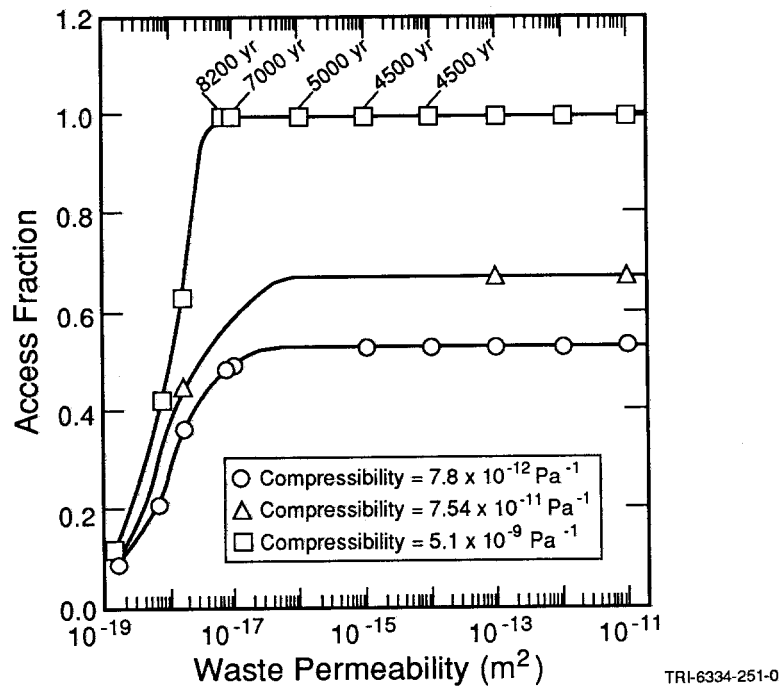
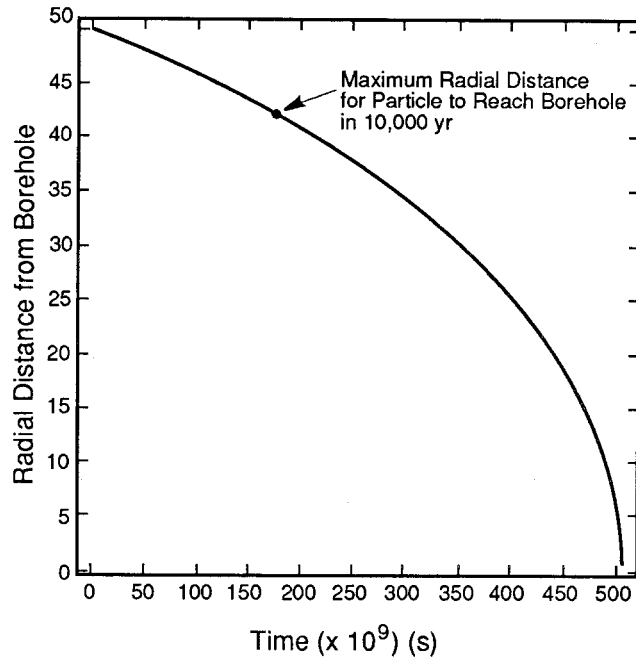


Figure 4-6. Variation of Fraction of Panel Accessed with Permeability at a Salado Formation Capacitance of $5.1 \times 10^{-9} Pa^{-1}$, $7.54 \times 10^{-11} Pa^{-1}$, and $7.8 \times 10^{-12} Pa^{-1}$.



TRI-6334-243-0

Figure 4-7. Radial Distance versus Time for Neutrally Buoyant Particle in Transient Velocity Field for Capacitance of $7.8 \times 10^{-12} \text{ Pa}^{-1}$ as Calculated by TRACKER.

TABLE 4-2. MAXIMUM REPOSITORY VOLUME ACCESSED BY BRINE AND CUMULATIVE MASS FLUX IN 10,000 YR UNDER TRANSIENT CONDITIONS FOR SALADO CAPACITANCE OF $5.1 \times 10^{-9} \text{ Pa}^{-1}$

Initial Waste Pressure P_i (MPa)	Waste Permeability k (m^2)	Volume Fraction of Panel*	Access Times for Entire Panel (yr)	Cumulative Brine Flux M (kg)
14.8	10^{-19}	0.12	--	7.15×10^5
14.8	10^{-17}	1.00	7000	1.57×10^7
14.8	10^{-13}	1.00	4500	1.99×10^7
6.3	10^{-13}	1.00	4800	1.82×10^7

* From TRACKER

4.2 CYLINDRICAL MODEL OF EFFECTS OF ANHYDRITE LAYERS ON SALADO BRINE FLOW THROUGH PANEL

PURPOSE

When flow is modeled for disturbed and undisturbed conditions, the Salado Formation is frequently treated as hydrologically homogeneous. However, the Salado Formation is composed of halite with thin interbeds of polyhalite, clay, anhydrite, and other minerals. Results of recent experiments at the WIPP indicate that far-field anhydrite permeability may be higher than the permeability of intact halite in the Salado Formation (Beauheim, 1990). Therefore, the amount of fluid entering the borehole from the panel may differ from previous estimates where a homogeneous Salado Formation was assumed. The purpose of this model is to estimate the potential influence of hydrologic inhomogeneity on brine inflow through a panel as the result of penetration by an exploratory borehole.

SUMMARY

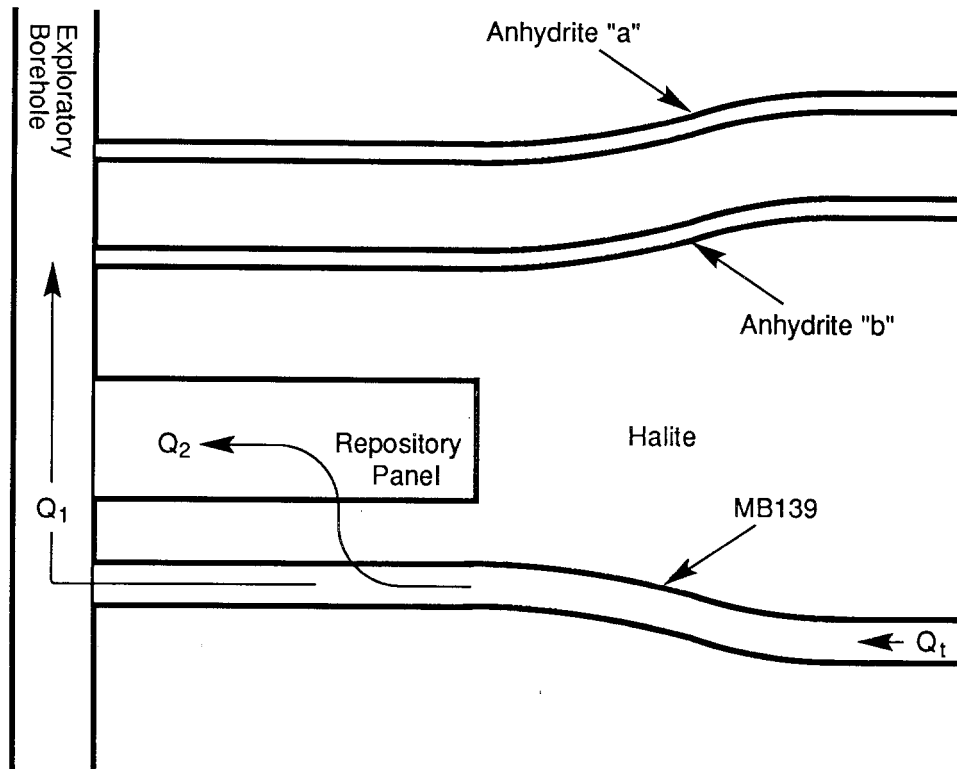
The tendency of anhydrite beds near the panel to act as a drain, diverting brine around the repository, or as a funnel, diverting brine to the repository, depends critically on the relative permeabilities of the anhydrite immediately above or below the repository and the waste. If, in the long term, anhydrite permeability above and below the repository remains high (e.g., $>10^{-14} \text{ m}^2$ [$>10 \text{ mD}$]) as expected, very little brine inflow from the anhydrite into the panel would occur if an exploratory borehole penetrated the repository. Brine inflow through the waste is, in this case, substantially less than brine inflow through the waste assuming homogeneous halite. If, however, strain-induced fractures in the anhydrite layers above or below the panel close or fill to the degree that anhydrite permeability is less than waste permeability, virtually all flow approaching the borehole through the anhydrite would divert through the panel.

Although the relative rates of flow in the panel and anhydrite discussed above depend on the relative permeabilities of the two materials, the amount of brine approaching the borehole from the far field through the anhydrite interbeds depends on the permeability of the anhydrite. As a conservative example, a uniform anhydrite permeability of 10^{-18} m^2 (10^{-3} mD) (below the waste and in the far field) produced an enhanced Salado Formation drainage rate in the far field along with a strong tendency for anhydrite fluid to discharge through the waste. Total brine inflow through the panel, in this case, exceeded the predicted inflow from a uniform halite formation by a factor of about two. However, if the anhydrite layer permeability is greater than the waste permeability because of expected fracturing, the majority of flow remains confined within the anhydrite, reducing the flow through the repository by more than an order of magnitude.

Over the range of permeabilities considered, the amount of brine inflow was virtually insensitive to the permeability of the halite that separates the repository from the anhydrite.

ANALYTICAL MODEL DESCRIPTION AND RESULTS

Figure 4-8 shows a schematic cross section through a repository panel, neighboring strata, and a penetrating exploratory borehole (see also Figure 1-4). The exploratory borehole is assumed to



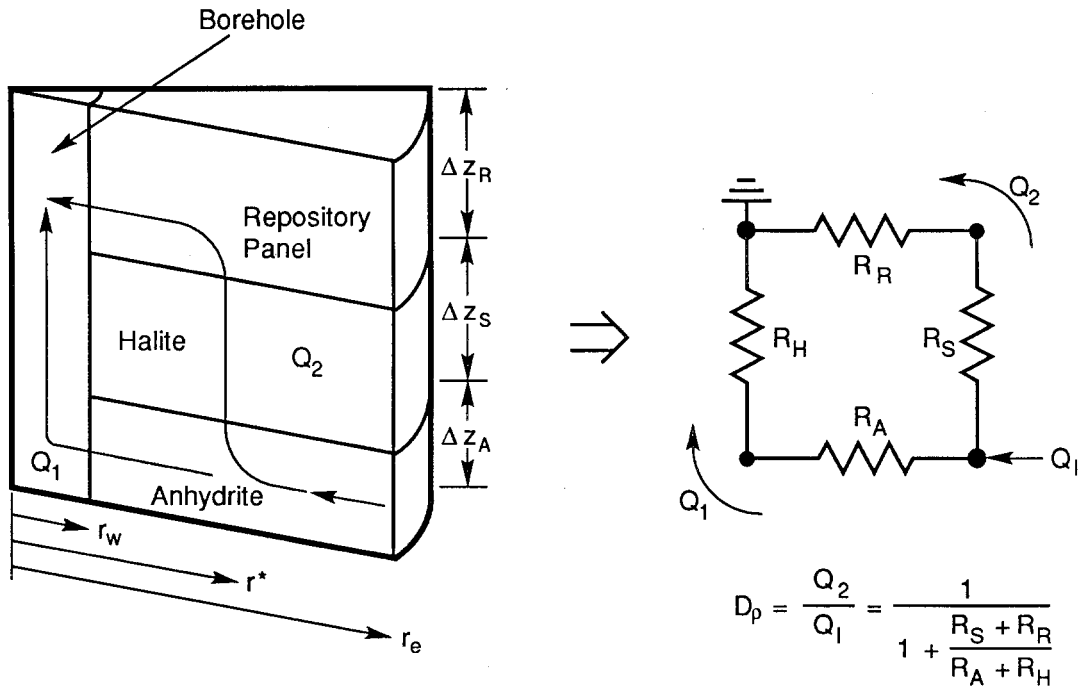
TRI-6334-188-0

Figure 4-8. Schematic Diagram of Stratigraphy Surrounding Repository Panel Showing Potential Discharge Paths to an Exploratory Borehole.

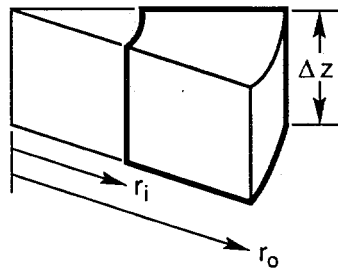
provide a drain for the Salado Formation, inducing convergent radial flow in the Salado Formation and the repository. Depending on the duration of drainage, the borehole may produce pressure gradients at great distances from the repository. With the assumption of relatively high anhydrite permeabilities, drainage of the Salado Formation may be expected to occur primarily through these strata. Near the repository, flow in an adjacent anhydrite bed (e.g., MB139) may enter the borehole either through the anhydrite (Path 1, Q_1) or through the waste (Path 2, Q_2).

Whether flow near the repository would preferentially travel on Path 2 depends on the effective hydrologic permeability of anhydrite versus waste. Simplified one-dimensional approximations of Paths 1 and 2 were developed to explore the conditions under which anhydrite flow might be diverted through the waste. The corresponding expressions for permeability allow the relative amount of flow through Path 2 to be estimated in terms of the permeability of the anhydrite, halite, waste, and borehole.

Figure 4-9 shows a schematic of the simplified diversion fraction model. The flow system is assumed to be radially symmetric. Because the exploratory borehole is the only disturbance, flow in the natural strata, provided the strata are homogeneous (see Figure 1-4), should satisfy this assumption. The complex geometry of the repository panel precludes radial flow; however, for the purposes of identifying sensitive parameters and producing order-of-magnitude estimates of flow rates corresponding to specific parameter values, the radial idealization represents the repository adequately (see Section 4.5).



In General:



$$\text{Vertical (Axial) Resistance} = \frac{\Delta z}{2 \pi k (r_o^2 - r_i^2)}$$

$$\text{Horizontal (Radial) Resistance} = \frac{\ln(r_o/r_i)}{2 \pi \Delta z k}$$

So that:

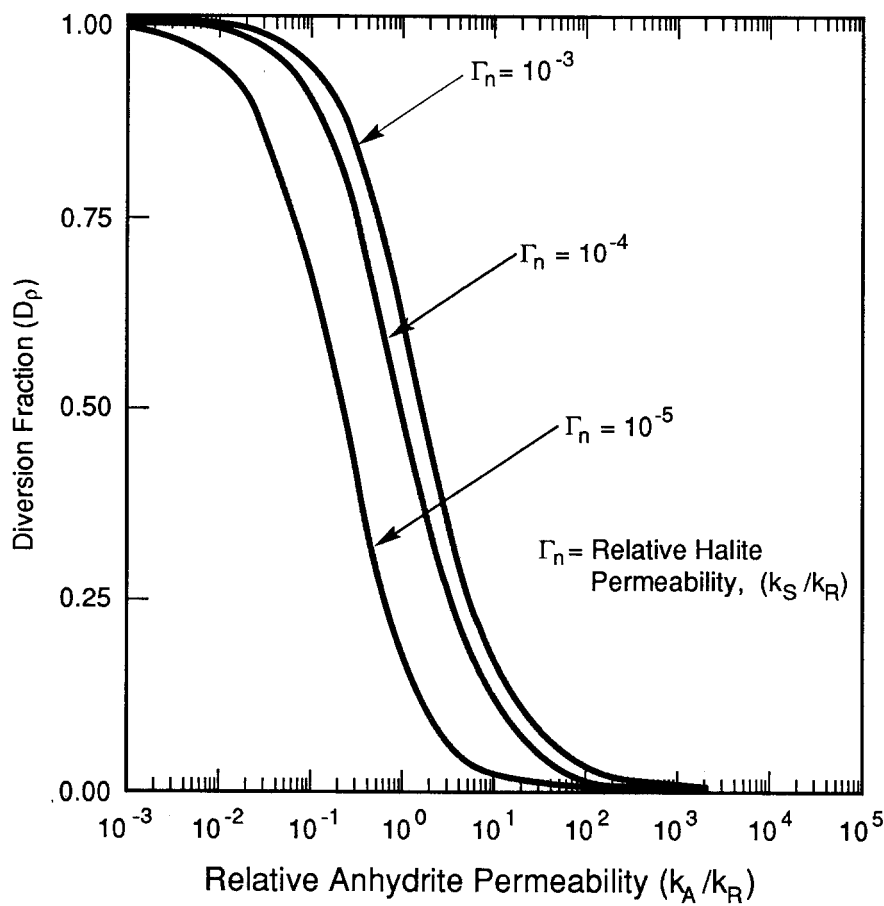
$$R_R = \frac{\ln(r^*/r_w)}{2 \pi \Delta z_R k_R}, \quad R_A = \frac{\ln(r^*/r_w)}{2 \pi \Delta z_A k_A}, \quad R_H = \frac{\Delta z_A/2 + \Delta z_S + \Delta z_R/2}{2 \pi k_H r_w^2}$$

$$R_S = \frac{1}{2 \pi (r_e^2 - r_w^2)} \left\{ \frac{\Delta z_A/2}{k_A} + \frac{\Delta z_S}{k_S} + \frac{\Delta z_R/2}{k_R} \right\}$$

TRI-6334-189-0

Figure 4-9. Simple Analytical Model for Potential Discharge Paths to an Exploratory Borehole.

Figure 4-10 presents the diversion fraction (ratio of flow diverted through the waste to total anhydrite flow) calculated using this simplified model, as a function of relative anhydrite permeability. Three values of relative Salado Formation halite permeability are considered; vertical permeability of the Salado Formation halite that separates the repository from the anhydrite is assumed to have been increased by deformation during closure. The results show that for anhydrite permeability (directly under the waste) less than waste permeability, flow entering the repository region through the anhydrite bed is diverted through the waste. In this situation, Path 2 is the path of least resistance to the borehole, regardless of the permeability of the intervening halite. For the expected case of anhydrite permeabilities larger than the waste permeability, Path 1 is the path of least resistance, and the majority of anhydrite flow remains confined within the anhydrite.

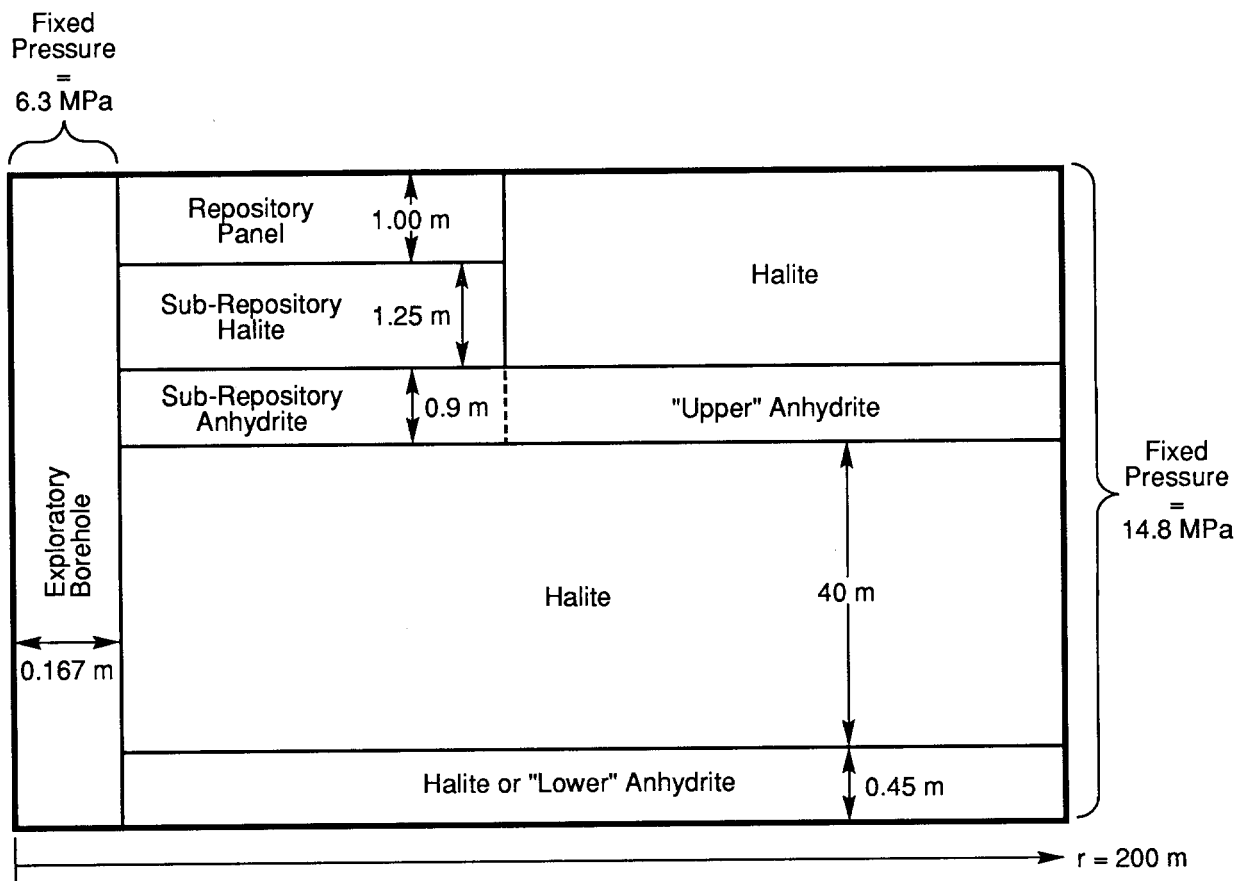


TRI-6334-190-0

Figure 4-10. Analytical Estimates of Diversion Fraction as a Function of Relative Anhydrite Permeability for Three Values of Relative Halite Permeability.

NUMERICAL MODEL OF FLOW DIVERSION NEAR PANEL

To supplement the results of the analytical model discussed above, a steady-state numerical model (SUTRA) was built to represent the near-repository flow system. The cylindrical SUTRA model included the lower half of a panel, an anhydrite layer with sub-repository depth and thickness corresponding to MB139, and 40 m (130 ft) of underlying Salado Formation halite. The wellbore was explicitly included and assigned a permeability of 10^{-12} m^2 (10^3 mD). Pressure at the upper surface of the borehole was fixed at 6.3 MPa; the far radial boundary, at a distance of 200 m (660 ft) from the borehole, was held at a pressure of 14.8 MPa (Figure 4-11). To explore the influence of anhydrite layers other than those immediately adjacent to the repository, some simulations included a second high-permeability layer along the base of the model. The effect of enhanced anhydrite permeability beneath the panel was also simulated.



TRI-6334-191-0

Figure 4-11. Geometry and Boundary Conditions for Diversion Fraction Finite-Element Model Assuming Steady-State Conditions.

Table 4-3 lists the hydrologic parameters and corresponding volumetric flux rates through the system as a whole, and through the panel. Panel flux rates were estimated from interstitial velocities calculated by SUTRA at the center of each element. The results confirm the conclusions from the analytical model: If the anhydrite permeability is lower than the waste permeability, the majority of flow approaching the repository through the anhydrite is diverted into the waste; if the anhydrite permeability is larger than the waste permeability as expected, flow remains confined to the anhydrite.

No change in panel flow was seen when the vertical permeability of the sub-repository halite was reduced from 10^{-18} m² (10^{-3} mD) to the expected halite permeability of 3×10^{-21} m² (3×10^{-6} mD). However, reducing the vertical permeability of the repository floor did slightly decrease total flow (Q_t) through the system, producing an unrealistic result of increasing diversion fraction when decreasing sub-repository halite permeability. Panel flux rates were derived from average element velocities and are consequently approximate. The relative error in this approximation of panel flux is evidently greater than the relative change in repository flux.

Including a second anhydrite layer 40 m (130 ft) below the base of the repository produced a slight increase in both the overall flux and the panel flux. Comparing the differences in total flux and panel flux suggests that approximately 60 percent of the flow in the lower anhydrite is diverted through the waste, but that the flow rate in the lower anhydrite is about 18 percent of the flow rate in the upper layer (Table 4-3).

This difference in flow rates within the upper and lower anhydrite layers is caused by the differences in effective radius of the borehole (sink) for these two layers. To elaborate, for the lower anhydrite layer, the effective radius (radius where flow resistance is significantly reduced) of the sink is the borehole radius (~ 0.17 m [0.56 ft]). For the upper anhydrite layer, the effective radius is the radius of the panel (~ 61 m [200 ft]). This is true for the upper anhydrite layer whether flow is diverted through the waste (because of the decreased permeability of the anhydrite layer), or flow is confined to the anhydrite layer (because of increased permeability of the anhydrite layer). These percent differences in effective radius of about 99.7 percent cause percent differences in flow rate of about 82 percent.

NUMERICAL MODEL OF FAR-FIELD FLOW FROM HETEROGENEOUS SALADO

The relative amount of anhydrite flow diverted into the panel is controlled by hydrologic properties near the panel: the permeabilities of the waste and of the anhydrite immediately beneath the waste. The amount of brine reaching the panel is controlled by the far-field characteristics of the anhydrite interbeds and halite of the Salado Formation. To estimate this volume of brine reaching the near-repository flow system under transient conditions with capacitance equal to 5.1×10^{-9} Pa⁻¹, three regional models were constructed. The first two models documented the decreasing importance of distant anhydrite interbeds on the total flow reaching the near-repository flow system. The third model evaluated how well representing the flow as the sum of three interbeds (a major simplification) bounded the first two more-detailed models. The first two models are discussed first.

TABLE 4-3. PARAMETER DESCRIPTIONS AND CORRESPONDING FLUXES AND DIVERSION FRACTIONS FOR THE STEADY-STATE LOCAL NUMERICAL MODEL

Upper Anhydrite Permeability, k (m ²)	Lower Anhydrite Permeability, k (m ²)	Sub-Repository Halite Permeability, k (m ²)	Total Flux Rate (m ³ /s)	Repository Flux Rate (m ³ /s)	Diversion Fraction
10 ⁻¹⁸ throughout	Not Included	k _h = 3x10 ⁻²¹ * k _v = 1x10 ⁻¹⁸ **	2.28x10 ⁻⁸	2.23x10 ⁻⁸	0.98
10 ⁻¹⁸ throughout	10 ⁻¹⁸ throughout	k _h = 3x10 ⁻²¹ k _v = 1x10 ⁻¹⁸	2.68x10 ⁻⁸	2.47x10 ⁻⁸	0.92
10 ⁻¹² below repository 10 ⁻¹⁸ elsewhere	Not Included	k _h = 3x10 ⁻²¹ k _v = 1x10 ⁻¹⁸	2.9x10 ⁻⁸	~ 0	~ 0
10 ⁻¹² below repository 10 ⁻¹⁸ elsewhere	10 ⁻¹⁸ throughout	k _h = 3x10 ⁻²¹ k _v = 1x10 ⁻¹⁸	3.44x10 ⁻⁸	~ 0	~ 0
10 ⁻¹⁸ throughout	Not Included	k _h = k _v = 3x10 ⁻²¹	2.23x10 ⁻⁸	2.23x10 ⁻⁸	~ 1.00
10 ⁻¹⁸ throughout	10 ⁻¹⁸ throughout	k _h = k _v = 3x10 ⁻²¹	2.63x10 ⁻⁸	2.47x10 ⁻⁸	0.94

* k_h = Horizontal permeability

**k_v = Vertical permeability

Besides a repository panel, the first model includes MB139 and a lumped representation of anhydrite layers "a" and "b," the most likely sources of leakage into the panel (Figure 4-8). The second model added two more anhydrite beds, arbitrarily placed 40 m (130 ft) from MB139 and the overlying composite anhydrite layer. The resulting average flux rates into the panel over 10,000 yr were 1.66 m³/yr (60 ft³/yr) for the first model, and 1.65 m³/yr (60 ft³/yr) for the second. The results are practically identical for the two different models: one with and one without distant interbeds. As discussed in the previous section, the potential contribution of more distant interbeds to the near-repository flow system is much less than nearby interbeds owing to the decreased effective drain radius, and therefore decreased interbed flow.

By way of comparison, the average inflow rate over 10,000 yr was 0.91 m³/yr (30 ft³/yr) from a SUTRA model of transient drainage into a repository panel from a homogeneous Salado Formation with an isotropic permeability of 3×10^{-21} (3×10^{-6} mD) and capacitance of 5.1×10^{-9} Pa⁻¹ (Section 4.1). Consequently, the calculations of this section suggest that if a waste panel is penetrated by an exploratory borehole, the maximum impact of a preferential path of flow through interbeds within the Salado Formation would be to increase the fluid flow through the panel by a factor of about two. Recall, however, that this prediction of enhanced repository throughflow occurs only if long-term permeabilities of anhydrite layers directly above and below the repository approach undisturbed values through fracture filling and closure. If the anhydrite permeability increases locally as expected, brine flow through the waste, in the event of penetration by an exploratory borehole, is only about 0.063 m³/yr (2.22 ft³/yr) (14 times less flow through the waste than for the model with a homogeneous Salado Formation) (Section 4.1).

The third model is a bounding estimate of total repository flow. It approximates the total repository flow as three times the flow from a generic anhydrite layer. The three separate interbeds represented were MB139, a composite anhydrite layer of layers "a" and "b," and a layer representing the more distant layers. SUTRA was used to simulate the transient drainage of a single anhydrite bed bounded above and below by halite, and having an effectively infinite outer radius. As discussed in the above section, the presence of the panel increases the effective borehole radius in near-repository anhydrites to approximately 61 m (200 ft). A fixed-pressure boundary was consequently imposed at a radius of 61 m (200 ft). Because the represented anhydrite was intended to be typical of anhydrites found near the elevation of the WIPP, the anhydrite thickness and bounding halite thickness were chosen to be 0.42 m (1.4 ft) and 10 m (33 ft), respectively. The expected Salado Formation permeability of 3×10^{-21} m² (3×10^{-6} mD) was used; the anhydrite was assumed to have a permeability of 10^{-18} m² (10^{-3} mD). The model calculated an average flow rate of 0.61 m³/yr (20 ft³/yr) over the 10,000 yr duration of the simulation. Hence, the average panel flow rate calculated by this grossly simplified model is 1.8 m³/yr (70 ft³/yr).

Consideration of near-repository stratigraphy (Figure 4-8) shows that MB139 and anhydrite "b" are the most likely sources of brine inflow in the repository. As discussed in the estimation of steady-state diversion fraction, potential contributions of more distant anhydrites to repository flow are expected to be less than contributions of near-repository anhydrites owing to the decrease in effective drain radius, and therefore total anhydrite flow.

POSSIBLE FUTURE WORK

Possible extensions of the work described in this section are as follows:

First, in estimating the effect of preferential flow through anhydrites, the far-field permeability of all anhydrite beds was assumed to be 10^{-18} m^2 (10^{-3} mD). The selection of this permeability is arbitrary; sensitivity analyses should be conducted to explore the variation of diversion fraction and anhydrite flow rate with permeability.

Second, all transient simulations used a large matrix compressibility of 10^{-9} Pa^{-1} to facilitate comparison of results of homogeneous versus nonhomogeneous idealizations of the Salado Formation. While total flow in both models may be expected to vary with compressibility, the degree of variation may not be the same in both cases. Sensitivity analyses should be performed.

Finally, to assess the importance of differences in repository flow between the homogeneous and nonhomogeneous idealizations of the Salado Formation, the distribution of brine inflow, in addition to the total brine inflow volume reported here, should be considered. The cylindrical representation of the waste panel may not be appropriate for this purpose.

4.3 CYLINDRICAL MODEL OF FLOW FROM BRINE POCKET THROUGH A ROOM

PURPOSE

The purpose of this model was (1) to estimate the volume of brine that would circulate through a room from a brine pocket following degradation of plugs and (2) to compare this volume to the volume of brine inflow from the Salado Formation as an indirect measure of the potential amount of waste that could be transported up the borehole. This model is based on the hypothesized sequence of episodes for the human intrusion scenario, E1, that was presented in Section 2.2. Current assumptions regarding flow and transport mechanisms in the Salado and Castile Formations, and current estimates of parameters of the corresponding Darcian flow model, are used.

SUMMARY

The flow field in the room, created by plug degradation and upward flow through the borehole, was assumed to consist of three components: net flow from the repository resulting from depressurization; circulation of brine through the repository, induced by pressure gradients along the borehole; and brine inflow from the Salado Formation to the borehole through the repository.

Depressurization of the room was estimated to expel 3 m^3 (106 ft^3) of room pore fluid using expected parameter values. Hence, depressurization of a room is not an important cause of contaminant transport to the borehole.

The outflow volume associated with room depressurization is proportional to waste capacitance, effective pressure change, and room volume, and therefore equally sensitive to each. The least certain of these parameters is capacitance of the room waste, which was estimated from an assumed waste compressibility of 10^{-9} Pa^{-1} .

The volume of brine-pocket fluid circulated through the repository was estimated to be in the range of 0.006 and $120,000 \text{ m}^3$ (0.2 to $4,000,000 \text{ ft}^3$) with corresponding volumes through which fluid circulates as a result of borehole diversion (access volumes) ranging between 0.03 and 240 m^3 (1 to $8,800 \text{ ft}^3$). These wide ranges reflect the uncertainty in estimates of permeabilities. Using expected permeabilities, the volume of brine pocket flux diverted through the waste is about $1,200 \text{ m}^3$ ($42,000 \text{ ft}^3$), and the volume of waste through which this brine flows is about 120 m^3 ($4,000 \text{ ft}^3$), or less than 10 percent of the room. The analysis suggests that the parameters affecting the circulating volume are capacity of the brine pocket and waste/borehole permeability ratio.

From simulations in Section 4.1, brine inflow from the Salado Formation was estimated to introduce an average of $0.11 \text{ m}^3/\text{yr}/\text{panel}$ ($3.5 \text{ ft}^3/\text{yr}/\text{panel}$) to the borehole ($\sim 1,100 \text{ m}^3/\text{panel}$ [$39,000 \text{ ft}^3/\text{panel}$] over 10,000 yr). Consequently, borehole diversion and Salado Formation brine inflow would be expected to independently introduce approximately $1,150 \text{ m}^3$ ($41,000 \text{ ft}^3$) of contaminated brine into the borehole over 10,000 yr, and, operating in conjunction, introduce less than double that amount. Although Salado Formation brine inflow contributes a similar fluid volume, the greater waste volume through which this fluid flows and the more uniform distribution of flow is expected to result in more brine contamination.

MODEL DESCRIPTION

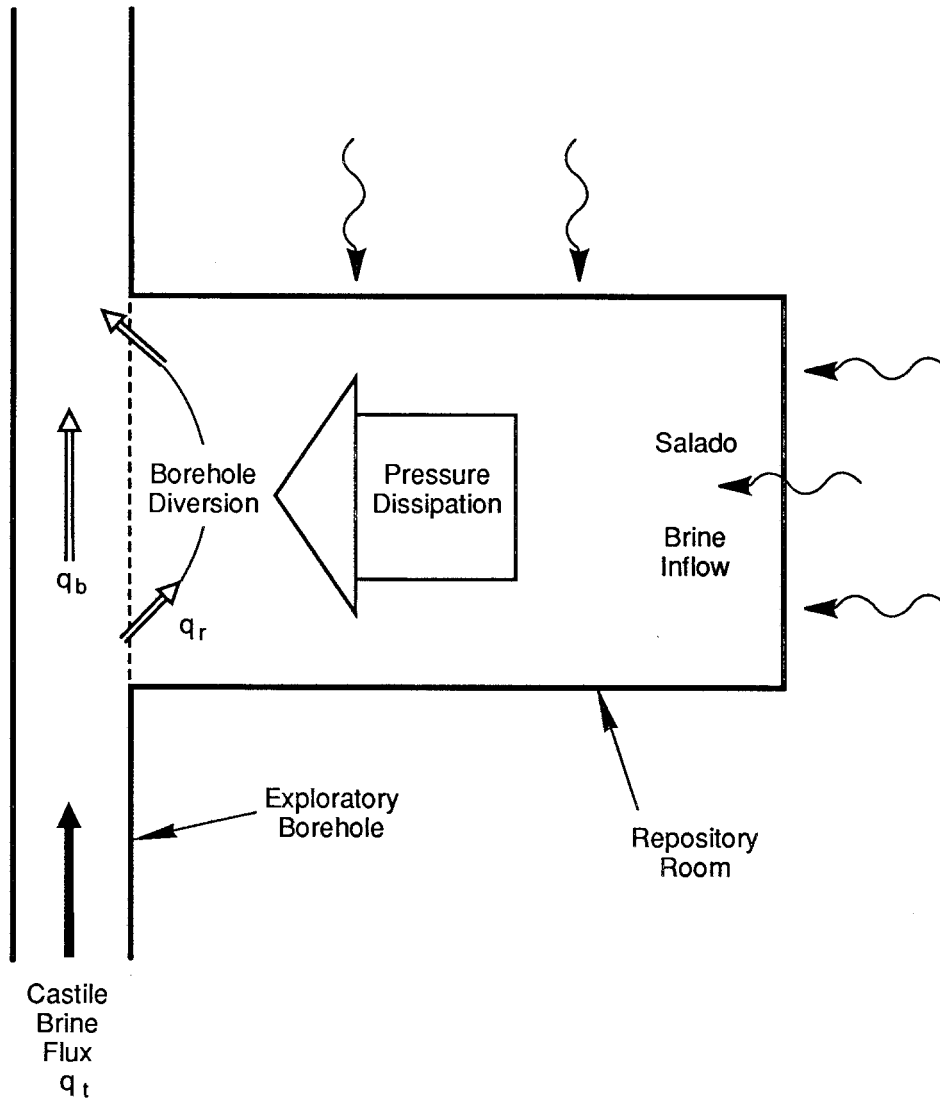
Under the human intrusion scenario described as E1, mechanisms that might introduce radionuclides from the repository into the borehole following plug degradation include (Figure 4-12): (a) release of repository fluid by depressurization, (b) circulation induced by pressure gradients in the borehole (borehole diversion), and (c) brine inflow from the Salado Formation, through the repository, into the borehole.

Response of the system to plug degradation would occur over a wide range of temporal and spatial scales. Some mechanisms might operate only immediately after plug degradation, such as depressurization in the repository. Others, such as borehole and brine inflow from the Salado Formation, might be active over much longer periods.

The possible effects of the operation of these mechanisms were estimated using the following schematic model (see Figure 4-13):

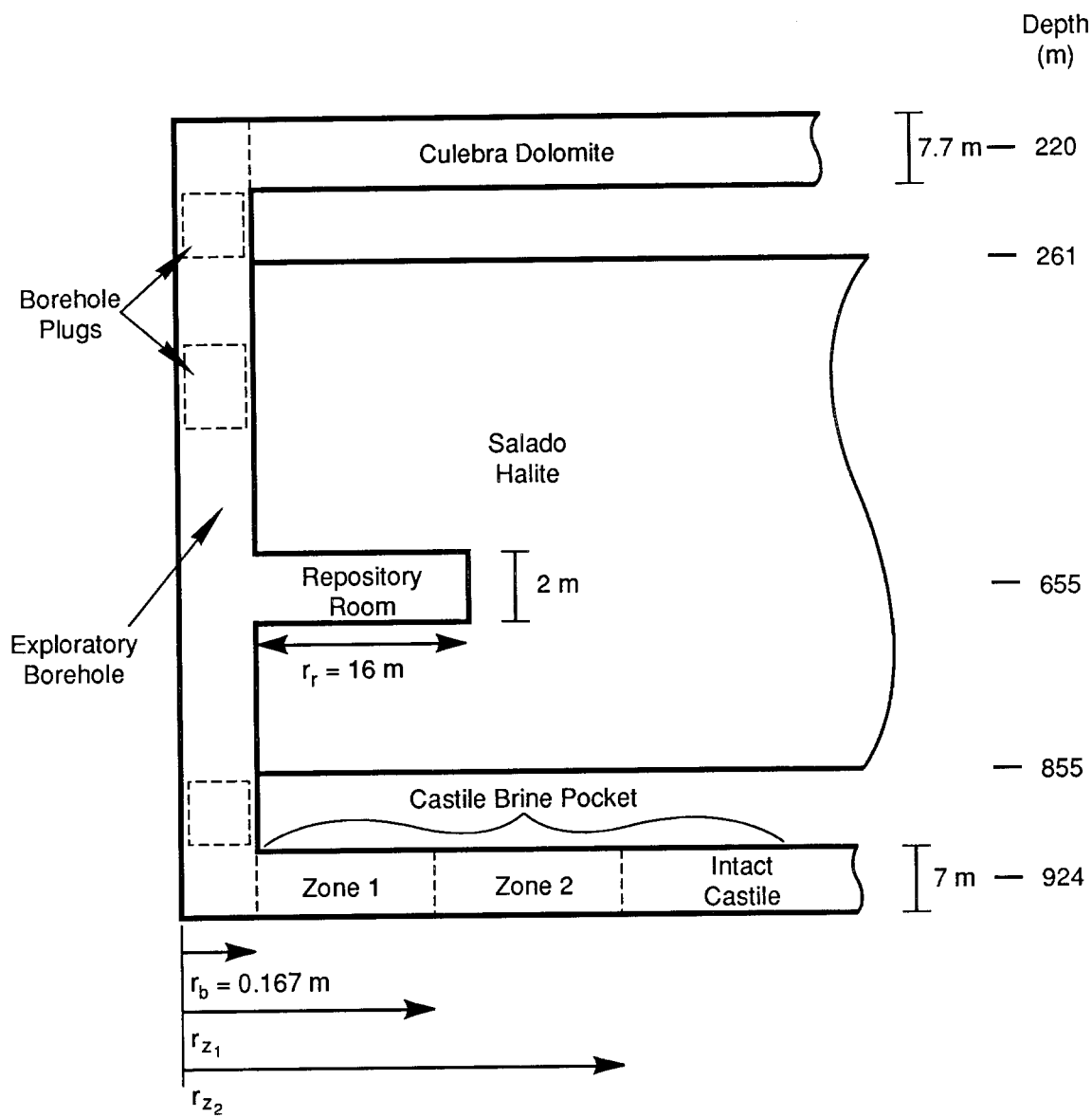
1. The Castile Formation brine pocket, repository room, Salado Formation, and Culebra Dolomite were assumed to be radially symmetric around the exploratory borehole. The cylindrical idealization is appropriate for two reasons. First, it allows relative simple numerical and analytical models to be used so that sensitivity analyses (in this report, parameter variations) can be easily performed. Second, properties of the Castile Formation brine pocket were originally derived using a cylindrical conceptual model; thus, the model for the brine pocket remains consistent. Finally, uncertainties in the hydraulic properties of the waste material do not warrant an exact representation of the room geometry.
2. The borehole, repository room, Salado Formation, and Culebra Dolomite were assumed to be homogeneous and isotropic. The Castile Formation brine pocket was assumed to be divided into three distinct concentric homogeneous regions, as indicated by the flow and shut-in tests at WIPP-12 (Lappin et al., 1989). Large uncertainties are associated with the hydraulic properties of most of the above components. The effective exploratory borehole permeability is assumed to increase from zero (after the placement of plugs at the brine pocket, below the McNutt Potash Zone, at the top of the Salado Formation, and possibly throughout the Rustler Formation), to some finite value, corresponding to the permeability of silty sand (regulatory upper limit), over a period of 75 yr.*
3. The scenario involves flow of brine-saturated fluid from the Castile and/or Salado Formations through the borehole. All fluids are therefore assumed to be at a constant density, corresponding to the estimated density of Castile Formation brine. Major ion transport and flow induced by density gradients are ignored.
4. Mechanisms of brine/waste interaction, radionuclide mobilization, transport, and retardation are not considered. Estimates of the consequences of flow through the waste are made (conservatively) in terms of advective transport of neutrally buoyant particles. Estimates of transported waste are derived exclusively from the repository flow field.

* Although not attempted here, it may be possible to improve upon this upper bound for borehole permeability because of numerous old borehole plugs that are present in the WIPP site and the WIPP region.



TRI-6334-174-0

Figure 4-12. Conceptual Model of Repository Flow Field Considered in Calculation of Access Fraction from Brine Pocket Flow.



TRI-6334-170-0

Figure 4-13. Schematic Diagram of the Geometry Used for Calculating Access Fraction from Brine Pocket Flow.

MODEL IMPLEMENTATION

An estimate of the fraction of waste accessible to brine requires an accurate definition of fluid velocities within the repository room. For flow field must therefore be defined over both the short- and long-term, with locally high resolution and large extent. Because of concurrent requirements for resolution, scope, and efficiency, a single numerical implementation of the conceptual model did not prove practical.

Therefore, the dynamic behavior of each component of the model was first considered independently, in order to understand which processes control the system response at various times, and to develop legitimate approximate representations of those processes. A simple analytical model was used to identify the time constants associated with transients in each component, induced by changes in boundary pressure, over the range of hydraulic properties (permeability and capacitance) considered before developing numerical models.

Flow in each component was assumed to be governed by the diffusion equation,

$$\nabla^2 H = \frac{1}{d} \frac{\partial H}{\partial t} \quad , \quad d = \frac{k}{\mu c} \quad (4-5)$$

where

- c = capacitance (Pa⁻¹)
- d = hydraulic diffusivity (m²/s)
- H = hydraulic head (m) = p/γ+z
- k = permeability (m²)
- p = pressure (Pa)
- z = depth (m)
- μ = fluid viscosity (Pa-s)
- γ = specific weight (kN/m³).

Solutions of which can be expressed as (Ozisk, 1968)

$$H(x, t) = \sum_{m=1}^{\infty} a_m \psi_m(x) e^{-\chi_m^2 t d} \quad (4-6)$$

where

- a_m = constants required by the initial/boundary conditions
- x = spatial position
- χ_m = eigenvalue
- ψ_m(x) = eigenfunctions appropriate for the given geometry and boundary conditions.

The time constant of solution H(x,t) is defined as the characteristic time associated with the smallest eigenvalue:

$$t_c = \frac{1}{\chi_1^2 d} \quad (4-7)$$

The three brine pocket zones, the repository room, and the Culebra Dolomite were idealized as homogeneous isotropic hollow cylinders. The borehole was considered to be a homogeneous one-dimensional region, with fixed pressure boundaries in the Castile Formation and Culebra Dolomite. General considerations used in estimating values of d and x_1 are discussed below. Specific values for each component are summarized in Table 4-4.

Eigenvalues. Transcendental expressions for eigenvalues corresponding to the geometries and boundary conditions considered here have been taken from Ozisik (1968). The eigenvalues are the positive roots of

$$\frac{J_0(r_b \chi)}{J_0'(r_r \chi)} - \frac{Y_0(r_b \chi)}{Y_0'(r_r \chi)} = 0 \quad (4-8)$$

where

- $J_0(\chi), J_0'(\chi)$ = Bessel function of 1st kind and its derivative, respectively
- r_b = Borehole radius
- r_r = Room radius
- $Y_0(\chi), Y_0'(\chi)$ = Bessel function of 2nd kind and its derivative, respectively.

In general, boundaries between components were assumed impermeable from the higher-permeability side, and to impose a fixed potential on the lower-permeability side. The borehole was assumed to impose a fixed potential in the Culebra Dolomite, repository, and zone 1 of the Castile Formation brine pocket.

Specific Storage. In the absence of a direct measurement, the specific storage (S_s) was estimated from Jacob's relationship (Lohman, 1972) for confined aquifers, converted to appropriate SI units (virtually identical to the expression used in SUTRA):

$$S_s = \gamma c = \gamma(\phi \beta_f + a \beta_s) \quad (4-9)$$

where

- a = dimensionless constant, equal to porosity in cemented aquifers, or 1 in unconsolidated materials (Lohman, 1972)
- c = capacitance
- β_f = compressibility of fluid (brine)
- β_s = compressibility of the solid matrix
- γ = specific fluid weight/unit area = $\rho_w g$
- ϕ = porosity.

In all such calculations, brine density was assumed to be 1,200 kg/m³ (75 lb/ft³), and brine compressibility to be 2.7×10^{-10} Pa⁻¹.

Hydraulic Conductivity. Hydraulic conductivity (K) was estimated from the expected range of permeability (k) values for each component assuming a fluid density (ρ) of 1,200 kg/m³ (75 lb/ft³) and a viscosity (μ) of 1.6×10^{-3} Pa-s.

TABLE 4-4. MAXIMUM RANGE OF CHARACTERISTIC TIMES AND INTERMEDIATE PARAMETER VALUES FOR COMPONENTS OF THE CYLINDRICAL MODEL OF FLOW FROM A BRINE POCKET

Model Component	k (m ²)	ϕ	β_s (Pa ⁻¹)	a*	S _s (m ⁻¹)	d (m ² /s)	χ_1 (m ⁻¹)	t _c (s)
Culebra	5.0 x 10 ⁻¹⁵	1.6 x 10 ⁻²	N/A	N/A	1.0 x 10 ^{-6**}	4.0 x 10 ⁻²	4.4 x 10 ⁻⁵	9 x 10 ⁶
	3.0 x 10 ⁻¹³					2	2.4 x 10 ⁻⁴	3 x 10 ⁸ 1.3 x 10 ¹⁰
Borehole	1.0 x 10 ⁻¹³					7.0 x 10 ⁻³		5 x 10 ⁴
	1.0 x 10 ⁻¹²	2.0 x 10 ⁻¹	1.0 x 10 ^{-8*}	1	1.2 x 10 ⁻⁴	7.0 x 10 ⁻²	4.5 x 10 ⁻³	5 x 10 ⁵
	1.0 x 10 ⁻¹¹					7.0 x 10 ⁻¹		5 x 10 ⁶
Room	1.0 x 10 ⁻¹⁸					6.0 x 10 ⁻⁷		8.3 x 10 ³
	1.0 x 10 ⁻¹⁵	1.8 x 10 ⁻¹	1.0 x 10 ^{-9*}	1	1.2 x 10 ⁻⁵	6.0 x 10 ⁻⁴	4.5 x 10 ⁻²	8.3 x 10 ⁵
	1.0 x 10 ⁻¹³					6.0 x 10 ⁻²		1.8 x 10 ⁸
Salado	1.0 x 10 ⁻²³					1.2 x 10 ⁻¹²	3.9 x 10 ⁻⁴	2.1 x 10 ¹²
	3.4 x 10 ⁻²¹	1.0 x 10 ⁻³	5.4 x 10 ⁻⁹	1	6.4 x 10 ⁻⁵	3.9 x 10 ⁻¹⁰		6.4 x 10 ¹⁴
	1.0 x 10 ⁻¹⁸					1.2 x 10 ⁻⁷	2.0 x 10 ⁻³	5.5 x 10 ¹⁸
Zone 1	1.0 x 10 ⁻¹³	1.0 x 10 ⁻³				8.0 x 10 ⁻²	5.6 x 10 ⁻⁴	4.0 x 10 ²
	1.0 x 10 ⁻¹¹	5.0 x 10 ⁻³	N/A	N/A	1.0 x 10 ^{-5***}	8.0 x 10 ⁰	5.8 x 10 ⁻³	4.0 x 10 ⁴
	1.0 x 10 ⁻⁹	1.0 x 10 ⁻²				8.0 x 10 ¹	5.9 x 10 ⁻³	4.0 x 10 ⁷
Zone 2	1.0 x 10 ⁻¹⁵	1.0 x 10 ⁻³				8.0 x 10 ⁻⁴	5.2 x 10 ⁻⁴	1.5 x 10 ⁴
	1.0 x 10 ⁻¹³	5.0 x 10 ⁻³	N/A	N/A	10 ^{-5***}	8.0 x 10 ⁻²		1.5 x 10 ⁶
	1.0 x 10 ⁻¹¹	1.0 x 10 ⁻²				8.0 x 10 ⁰	2.6 x 10 ⁻³	4.0 x 10 ⁹
Castile		1.0 x 10 ⁻³					5.4 x 10 ⁻⁴	5.0 x 10 ¹²
	1.4 x 10 ⁻¹⁹	5.0 x 10 ⁻³	N/A	N/A	1.0 x 10 ^{-5***}	1.0 x 10 ⁻⁷		
		1.0 x 10 ⁻²					1.4 x 10 ⁻³	3.0 x 10 ¹³

* Assumed value

** WIPP-13 pump test analysis

*** Lappin et al., 1989, p. 3-145

N/A = Not applicable, estimate of S_s available

Characteristic Times. The characteristic time represents the time required for the component to respond to changes in boundary pressure. A summary of the characteristic times reported in Table 4-4 for each component, including extreme values from the ranges of properties considered, is shown in Figure 4-14. Changes in boundary pressure would be produced by degradation of borehole plugs and depletion of the Castile Formation brine pocket discussed below.

Because plug degradation is assumed to take place over a period of 75 yr (2.4×10^9 s) (Lappin et al., 1989, Appendix C), the comparatively short duration of transients in the Culebra Dolomite, borehole, repository, and brine pocket suggests that degradation will produce a succession of quasi steady-states in these components.

Characteristic time to depressurize the brine pocket because of brine depletion may be estimated by

$$\tau_c = \frac{\Omega}{q_D} \quad (4-10)$$

where

$$q_D = \text{average depletion discharge rate (m}^3/\text{s)}$$

$$\Omega = \text{total brine pocket volume (m}^3\text{)}.$$

Depletion rate is given by Darcy's law:

$$q_D = K_b i A_B \quad (4-11)$$

where

$$A_B = \text{borehole cross-sectional area (m}^2\text{)}$$

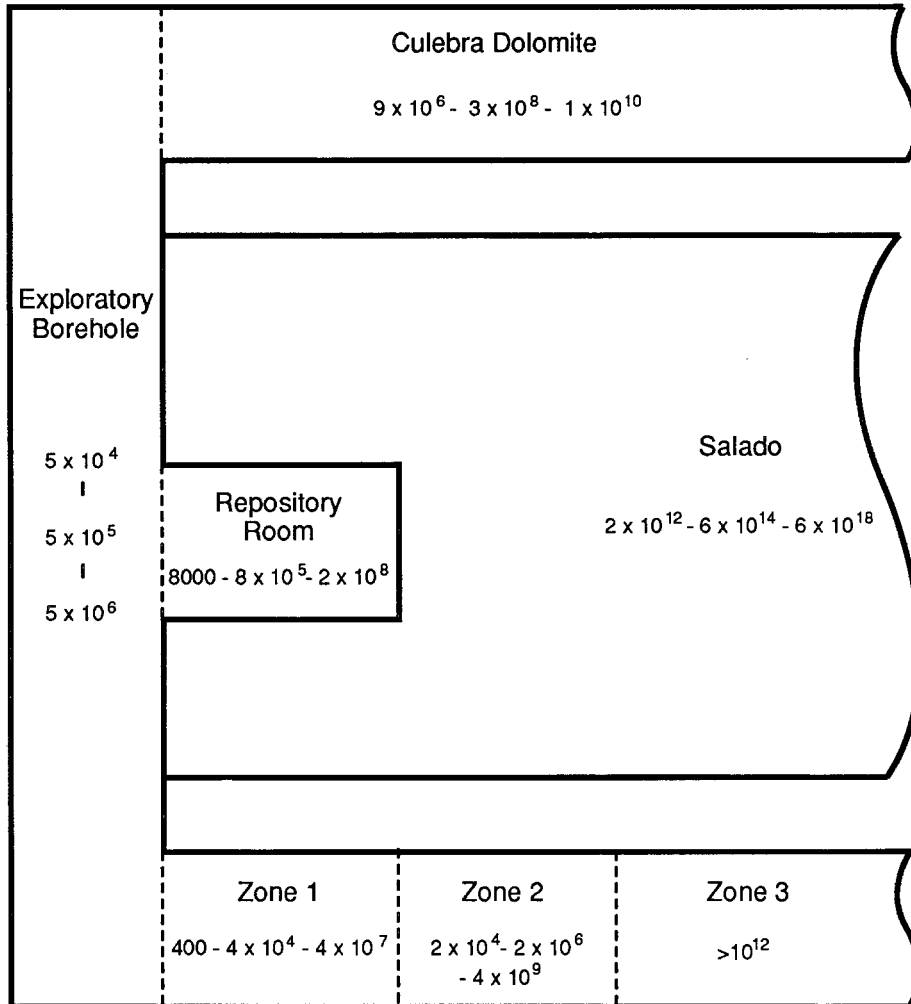
$$K_b = \text{hydraulic conductivity (m/s)}$$

$$i = \text{hydraulic gradient.}$$

Using the expected hydraulic conductivity and the expected initial hydraulic gradient results in an upper bound for the expected average depletion rate of 2.1×10^{-7} m³/s (7×10^{-6} ft³/s) (see also Lappin et al., 1989, p. E-13). The WIPP-12 brine pocket has an estimated capacity of 3.5×10^6 m³ (1.7×10^7 barrels) (Lappin et al., 1989, p 3-134), giving an estimated time of 1.7×10^{13} s ($\sim 5.3 \times 10^5$ yr) to depressurize the brine pocket. (Note that these calculations use the estimated capacitance of the WIPP-12 borehole of 10^{-5} Pa⁻¹.) Comparing the expected duration of depressurization to the time constants in Figure 4-14 suggests that brine pocket depressurization will also produce a succession of quasi steady-states in the Culebra Dolomite, borehole, repository, and brine pocket.

SIMPLIFYING APPROXIMATIONS AND CALCULATIONS MADE BASED ON CHARACTERISTIC TIMES

Relative values of component characteristic times and the characteristic times associated with plug degradation and brine pocket depletion suggest the following simplifications in estimating the effects of the repository flow components discussed above.



TRI-6334-171-0

Figure 4-14. Estimated Characteristic Response Time in Seconds of Each Model Component to Stress Changes at the Region Boundary for Flow from a Brine Pocket.

Repository Depressurization. The small time constant for a repository room relative to the expected duration of degradation, the expected duration of brine pocket depletion, and the characteristic time of the Salado Formation, all imply that pressure in the repository room may be considered to be in equilibrium with repository boundary stresses over the time scale of interest. The volume of water expelled because of depressurization between any two times can therefore be approximated from the difference in the average room pressures in equilibrium with the boundary pressures.

The average pressure in the repository room may be expected to vary as the plugs degrade and the brine pocket is dissipated. Consideration of the maximum estimated brine pocket pressure (17.4 MPa) and the difference in elevations for the repository and brine pocket suggests that connecting the repository to the brine pocket will produce a maximum repository pressure of

$$\begin{aligned} P_r &= P_o - \gamma \Delta z \\ &= 14.1 \text{ MPa} \end{aligned} \quad (4-12)$$

Average room pressure is therefore assumed to decrease monotonically from lithostatic to the discharge pressure in the Culebra Dolomite of 1.23 MPa. The total volume expelled as a result of depressurization (Ω_d) is given by

$$\Omega_d = \Omega_r S_s \Delta H_r \quad (4-13)$$

where

$$\begin{aligned} S_s &= \text{specific storage (m}^{-1}\text{)} \\ \Delta H_r &= \text{change in hydraulic head between initial and final room states (m)} \\ \Omega_r &= \text{room volume (m}^3\text{)}. \end{aligned}$$

This estimate assumes a constant volume Ω_r and does not include any additional fluid expelled as a result of any repository closure induced by depressurization.

Using Eq. 4-13, with $\Omega_r = 1,600 \text{ m}^3$, $S_s = 3 \times 10^{-6} \text{ m}^{-1}$, and the change in hydraulic head estimated as follows:

$$\begin{aligned} \Delta H_r &= (p_{\text{initial}} - p_{\text{final}}) / \gamma \\ p_{\text{initial}} &= p_{\text{lithostatic}} = 14.8 \text{ MPa} \\ p_{\text{final}} &= p_{\text{Culebra}} + \gamma \Delta z = 6.6 \text{ MPa} \\ \therefore \Delta H_r &= 670 \text{ m} \end{aligned}$$

Gives

$$\Omega_d = \Omega_r S_s \Delta H_r = 3 \text{ m}^3$$

The volume of the repository from which fluid is expelled may be estimated as

$$\Omega_e = \frac{\Omega_d}{\phi} = 17 \text{ m}^3 \quad (4-14)$$

Salado Formation Brine Inflow. The time constants for the Salado Formation imply that brine inflow to the borehole through the repository would be a long-term transient phenomenon superimposed on the quasi steady-state flow field established by borehole diversion. Qualitatively, the effect of superimposing brine inflow from the Salado Formation on the circulation flow field in the room induced by borehole fluid will be to confine a greater portion of the borehole fluid to the borehole, consequently reducing the diversion fraction.

In Lappin et al. (1989), the steady-state Salado Formation brine inflow rate was estimated as $1.0 \text{ m}^3/\text{yr}/\text{room}$ ($3.5 \text{ ft}^3/\text{yr}/\text{room}$) with a corresponding panel brine inflow rate of $1.3 \text{ m}^3/\text{yr}$ ($45 \text{ ft}^3/\text{yr}$). More detailed simulations of transient panel brine inflow, using a capacitance of $7.54 \times 10^{-11} \text{ Pa}^{-1}$, show an average panel inflow rate of approximately $0.11 \text{ m}^3/\text{yr}$ ($3.9 \text{ ft}^3/\text{yr}$) (Section 4.1), the expected permeability values. Using a much larger capacitance, the inflow averages about $0.91 \text{ m}^3/\text{yr}$ ($32 \text{ m}^3/\text{yr}$) and could range between 0.063 and $1.6 \text{ m}^3/\text{yr}$ (2.2 and $56 \text{ ft}^3/\text{yr}$) (Section 4.2). (Assuming that the transient room/panel inflow rate ratio is similar to the estimated steady-state ratio, the transient room brine inflow rate is expected to average $0.084 \text{ m}^3/\text{yr}/\text{room}$ [$3.0 \text{ ft}^3/\text{yr}/\text{room}$].) This average inflow rate ($\sim 1,100 \text{ m}^3$ [$39,000 \text{ ft}^3$] over $10,000 \text{ yr}$ or 10 times final pore volume) has been used to examine qualitatively the effects of brine inflow operating in conjunction with borehole diversion, and to provide upper bound estimates on access fraction.

Borehole Diversion. Pressure gradients associated with borehole flow, are expected to induce circulation of some portion of the borehole fluid, q_r , through the waste, q_w (see Figure 4-12). Borehole flow is in turn created by depressurization of pressure in the brine pocket, and will consequently vary with time. The problem has been addressed by the following considerations.

Recalling the relative time constants of the repository and borehole, and the fact that pressure changes in the borehole result from pressure changes in the Castile Formation and Culebra Dolomite, we may assume that, except for a brief transient associated with average pressure decrease in the room, the repository pressure will be in equilibrium with borehole pressure at any time.

Whatever the dependence of q_r on q_t , we may assume that (given some constant material properties), if q_t is changed, then the equilibrium values of both q_b and q_r will change by the same factor. Similarly, given a constant q_t , if the borehole conductivity and waste conductivity are changed together, the pressure difference between the top and bottom of the room will change inversely, leaving q_b and q_r unchanged. The ratio of the amount of flow through the waste (q_w) to the total flow (q_t) (defined as the diversion fraction) therefore depends only on the relative permeabilities of the borehole fill and waste.

Because the relative values of q_r and q_t depend only on the relative permeabilities of the borehole fill and waste, the total volume of flow through the waste will depend only on those permeabilities and the total volume of flow through the system. Total flow volume may be estimated as the brine pocket capacity (e.g., Lappin et al., 1989, p 3-134), or from a limiting flow rate and duration of drainage.

Note that the diversion fraction depends on the ratio of waste to borehole permeability. Although we have an estimate of the upper bound on borehole permeability (Lappin et al., 1989, Appendix C), the uncertainty in this value does not reflect the variability of permeability

within the borehole resulting from plug placement and degradation. Because of the long distance between expected plug locations and the repository elevation, the permeability of the borehole fill adjacent to the room is expected to be relatively high. The proposed range of effective permeabilities has been retained as a local estimate, providing a low estimate of local borehole permeability, and a corresponding high estimate of diversion fraction.

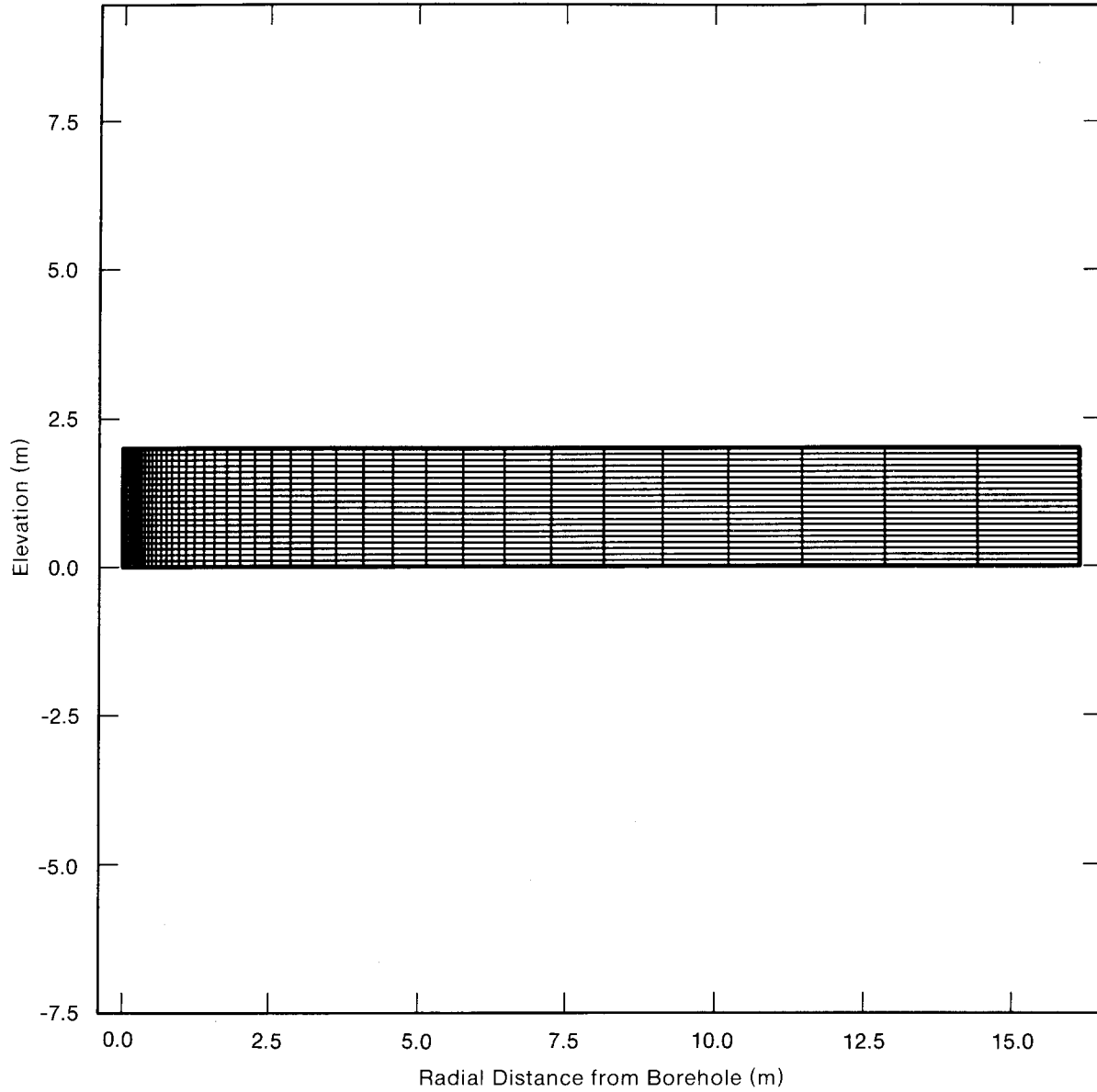
As discussed above, the access fraction resulting from borehole diversion can be estimated from the total borehole flow and the steady-state diversion fraction associated with the borehole/waste permeability ratio. SUTRA was used to estimate steady-state diversion fractions for several values of the borehole/waste conductivity ratio. Figure 4-15 shows the model grid and boundary condition locations. Fixed-pressure boundaries were imposed at the top and bottom of the borehole.

As described above, the diversion fraction is defined as the ratio of flow diverted into the waste (q_r) to total flow (q_t) through the waste and borehole. Waste flow rate was estimated as the sum of the element fluxes in the positive x direction over those waste elements adjacent to the borehole. Table 4-5 presents the diversion fraction associated with five ratios of borehole permeability to waste permeability. Figure 4-16 shows a log-log plot of the same results. The range presented covers the possible ratios given the assumed permeability uncertainties. At ratios less than approximately 10, more than half of the system flow is diverted through the waste. The diversion ratio approaches 1 as the permeability ratio decreases below 10. Above a permeability ratio of 10, flow diverted through the waste does not significantly perturb flow in the borehole, so that the borehole potential gradient is approximately uniform. Relative flow through the waste therefore varies in proportion to relative waste permeability.

Table 4-6 presents the estimated flow volume through the waste associated with various combinations of total flow from a brine pocket and diversion fraction. Note that the maximum estimated diversion fraction of 0.85, associated with a permeability ratio of 1.0 is not compatible with the maximum total flow from the brine pocket of $1.8 \times 10^6 \text{ m}^3$ ($64 \times 10^6 \text{ ft}^3$) within the range of parameters considered.

The WIPP-12 brine pocket capacity has been estimated at $3.5 \times 10^6 \text{ m}^3$ (1.7×10^7 barrels) (Lappin et al., 1989, p. 3-134). The range of effective conductivities considered for the borehole, however, will restrict the total flow during the period of regulatory interest to something less than this value. Upper bounds on total flow through the borehole used in Table 4-6 for various combinations of parameters are estimated from the initial upward gradient as follows:

$$\begin{aligned}
 q_r &= KiA \\
 K &= \frac{\gamma}{\mu} k, \quad k = 10^{-11}, 10^{-12}, 10^{-13} \text{ m}^2 \\
 i &= \frac{P_{\text{pocket}} - P_{\text{Culebra}}}{\gamma \Delta z} - 1, \quad P_{\text{Culebra}} = 1.23 \text{ MPa}, \\
 &P_{\text{pocket}} = 7, 12.7, 17.4 \text{ MPa} \\
 &\Delta z = 716 \text{ m}, \quad \rho = 1240 \text{ kg/m}^3 \\
 A &= \pi r_w^2, \quad r_w = 0.167 \text{ m}
 \end{aligned} \tag{4-15}$$

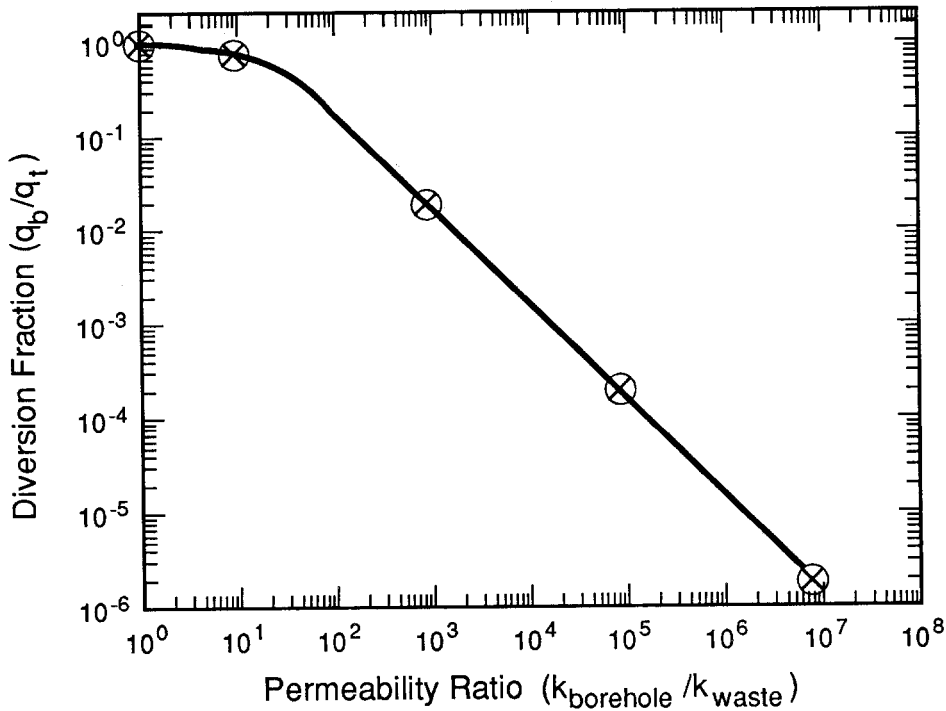


TRI-6334-245-0

Figure 4-15. Model Grid and Boundary Condition Locations for Brine Pocket Calculation. Fixed-pressure boundaries were imposed at the top and bottom of the borehole.

TABLE 4-5. FLOW RATES AND ASSOCIATED DIVERSION FRACTIONS ESTIMATED WITH SUTRA FOR FIVE BOREHOLE/WASTE PERMEABILITY RATIOS

Run ID	Borehole Permeability (m ²)	Waste Permeability (m ²)	q _t (m ³ /s)	q _r (m ³ /s)	Diversion Fraction = q _r /q _t
1	10 ⁻¹¹	10 ⁻¹⁸	2.67 × 10 ⁻⁴	5.15 × 10 ⁻¹⁰	1.9 × 10 ⁻⁶
2	10 ⁻¹²	10 ⁻¹³	6.09 × 10 ⁻⁵	3.88 × 10 ⁻⁵	6.4 × 10 ⁻¹
3	10 ⁻¹²	10 ⁻¹⁵	2.71 × 10 ⁻⁵	5.13 × 10 ⁻⁷	1.9 × 10 ⁻²
4	10 ⁻¹³	10 ⁻¹³	2.32 × 10 ⁻⁵	1.98 × 10 ⁻⁵	8.5 × 10 ⁻¹
5	10 ⁻¹³	10 ⁻¹⁸	2.67 × 10 ⁻⁶	5.15 × 10 ⁻¹⁰	1.9 × 10 ⁻⁴



TRI-6334-173-0

Figure 4-16. Steady-State Diversion Fraction versus Borehole/Waste Permeability Ratio.

TABLE 4-6. VOLUME OF FLOW DIVERTED THROUGH REPOSITORY FOR SELECTED COMBINATIONS OF DIVERSION FRACTION AND BRINE POCKET DISCHARGE VOLUME

Borehole Permeability (m ²)	Brine Pocket Pressure (MPa)	10,000-yr Flow Volume (Q _b) (m ³)	Relative Permeability (k _{borehole} /k _{waste})			
			10 ⁷	10 ³	10 ¹	1
			Diversion Fraction (Figure 4-16)			
			1.9 x 10 ⁻⁶	1.9 x 10 ⁻²	6.4 x 10 ⁻¹	8.5 x 10 ⁻¹
			Flow Volume Diverted Through Repository in 10,000 yr (Q _d) (m ³)			
--	--	3.0 x 10 ³	5.7 x 10 ⁻³	5.7 x 10 ¹	1.9 x 10 ³	2.5 x 10 ³
10⁻¹²	12.7	6.5 x 10⁴	1.2 x 10 ⁻¹	1.2 x 10³	4.2 x 10 ⁴	X
10 ⁻¹²	17.4	1.8 x 10 ⁵	3.4 x 10 ⁻¹	3.4 x 10 ³	1.2 x 10 ⁵	X
10 ⁻¹¹	17.4	1.8 x 10 ⁶	3.4 x 10 ⁰	3.4 x 10 ⁴	X	X

Boldface = Expected Value
X = Inappropriate Value

TRI-6334-196-0

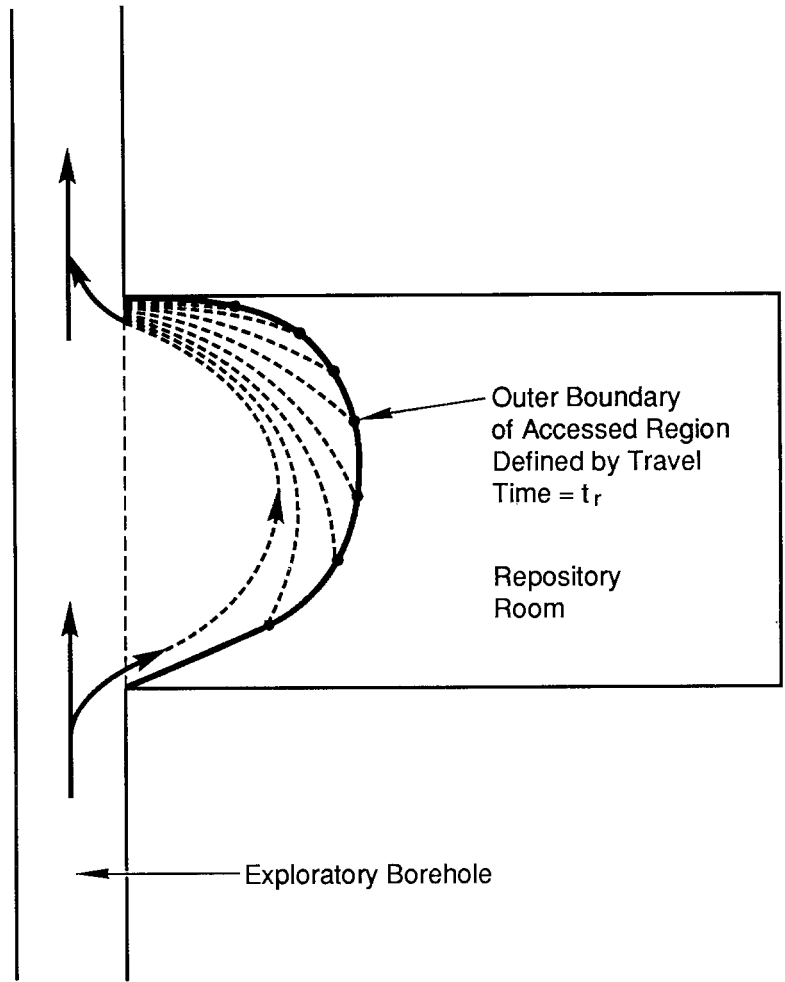
Access Fraction. In calculating the access fraction (or relative amount of waste mobilized), waste transport was assumed to occur through advection of neutrally buoyant nonreactive particles. Consequently, the amount of waste transported was a function of the flow field alone. The appropriate measure of access fraction does, however, depend on whether the mobile species is limited by solubility, or availability of waste.

Total flow through the repository, along with maximum solubility and initial inventory, determine the access fraction for solubility-limited species. Transport of leachate-limited species is controlled by the flow field "access volume," or room volume from which fluid is accessed during discharge of the Castile Formation brine pocket. Figure 4-17 illustrates the region from which soluble species will be removed by flow from a brine pocket in a specified time.

Because the repository flow field may be considered to undergo a succession of steady states, each induced by a specific total flux, the flow field in the room will vary in magnitude, but not in direction, as the brine pocket dissipates. The final position of a flow path beginning at any point can therefore be described as a function of total flow through the room. The access volume associated with an arbitrary sequence of quasi steady-state fields is therefore identical to the access volume of a single steady-state field involving the exchange of the same fluid volume.

Access volumes associated with the expected and extreme conductivity ratios were estimated as follows:

- The travel times from various radii along the center elevation of the room to the grid boundary were estimated using TRACKER (Rechard et al., 1989).



TRI-6334-172-0

Figure 4-17. Schematic Diagram Illustrating the Region from which Soluble Species Will Be Removed by Flow from a Brine Pocket in Specified Time, t_r .

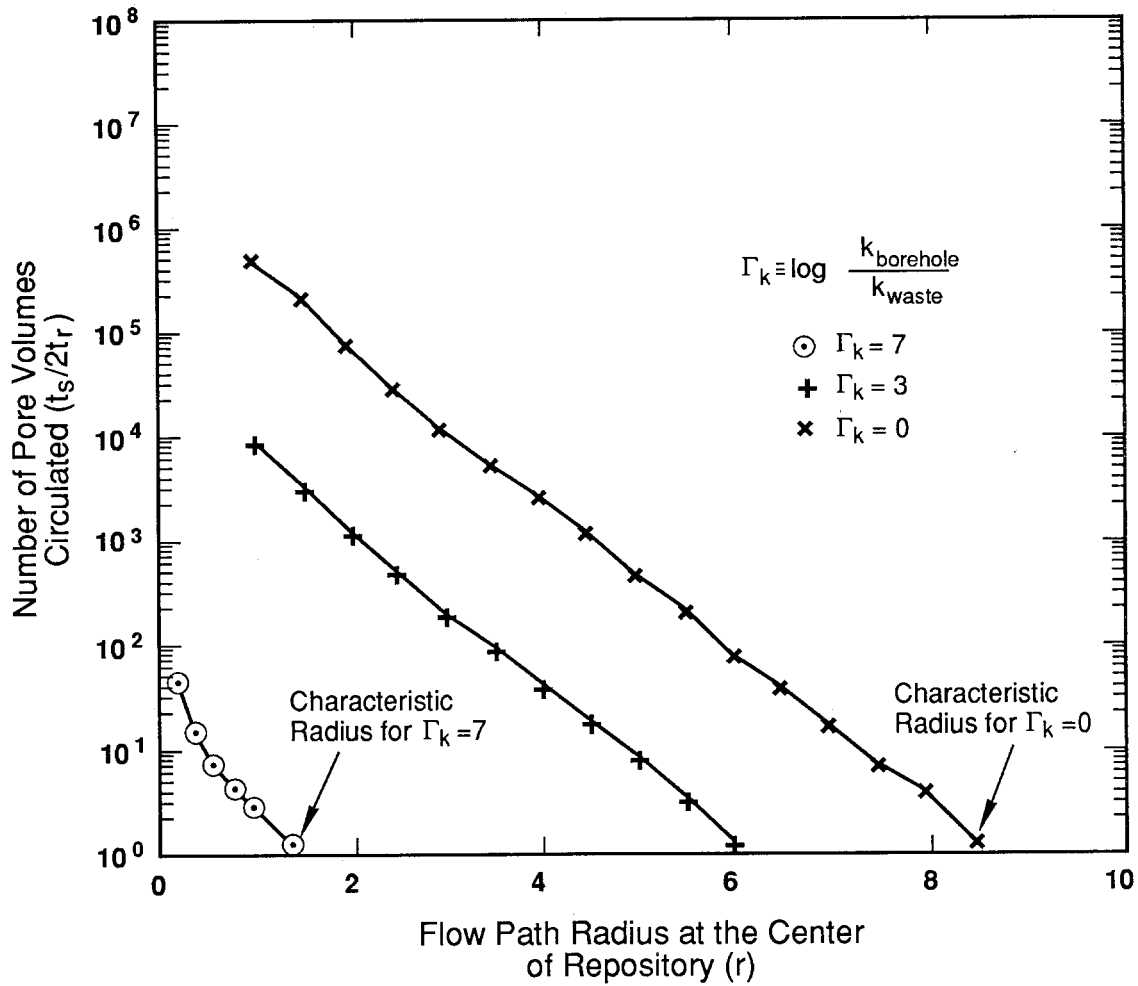
- The fixed-pressure boundary fluxes were used to calculate the time required to pass a reference total volume of fluid through the borehole/repository system.
- The number of pore volumes circulated through the stream tube associated with each radius by the transfer of the reference volume was calculated using the ratio of the time required to transfer the reference volume to the travel time associated with each flow path. Each flow path may be thought of as an infinitesimal stream tube, and the travel time along this path as the time required to circulate one pore volume of fluid through the stream tube.

A heuristic measure of how much of the repository is accessed by the discharge of the brine pocket can be defined as the radius of the flow path that has a travel time equal to the time of brine pocket discharge (defined as characteristic radius). As discussed above, the final location of any particle subject to a succession of quasi steady-state flow fields is a function only of the total volume passing through the system. A more general definition of the characteristic radius is therefore: the radius associated with the infinitesimal stream tube that exchanges one pore volume in the course of discharging the brine pocket.

Figure 4-18 shows the ratio of the reference volume time (t_s^*) to two times the corresponding travel time ($2t_T$) of a particle release at the midpoint of the waste as a function of flow path radius for the three conductivity ratios considered. (The reference volume time, t_s^* , is equal to an arbitrary [reference] fluid volume divided by the steady-state discharge rate, and the travel time, $2t_T$, was calculated by TRACKER.) The reference time/travel time ratio for a given radius is identical to the number of pore volumes circulated through the stream tube associated with this radius during the discharge of the reference brine pocket volume. The characteristic radius for the discharge of the reference volume is therefore the radius associated with $t_s/2t = 1$. Discharge of a lesser volume will reduce the number of pore volumes passed through each stream tube proportionally, e.g., the characteristic radius for a discharge of 1/10th of the reference volume is the radius associated with $t_s/2t = 10$.

Figure 4-18 can be used to estimate access volume and to explore the effects of the capacity of the brine pocket on access volume.

As illustrated in Figure 4-17, the boundary of the accessed region does not lie along any particular pathline. Identifying this boundary for a given conductivity ratio and discharge volume would entail iterative selection of multiple release points in order to approximate the curve of equal travel time. Because this procedure would be very time consuming when repeated for each flow volume and conductivity ratio, the access volume was approximated from the characteristic radius associated with twice the expelled pore volume (i.e., the position along the center elevation from which a particle would just reach the borehole when the specified volume is expelled), referred to as the access radius. Trajectories near the borehole (i.e., with radii less than the repository height) appear approximately spherical. Those with greater radii show significant vertical displacement near the maximum radius. The access volume has therefore been estimated as either the volume of the sphere or the volume of the right cylinder with the radius defined above, depending on whether the access radius is greater than or less than the final repository height of 2 m (6.5 ft).



TRI-6334-169-0

Figure 4-18. Estimated Number of Pore Volumes Circulated as a Function of Flow Radius at the Center of Repository for Three Values of $k_{\text{borehole}}/k_{\text{waste}}$.

Table 4-7 presents the estimated access radii, access volumes, and access fractions corresponding to the ranges of brine pocket discharge volumes and borehole/waste conductivity ratios. Note that the upper limit of conductivity ratio implies a borehole permeability of 10^{-13} m^2 (10^2 mD) given the range of waste permeabilities considered, and is therefore inconsistent with the expected and upper limit discharge volume.

DISCUSSION

Table 4-8 presents a summary of the estimated ranges of repository flow volume and access volume for the three components of repository flow considered.

The expected parameter values suggest that room depressurization is not an important cause of contaminant transport to the borehole. The outflow volume associated with pressure dissipation is proportional to waste specific storage, effective pressure change, and repository room volume, and therefore sensitive to each equally. The least certain of these parameters is specific storage, for which a maximum value of $5.1 \times 10^{-9} \text{ Pa}^{-1}$ has been assumed in this analysis.

Borehole diversion and Salado Formation brine inflow would be expected to independently introduce about $1,150 \text{ m}^3$ ($41,000 \text{ ft}^3$) of contaminated brine into the borehole, and, operating in conjunction, introduce less than double that amount. Although Salado Formation brine inflow and borehole diversion contribute similar fluid volume, the more uniform distribution of the brine inflow velocity field and the greater waste volume through which this fluid flows is expected to result in more contained brine.

The analysis suggests that the parameters affecting borehole-diversion volume are brine pocket capacity and waste/borehole permeability ratio. Uncertainties in important parameters produce a large uncertainty in estimated behavior. Borehole-diversion volumes ranging from 0.006 to $120,000 \text{ m}^3$ (0.2 to $4,000,000 \text{ ft}^3$) are consistent with the available data, with corresponding access volumes ranging from 0.03 to 240 m^3 (1 to $8,800 \text{ ft}^3$). Using expected values, the total repository volume through which fluid passes is estimated at approximately 120 m^3 ($4,000 \text{ ft}^3$), or less than 10 percent of the room volumes.

Although mechanical deformation of the components was neglected in this model, effects of deformation should be considered in a more rigorous model. In particular, salt creep may cause the exploratory borehole to close before plug degradation, or before the regulatory lifetime of the facility, thereby eliminating or reducing fluid flow from the repository. Also, deformation of the Salado Formation or Castile Formation may effectively increase long-term capacitance of the Salado Formation, repository, or brine pocket. Finally, consideration of brine geochemistry may reveal other important processes, such as gas exsolution accompanying depressurization, or precipitation of salt along the borehole because of outgassing of the brine.

The slow repository flow rates associated with some parameter combinations suggest that molecular diffusion may be as significant as advection in repository waste transport.

TABLE 4-7. ACCESS RADIUS, ACCESS VOLUME, AND VOLUMETRIC ACCESS FRACTION FOR SELECTED COMBINATIONS OF BOREHOLE/WASTE PERMEABILITY RATIO AND BRINE POCKET DISCHARGE VOLUME

Q _t Flow Volume (m ³)	Q _{ref} * 2xQ _t	Relative Permeability (k _{borehole} /k _{waste})								
		10 ⁷	10 ³	10 ⁰	10 ⁷	10 ³	10 ⁰	10 ⁷	10 ³	10 ⁰
		Access Radius (m)			Access Volume (m ³)			Volumetric Access Fraction		
3.0 x 10 ³	580	< 0.2	2.6	5.1	< 0.03	42	160	< 2.0 x 10 ⁻⁵	2.6 x 10 ⁻²	1.0 x 10 ⁻¹
6.5 x 10 ⁴	27	0.3	4.3	X	0.4	120	X	2.5 x 10 ⁻⁴	7.5 x 10⁻²	X
1.8 x 10 ⁶	1.0	1.5	6.2	X	14	240	X	8.8 x 10 ⁻³	1.5 x 10 ⁻¹	X

*Q_{ref} = 3.5 x 10⁶ m³
Boldface = Expected Value
 X = Inappropriate Value

TRI-6334-194-0

TABLE 4-8. ESTIMATED ACCESS VOLUMES AND REPOSITORY FLOW VOLUMES ASSOCIATED WITH THE THREE REPOSITORY FLOW FIELD COMPONENTS CREATED BY EXPLORATORY BOREHOLE PLUG DEGRADATION IN 10,000 YR

Flow Component	Capture Volume (m ³)	Repository Flow (m ³)
Pressure Dissipation	1.7 x 10 ¹	3.0
Borehole Diversion	3.0 x 10 ⁻²	5.7 x 10 ⁻³
	1.2 x 10²	1.2 x 10³
	2.4 x 10 ²	1.2 x 10 ⁵
Brine Inflow	7.6 x 10 ³	1.1 x 10 ³

Boldface = expected value

4.4 CHARACTERISTIC FLOW TIMES FOR THE CYLINDRICAL MODELS OF ROOM AND PANEL

PURPOSE

Although panels in the repository are expected to be partially or entirely filled with gas for the majority of their undisturbed lifetime, penetration of a panel by an exploratory borehole, and subsequent failure of borehole plugs, will allow depressurization of pressurized gas and/or brine in the repository through the borehole and discharge into the Culebra Dolomite. The purpose of this model is to estimate the characteristic time of room and panel depressurization for both gas and brine.

SUMMARY

The characteristic time of gas and brine depressurization for the room or panel was identified from the pressure response at the outer boundary of the cylinder used to represent the room or panel. The characteristic time was estimated as the time in which pressure changes by a factor of $(1-e^{-1})\Delta p_{\max}$ where Δp_{\max} is maximum pressure change. The expected characteristic time for depressurization of gas through the borehole is 10^5 s (1.2 days) for a room, or 2×10^6 s (~23 days) for a panel assuming a waste permeability of 10^{-15} m² (1 mD). The characteristic times for brine depressurization are 8.3×10^5 s (9.6 days) for a room or 1.5×10^7 s (0.5 yr) for a panel. The characteristic times for brine depressurization are about 7.5 times larger than characteristic times for gas depressurization. The room and panel characteristic times vary inversely with waste permeability. Hence, a wide range in characteristic depressurization times for the waste are possible, yet they will remain short in relation to 10,000 yr.

Characteristic times for all the numerical simulations lie between the analytical estimate using bounding gas compressibilities, suggesting that an analytical solution of the linearized gas flow equation may be a useful screening tool in other applications.

DESCRIPTION OF GRID AND BOUNDARY CONDITIONS FOR NUMERICAL MODEL FOR GAS

Both the room and panel were represented by cylindrical sections of equivalent volume. For the gas calculations, the modified SUTRA code, as discussed in Section 3.3, was used to simulate the flow of hydrogen through the repository. Because of the relatively high permeability of the waste in comparison to the Salado Formation, the Salado Formation was assumed to act as an impermeable boundary. The initial pressure was assumed to be lithostatic; the exploratory borehole was assumed to impose a fixed-pressure boundary of 6.3 MPa (Figure 4-19). Figure 4-20 shows the grid used to represent the room.

ANALYTIC MODEL FOR GAS

In addition to the SUTRA simulations, an analytical model was used to estimate gas depressurization characteristic times. As more thoroughly discussed in Section 4.3, the characteristic time (t_c) associated with transient pressure changes in constant-density, constant-compressibility fluids is (refer to Eq. 4-8 in Section 4.3)

$$t_c = \frac{1}{\alpha_1^2 d} \quad (4-16)$$

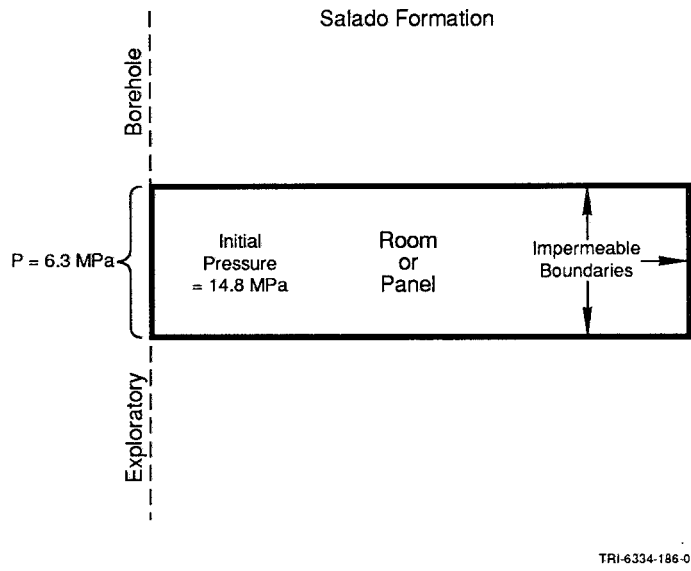


Figure 4-19. Schematic Diagram Showing Repository Region and Boundary Conditions for Evaluating Characteristic Depressurization Times.

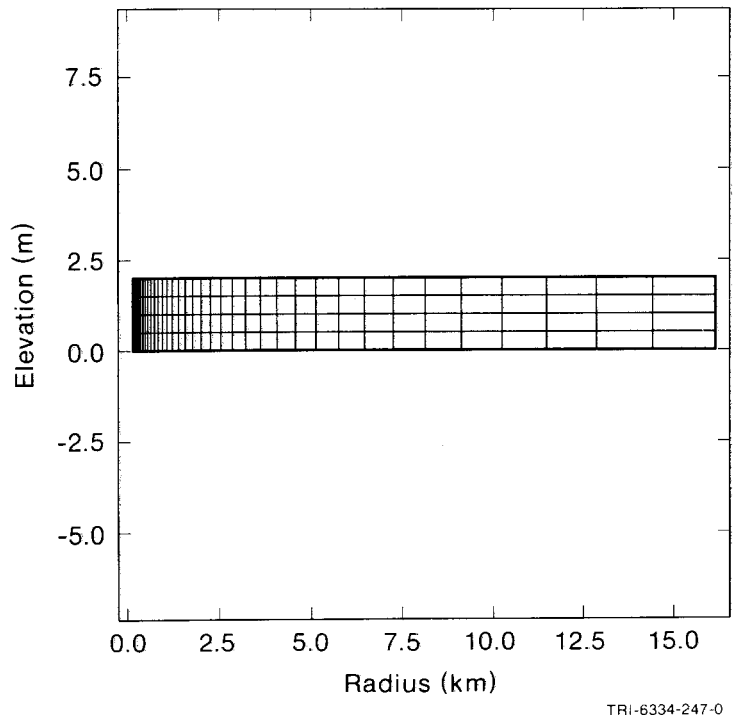


Figure 4-20. Mesh for Cylindrical Model of Room with Gas for Evaluating Characteristic Depressurization Times.

where

d = hydraulic diffusivity
 χ_1 = first eigenvalue of the pressure response.

For fluid compressibilities much larger than matrix compressibility, hydraulic diffusivity may be expressed as (refer to Eqs. 4-6 and 4-10 in Section 4.3)

$$d = \frac{k}{\phi\mu\beta_f} \quad (4-17)$$

where

k = permeability
 β_f = fluid compressibility
 μ = viscosity
 ϕ = porosity.

Furthermore, for an ideal gas, fluid compressibility is the reciprocal of pressure (p). Hence, the analytic model is

$$\tau_c = \frac{\phi\mu}{pk\chi_1^2} \quad (4-18)$$

In the present problem, fluid pressure varies between 14.8 and 6.3 MPa. Therefore, two bounding compressibilities corresponding to these limiting pressures were considered.

The analytic model for the brine depressurization was similar and was already described in Section 4.3.

VARIED AND CONSTANT PARAMETERS

The repository gas was assumed to be pure hydrogen with a constant viscosity of 9.7×10^{-6} Pa-s. Porosity was fixed at 0.18. Waste permeabilities of 10^{-18} , 10^{-15} , and 10^{-13} m² (10^{-3} , 1, and 10^2 mD) were considered.

The exploratory borehole had a radius of 0.167 m (0.6 ft). The equivalent cylinders for a room and panel had radii of 16 m (53 ft) and 60 m (200 ft). The first eigenvalues (χ_1) for the pressure solution were then 0.045 m^{-1} and 0.0104 m^{-1} for the room and panel, respectively.

RESULTS

Table 4-9 presents the characteristic times for gas depressurization identified from the SUTRA simulations of the room and panel, as well as the analytical time constants for the bounding values of compressibility. The expected room response time is about 10^5 s (1.2 days). Expected panel response time is about 2×10^6 s (23 days). The characteristic time for the cylindrical section (room or panel) was estimated as the time required for pressure at the outer radius to decrease by a factor of $(1 - e^{-1})\Delta p_{\max}$ where Δp_{\max} is the difference between the initial and final pressures (i.e., $14.8 - 8.3 = 6.5$ MPa).

TABLE 4-9. ESTIMATED GAS DEPRESSURIZATION TIME CONSTANTS FOR SELECTED VALUES OF WASTE PERMEABILITY

Repository Region	Waste Permeability (m ²)	Time Constant (s)		
		SUTRA*	Analytic	
			$\beta_f = 1/14.8 \text{ MPa}$	$\beta_f = 1/6.3 \text{ MPa}$
Room	10 ⁻¹⁸	1.13 x 10 ⁸	5.82 x 10 ⁷	1.44 x 10 ⁸
Room	10 ⁻¹⁵	1.13 x 10 ⁵	5.82 x 10 ⁴	1.44 x 10 ⁵
Room	10 ⁻¹³	1.13 x 10 ³	5.82 x 10 ²	1.44 x 10 ³
Panel	10 ⁻¹⁸	1.6 x 10 ⁹	1.09 x 10 ⁹	2.69 x 10 ⁹
Panel	10 ⁻¹⁵	2.06 x 10 ⁶	1.09 x 10 ⁶	2.69 x 10 ⁶
Panel	10 ⁻¹³	1.6 x 10 ⁴	1.09 x 10 ⁴	2.69 x 10 ⁴

*As modified for gas flow simulation

Room response time varies inversely with waste permeability. The five order-of-magnitude change in waste permeability examined in Table 4-4 is directly reflected in the change in characteristic time. Characteristic times for all simulations lie between the analytical estimates using bounding gas compressibilities. This result suggests that an analytical solution of the linearized gas flow equation may be a useful screening tool in other applications.

Table 4-10 presents the characteristic times for brine depressurization using the analytic expressions developed in Section 4.3. The expected room response time is 8.3×10^5 s (9.6 days). Expected panel response time is 1.5×10^7 s (0.5 yr). These response times for brine depressurization are about 7.5 times larger than the response times for gas depressurization.

TABLE 4-10. ESTIMATED BRINE DEPRESSURIZATION TIME CONSTANTS FOR SELECTED VALUES OF WASTE PERMEABILITY

Repository Region	Waste Permeability (m ²)	Analytic Time Constant* (s)
Room	10 ⁻¹⁸	8.3 x 10 ⁸
Room	10 ⁻¹⁵	8.3 x 10 ⁵
Room	10 ⁻¹³	8.3 x 10 ²
Panel	10 ⁻¹⁸	1.5 x 10 ¹⁰
Panel	10 ⁻¹⁵	1.5 x 10 ⁷
Panel	10 ⁻¹³	1.5 x 10 ⁵

*Solid compressibility (β_S) for waste assumed at $1 \times 10^{-9} \text{ Pa}^{-1}$.

4.5 TWO- AND THREE-DIMENSIONAL MODELS OF QUARTER PANEL

PURPOSE

The models described here focused on the brine inflow rate from the Salado Formation into the disposal area in the event of long-term discharge through an exploratory borehole in either scenario E1 or E2. The general purpose of the models described here was the same as for these earlier analyses, namely, to refine the access fraction to a more realistic value (i.e., to more accurately determine the maximum volume of waste through which a neutrally buoyant particle can travel in 10,000 yr and still reach the borehole). The specific purpose here was to examine the influence of the current panel shape on the access fraction. Earlier analyses on brine flow to a borehole approximated a waste panel as a cylindrical disk (Section 4.1). Model refinements are important because fluid flow rates in the borehole and concentrations of contaminants depend on the flow conditions in the repository induced by the borehole.

The first refinement in the simulations described here was to use a two-dimensional model with boundary conditions derived from the cylindrical calculations of Section 4.1. A few preliminary results from these models were summarized in Marietta et al. (1989).

A second refinement was to use a three-dimensional model. Although this latter refinement is incomplete, some interesting preliminary results are presented.

SUMMARY

SUTRA was used to estimate the access fraction using a two-dimensional model in the horizontal plane. Vertical flux from the Salado Formation into the panel was included using uniform source terms in each of the elements within the waste panel. The fluid source term values for each cell of the SUTRA model were determined from the cylindrical model simulations described in Section 4.1. According to the two-dimensional model described here and the flux terms from SUTRA in Section 4.1, the volume of waste accessed, assuming an unmodified permeability of 10^{-13} m^2 (10^2 mD) and Salado Formation capacitance of $7.8 \times 10^{-12} \text{ Pa}^{-1}$, was about 23 percent of a panel. The percentage of panel accessed increases to 35 percent for a capacitance of $7.54 \times 10^{-11} \text{ Pa}^{-1}$ and 95 percent for a capacitance of $5.1 \times 10^{-9} \text{ Pa}^{-1}$. At a permeability of 10^{-19} m^2 (10^{-4} mD), varying capacitance had little effect. The access fraction was about 6 percent for all cases.

The three-dimensional models using HST3D provided some interesting results. Unfortunately, the full three-dimensional model with both waste and Salado Formation host salt was numerically unstable because of the large contrast in permeability between the two media. However, a three-dimensional model that represented the waste panel as a pressure boundary was stable. The brine inflow rates from the Salado were markedly higher (but less than a factor of 3) than the corresponding estimates made with the cylindrical SUTRA models of Section 4.1. The following two causes for this discrepancy were identified:

- Eliminating the room-scale features when approximating the panel as a disk produced one-dimensional flow near the panel much earlier than for the accurate representation in HST3D.

- Equating the volume of the cylindrical disk to the excavated volume of the panel (rather than the total enclosed [excavated volume plus salt pillars]) incorrectly estimated the effective panel area as a sink for the Salado Formation.

Both causes tend to produce less brine inflow to the cylindrical disk of the panel with an equivalent volume. Although this underestimation of brine inflow can be important when discussing the absolute values of results for the cylindrical approximation, the underestimate will not affect the relative results that are important for evaluating the sensitivity to varying model parameters. Furthermore, the cylindrical models overestimated the access fraction by a factor of 2.3, which compensates somewhat for underestimated brine inflow.

As shown by the three-dimensional modeling, the pressure disturbance remains near the repository (especially for high capacitance). Consequently, representing the panels as a series of tunnels (Lappin et al., 1989; Nowak et al., 1988) is quite accurate.

DESCRIPTION OF GRID AND BOUNDARY CONDITIONS

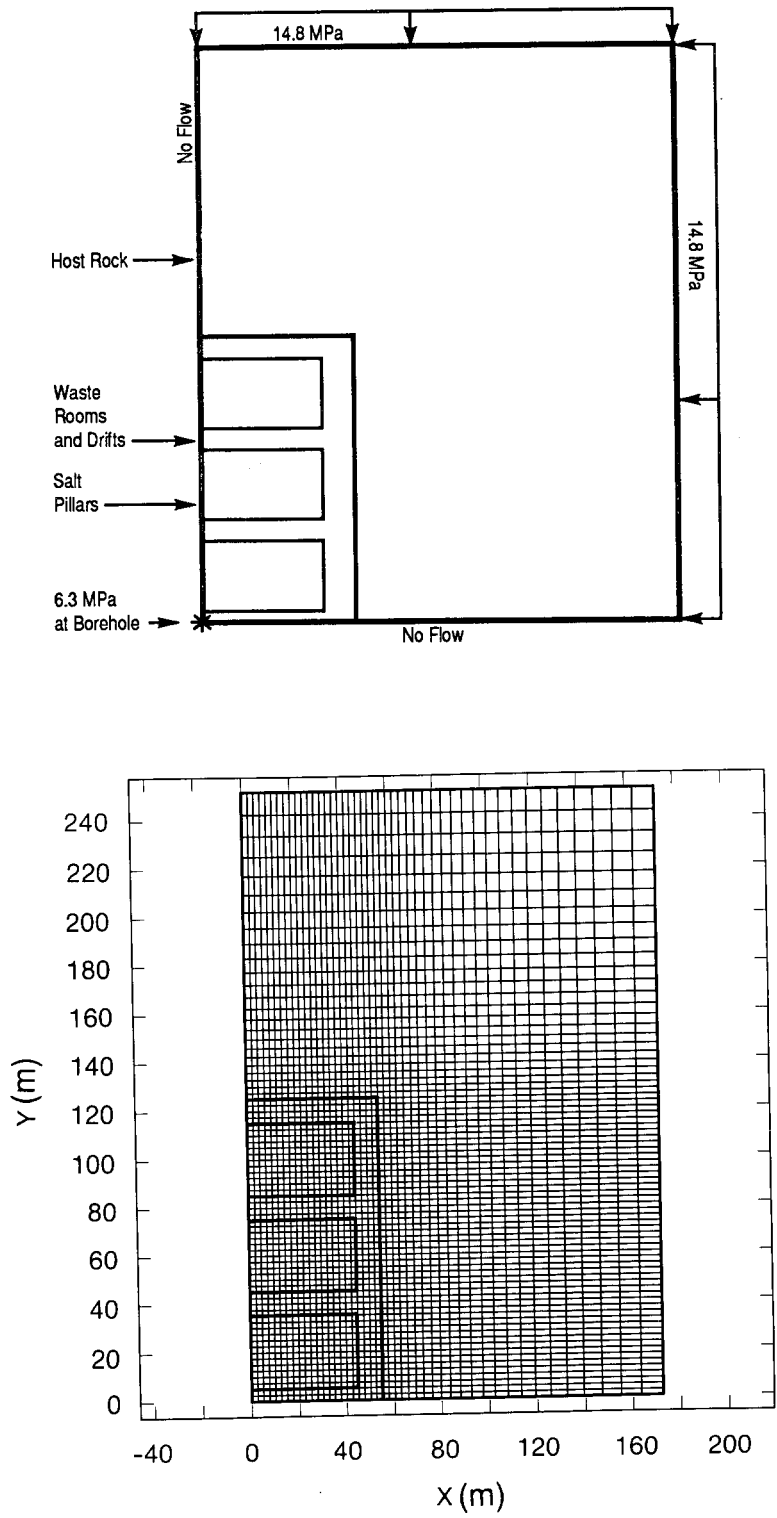
Two-Dimensional Model Description. Using panel symmetry, only one-quarter of a panel is modeled with SUTRA (Figure 4-21). The panel was 2 m (6.5 ft) thick. The boundary conditions use the maximum conceivable pressure gradient, 6.3 MPa in the borehole and 14.8 MPa at the far boundary (Figure 4-21). No flow boundary conditions were applied along planes of symmetry. Waste permeability was varied between 10^{-19} and 10^{-13} m² (10^{-4} and 10^2 mD).

The fluid source terms (representing vertical flux) for each cell of this two-dimensional model were evaluated from the cylindrical model simulations already described in Section 4.1 (Figure 4-22).

Three-Dimensional Model Description. Although flow within the panel would be approximately planar, brine inflow from the Salado Formation into the excavation would be three-dimensional if depressurization extended to a significant distance from the excavation. To evaluate the calculations made using radial symmetry, two three-dimensional models of a waste panel were configured for HST3D using the actual panel shape. The borehole was assumed to penetrate the center of a panel: symmetry across the coordinate planes reduced the modeled region to the upper half of a quarter panel. Sixty meters (200 ft) of overlying Salado Formation and 75 m (250 ft) of Salado Formation beyond the panel boundaries were also included. The exploratory borehole was assumed to maintain a pressure of 6.3 MPa at the elevation of the repository.

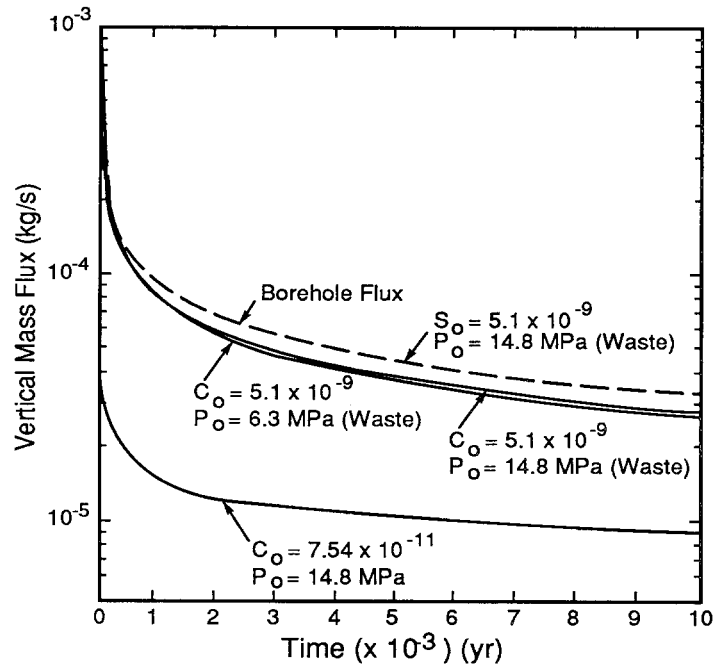
The first model included the waste explicitly. The large contrast in hydraulic conductivity between the waste and the Salado Formation, and the shape of the excavation, resulted in an unstable set of equations for the numerical model for all attempted discretizations (details are provided in the Results section).

The relatively large expected waste permeability, compared to the expected permeability of the Salado Formation, suggests that equilibration of waste pressure to borehole pressure would be very rapid in comparison to the response time of the Salado Formation (see, for example, Table 4-4). For high relative waste permeabilities, the borehole will effectively create a fixed-pressure surface on the boundaries of the excavation. Consequently, the second three-dimensional model represented the portion of the Salado Formation immediately above the quarter panel, with the shape of the panel surface represented as a fixed-pressure boundary (Figure 4-23).



TRI-6334-259-0

Figure 4-21. Quarter Panel Mesh and Boundary Conditions for Two-Dimensional SUTRA Calculation.



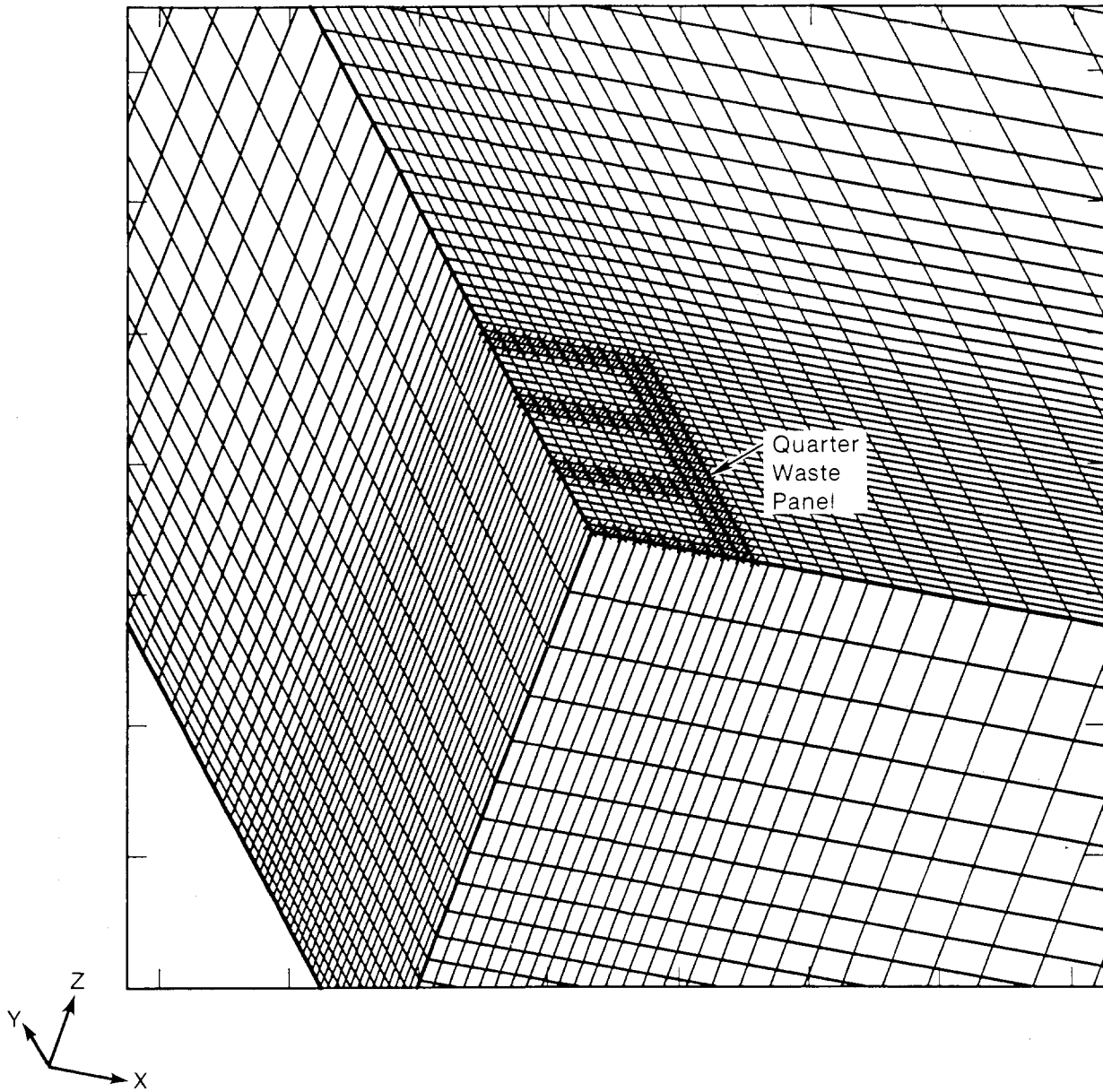
TRI-6334-248-0

Figure 4-22. Vertical Mass Flux as a Function of Time as Calculated by Cylindrical SUTRA Model.

RESULTS OF TWO-DIMENSIONAL MODEL

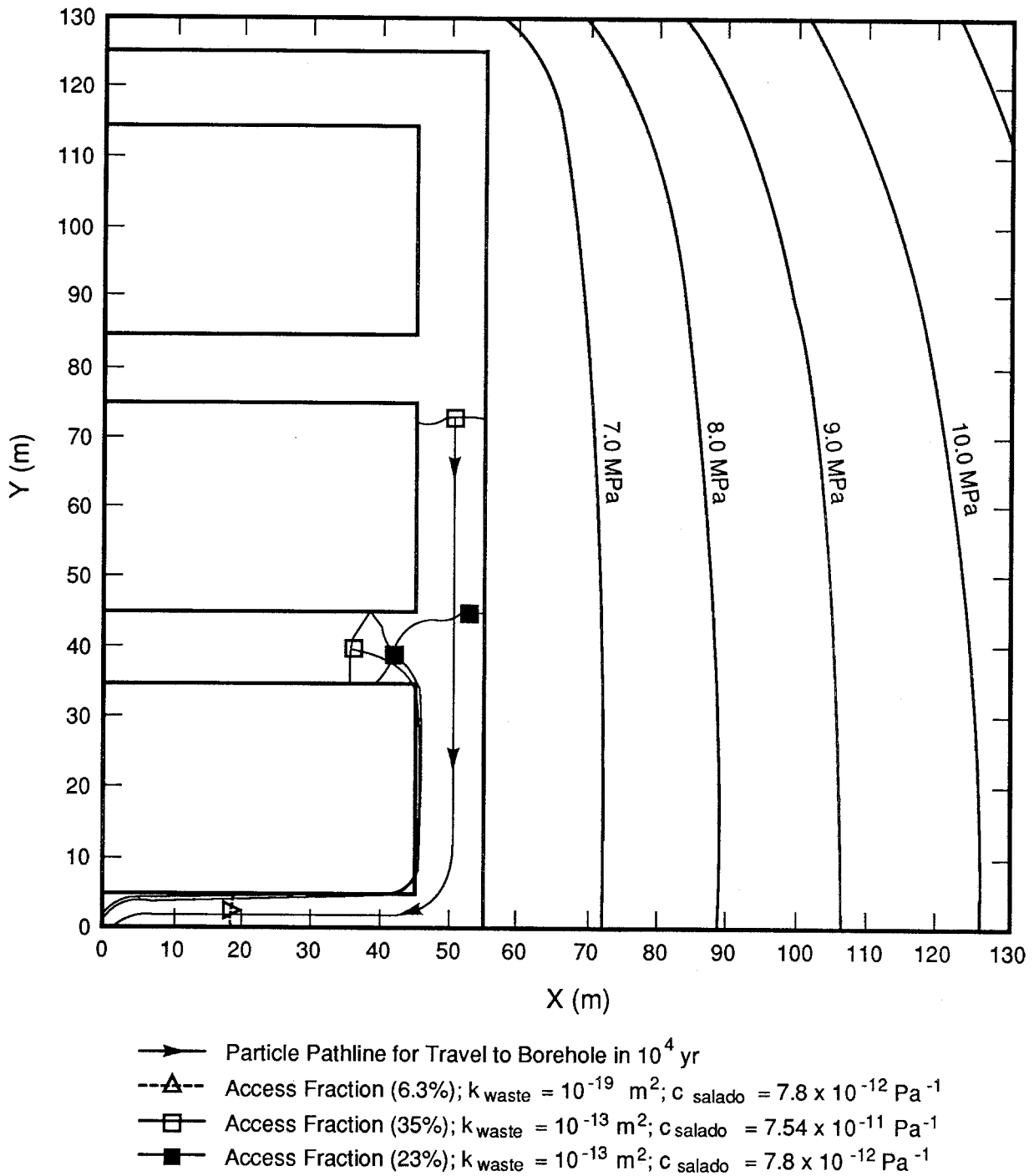
Numerical Results. According to the two-dimensional SUTRA model described here and the vertical flux terms from Section 4.1, the percentage of one panel accessed by brine seeping from the Salado Formation in 10,000 yr is between 23 and 35 percent, assuming a small expected capacitance (between 7.8×10^{-12} and $7.54 \times 10^{-11} \text{ Pa}^{-1}$) for the Salado Formation (Figure 4-24). (A similar version of this figure, using steady-state brine inflow values and showing slightly higher access fractions, was published in Marietta et al., 1989.) This access fraction does, however, increase to 95 percent, assuming the current upper bound on capacitance ($5.1 \times 10^{-9} \text{ Pa}^{-1}$) (Figure 4-25). Comparing these data points with the access fractions calculated with the cylindrical disk approximation to the panel (Figure 4-26), shows that the panel shape does affect the access fractions at low capacitance. The effect is as great at high capacitance, but it is not readily evident in Figure 4-26 unless one notes the access time of 4,500 yr for complete access using the cylindrical disk approximation to the panel shape versus the access time of 10,000 yr for 95 percent access using the actual panel shape.

Analytical Estimate of Inflow Rate. In the human intrusion scenarios, the borehole rapidly reduces the fluid pressure within the panel (see Table 4-10, Section 4.4). After waste depressurization, the pressure at the face of the panel excavation is approximately equal to the borehole pressure, and fluid flow in the Salado Formation is approximately perpendicular to the excavation.



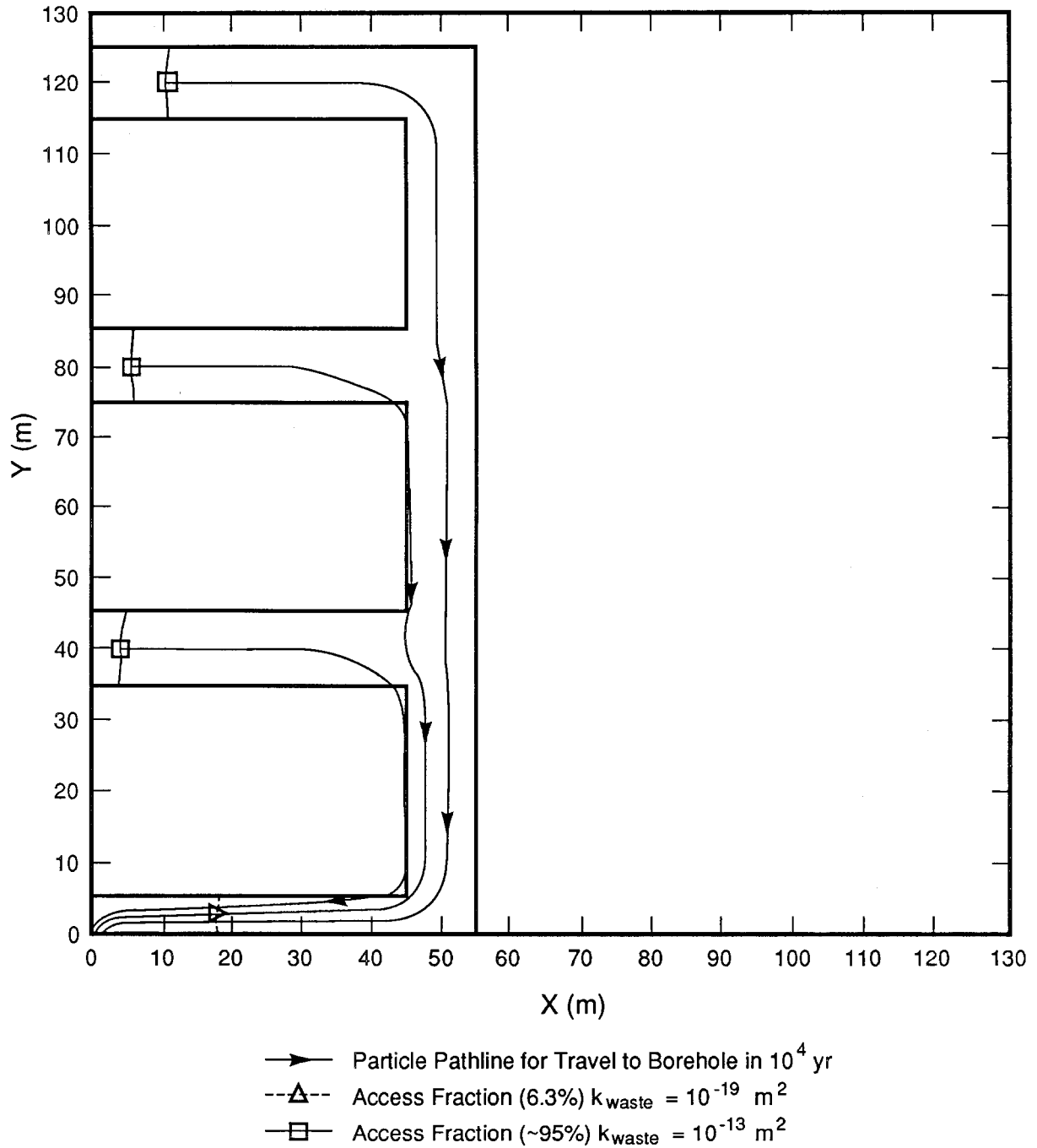
TRI-6334-222-0

Figure 4-23. Mesh for HST3D Flow Simulation of WIPP Quarter Panel.



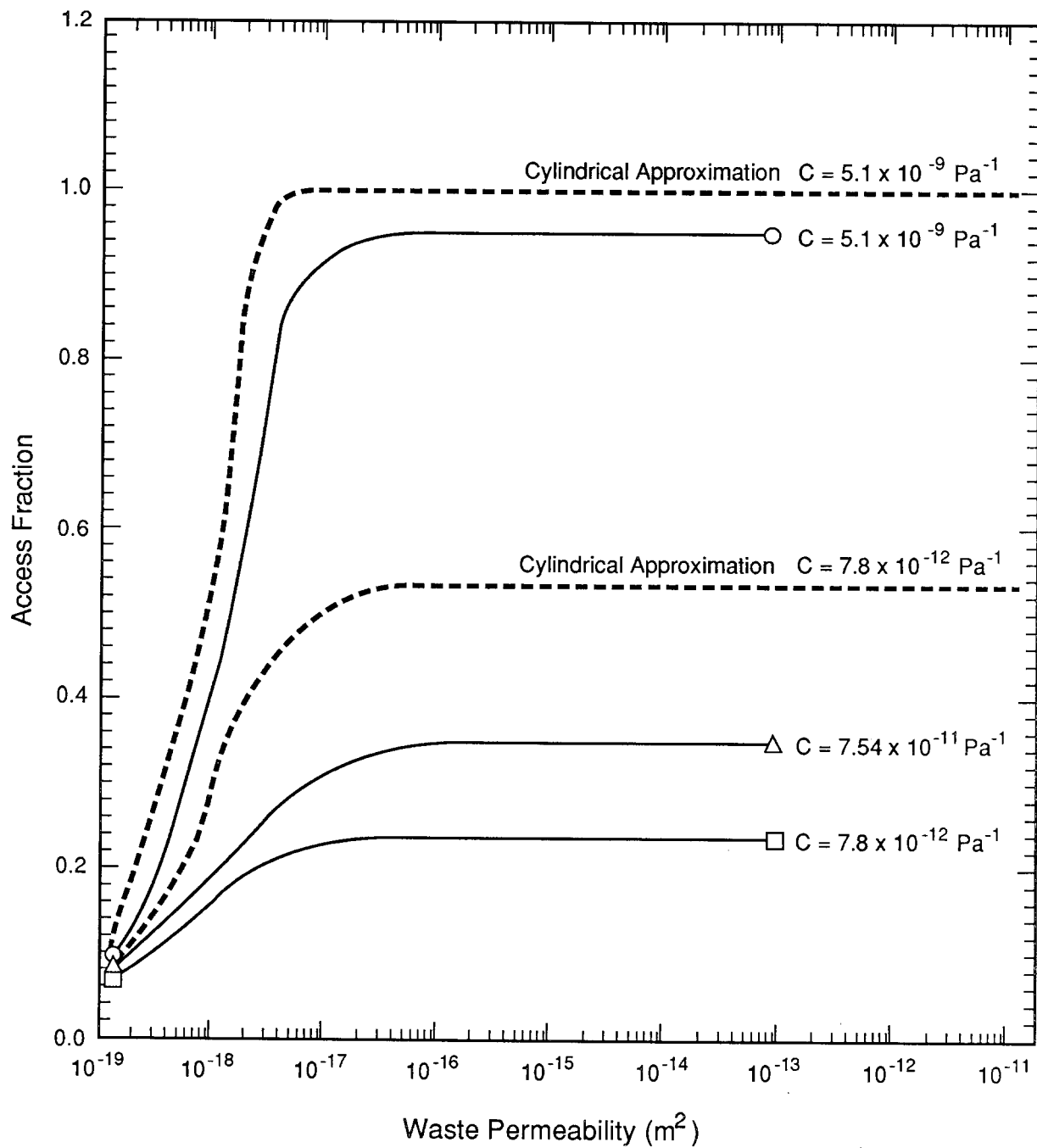
TRI-6334-264-0

Figure 4-24. Fraction of Waste Accessed in 10,000 Yr with Waste Permeabilities of 10^{-13} and 10^{-19} m^2 , and Capacitances of $7.8 \times 10^{-12} \text{ Pa}^{-1}$ and $7.54 \times 10^{-11} \text{ Pa}^{-1}$.



TRI-6334-253-0

Figure 4-25. Fraction of Waste Accessed in 10,000 Yr with Waste Permeabilities of 10^{-13} and 10^{-19} m^2 , and Capacitance of $5.1 \times 10^{-9} \text{ Pa}^{-1}$.



TRI-6334-261-0

Figure 4-26. Comparison of Access Fraction versus Waste Permeability for Cylindrical and Actual Panel Geometry (see Figure 4-6).

As shown in Figure 4-4a (and later, in Figure 4-28), pressure profiles even after 10,000 yr of drainage remain parallel to the repository boundaries (assuming a capacitance of $5.1 \times 10^{-9} \text{ Pa}^{-1}$), suggesting that for the cylindrical approximation of the panel, flow in the Salado Formation is locally one dimensional.

The diffusion equation describing Darcian flow may be solved analytically for certain simple geometries and boundary conditions. In particular, the potentiometric head in a semi-infinite one-dimensional medium having an initial head of H_0 , with a fixed boundary pressure of H_b at $x = 0$, is given by (see, for example, Ozisik, 1968):

$$H = (H_0 - H_b) \operatorname{erf} \left[\frac{x}{2\sqrt{dt}} \right] + H_b \quad (4-19)$$

where

c = capacitance

$d = \frac{k}{\mu c}$

H = hydraulic head = $p/\gamma + z$

k = permeability (m^2).

The flux rate per unit area at $x = 0$ is then

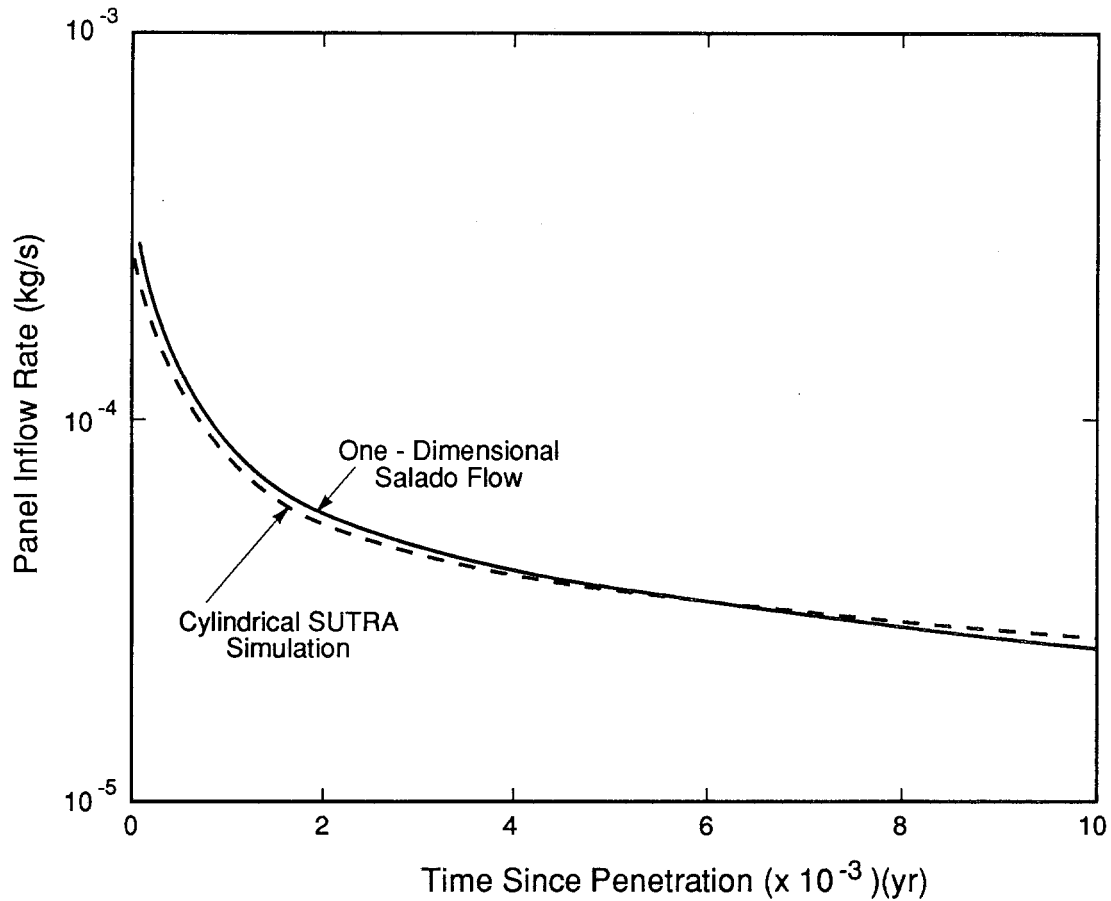
$$q/A = \frac{k\gamma}{\mu} \frac{\partial H}{\partial x} \Big|_{x=0} = \gamma(H_0 - H_b) \left(\frac{kc}{\pi\mu t} \right)^{1/2} \quad (4-20)$$

Figure 4-27 shows the brine inflow rate into a panel estimated from Eq. 4-20, assuming a surface area corresponding to the surface area of the cylindrical idealization of the panel ($23,400 \text{ m}^2$ [$250,000 \text{ ft}^2$]) and expected Salado Formation properties. Results of a SUTRA simulation (Section 4.1) are included.

The brine inflow rate estimated by Eq. 4-20 assumes an instantaneous change in boundary pressure, and thus slightly exceeds brine inflow rates from the SUTRA simulation before 4,000 yr while the waste depressurizes. As brine inflow proceeds, convergent flow from the far-field to the excavation produces inflow rates slightly exceeding the one-dimensional estimates by Eq. 4-20.

RESULTS OF THREE-DIMENSIONAL MODEL

Full Model. The expected waste permeability of 10^{-15} m^2 (1 mD) is more than five orders of magnitude larger than the expected Salado Formation permeability of $3 \times 10^{-21} \text{ m}^2$ (3×10^{-6} mD). In general, fluid flowing across a boundary separating regions of "high" and "low" permeability create an abrupt change in hydraulic gradient across the boundary. To resolve similar pressure changes on both sides of the boundary, grid spacing normal to the boundary must be much smaller in the low-permeability material than in the high-permeability material. In terms of the algebraic equations developed from the material properties and mesh, smaller grid spacing in less permeable regions creates elements of the coefficient matrix having similar magnitudes, facilitating solution of the system of equations.



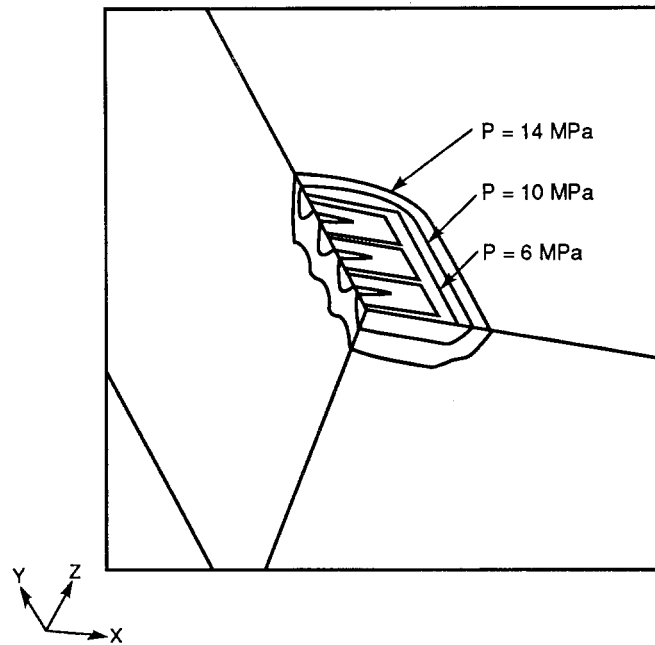
TRI-6334-201-0

Figure 4-27. Comparison of Salado Formation Inflow Rates from SUTRA and One-Dimensional Model for Base-Case Parameter Values.

The relatively small permeability of the Salado Formation mandates an abrupt reduction in grid spacing across all waste/Salado Formation interfaces. The shape of the panel excavation, and the requirement that the mesh be rectilinear, necessarily create abrupt changes in grid spacing within the waste, which introduce disproportionate terms in the coefficient matrix. No gridding of the combined waste/Salado Formation system tried to date produced an acceptable pressure solution using the HST3D code.

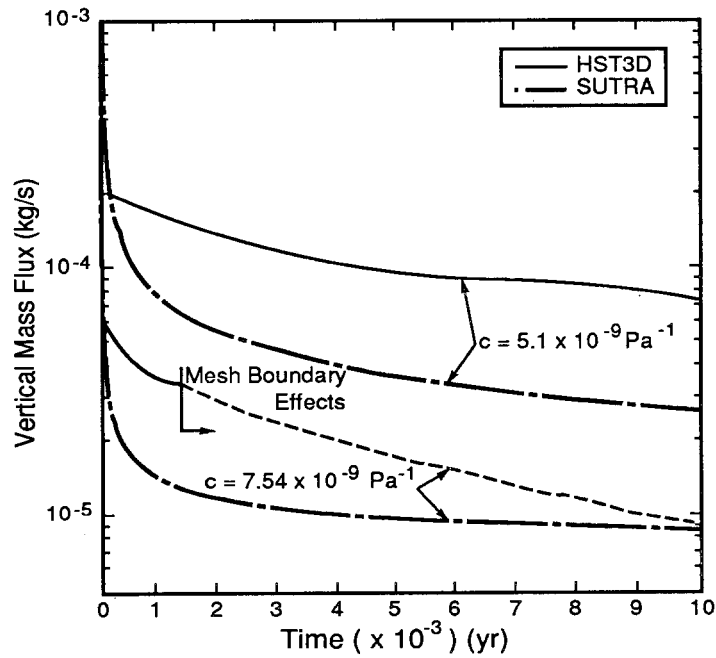
Simple Pressure Boundary Condition Model. Figure 4-28 shows a portion of the HST3D model grid with the pressure contours plotted for 10,000 yr. Very little pressure disturbance occurs about a quarter panel with a capacitance of $5.1 \times 10^{-9} \text{ Pa}^{-1}$ (similar to Figure 4-4a in Section 4.1).

Figure 4-29 shows the vertical mass flux into the panel versus time calculated for compressibility values of $5.1 \times 10^{-9} \text{ Pa}^{-1}$ and $7.54 \times 10^{-11} \text{ Pa}^{-1}$ using HST3D. The corresponding vertical mass fluxes calculated using SUTRA are also shown for comparison. For both values of compressibility, inflow rates calculated with HST3D exceed corresponding SUTRA calculations over most of the simulated period by about a factor of 3.



TRI-6334-200-0

Figure 4-28. Pressure Contours Showing Very Little Pressure Disturbance about WIPP Quarter Panel after 10,000 Yr with Capacitance Equal to $5.1 \times 10^{-9} \text{ Pa}^{-1}$.



TRI-6334-265-0

Figure 4-29. Comparison of Vertical Flux into a Waste Panel as Calculated by SUTRA and HST3D.

Because the lateral extent of the HST3D model was selected to cover the depressurized region of the Salado Formation for the higher compressibility, lower compressibility causes more rapid development of the pressure field. Consequently, inflow rates for the lower compressibility are influenced by the impermeable model boundaries, and underestimate brine inflow (dashed lines in Figure 4-29).

The following section explains the marked differences in results between HST3D and SUTRA.

DIFFERENCES BETWEEN TWO-DIMENSIONAL SUTRA AND THREE-DIMENSIONAL HST3D MODELS

Minor Influence of Brine Flow in Waste on Salado Formation Brine Inflow Rates. The problems solved by the SUTRA and HST3D computational models are not identical. The SUTRA model, for example, imposed a fixed-pressure boundary at the borehole, and explicitly included flow through the waste. Because Salado Formation brine inflow rates are lower than rates estimated by neglecting pressure variations within the waste, the HST3D simulations neglect the influence of pressure gradients in the waste. The minor influence of this difference may be gauged as follows:

An upper bound on the maximum pressure variation within the waste may be established by assuming that, at any time, all brine inflow occurs through the outer boundary of a cylinder representing the waste. The pressure difference (Δp) between the outer boundary and the borehole required to maintain a mass flow rate (m) at steady state (recall the short transient characteristic times for the panel) (Table 4-10, Section 4.4) is then

$$\Delta p = \frac{m\mu}{2\pi\rho bk} \ln \left[\frac{r_e}{r_w} \right] \quad (4-21)$$

Using the appropriate well and panel radius (r_w and r_e), depth (b), viscosity (μ), permeability (k), brine density (ρ), and mass flow rate of 1×10^{-4} kg/s (Figure 4-27) implies a pressure difference of only 600 Pa. Therefore, the difference in brine inflow rates between the SUTRA and HST3D simulations is not attributable to the differences in applied boundary conditions at the waste. (Recall that this minor difference was also shown in Figure 4-27.)

Minor Influence of Flow Through Vertical Panel Faces. In discussing the distinctions between the flow fields created by the HST3D quarter panel and the SUTRA equivalent cylinder, flow entering the excavation through the upper and lower boundaries has been emphasized. Regarding the vertical excavation faces, the following three points can be made:

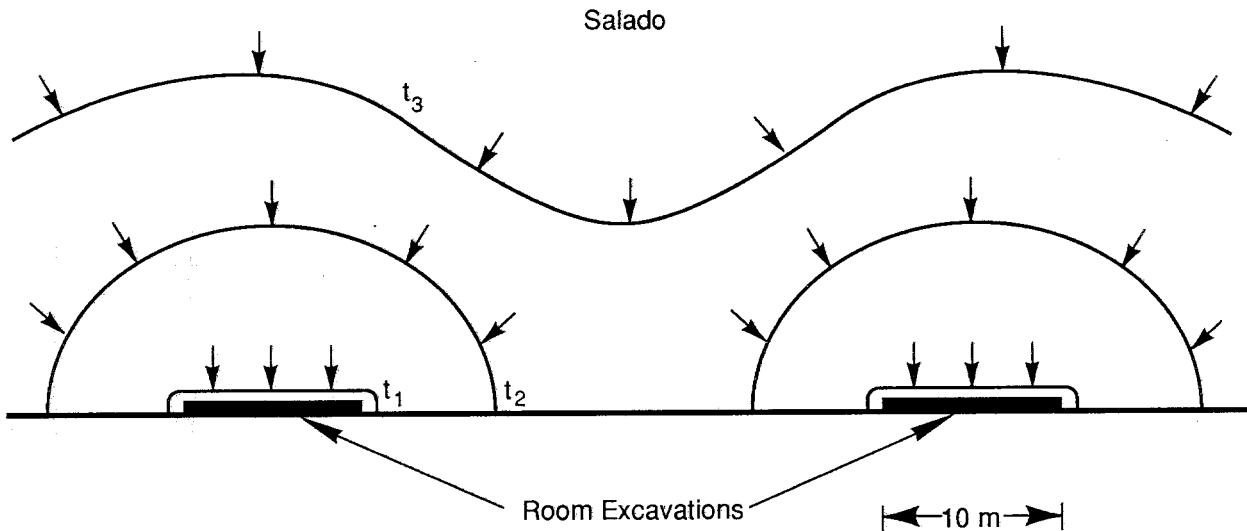
First, the cylindrical model of Section 4.1 preserves the final excavation thickness, and should, therefore, accurately simulate the onset of convergent flow into the vertical faces. However, the total area of vertical faces is not preserved in the equivalent cylinder. To this extent, the flow through the vertical faces will be greater than expected from the SUTRA results.

Second, the working HST3D model did not include vertical faces; hence HST3D also somewhat underestimates brine inflow.

Third, the difference in total surface area between the two models discussed is less than 4 percent as a result of omitting vertical panel boundaries in the HST3D model. Hence, any discrepancy in brine inflow rate produced by this omission is overwhelmed by the discrepancy introduced by the different representations of the horizontal surfaces in the two models.

Major Influence of Convergent Radial Flow vs. One-Dimensional Flow. The difference between the two estimates of brine inflow can be understood by considering the effects of the panel shape on the development of the Salado Formation flow field as brine drains through the excavation surface.

Figure 4-30 shows a diagrammatic section through the two panel rooms, and a portion of the overlying Salado Formation. One arbitrary contour of pressure (between the initial Salado Formation pressure and the boundary pressure) at three different times during drainage is shown to illustrate the development of the flow field. Although the three-dimensional contour plot (Figure 4-28) shows several different pressure contours at one time, the effect is similar.

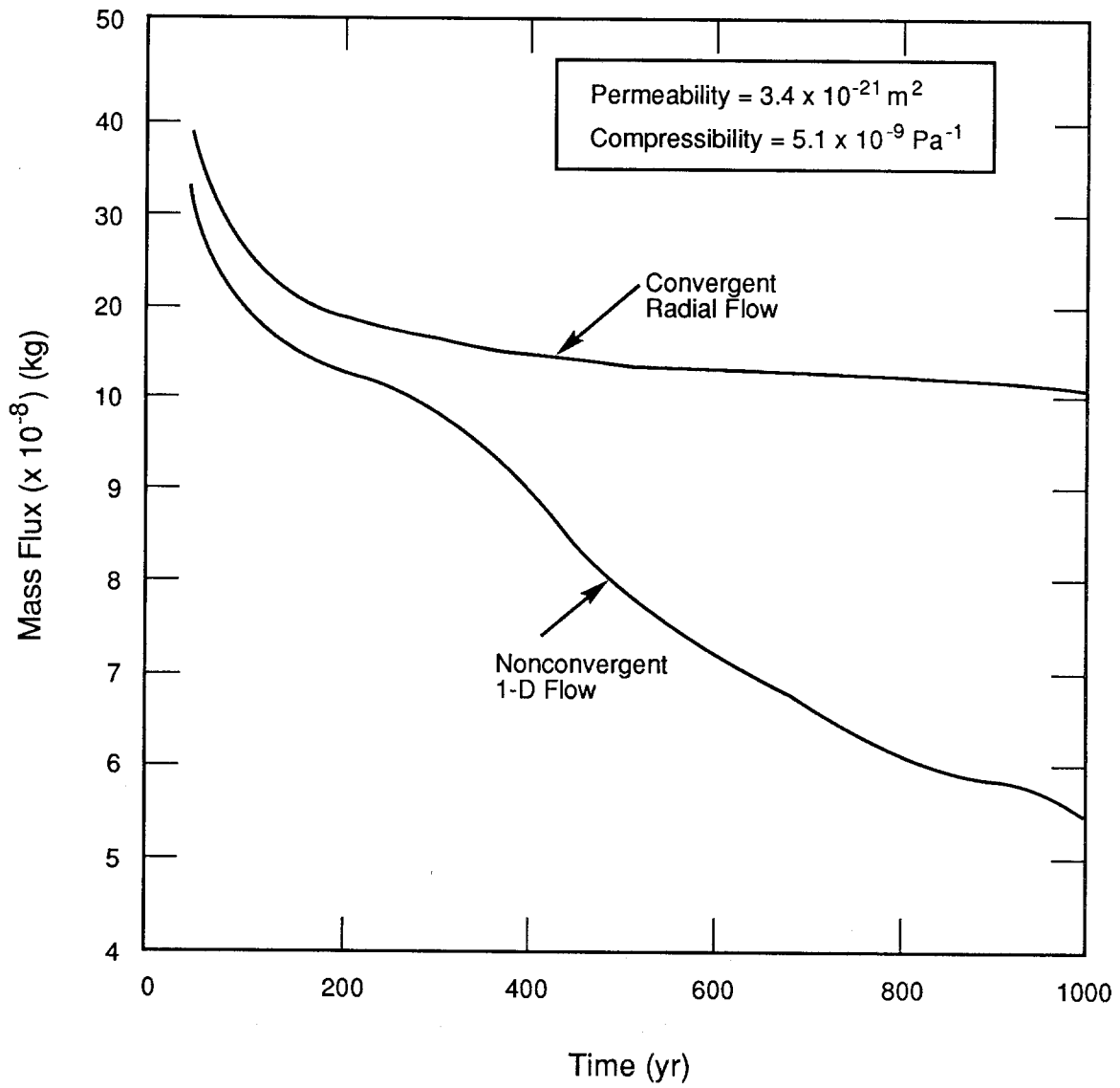


TRI-6334-254-0

Figure 4-30. Schematic Diagram of Salado Formation Pressure Development Due to Depressurization of Two Parallel Room Excavations.

Following the rapid depressurization of the waste, the room surface imposes a uniform fixed-pressure boundary on the Salado Formation. In the initial stage of drainage (e.g., t_1), the large size of the boundary surface in comparison to the depth depressurized in the Salado Formation will produce flow approximately normal to the surface of the excavated area. Continued brine inflow removes fluid from deeper within the Salado Formation, accessing areas peripheral to the sink (t_2). Flow then converges on the separate boundary elements, producing a higher flux density than created by nonconvergent (one-dimensional) flow. As the depressurization fronts of adjacent boundary surfaces begin to interfere (t_3), the influence of the separate drains on the far-field Salado Formation becomes similar to the influence of a single larger sink.

Figure 4-31 illustrates the effect of convergent vs. nonconvergent (one-dimensional) flow on infiltration rates. The figure shows drainage rates per unit length into an infinitely long fixed-pressure sink having a surface area per unit length of a typical WIPP excavation (room or drift). Salado Formation properties, and the initial and boundary pressures, are identical to those used for the higher compressibility SUTRA and HST3D calculations.



TRI-6334-262-0

Figure 4-31. Radial and One-Dimensional Estimates of Flow Rate per Unit Length of Room Excavation.

The time at which flow to a planar sink deviates significantly from one-dimensional flow, as a result of flow convergence, depends on the dimensions of the sink. As the distance from the sink increases beyond the characteristic dimension of the sink (e.g., 10 m [33 ft] in Figure 4-30), the sink begins to "look" like a discrete rather than infinite feature. Qualitatively, once drainage induces flow at points more distant than the characteristic dimension, the flow field becomes convergent. The average flux density through the sink then exceeds the density expected for strictly one-dimensional flow, and approaches the flux density for radial flow.

Brine inflow rates estimated with SUTRA for the higher compressibility show good agreement with rates estimated for a one-dimensional flow field having the same area (Figure 4-27). Pressure contours around the cylindrical panel likewise show predominantly one-dimensional flow across the surface of the panel after 10,000 yr of drainage (see Figure 4-4a). Brine inflow rates in this representation cannot increase above those expected for one-dimensional flow until extensive depressurization of the Salado Formation produces convergent flow on the scale of the cylinder, i.e., approximately 120 m (400 ft).

Unlike the cylindrical representation, the HST3D model of the panel includes room-scale (~10 m [~33 ft]) features of the panel. Because the time required to establish convergent flow depends on the characteristic dimensions of the sink, convergent flow, and the associated higher flux densities, develop much sooner in the HST3D model than in the SUTRA model, which can only develop convergence on the scale of the entire excavation area.

Note that while the SUTRA inflow rates agree closely with one-dimensional estimates, the relative deviation of the HST3D rate from the SUTRA rate after 1,000 yr agrees with the relative deviation of convergence from one-dimensional flow in Figure 4-31.

The discrepancy between the estimates of panel inflow rate for the SUTRA and HST3D simulations can therefore be explained by the more rapid onset of convergent flow in the HST3D model, which is in turn due to the more detailed representation of the panel geometry.

Because the pressure disturbance remains near the repository (especially for high capacitance), the estimates of brine inflow representing the panel as a series of tunnels (e.g., Lappin et al., 1989; Nowak et al., 1988) should be quite accurate. For example, at 1,000 yr and $c = 5.1 \times 10^{-9} \text{ Pa}^{-1}$, radial discharge (q) is $1.13 \times 10^{-7} \text{ kg/s/m}$ (Figure 4-31). The total equivalent panel length equals 1,200 m (4,000 ft), hence the panel brine inflow (q_{panel}) is $1.36 \times 10^{-4} \text{ kg/s}$. The discharge as calculated by HST3D is $1.37 \times 10^{-4} \text{ kg/s}$ (Figure 4-29).

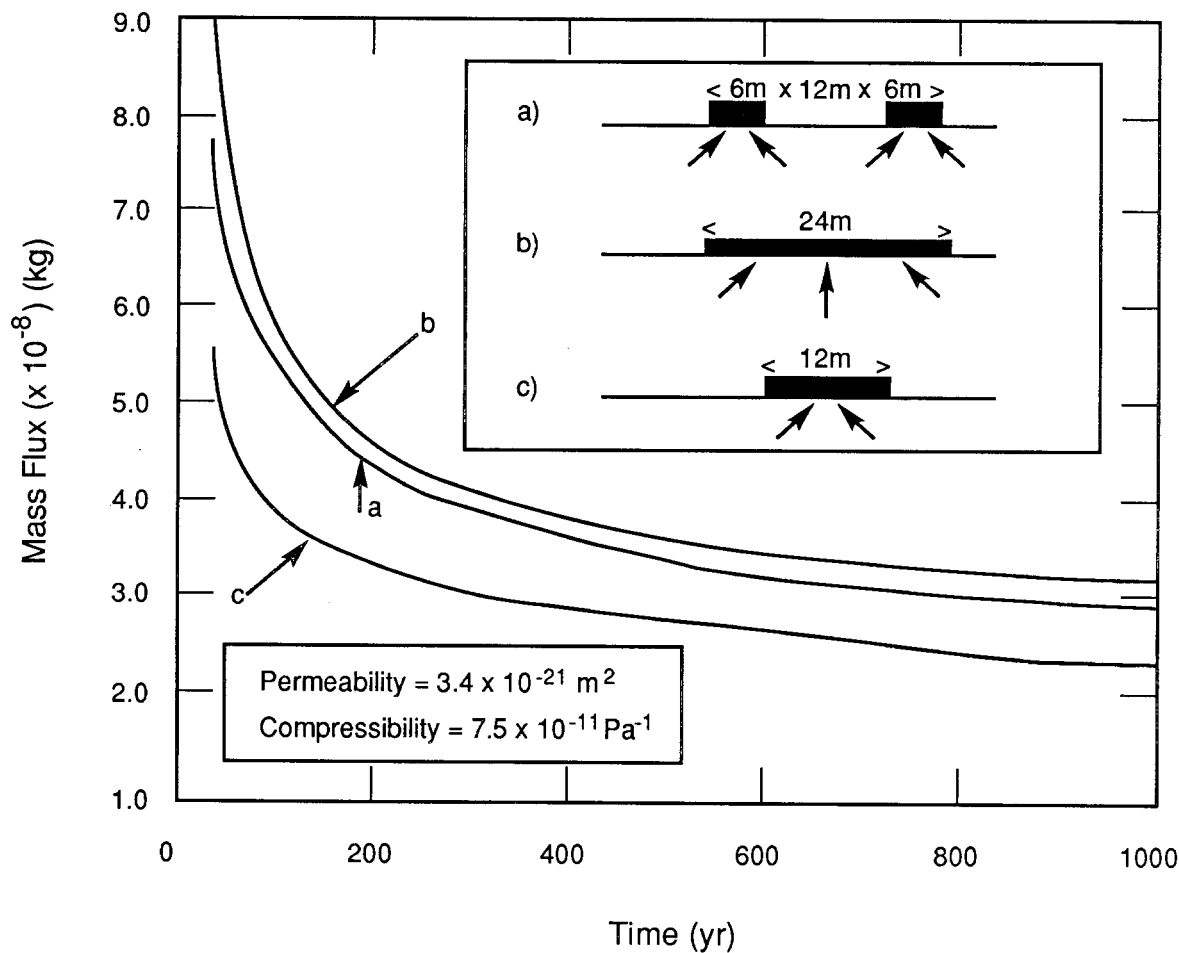
Clearly an accurate representation of the panel boundary surface (or tunnel approximation) is essential for accurately estimating brine inflow rates, at least as long as the Salado Formation flow field is confined within the characteristic dimension of the panel. As the flow field extends beyond the characteristic panel dimension, we can expect that the influence of the separate rooms will overlap (e.g., t_3 in Figure 4-30), and that a simplified equivalent representation of the panel is possible.

Equivalent Panel Dimension at Large Times. Figure 4-32 shows the total infiltration rate to three generic boundary configurations. The lower value of compressibility used in the SUTRA and HST3D calculations was adopted to create more rapid depressurization at large distances.

Boundary configuration "a" is analogous to two parallel drifts of rooms, and consists of two 6-m (20 ft) fixed-pressure boundary segments 12 m (40 ft) apart. Boundary configurations "b" and "c" are potential approximations of "a."

Flow through boundary "a" is clearly better approximated by boundary "b" than boundary "c," implying that the most appropriate approximation for a WIPP panel preserves the lateral area "covered" by the panel, rather than the total area of the individual drifts and rooms comprising the panel.

Because the equivalent volume cylinder in Section 4.1 preserves the lateral area of the excavation, rather than the larger area of the panel as a whole, it produces an underestimate of brine inflow even after the flow field has developed sufficiently to permit a simplification of the panel geometry.



TRI-6334-263-0

Figure 4-32. Two-Dimensional Flow Rates to Three Different Fixed-Pressure Boundaries.

5. SUMMARY AND CONCLUSIONS

This status report presents preliminary parameter sensitivity studies from the repository/shaft system. Some models described here are refined versions of the models reported in Marietta et al. (1989) and Lappin et al. (1989); others include rudimentary studies of an additional phenomenon, gas flow. The usual performance measure was gas or brine flow. The flow parameters varied were material permeability and capacitance, where capacitance is the specific storativity divided by fluid specific weight. Although the studies reported here are ongoing, and therefore incomplete, in general the refined models show that human intrusion into the repository (rather than any natural processes) will determine compliance or noncompliance of the WIPP with *40 CFR 191, Subpart B*. Hence,

- Major decisions about design of the repository, waste form, backfill, and other components will be determined by the conditions assumed within *40 CFR 191, Subpart B*, for a hypothetical and rather arbitrary human intrusion scenario.

The results and conclusions for both the undisturbed repository models and the human intrusion models are summarized below.

5.1 UNDISTURBED REPOSITORY MODELS

The two-dimensional models of an undisturbed repository substantiated the bounding results of earlier one-dimensional models (Marietta et al., 1989; Lappin et al., 1989) which showed that no contaminants leave the vicinity of the disposal area in 10,000 yr. The models that study gas flow fundamentally agree with this position; however, the models are still too rudimentary to permit conclusive statements. In short,

- The current specifications for the shaft, drift, and panel seals and the backfill probably exceed the requirements for undisturbed performance by orders of magnitude.
- The undisturbed scenario will not be analyzed further if future studies of gas effects and anhydrite layer permeability (described below) do not show greatly increased contaminant movement. (This same conclusion was reached in Marietta et al., 1989).

Future work should

- Collect data on and evaluate effects of far-field anhydrite-interbed (e.g., MB139) permeability and relative permeability (for gas flow).
- Continue evaluation of salt response to gas pressurization.

The results for each of the four models are summarized below.

TWO-DIMENSIONAL MODELING OF MIGRATION PATHWAY

The two-dimensional SUTRA model of the repository/shaft system assuming Darcy flow shows that over the 10,000-yr regulatory period, contaminated brine from the rooms generally moves from the disposal region and MB139 into the host salt in all directions, with only a very slight preference to travel up the access shaft, even when MB139 terminates at the shaft. Previous

one-dimensional calculations used the shaft as the preferred pathway to the near-surface environment, but this model demonstrates that although this assumption is conservative, it is not completely accurate.

A somewhat localized migration pathway does exist from the room into MB139, but, using expected properties, the contaminated brine does not reach the shaft within 10,000 yr. The greater porosity does not compensate sufficiently for the small disturbed area of MB139; hence, contaminants move directly into the host salt. Consequently, MB139 would not be a pathway to the lateral limits of the accessible environment, unless the hydrologic permeability is much higher than expected (either initially or through gas fracturing). The permeability threshold at which MB139 would become a horizontal pathway should be explored. This study would help evaluate the required accuracy of future permeability tests of the anhydrite interbeds.

The two-dimensional modeling also showed that the reference-design drift seals were effective without the shaft seal and thus were a redundant component of the engineered barrier. (The redundancy is possibly desirable.)

CYLINDRICAL MODELING OF SHAFT SATURATION

The sensitivity of brine flow into the Air Intake Shaft to Salado Formation permeability was evaluated using a cylindrical model to provide input for shaft seal design. In the model, the capacitance was set at an upper bounding value and the permeability varied.

Over the range of Salado Formation permeabilities explored (10^{-21} to 10^{-20} m² [10^{-6} to 10^{-5} mD]), estimates of cumulative inflow volume into the Air Intake Shaft over 200 yr varied from 200 to 1,000 m³ (7,000 to 35,000 ft³). The results bracket the estimated range of available shaft pore volume at the desired minimum relative backfill density of 95 percent. (No evidence exists that brine contents higher than desirable would prevent consolidation, especially because the shaft consolidates from the bottom to the top and therefore excess brine, if present, could migrate up the shaft into less consolidated, more permeable zones.)

The effect of preferential inflow through anhydrite interbeds was approximated by uniformly increasing horizontal permeability within the Salado Formation to 10^{-19} m² (10^{-4} mD). Little change in the cumulative flow into the Air Intake Shaft occurred. However, this result should be verified for transient conditions using a model that explicitly includes anhydrite interbeds with varying permeabilities.

CYLINDRICAL MODELING OF GAS MOVEMENT IN DRIFT WITH SUTRA

The two-dimensional SUTRA model of gas movement simulated the flow of hydrogen gas in the disposal area, panel seal, and drift backfill materials leading to a shaft. The intent of the model was to evaluate whether gas from the disposal area would reach the bottom of the shaft before consolidation of crushed salt in the shaft was complete.

Using permeability values of unconsolidated seals and backfill, the entire disposal area and drift were uniformly pressurized in less than 5 yr, as expected. Using permeability values for fully consolidated seals and backfill, the seal prevented gas flow, and the pressure at the base of the shaft did not change from the initial state even after about 1,600 yr. Additional calculations

assuming a time-dependent decrease in permeability for the disposal-area and drift-backfill materials showed that without the seal, the pressure at the base of the shaft increased to about 10 MPa after about 70 yr, but did not significantly increase beyond that level even to times as great as 1,600 yr. When calculations included the seal, shaft pressure rose to about 2.5 MPa after about 25 yr, but remained at that level until at least 1,600 yr.

Although more details (e.g., modeling the shaft) must be added to this rudimentary gas flow model before conclusive statements about gas movement can be made, these calculations suggest that the salt components of the seals and drift backfill would rapidly (relatively speaking) prevent gas movement along the drifts, even if unsaturated with brine.

ONE-DIMENSIONAL MODELING OF GAS AND BRINE MOVEMENT IN DRIFT AND MB139 WITH BOAST

A one-dimensional model of the drift using BOAST probed the flow of gas and brine when the seals and drifts were initially saturated with brine. Under conditions of complete brine saturation, generation of gas in the waste resulted in gas pressures exceeding lithostatic very rapidly (i.e., in less than 2 yr). This result was expected because of the overly simplified model. In the one-dimensional model, the gas could move only through the seals and drifts; with no free volume into which gas could expand, gas pressure increased very rapidly.

The above results prompted an examination of slightly more realistic conditions, still using the one-dimensional grid. Rather than modeling the drifts, MB139 was modeled as the predominant flow path, which allowed substantially greater gas flow to the shaft. MB139 and its seals were again assumed to be initially saturated with brine, but the waste was modeled as initially saturated with gas. (A gas pressure of 6.3 MPa was maintained at the access shaft to maximize the pressure gradient.)

For this model of MB139, hydrogen generated continuously over 600 yr reached the access shaft in about 3 yr for an MB139 permeability of 10^{-9} m² (10⁶ mD) and in about 300 yr for a permeability of 10^{-15} m² (1 mD). At high permeability (10^{-9} m² [10⁶ mD]), pressures throughout the grid were nearly uniform. When the marker bed was assigned a moderate permeability (10^{-15} m² [1 mD]), pressures in the waste exceeded lithostatic pressure (14.8 MPa) in less than 500 yr, but at later times, as gas saturation throughout MB139 increased, the pressure rapidly dropped.

In summary, if MB139 has only moderate permeabilities after closure, rather than the high permeabilities speculated for current conditions, the presence of brine in MB139 will prevent gas movement. Future work will focus on evaluating the distribution of gas, gas-saturated brine, and brine within and around the repository to establish initial conditions for the human intrusion model.

5.2 HUMAN INTRUSION MODELS

The Standard, *40 CFR 191, Subpart B*, requires that the repository must show compliance when a major part of the geologic barrier system is effectively removed from the disposal system as the result of intrusion into the repository by an exploratory borehole. (Human intrusion is not a part of the RCRA requirements for hazardous chemical wastes.) Consequently, the human

intrusion scenario requires a fairly detailed understanding of the behavior of (1) the waste, disposal rooms, drifts, and anhydrite and clay interbeds and (2) any remaining geologic barrier. This portion of the report focused on the behavior of the waste, disposal rooms, and the Salado Formation. (The detailed understanding of the transport properties of the remaining portion of the geologic barrier [i.e., Culebra Dolomite] will be reported elsewhere.)

In general, for the scenario in which one borehole passes through the disposal area and penetrates a brine pocket (E1),

- Modifications to the waste that are intended to decrease brine flow through the waste must reduce waste permeability to within four orders of magnitude of the Salado Formation.
- Preferential brine flow to a borehole through anhydrite layers could reduce brine flow through the waste by an order of magnitude. (Permeability data on anhydrite layers must be gathered.)
- Brine inflow from the Salado Formation (rather than flow from the brine pocket) has the greatest impact on how much waste is accessible to brine.
- Complete depressurization of a panel (filled with gas or brine) would not occur in the initial intrusion of the repository if the borehole was plugged "soon" (about one month). (However, this conclusion assumes that the waste compressibility evaluated from future tests, tentatively planned, would confirm the crudely approximated waste compressibility.)

Future modeling should focus on the following areas:

- Evaluating the effects of the possible range of permeability for an exploratory borehole over time considering salt creep.
- Evaluating the effects of radionuclide transport (not just brine flow) by incorporating solubility estimates within a room submodel.
- Evaluating the effects of transport characteristics of the Culebra Dolomite.
- Refining estimates of waste removal reported in Lappin et al. (1989) while drilling into the repository.
- Evaluating the consequences of more than one borehole hitting a panel.
- Continuing to evaluate the effects of interbed heterogeneity within the Salado Formation on brine inflow (also useful for undisturbed conditions).
- Evaluating the influence of dissolved gas within the brine surrounding the repository on discharge rates into the borehole.

The first modeling area is important because the brine inflow through the waste from the Salado Formation could be greatly affected by the borehole permeability -- a modeling component ignored in all of the human intrusion analyses described here -- and borehole permeability could greatly decrease over time because of salt creep.

The last two modeling areas necessitate the collection of more data, such as far-field permeability estimates of the anhydrite layers and relative permeabilities for gas and brine in both the Salado Formation and anhydrite layers. These data are also necessary for modeling undisturbed behavior of the repository. Data are also needed, as previously mentioned, on the compressibility of the waste.

Results from this report and future work will be incorporated into future performance assessments of the WIPP. However, separate from this consequence modeling is the need to develop decision-making procedures for estimating the scenario probability of the rare human intrusion event. (*40 CFR 191, Subpart B* limits the product of the scenario probability and its consequence with respect to a release limit, not just consequences.)

The results from the five models developed to explore the importance of various phenomena under the human intrusion scenario are summarized below.

CYLINDRICAL MODELING OF SALADO BRINE FLOW THROUGH PANEL TO BOREHOLE

Cylindrical modeling of Salado brine flow through panel to borehole is an axisymmetric simulation that evaluated the access fraction (i.e., the fractional volume of the saturated brine that drains into the borehole over 10,000 yr). Earlier analyses assumed that the radionuclide source is solubility limited until the radionuclide is depleted (Lappin et al., 1989). The time of depletion depends upon the volume of waste accessed. As a conservative assumption, those analyses assumed that an entire panel could be accessed. This study explored the validity of this conservative assumption. Determining realistic values for the calculations is important because if engineered modifications are needed, they should be designed using values that are realistic and not inflated.

The results from these axisymmetric models show that under steady-state conditions, mass flux to an exploratory borehole varies with permeability when the permeability of the waste is less than three orders of magnitude above the permeability of the Salado Formation. Under transient conditions, mass flux varies when the permeability difference is less than four orders of magnitude. Similar to strictly radial flow, flow to the borehole varies linearly with the changes in pressure gradient, Δp . Clearly, if the sole purpose of engineered modifications is to reduce waste permeability, then they must reduce the permeability to within four orders of magnitude of the Salado Formation to reduce the amount of brine passing through the waste.

Varying the capacitance of the Salado Formation had a significant effect on the amount of brine inflow only at high permeabilities. Because of the large variation in fluxes at high permeabilities, the amount of waste accessed in these axisymmetric models varied greatly, also. At the estimated upper bound of capacitance ($5.1 \times 10^{-9} \text{ Pa}^{-1}$), essentially the entire panel is accessed using a cylindrical approximation of a panel. At the lower calculated bound of capacitance ($7.8 \times 10^{-12} \text{ Pa}^{-1}$), a maximum of 54 percent of the panel is accessed.

CYLINDRICAL MODELING OF EFFECTS OF ANHYDRITE LAYERS ON BRINE FLOW THROUGH PANEL

Although the Salado Formation is frequently treated as hydrologically homogeneous, it is composed of interbedded halite, polyhalite, clay, and anhydrite layers. If the permeabilities of the anhydrite beds are significantly higher than the permeability of the Salado Formation halite, the anhydrite layers will create preferential paths for horizontal flow. During drainage to an intrusion borehole, the effect of preferential flow through the anhydrites may be either (1) to intercept flow that would otherwise pass through the repository, or (2) to augment the amount of brine flowing into the repository.

The results of cylindrical modeling of anhydrite layers show that if the permeability of the fractured anhydrites directly above and below a panel is lower than waste permeability, flow entering the repository region from the far field through the anhydrites is diverted through the waste (Case 2). For this case, the flow through a panel is about two times larger than flow using a model with a homogeneous Salado Formation.

However, if the anhydrite permeabilities are larger than the waste permeability as expected because of fracturing, the majority of flow remains confined within the anhydrite, reducing the flow through the repository by more than an order of magnitude. This dramatic effect warrants further study if the anhydrite layers near the repository have permeabilities several orders of magnitude higher than the intact Salado Formation salt.

Over the range of permeabilities considered, the amount of brine inflow was insensitive to the permeability of the halite that separates the repository from the nearest anhydrite layer.

CYLINDRICAL MODELING OF CASTILE BRINE POCKET FLOW THROUGH A ROOM

Analytical and numerical approximations of the WIPP repository/shaft system were used to estimate the brine flow circulated through a room from a brine pocket as an indirect measure of the potential amount of waste that would be transported up an exploratory borehole following degradation of plugs in a human intrusion scenario.

The flow field in the repository, created by plug degradation and upward flow through the borehole, was considered to consist of three components: net flow from the repository resulting from depressurization; circulation of brine through the repository, induced by pressure gradients along the borehole; and brine inflow from the Salado Formation to the borehole through the repository. Depressurization of the room was estimated to expel 3 m^3 (106 ft^3) of room pore fluid. The volume of fluid circulated through the repository was estimated to be between 0.006 m^3 and $120,000 \text{ m}^3$ (0.2 ft^3 to $4,000,000 \text{ ft}^3$). The wide range results from uncertainty in borehole and repository permeability. From previous calculations reported herein, brine inflow from the Salado Formation was estimated to produce $0.11 \text{ m}^3/\text{yr}/\text{panel}$ ($3.9 \text{ ft}^3/\text{yr}/\text{panel}$) to the borehole.

Using expected parameter values suggests first that depressurization of a repository pressure pulse is not an important cause of contaminant transport to the borehole; second, that the total repository volume through which brine pocket fluid passes is approximately 120 m^3 ($4,000 \text{ ft}^3$), or less than 10 percent of the room volume; and finally, that brine pocket fluid and Salado Formation brine inflow independently introduce about $1,150 \text{ m}^3$ ($41,000 \text{ ft}^3$) of contaminated brine into the borehole over 10,000 yr.

Concerning the latter point, although brine inflow from the Salado Formation contributes a similar fluid volume, the greater volume of waste accessed is expected to result in a greater contaminated brine. Hence, brine inflow is the most important flow process within the repository for the human intrusion scenario, although the brine pocket pressure may affect flow in the Culebra Dolomite (Lappin et al., 1989). Therefore, evaluating the characteristics of the brine pocket is not as pressing in the immediate future as a detailed modeling of the repository system. (Shaft and drift permeabilities are of minor importance for human intrusion.)

CHARACTERISTIC FLOW TIMES FOR THE ROOM AND PANEL

The purpose of the SUTRA model of a room and panel was to estimate the characteristic time of gas and brine depressurization following penetration by an exploratory borehole. Here, the characteristic time was estimated to be the time for pressure to change at a boundary of interest by a factor of $(1-e^{-1}) \Delta p_{\max}$, where Δp_{\max} is the maximum possible pressure change. Consequently, the characteristic time varies inversely with waste permeability. Note that the characteristic time is not the time for complete depressurization.

For an expected waste permeability of 10^{-15} m^2 (1 mD), the expected characteristic time for depressurization of gas is 10^5 s (1.3 days) for a room, or $2 \times 10^6 \text{ s}$ (~23 days) for a panel. The characteristic time for brine depressurization is $8.3 \times 10^5 \text{ s}$ (9.6 days) for a room, or $1.5 \times 10^7 \text{ s}$ (0.5 yr) for a panel. This latter brine characteristic time is about 7.5 times larger than that for gas depressurization.

In all cases, the characteristic times are short with respect to geologic time, but do bracket the one month in which an intruder might "soon" detect the repository. The times indicate that complete depressurization of a panel filled with gas or brine would not occur during the initial intrusion.

Characteristic times for all simulations lie between the analytical estimates using bounding gas compressibilities. This result suggests that an analytical solution of the linearized gas flow equation may be a useful screening tool in other applications.

TWO- AND THREE-DIMENSIONAL MODELING OF SALADO BRINE FLOW THROUGH QUARTER PANEL

The purpose of the two- and three-dimensional models described here was to examine the influence of panel shape on the access fraction.

According to the two-dimensional SUTRA model, which uses boundary conditions derived from the cylindrical simulations described earlier ("Cylindrical Modeling of Salado Brine Flow through Panel to Borehole"), the maximum volume of waste accessed, assuming the maximum waste permeability of 10^{-13} m^2 (10^2 mD) and Salado Formation capacitance of 7.8×10^{-12} , was about 23 percent (about a factor of 2.3 less than when panel shape was ignored). The percentage of panel accessed increases to about 35 percent for a capacitance of 7.54×10^{-11} and 95 percent for a capacitance of 5.1×10^{-9} . At a permeability of 10^{-19} m^2 (10^{-4} mD), varying capacitance had little effect. The access fraction was about 6 percent for all cases.

These limits on maximum accessible waste will be used to adjust the initial waste inventory available for transport in simple repository models used in the overall compliance assessment (i.e., Marietta et al., 1989) after corrections have been made for the errors discussed below.

The three-dimensional HST3D model of the waste panel showed that the brine inflow rates from the Salado Formation in the waste were markedly higher (but by less than a factor of 3) than corresponding estimates made with the cylindrical models used above ("Cylindrical Modeling of Salado Brine Flow Through Panel to Borehole"). The discrepancy was caused by (1) the smaller mass flux of nonconvergent flow in the cylindrical model versus the larger mass flux of convergent flow in the more accurate HST3D model and (2) equating the volume of the disk in the cylindrical model to the excavated volume rather than the total enclosed volume (excavated volume plus salt pillars).

Although the underestimation of brine inflow by the cylindrical models is important for discussing the absolute values of brine inflow, the underestimate will not affect the sensitivity of the brine inflow to varying model parameters summarized above. Furthermore, the cylindrical models ignored waste panel shape, which overestimated access fraction by about 2.3 times and thereby compensates somewhat for the underestimated brine inflow.

As shown by the three-dimensional modeling, the pressure disturbances remain near the repository over 10,000 yr (especially for large Salado Formation salt capacitance); consequently, representing the panel as a series of tunnels (e.g., Lappin et al., 1989) is quite accurate and will be used in future studies.

GLOSSARY

- Access Fraction** - The amount of contaminants transported from a repository region compared to the region's total inventory. In this report, it was bounded by evaluating the ratio of access volume to specified waste volume (usually waste panel volume).
- Access Volume** - The maximum volume of waste through which neutrally buoyant particles can pass (by means of being carried along with brine) within a given time period (usually 10,000 years).
- Accessible Environment** - The accessible environment means (1) the atmosphere, (2) land surfaces, (3) surface waters, (4) oceans, and (5) all of the lithosphere that is beyond the controlled area (40 CFR 191.12[k]).
- Advection** - The process of transport of an aqueous property by mass motion.
- Alpha Particle** - A positively charged particle emitted in the radioactive decay of certain nuclides. Made up of two protons and two neutrons bound together, it is identical to the nucleus of a helium atom. It is the least penetrating of the three common types of radiation -- alpha, beta, and gamma.
- Anhydrite** - A mineral consisting of anhydrous calcium sulfate (CaSO_4). It is gypsum without water, and is denser, harder, and less soluble.
- Anisotropic** - Variation in a property (e.g., hydraulic conductivity) with direction.
- Anoxic** - Without oxygen.
- Aperture** - The open space along a fracture in rock.
- Argillaceous** - Pertaining to, largely composed of, or containing clay-sized particles or clay minerals.
- Argillaceous Rocks** - Rocks containing appreciable amounts of clay.
- Backfill** - Material placed around the waste containers, filling the open space in the room.
- Bell Canyon Formation** - A sequence of rock strata that form the topmost formation of the Delaware Mountain Group.
- Bentonite** - A commercial term applied to clay materials containing montmorillonite (smectite) as the essential mineral.
- Borehole** - (1) A manmade hole in the wall, floor, or ceiling of a subsurface room used for verifying the geology, observation, or the emplacement of waste canisters. The horizontal wall holes are used for remote-handled (RH-TRU) waste. (2) A hole drilled from the surface for purposes of geologic or hydrologic testing, or to explore for resources; sometimes referred to as a borehole.
- Brine Pocket** - Pressurized brine of unknown origin but of limited extent contained in fractured anhydrite within the Castile Formation (also frequently referred to as a brine reservoir). Although a portion of the WIPP waste panels are assumed to have brine pockets beneath them, the pockets are only of concern for human intrusion scenarios where exploratory boreholes penetrate a waste panel and then continue down 210 m (700 ft) to the Castile Formation (Lappin et al., 1989).
- CAM** - Compliance Assessment Methodology

CAMCON - Compliance Assessment Methodology CONTroller; controller (driver) for compliance evaluations developed for the WIPP.

CAMDAT - Compliance Assessment Methodology DATA base; computational data base developed for the WIPP.

Capacitance - The combined compressibility of the solid porous matrix and the fluid within the pores.

Castile Formation - A formation of evaporite rocks (interbedded halite and anhydrite) of Permian age that immediately underlies the Salado Formation (in which the WIPP disposal level is being built).

CH-TRU Waste - Contact-Handled TRansUranic waste, packaged TRU waste whose external surface dose rate does not exceed 200 mrem per hour.

Compaction - Mechanical process by which the pore space in the waste is reduced prior to waste emplacement.

Complementary Cumulative Distribution Function (CCDF) - One minus the cumulative distribution function.

Compliance Evaluation or Assessment - The process of assessing the regulatory compliance of a geologic waste repository.

Compressibility - The property of a substance capable of being reduced in volume by application of pressure; quantitatively, the reciprocal of the bulk modulus.

Computational Model - The computer model plus the appropriate values for the parameters.

Computer Model - The appropriately coded analytical, quasi-analytical, or numerical solution technique used to solve the mathematical model using a computer.

Conceptual Model - The set of hypotheses and data that postulate the description and behavior of the disposal system (e.g., structural geometry, material properties, and all significant physical processes that affect behavior) (Silling, 1983). For WIPP, the data pertinent for a conceptual model are stored in the secondary data base. Several secondary data bases exist since each scenario may have a slightly different conceptual model.

Consequence Module - A module of the Compliance Assessment Methodology (CAM) that assesses the consequences of radionuclides being transported from the repository.

Controlled Area - The controlled area means (1) a surface location, to be identified by passive institutional controls, that encompasses no more than 100 km and extends horizontally no more than 5 km in any direction from the outer boundary of the original location of the radioactive wastes in a disposal system; and (2) the subsurface underlying such a surface location (*40 CFR 191.12[g]*).

Creep - A usually very slow deformation of solid rock resulting from constant stress; refers to the geologic phenomenon experienced as the gradual flow of salt under high compressive loading.

Creep Closure - Closure of underground openings, especially openings in salt, by plastic flow of the surrounding rock under pressure.

Culebra Dolomite Member - The lower of two layers of dolomite within the Rustler Formation that are locally water bearing.

- Cumulative Distribution Function** - The sum (integral) of the probability density of frequency values that are less than or equal to a specified value.
- Darcy** - An English standard unit of permeability, defined by a medium for which a flow of $1 \text{ cm}^3/\text{s}$ is obtained through a section of 1 cm^2 , for a fluid viscosity of 1 cP and a pressure gradient of 1 atm/cm . (One Darcy is equal to $0.987 \times 10^{-12} \text{ m}^2$).
- Delaware Basin** - The part of the Permian Basin in southeastern New Mexico and adjacent parts of Texas where a sea deposited large thicknesses of evaporites some 200 million years ago. It is partially surrounded by the Capitan Reef.
- Deterministic** - Pertaining to an exact mathematical relationship between the dependent and independent variables in a system.
- Dewey Lake Red Beds** - A formation that overlies the Rustler Formation and is composed of reddish brown marine mudstones and siltstones interbedded with finegrained sandstone.
- Diffusive** - Characterized by the transfer of chemical components from a region of higher to one of lower concentration.
- Disposal** - Emplacement of waste in a manner that assures isolation from the biosphere with no intent of retrieval and that requires deliberate action to regain access to the waste.
- Disposal System** - Any combination of engineered and natural barriers that isolate spent nuclear fuel or radioactive waste after disposal (*40 CFR 191.12(a)*). The natural barriers extend to the accessible environment.
- DOE** - The U.S. Department Of Energy, established in 1978 as a successor to ERDA and the AEC.
- Drift** - A horizontal passageway in a mine.
- E1** - An event or scenario: intrusion of a borehole through a disposal panel into a pressurized brine occurrence in the Castile Formation (Guzowski, 1990).
- E2** - An event or scenario: intrusion of a borehole into a disposal panel (Guzowski, 1990).
- EPA** - Environmental Protection Agency of the U.S. Government.
- Evaporite** - A sedimentary rock composed primarily of minerals produced by precipitation from a solution that has become concentrated by the evaporation of a solvent, especially salts deposited from a restricted or enclosed body of seawater or from the water of a salt lake. In addition to halite (NaCl) these salts include potassium, calcium, and magnesium chlorides and sulfates.
- Flowpath** - The path traveled by a neutrally buoyant particle released into a groundwater flow field.
- Half-life** - The time required for the activity of a group of identical radioactive nuclei to decay to half its initial value.
- Interbedded** - Pertaining to sedimentary beds lying between or alternating with other beds with different characteristics.
- Isotope** - A species of atom characterized by the number of protons and the number of neutrons in its nucleus. In most instances an element can exist as any of several isotopes, differing in the number of neutrons, but not the number of protons, in their nuclei. Isotopes can be either stable isotopes or radioactive isotopes (also called radioisotopes or radionuclides).

Isotropic - Hydraulic conductivities of a porous media independent of direction of measurement.

Latin Hypercube Sampling - A Monte Carlo sampling technique that divides the distribution into intervals of equal probability and samples from each interval.

Lithostatic Pressure - Subsurface pressure caused by the weight of overlying rock or soil, ~14.9 MPa at the WIPP repository level.

Material - Substance (e.g., rock type) out of which a numerical model is constructed.

Material Attribute - Material characteristic that varies at each element of a numerical mesh.

Material Property - Characteristic of the material that remains constant throughout the numerical mesh.

Mathematical Model - The mathematical representation of a conceptual model (Silling, 1983) (e.g., the coupled algebraic, differential, or integral equations with proper boundary conditions that approximate the physical processes in a specified domain of the conceptual model).

MB139 - Marker Bed 139: One of 45 siliceous or sulfatic units within the Salado Formation consisting of about 1 m of polyhalitic anhydrite and anhydrite. MB139 is located within the WIPP horizon.

Modular - Constructed with standardized units or dimensions for flexibility and variety in use.

Module - A standardized unit or packaged functional computer code assembly.

Monte Carlo Sampling - A random sampling technique using computer simulation to obtain approximate solutions to mathematical or physical problems, especially in terms of a range of values each of which has a calculated probability of being the solution.

Neutron - An elementary particle that has approximately the same mass as the proton but lacks electric charge, and is a constituent of all nuclei having mass number greater than 1.

Panel - A group of several underground rooms bounded by two pillars and connected by drifts. Within the WIPP, a panel usually consists of seven rooms connected by 10-m-wide drifts at each end.

Performance Assessment - The process of assessing the compliance of a deep, geologic, waste repository with the Containment Requirements of *40 CFR 191*, Subpart B. Performance assessment is defined by *Subpart B* as an analysis that (1) identifies the processes and events that might affect the disposal system, (2) examines the effects of these processes and events on the performance of the disposal system, and (3) estimates the cumulative releases of radionuclides, considering the associated uncertainties, caused by all significant processes and events. These estimates are incorporated into an overall probability distribution of cumulative release to the extent practicable (*40 CFR 191.12(q)*).

Permeability - A measurement of the ability of a rock or soil to transmit fluid under hydraulic gradient.

Permian Basin - A region in the south-central United States, where during Permian times (248 to 286 million years ago), there were many shallow sub-basins in which vast beds of marine evaporites were deposited.

- Polyhalite** - An evaporite mineral: $K_2MgCa_2(SO_4)_4 \cdot 2H_2O$; a hard, poorly soluble mineral.
- Potash** - Specifically K_2CO_3 . Also loosely used for many potassium compounds, especially as used in agriculture or industry.
- Quality Assurance** - All those planned and systematic actions necessary to provide adequate confidence that a structure, system, or component will perform satisfactorily in service.
- Radioactive Waste** - Solid, liquid, or gaseous material of negligible economic value that contains radionuclides in excess of threshold quantities.
- RH-TRU Waste** - Remote-Handled TRansUranic waste. Packaged TRU waste whose external surface dose rate exceeds 200 mrem per hour, but not greater than 1,000 rem per hour.
- Room** - An excavated cavity underground. Within the WIPP, a room is 10 m wide, 4 m high, and 91 m long.
- Rustler Formation** - A sequence of upper Permian age elastic and evaporite sedimentary rocks that contains two dolomite marker beds, and overlies the Salado Formation.
- Scenario** - A combination of events and processes that represents a possible future condition of the repository, geologic, and groundwater systems that could contribute to the escape of radionuclides from the repository, and release into the accessible environment.
- Sealing** - Formation of barriers within man-made penetrations (shafts, boreholes, tunnels, drifts).
- Shaft** - A manmade hole, either vertical or steeply inclined, that connects the surface with the underground workings of a mine.
- Solute** - The material dissolved in a solvent.
- Source term** - The kinds and amounts of radionuclides that make up the source of a potential release of radioactivity. For the performance assessment, the source term is defined as the sum of the quantities of the important radionuclides in the WIPP inventory that will be mobilized for possible transport to the accessible environment, and the rates at which these radionuclides will be mobilized.
- Stochastic Process** - Involving a random variable or random vector synonymous with random function or random process.
- Storativity** - The volume of water released by an aquifer per unit surface area per unit drop in hydrologic head.
- Tortuosity** - Measurement of actual path of flow through a porous medium.
- Translator** - A code that translates output from one code to input for another code. Also referred to as pre- and post-processors.
- Transmissivity** - The rate at which water of the prevailing kinematic viscosity is transmitted through a unit width of the aquifer under a unit hydraulic gradient.
- Transuranic Radioactive Waste (TRU Waste)** - Waste that, without regard to source or form, is contaminated with more than 100 nCi of alpha-emitting transuranic isotopes with half-lives greater than 20 yr, per gram of waste, except for: (1) HLW; (2) wastes that the DOE has determined, with the concurrence of the EPA Administrator, do not need the degree of isolation required by *40 CFR 191*; or (3) wastes that the NRC Commission has approved for disposal on a case-by-case basis in accordance with *10 CFR 61*. Heads of DOE field organizations can determine that other alpha-contaminated wastes, peculiar to a specific site, must be managed as TRU waste.

Undisturbed Performance - Undisturbed performance means the predicted behavior of a disposal system, including consideration of the uncertainties in predicted behavior, if the disposal system is not disrupted by human intrusion or the occurrence of unlikely natural events (*40 CFR 191.12(p)*).

APPENDIX A
MATERIAL PROPERTY VALUES

APPENDIX A

MATERIAL PROPERTY VALUES

The tables in this appendix contain the material properties that are used in the calculations described in this report. Any exceptions to these values are specifically noted in the descriptions of the simulations (Chapters 3 and 4). The sources of the data are noted in the tables. The primary source of information is the deterministic disposal system analysis by Lappin et al. (1989). However, an important addition to the data is an expanded range for the capacitance (i.e., specific storativity divided by specific weight) for the Salado Formation, which is three orders of magnitude larger than the expected value of Lappin et al. (1989) (McTigue, 1989). A significant revision might occur in this capacitance value, but it currently provides an upper bound. Also included are data for two-phase properties to account for waste-generated gas. These later parameter values are rough estimates, and significant revisions are expected in the future.

TABLE A-1. PARAMETER VALUES FOR SALADO FORMATION

Parameter	Expected Value	Range		Units	Source
Capacitance (c)	7.54×10^{-11}	7.8×10^{-12}	5.1×10^{-9}	Pa ⁻¹	McTigue, 1989; Lappin et al., 1989, p. A-87
Density					
Average (ρ_b)	2.30×10^3			kg/m ³	Krieg, 1984, Table 4
Intact salt (ρ_b)	2.14×10^3			kg/m ³	Holcomb and Shields, 1987, p. 17
Dispersivity					
Longitudinal (α_L)	1.52×10^1			m	Lappin et al., 1989, Table D-2
Pressure at repository level (657 m) (p)					
Lithostatic	1.49×10^1	1.43×10^1	1.79×10^1	MPa	Wawersik and Stone, 1985
Hydrostatic					
Brine	7.7			MPa	$\rho_{\text{brine}} \cdot g \cdot d$
Water	6.4			MPa	$\rho_{\text{water}} \cdot g \cdot d$
Permeability (k)	3.4×10^{-21}	1×10^{-23}	1×10^{-18}	m ²	Lappin et al., 1989, Table 3-2, Fig. 4-1, p. 4-43
Porosity (ϕ)		1×10^{-3}	1×10^{-2}		Lappin et al., 1989, p. 4-45; Black et al., 1983

TABLE A-2. PARAMETER VALUES FOR MARKER BED 139

Parameter	Expected Value	Range		Units	Source
Density, rock (ρ)	(See Table A-9, anhydrite.)				
Condition, disturbed					
Permeability (k)	3.3×10^{-7}			m^2	Lappin et al., 1989, Table D-2
Porosity (ϕ)	1.0				Lappin et al., 1989, Table D-2
Fracture	1×10^{-1}				Lappin et al., 1989, p. 4-62
Condition, undisturbed					
Permeability (k)	1×10^{-19}	1×10^{-20}	1×10^{-18}	m^2	DOE, 1989, §1.2
Thickness	9.0×10^{-1}	6.5×10^{-1}	1.05	m	Borns, 1985, Fig. 3

TABLE A-3. PARAMETER VALUES FOR CULEBRA DOLOMITE MEMBER OF RUSTLER FORMATION

Parameter	Expected Value	Range		Units	Source
Density, grain (ρ_g)	2.82x10 ³	2.78x10 ³	2.86x10 ³	kg/m ³	Lappin et al., 1989, Table E-6
Depth, average (z)	2.24x10 ²			m	See Table A-13.
Dispersivity (α)					
Longitudinal (α_L)	1x10 ²	5x10 ¹	3x10 ²	m	Lappin et al., 1989, Table E-6
Transverse (α_T)	0.05 • α_L				Haug et al., 1987, p. 3-21
Fracture spacing	2.0	2.5x10 ⁻¹	7.0	m	Lappin et al., 1989, Table 1-2, Table E-6
Hydraulic conductivity (K)					
path to WIPP boundary	7.81x10 ⁻⁷	1.77x10 ⁻⁷	1.20x10 ⁻⁵	m/s	
path to 5-km boundary	1.38x10 ⁻⁶	1.77x10 ⁻⁷	1.20x10 ⁻⁵	m/s	
Partition Coefficients Matrix (K_d)					
Am, Cm	2x10 ⁻¹			m ³ /kg	Lappin et al., 1989, Table E-10
Np, U	1x10 ⁻³			m ³ /kg	Lappin et al., 1989, Table E-10
Pb, Ra	1x10 ⁻³			m ³ /kg	Lappin et al., 1989, Table E-10
Pu	1x10 ⁻¹			m ³ /kg	Lappin et al., 1989, Table E-10
Th	1x10 ⁻¹			m ³ /kg	Lappin et al., 1989, Table E-10
Clays (K_d)					
Am, Cm	5x10 ⁻¹			m ³ /kg	Lappin et al., 1989, Table E-11
Np, U	1x10 ⁻²			m ³ /kg	Lappin et al., 1989, Table E-11
Pb, Ra	1x10 ⁻¹			m ³ /kg	Lappin et al., 1989, Table E-11
Pu	3x10 ⁻¹			m ³ /kg	Lappin et al., 1989, Table E-11
Th	3x10 ⁻¹			m ³ /kg	Lappin et al., 1989, Table E-11
Fractures (K_a)					
Am, Cm	1x10 ⁻²			m ³ /m ²	Lappin et al., 1989, Table E-12
Np, U	2x10 ⁻⁴			m ³ /m ²	Lappin et al., 1989, Table E-12
Pb, Ra	2x10 ⁻³			m ³ /m ²	Lappin et al., 1989, Table E-12
Ru	6x10 ⁻³			m ³ /m ²	Lappin et al., 1989, Table E-12
Th	6x10 ⁻³			m ³ /m ²	Lappin et al., 1989, Table E-12
Permeability (pathway)		5x10 ⁻¹⁵	3x10 ⁻¹³	m ²	Lappin et al., 1989, Table 1-2
Porosity (ϕ)					
Matrix (ϕ_m)	1.6x10 ⁻¹	7x10 ⁻²	3x10 ⁻¹		Lappin et al., 1989, Table E-6
Fracture (ϕ_f)	1.5x10 ⁻³	1.5x10 ⁻⁴	1.5x10 ⁻²		Lappin et al., 1989, Table 1-2, Table E-6
Storativity (S_s)		4.6x10 ⁻⁶	9.4x10 ⁻⁴		LaVenue et al., 1988, Table 3-3
Thickness (Δz)					
WIPP area	7.7	5.5	1.13x10 ¹	m	LaVenue et al., 1988, Table B-1
Tortuosity (τ)	1.4x10 ⁻¹	3x10 ⁻²	3.3x10 ⁻¹		Lappin et al., 1989, Table E-9

TABLE A-4. PARAMETER VALUES FOR CASTILE FORMATION BRINE POCKET

Parameter	Expected Value	Range		Units	Source
Compressibility (β)	1×10^{-5}	1×10^{-9}	1×10^{-4}	Pa^{-1}	Lappin et al., 1989, p. 3-145, Table 3-19
Density, rock (ρ)	(See Table A-8, anhydrite.)				
Depth (z)	9.24×10^2			m	Lappin et al., 1989, Fig. E-5
Permeability (k)					
Inner zone	1×10^{-11}	1×10^{-13}	1×10^{-9}	m^2	Lappin et al., 1989, Table 3-19
Middle zone	1×10^{-13}	1×10^{-15}	1×10^{-11}	m^2	Lappin et al., 1989, Table 3-19
Outer zone	1.4×10^{-19}			m^2	Lappin et al., 1989, Table 3-19
Porosity (ϕ)	5×10^{-3}	1×10^{-3}	1×10^{-2}		Lappin et al., 1989, Table 3-19
Pressure, initial (p_i)	1.27×10^1	7.0	1.74×10^1	MPa	Lappin et al., 1989, Table 3-19
Radius of					
Inner zone	3×10^2	1×10^2	9×10^2	m	Lappin et al., 1989, Table 3-19
Middle zone	2×10^3	3×10^1	8.6×10^3	m	Lappin et al., 1989, Table 3-19
Thickness (all)	7.0			m	Lappin et al., 1989, Table 3-19

TABLE A-5. RELATIVE PERMEABILITIES FOR TYPICAL SALT (Rough Estimates)

Saturation (S)	for water (k_{rw})	Saturation (S)	for gas (k_{rg})
0.275	0.0	0.0	0.0
0.2875	4.600×10^{-8}	0.035	0.0
0.30	8.525×10^{-7}	0.0425	2.554×10^{-6}
0.35	8.718×10^{-5}	0.05	2.032×10^{-5}
0.40	7.497×10^{-4}	0.10	1.593×10^{-3}
0.50	8.915×10^{-3}	0.20	2.408×10^{-2}
0.60	4.195×10^{-2}	0.30	9.154×10^{-2}
0.70	1.299×10^{-1}	0.40	2.177×10^{-1}
0.80	3.163×10^{-1}	0.50	4.059×10^{-1}
0.90	6.592×10^{-1}	0.60	6.485×10^{-1}
0.95	9.116×10^{-1}	0.65	7.850×10^{-1}
0.9575	9.550×10^{-1}	0.70	9.276×10^{-1}
0.965	1.000	0.7125	9.638×10^{-1}
		0.725	1.0000

TABLE A-6. PARAMETER VALUES FOR ENGINEERED MATERIALS

Parameter	Expected Value	Range		Units	Source
Crushed Salt					
Upper Shaft Seal					
Permeability (k)	1x10 ⁻¹²	1x10 ⁻¹⁴	1x10 ⁻¹⁰	m ²	Lappin et al., 1989, p. 4-67
Porosity (ϕ)	2x10 ⁻¹	1x10 ⁻¹	3x10 ⁻¹		Lappin et al., 1989, p. 4-67
Drift and Panel Backfill					
Density (ρ_b)					
Initial (0.6 ρ_{Salado})	1.35x10 ³	1.3x10 ³	1.4x10 ³	kg/m ³	Lappin et al., 1989, p. 4-58; Nowak et al., 1990.
Final	2.01x10 ³			kg/m ³	Holcomb and Shields, 1987, Fig. 4
Permeability (k)					
Initial	1x10 ⁻¹⁰			m ²	Holcomb and Shields, 1987, Fig. 4 extrapolated
Final	1x10 ⁻²⁰			m ²	Holcomb and Shields, 1987, Fig. 4
Porosity (ϕ)					
Initial	3.7x10 ⁻¹				Lappin et al., 1989, p. 4-58
Final	6.0x10 ⁻²				Holcomb and Shields, 1987, Fig. 4
Drift, Panel, and Consolidated Lower Shaft Seals					
Density (ρ_b)					
Initial (0.8 ρ_{Salado})	1.7x10 ³			kg/m ³	Holcomb and Shields, 1987, Fig. 4
Final	2.01x10 ³			kg/m ³	Holcomb and Shields, 1987, Fig. 4
Permeability (k)					
Initial (salt)	1x10 ⁻¹⁴			m ²	Holcomb and Shields, 1987, Fig. 4
Final (salt)	1.65x10 ⁻²⁰	3x10 ⁻²¹	4x10 ⁻¹⁹	m ²	Holcomb and Shields, 1987, Fig. 4; Nowak et al., 1990 Lappin et al., 1989, p. 4-60
Porosity (ϕ)					
Initial	2.0x10 ⁻¹				Holcomb and Shields, 1987, Fig. 4
Final	6.0x10 ⁻²	1x10 ⁻³	9x10 ⁻²		Holcomb and Shields, 1987, Fig. 4; Lappin et al., 1989, p. 4-64
Interbed Seals					
Permeability (k)	4x10 ⁻¹⁹	1x10 ⁻¹⁹	4x10 ⁻¹⁹	m ²	Lappin et al., 1989, p. 4-63
Porosity (ϕ)	3x10 ⁻²	2x10 ⁻²	4x10 ⁻²		Lappin et al., 1989, p. 4-63
Concrete					
Lower Shaft, Drift, Panels					
Unconfined					
compressive strength	3.1x10 ¹			MPa	Gulick and Wakeley, 1990.
Young's modulus (E)	2.1x10 ¹			GPa	Gulick and Wakeley, 1990.
Poisson's ratio (ν)	2.0x10 ⁻¹				Gulick and Wakeley, 1990.
Restrained expansion	9.0x10 ⁻²				Gulick and Wakeley, 1990.
Permeability (k)			2.7x10 ⁻¹⁹	m ²	Gulick and Wakeley, 1990.
Upper Shaft					
compressive strength	6.9x10 ¹			MPa	Gulick and Wakeley, 1990.
Young's modulus (E)	3.3x10 ¹			GPa	Gulick and Wakeley, 1990.
Poisson's ratio (ν)	1.7x10 ⁻¹				Gulick and Wakeley, 1990.
Restrained expansion	3.0x10 ⁻²				Gulick and Wakeley, 1990.
Permeability (k)			2.7x10 ⁻¹⁹	m ²	Gulick and Wakeley, 1990.
Wyoming Bentonite					
Hydraulic conductivity to brine (max) (K)			1.4x10 ⁻¹⁹	m ²	Nowak et al., 1990.

TABLE A-7. PARAMETER VALUES FOR UNMODIFIED AVERAGE WASTE

Parameter	Expected Value	Range		Units	Source
Compressibility (β_s)	1×10^{-9}			Pa ⁻¹	Author's opinion, based on Freeze and Cherry, 1979, Table 2.5.
Gas generation					
Rates					
Corrosion (H ₂)		0	1.7	mole/drum/yr	Lappin et al., 1989, p. 4-84
Microbiological		0	8.5×10^{-1}	mole/drum/yr	Lappin et al., 1989, p. 4-84
Potential					
Corrosion (H ₂)		0	8.9×10^2	mole/drum-eq	Lappin et al., 1989, p. 4-78
Microbiological		0	6.0×10^2	mole/drum-eq	Lappin et al., 1989, p. 4-78
Permeability (k)					
Initial	5×10^{-11}			m ²	Holcomb and Shields, 1987, Fig. 4, extrapolated
Final	1×10^{-15}	1×10^{-18}	1×10^{-13}	m ²	Lappin et al., 1989, Table 4-6
Porosity (ϕ)					
Initial	6.8×10^{-1}				Lappin et al., 1989, Fig. 4-8
Final	1.8×10^{-1}	1.5×10^{-1}	2.1×10^{-1}		Lappin et al., 1989, Table 4-6
Solubility (S)	1×10^{-6}	1×10^{-9}	1×10^{-3}	Molar	Lappin et al., 1989, p. 4-29

TABLE A-8. PARAMETER VALUES FOR SPECIFIC MATERIALS

Parameter	Expected Value	Range	Units	Source
Anhydrite @ 25 °C				
Density, grain (ρ_g)	2.963x10 ³		kg/m ³	Clark, 1966, p. 46;
Young's modulus (E)	7.51x10 ¹		GPa	Krieg, 1984, p. 14
Poisson's ratio (ν)	3.5x10 ⁻¹			Krieg, 1984, p. 16
Distribution Coefficients				
k_d				
Am, Cm	2.5x10 ⁻²		m ³ /kg	Lappin et al., 1989, Table D-5
Np, U	1x10 ⁻³		m ³ /kg	Lappin et al., 1989, Table D-5
Pb, Ra	1x10 ⁻³		m ³ /kg	Lappin et al., 1989, Table D-5
Pu, Th	1x10 ⁻¹		m ³ /kg	Lappin et al., 1989, Table D-5
k_a				
Am, Cm	9.2x10 ⁻¹		m ³ /m ²	Lappin et al., 1989, Table D-5
Np, U	3.7x10 ⁻²		m ³ /m ²	Lappin et al., 1989, Table D-5
Pb, Ra	3.7x10 ⁻²		m ³ /m ²	Lappin et al., 1989, Table D-5
Pu, Th	3.7		m ³ /m ²	Lappin et al., 1989, Table D-5
Clay				
Distribution Coefficients (k_d)				
Am, Cm	1x10 ⁻¹		m ³ /kg	Lappin et al., 1989, Table D-5
Np,	1x10 ⁻²		m ³ /kg	Lappin et al., 1989, Table D-5
Pb, Ra	1x10 ⁻³		m ³ /kg	Lappin et al., 1989, Table D-5
Pu, Th	1x10 ⁻¹		m ³ /kg	Lappin et al., 1989, Table D-5
U	1x10 ⁻³		m ³ /kg	Lappin et al., 1989, Table D-5
Halite @ 25 °C				
Density, grain (ρ_g)	2.163x10 ³		kg/m ³	Carmichael, 1984, Table 2;
Young's modulus (E)	3.1x10 ¹		GPa	Krieg, 1984, p. 14; Clark, 1966, p. 44
Poisson's ratio (ν)	2.5x10 ⁻¹			Krieg, 1984, p. 16
Polyhalite @ 25 °C				
Density, grain (ρ_g)	2.78x10 ³		kg/m ³	Shakoor and Hume, 1981
Young's modulus (E)	5.53x10 ¹		GPa	Krieg, 1984, p. 16
Poisson's ratio (ν)	3.6x10 ⁻¹			Krieg, 1984, p. 16
Molecular diffusion (D°)	1x10 ⁻¹⁰	5x10 ⁻¹¹ 2x10 ⁻⁹	m ² /s	Lappin et al., 1989, Table E-6;
Radionuclides				
²⁴¹Am				
Molecular Diffusion (D°)		5.3x10 ⁻¹¹ 3x10 ⁻¹⁰	m ² /s	Lappin et al., 1989, Table E-7
Solubility	1x10 ⁻⁶	1x10 ⁻⁹ 1x10 ⁻³		Lappin et al., 1989, p. 4-29, Table E-1
Activity-conversion	3.43x10 ⁻³		kg/Ci	
Half-Life ($t_{1/2}$)	4.32x10 ²		yr	ICRP, Pub 38, 1983
Inventory				
Initial	6.37x10 ⁵		Ci	Lappin et al., 1989, Table 4-2a
Modified	7.75x10 ⁵		Ci	Lappin et al., 1989, Table 4-2b
²⁴⁴Cm				
Molecular Diffusion (D°) (no data, use Am)		1x10 ⁻⁹ 1x10 ⁻³		Lappin et al., 1989, p. 4-29, Table E-1
Solubility	1x10 ⁻⁶			
Activity-conversion	8.09x10 ⁻⁴		kg/Ci	
Half-Life ($t_{1/2}$)	1.81x10 ¹		yr	ICRP, Pub 38, 1983
Inventory				
Initial	1.27x10 ⁴		Ci	Lappin et al., 1989, Table 4-2a
Modified	0.0		Ci	Lappin et al., 1989, Table 4-2b

TABLE A-8. PARAMETER VALUES FOR SPECIFIC MATERIALS (Continued)

Parameter	Expected Value	Range		Units	Source
²³⁷Np					
Molecular Diffusion (D°)		5.2x10 ⁻¹¹	3.10 ⁻¹⁰	m ² /s	Lappin et al., 1989, Table E-7
Solubility	1x10 ⁻⁶	1x10 ⁻⁹	1x10 ⁻³		Lappin et al., 1989, p. 4-29, Table E-1
Activity-conversion	7.05x10 ⁻⁷			kg/Ci	
Half-Life ($t_{1/2}$)	2.14x10 ⁶			yr	ICRP, Pub 38, 1983
Inventory					
Initial	8.02			Ci	Lappin et al., 1989, Table 4-2a
Modified	8.02			Ci	Lappin et al., 1989, Table 4-2b
Pu (element)					
Molecular Diffusion (D°)		4.8x10 ⁻¹¹	3x10 ⁻¹⁰	m ² /s	Lappin et al., 1989, Table E-7
Solubility	1x10 ⁻⁶	1x10 ⁻⁹	1x10 ⁻³		Lappin et al., p. 4-29, 1989, Table E-1
²³⁸Pu					
Activity-conversion	1.71x10 ⁻⁴			kg/Ci	
Half-Life ($t_{1/2}$)	8.77x10 ¹			yr	ICRP, Pub 38, 1983
Inventory					
Initial	3.90x10 ⁶			Ci	Lappin et al., 1989, Table 4-2a
Modified	3.90x10 ⁶			Ci	Lappin et al., 1989, Table 4-2b
²³⁹Pu					
Activity-conversion	6.22x10 ⁻⁵			kg/Ci	
Half-Life ($t_{1/2}$)	2.41x10 ⁴			yr	ICRP, Pub 38, 1983
Inventory					
Initial	4.25x10 ⁵			Ci	Lappin et al., 1989, Table 4-2a
Modified	4.25x10 ⁵			Ci	Lappin et al., 1989, Table 4-2b
²⁴⁰Pu					
Activity-conversion	2.28x10 ⁻⁴			kg/Ci	
Half-Life ($t_{1/2}$)	6.54x10 ³			yr	ICRP, Pub 38, 1983
Inventory					
Initial	1.05x10 ⁵			Ci	Lappin et al., 1989, Table 4-2a
Modified	1.05x10 ⁵			Ci	Lappin et al., 1989, Table 4-2b
²⁴¹Pu					
Activity-conversion	1.03x10 ⁻¹			kg/Ci	
Half-Life ($t_{1/2}$)	1.44x10 ¹			yr	ICRP, Pub 38, 1983
Inventory					
Initial	4.08x10 ⁶			Ci	Lappin et al., 1989, Table 4-2a
Modified	0.0			Ci	Lappin et al., 1989, Table 4-2b
Pb (element)					
Molecular Diffusion (D°)	4x10 ⁻¹⁰				
Solubility	1x10 ⁻⁶	1x10 ⁻⁹	1x10 ⁻³		Lappin et al., p. 4-29, 1989, Table E-1
²¹⁰Pb					
Activity-conversion	7.63x10 ⁻²			kg/Ci	
Half-Life ($t_{1/2}$)	2.23x10 ¹			yr	ICRP, Pub 38, 1983
Inventory					
Initial	0.0			Ci	Lappin et al., 1989, Table 4-2a
Modified	0.0			Ci	Lappin et al., 1989, Table 4-2b

TABLE A-8. PARAMETER VALUES FOR SPECIFIC MATERIALS (Concluded)

Parameter	Expected Value	Range		Units	Source
²²⁶Ra					
Molecular Diffusion (D°)	7.5×10^{-6}				
Solubility	1×10^{-6}	1×10^{-9}	1×10^{-3}		Lappin et al., 1989, p. 4-29, Table E-1
Activity-conversion	9.89×10^{-4}			kg/Ci	
Half-Life ($t_{1/2}$)	1.60×10^3			yr	ICRP, Pub 38, 1983
Inventories					
Initial	0.0				Lappin et al., 1989, Table 4-2a
Modified	0.0				Lappin et al., 1989, Table 4-2b
²³²Th					
Molecular Diffusion (D°)		5×10^{-11}	1.5×10^{-10}	m^2/s	Lappin et al., 1989, Table E-7
Solubility	1×10^{-6}	1×10^{-9}	1×10^{-3}		Lappin et al., 1989, p. 4-29, Table E-1
Activity-conversion	1.10×10^{10}			kg/Ci	
Half-Life ($t_{1/2}$)	1.41×10^{10}			yr	ICRP, Pub 38, 1983
Inventories					
Initial	2.74×10^{-1}			Ci	Lappin et al., 1989, Table 4-2a
Modified	0.0			Ci	Lappin et al., 1989, Table 4-2b
U (element)					
Molecular Diffusion (D°)		1.1×10^{-10}	4.3×10^{-10}	m^2/s	Lappin et al., 1989, Table E-7
Solubility	1×10^{-6}	1×10^{-9}	1×10^{-3}		Lappin et al., 1989, p. 4-29, Table E-1
²³³U					
Activity-conversion	9.68×10^{-6}			kg/Ci	
Half-Life ($t_{1/2}$)	1.59×10^5			yr	ICRP, Pub 38, 1983
Inventories					
Initial	7.72×10^3			Ci	Lappin et al., 1989, Table 4-2a
Modified	7.72×10^3			Ci	Lappin et al., 1989, Table 4-2b
²³⁵U					
Activity-conversion	2.16×10^{-9}			kg/Ci	
Half-Life ($t_{1/2}$)	7.40×10^8			yr	ICRP, Pub 38, 1983
Inventories					
Initial	3.7×10^{-1}			Ci	Lappin et al., 1989, Table 4-2a
Modified	3.7×10^{-1}			Ci	Lappin et al., 1989, Table 4-2b
²³⁸U					
Activity-conversion	3.36×10^{-10}			kg/Ci	
Half-Life ($t_{1/2}$)	4.47×10^9			yr	ICRP, Pub 38, 1983
Inventories					
Initial	1.47			Ci	Lappin et al., 1989, Table 4-2a
Modified	0.0			Ci	Lappin et al., 1989, Table 4-2b

TABLE A-9. FLUID PROPERTIES

Parameter	Expected Value	Range	Units	Source
Brine, Culebra				
Density (ρ_f)	1.092×10^3		kg/m ³	Marietta et al., 1989, Table 3-9
Diffusivity (D°)	2×10^{-9}		m ² /s	Haug et al., 1987, p. 3-22
Viscosity (μ)	1.0×10^{-3}		Pa-s	Haug et al., 1987, p. 3-20
Brine, Castile Reservoir				
Density (ρ_f)	1.24×10^3		kg/m ³	Lappin et al., 1989, Table 3-19
Brine, Salado, 1.013×10^5 Pa, @ 28 °C				
Density (ρ_f)	1.2×10^3		kg/m ³	Stein and Krumhansl, 1986
Compressibility (β_f)	2.7×10^{-10}		Pa ⁻¹	Kaufman, 1960, p. 609
Viscosity (μ)	1.6×10^{-3}		Pa-s	Kaufman, 1960, p. 622
Gas, 100% H ₂ , 1.013×10^5 Pa, @ 25 °C				
Viscosity (μ)		8.84×10^{-6} 9.8×10^{-6}	Pa-s	Buddenberg and Wilke, 1949; Streeter and Wylie, 1975, Fig. C-1
Water @ 25 °C				
Compressibility (β_f)	4.53×10^{-10}		Pa ⁻¹	Haug et al, 1987, p. 3-17
Density (ρ_f)	9.971×10^2		kg/m ³	Weast, 1974, p. F-11
Viscosity (μ)	8.90×10^{-4}		Pa-s	Weast, 1974, p. F-49

TABLE A-10. SALADO BRINE COMPRESSIBILITY (Rough Estimates)

Pressure (MPa)	Compressibility (β_f) (Pa ⁻¹ x 10 ⁻¹⁰)	Formation Volume Factor
0.1	2.70	1.00000
1.0932	2.70	0.99954
2.0	2.70	0.99912
5.0	2.69	0.99773
10.0	2.69	0.99541
20.0	2.68	0.99077
50.0	2.64	0.97685
100.0	2.57	0.95365

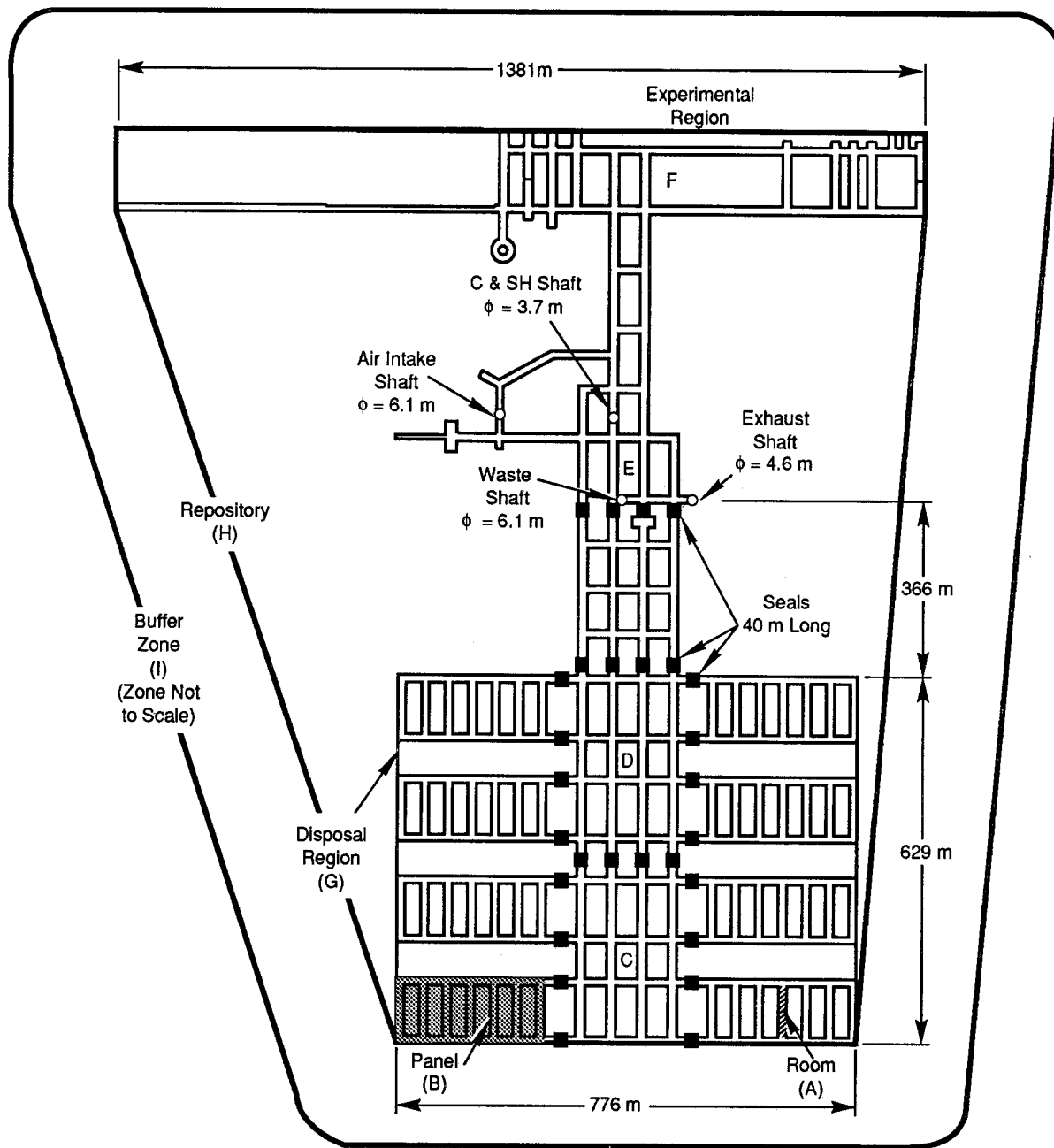
TABLE A-11. CLIMATE VARIABILITY AND INTRUSION CHARACTERISTICS

Parameter	Expected Value	Range		Units	Source
Climate Variability					
Glaciation, next	8×10^4	4×10^4	1.2×10^5	yr	Marietta et al., 1990
Peak precipitation	6×10^1	4.5×10^1	9.0×10^1	cm/yr	Marietta et al., 1990
Human Intrusion					
Borehole properties					
Compressibility (β_s)	1×10^{-8}	1×10^{-7}	1×10^{-9}	Pa ⁻¹	Freeze and Cherry, 1979, Table 2.5
Permeability, fill (k)	1×10^{-12}	1×10^{-13}	1×10^{-11}	m ²	Lappin et al., 1989, Table 1-2, Table C-1
Porosity (ϕ)	2×10^{-1}	1×10^{-1}	3×10^{-1}		Marietta et al., 1989, Table 3-10
Radius (r)	1.67×10^{-1}	8.89×10^{-2}	2.54×10^{-1}	m	Lappin et al., 1989, Table C-1; well logs
Time of intrusion t	3.15×10^{10}	3.15×10^9	3.15×10^{11}	s	Marietta et al., 1989, Table 3-10

TABLE A-12. SUMMARY OF EXCAVATED AND ENCLOSED AREAS AND INITIAL VOLUMES OF EXCAVATED REGIONS WITHIN THE WIPP REPOSITORY, NOT CONSIDERING CLOSURE (after Lappin et al., 1989)

Region*	Areas		Volume	
	Excavated (10 ³ m ²)	Enclosed (10 ³ m ²)	Excavated (10 ³ m ³)	Enclosed (10 ³ m ³)
Room (A)	0.9197	0.9197	3.644	3.644
One panel (B)	11.53	28.26	45.70	111.96
Southern equivalent panel (C)	8.413	35.44	33.34	140.4
Northern equivalent panel (D)	8.701	35.79	34.48	141.8
Access drifts (E)	21.84	283.6	78.07	1037.2
Experimental area (F)	21.61	298.1	71.90	1090
Total disposal area (G)	109.38	488.0	433.4	1934
Total repository (H)	152.83	1748	583.4	6926
Buffer zone (only) (I)	-	2667	-	1057
Land-withdrawal zone (less H and I)	-	37020	-	14670
Four shafts (only) to base of Rustler Fm.	0.08691	0.08691	34.76	34.76
DRZ in storage region	-	-	-	574.0

*Regions shown in Figure A-1; detailed dimensions of disposal region shown in Figure A-2.



TRI-6334-206-0

Figure A-1. Excavated and Enclosed Areas in the WIPP Repository (after Lappin et al., 1989).

TABLE A-13. DEPTHS OF STRATIGRAPHIC LAYERS AROUND WASTE, EXHAUST, AND C&SH SHAFTS
(after Nowak et al., 1990)

Layer	Average Depth (m)	Waste		Exhaust		C&SH	
		Depth (m)	Diameter (m)	Depth (m)	Diameter (m)	Depth (m)	Diameter (m)
Surface	0.0	0.0	N/A	0.0	N/A	0.0	N/A
Top of Magenta	182.1	182.0	7.0	183.8	5.0	180.4	3.6
Bottom of Magenta	190.4	189.0	7.0	191.1	5.0	191.1	3.6
Top of Culebra	216.3	214.9	7.0	217.6	5.0	216.4	3.6
Bottom of Culebra	223.7	221.6	7.0	224.3	5.0	225.2	3.6
Rustler/Salado contact	258.7	257.3	8.4	259.4	6.4	259.4	4.6
Top of Vaca Triste	411.6	411.2	6.1	412.7	4.6	410.9	3.6
Bottom of Vaca Triste	412.7	413.3	6.1	413.6	4.6	411.2	3.6
Top of station	653.8	654.4	7.0	654.4	4.6	652.6	3.6
Station	658.3	658.4	N/A	657.5	N/A	659.0	N/A
Top of sump	658.7	658.4	7.0	N/A	N/A	659.0	3.6
Bottom of sump	694.7	696.8	7.0	N/A	N/A	692.5	3.6

REFERENCES

- Arguello, J. G. and T. M. Torres, 1987. *WIPP Panel Entryway Seal -- Numerical Simulation of Seal Component/Formation Interaction for Preliminary Seal Design Evaluation*, SAND87-2591. Sandia National Laboratories, Albuquerque, NM.
- Beauheim, R. L. 1990 (in preparation). *Interpretation of Brine-Permeability Test of the Salado Formation at the Waste Isolation Pilot Plant (WIPP) Site: First Interim Report*, SAND90-0083. Sandia National Laboratories, Albuquerque, NM.
- Bertram-Howery, S. G. and R. L. Hunter, eds., 1989. *Preliminary Plan for Disposal-System Characterization and Long-Term Performance Evaluation of the Waste Isolation Pilot Plant*, SAND89-0178. Sandia National Laboratories, Albuquerque, NM.
- Bertram-Howery, S. G., M. G. Marietta, D. R. Anderson, K. F. Brinster, L. H. Brush, M. S. Y. Chu, L. S. Gomez, R. V. Guzowski, R. L. Hunter, R. P. Rechar, 1989. *Draft Forecast of the Final Report for the Comparison to 40 CFR 191, Subpart B for the Waste Isolation Pilot Plant*, SAND88-1452. Sandia National Laboratories, Albuquerque, NM.
- Black, S. R., R. S. Newton, and D. K. Shukla, eds., 1983. "Brine Content of the Facility Interval Strata" in *Results of the Site Validation Experiments*, Vol II, Supporting Document 10. Waste Isolation Pilot Plant, U.S. Department of Energy.
- Borns, D. J., 1985. *Marker Bed 139: A Study of Drillcore From a Systematic Array*, SAND85-0023. Sandia National Laboratories, Albuquerque, NM.
- Bredehoeft, J. D., "Will Salt Repositories be Dry?," in *EOS, Transactions of the American Geophysical Society*, Vol. 69, pp 121-4.
- Buddenberg, J. W., and C. R. Wilke, 1949. *Ind. Eng. Chem.* Vol. 41, pp. 1345-7.
- Butcher, B. M., 1990. *Preliminary Evaluation of Potential Engineered Modifications for the Waste Isolation Pilot Plant (WIPP)*, SAND89-3095. Sandia National Laboratories, Albuquerque, NM.
- Carmichael, R. S., ed., 1984. *CRC Handbook of Physical Properties of Rocks*, Vol III. CRC Press, Inc., Boca Raton, FL.
- Clark, S. P., 1966. *Handbook of Physical Constants*. The Geological Society of America, Inc., New York, NY.
- DOE (United States Department of Energy), 1986. *WIPP Design Validation Final Report*, DOE/WIPP-86-010. Bechtel National Inc., San Francisco, CA.
- DOE (United States Department of Energy), 1988. *Waste Isolation Pilot Plant Compliance Strategy for 40 CFR 191*, DOE/WIPP-86-013. Carlsbad, NM.
- DOE (United States Department of Energy), 1989. *Addendum to No-Migration Variance Petition for Waste Isolation Pilot Plant*, DOE/WIPP-89-003. U.S. Department of Energy, Carlsbad, NM, §2.1.
- DOE/NM (United States Department of Energy/State of New Mexico), 1984. U.S. Department of Energy and State of New Mexico, 1981, First Modification to the July 1, 1981 "Agreement for Consultation and Cooperation" on WIPP by the State of New Mexico and U.S. Department of Energy, November 30, 1984.

References

- Fanchi, J. R., J. E. Kennedy, and D. L. Dauben, 1987. *BOAST II: A Three-Dimensional Three-Phase Black Oil Applied Simulation Tool*, DOE/BC-88/2/SP (DE 88001205). U.S. Department of Energy.
- Freeze, R. A. and J. C. Cherry, 1979. *Groundwater*. Prentice-Hall, Inc., Englewood Cliffs, NJ, p. 55.
- Gilkey, A. P., 1988. *ALGEBRA - A Program That Algebraically Manipulates the Output of a Finite Element Analysis (EXODUS version)*, SAND88-1431. Sandia National Laboratories, Albuquerque, NM.
- Gilkey, A. P. and J. H. Glick, 1989. *BLOT - A Mesh and Curve Plot Program For the Output of a Finite Element Analysis*, SAND88-1432. Sandia National Laboratories, Albuquerque, NM.
- Gulick, C. W. and L. D. Wakeley, 1990 (in preparation). *Reference Properties of Cement-Based Plugging and Sealing Materials for the Waste Isolation Pilot Plant*, SAND87-2817. Sandia National Laboratories, Albuquerque, NM.
- Guzowski, R. V., 1990 (in preparation). *Preliminary Identification of Scenarios that May Affect the Release and Transport of Radionuclides from the Waste Isolation Pilot Plant, Southeastern New Mexico*, SAND89-7149. Sandia National Laboratories, Albuquerque, NM.
- Haug, A., V. A. Kelley, A. M. LaVenue, and J. F. Pickens, 1987. *Modeling of Groundwater Flow in the Culebra Dolomite at the Waste Isolation Pilot Plant (WIPP) Site: Interim Report*, Contractor Report SAND86-7167. Sandia National Laboratories, Albuquerque, NM.
- Holcomb, D. J. and D. W. Hannum, 1982. *Consolidation at Crushed Salt under Conditions Appropriate to the WIPP Facility*, SAND82-0630. Sandia National Laboratories, Albuquerque, NM.
- Holcomb, D. J. and M. Shields, 1987. *Hydrostatic Creep Consolidation of Crushed Salt with Added Water*, SAND87-1990. Sandia National Laboratories, Albuquerque, NM.
- Hunter, R. L., 1989. *Events and Processes for Constructing Scenarios for the Release of Transuranic Waste from the Waste Isolation Pilot Plant, Southeastern New Mexico*, SAND89-2546. Sandia National Laboratories, Albuquerque, NM.
- ICRP, Pub 38, 1983. *Radionuclide Transformations Energy and Intensity of Emissions*, ICRP Publication 38, *Annals of the International Commission on Radiological Protection (ICRP)*, Vol 11-13.
- Kaufman, D. W. ed., 1960. *Sodium Chloride, the Production and Properties of Salt and Brine*, Monograph No. 145. American Chemical Society, Washington, DC.
- Kipp, K. L., 1987. *HST3D: A Computer Code for Simulation of Heat and Solute Transport in Three-Dimensional Ground-Water Flow Systems*, WRIR 86-4095. U.S. Geological Survey, Denver, CO.
- Krieg, R. D., 1984. *Reference Stratigraphy and Rock Properties for the Waste Isolation Pilot Plant (WIPP) Project*, SAND83-1908. Sandia National Laboratories, Albuquerque, NM.
- Lappin, A. R., 1988. *Summary of Site Characterization Studies Conducted from 1983 through 1987 at Waste Isolation Pilot Plant (WIPP) Site, Southeastern New Mexico*, SAND88-0157. Sandia National Laboratories, Albuquerque, NM.

- Lappin, A. R., R. L. Hunter, D. P. Garber, and P. B. Davies, eds., 1989. *Systems Analysis Long-Term Radionuclide Transport, and Dose Assessments, Waste Isolation Pilot Plant (WIPP), Southeastern New Mexico; March 1989*, SAND 89-0462. Sandia National Laboratories, Albuquerque, NM.
- LaVenue, A. M., A. Haug, V. A. Kelley, 1988. *Numerical Simulation of Ground-Water Flow in the Culebra Dolomite at the Waste Isolation Pilot Plant (WIPP) Site: Second Interim Report*, SAND88-7002. Sandia National Laboratories, Albuquerque, NM.
- Lohman, S. W., 1972. *Ground-Water Hydraulics*, U.S. Geological Survey Professional Paper 708, U.S. Department of the Interior, Washington, DC.
- Longsine, D. E., E. J. Bonano, C. P. Harlan, 1987. *User's Manual for the NEFTRAN Computer Code*, SAND86-2405, NUREG/CR-4766. Sandia National Laboratories, Albuquerque, NM.
- Marietta, M. G., S. G. Bertram-Howery, D. R. Anderson, K. F. Brinster, R. V. Guzowski, H. J. Iuzzolino, R. P. Rechard, 1989. *Performance Assessment Methodology Demonstration: Methodology Development for Purposes of Evaluating Compliance with EPA 40 CFR 191, Subpart B, for the WIPP*, SAND89-2027. Sandia National Laboratories, Albuquerque, NM.
- Marietta, M. G., P. Swift, R. V. Guzowski, K. F. Brinster, 1990 (in preparation). *Parameter and Boundary Condition Sensitivity Studies Related to Climate Variability and Scenario Screening for the WIPP*, SAND89-2029. Sandia National Laboratories, Albuquerque, NM.
- McTigue, D. F., 1989. *Effect of Large Capacitance on Calculated Brine Volume Due to Darcy Flow*, memorandum. Sandia National Laboratories, Albuquerque, NM, October 27, 1989.
- Nowak, E. J. and J. C. Stormont, 1987. *Scoping Model Calculations of the Reconsolidation of Crushed Salt in WIPP Shafts*, SAND87-0879. Sandia National Laboratories, Albuquerque, NM.
- Nowak, E. J. and L. D. Tyler, 1989. *The Waste Isolation Pilot Plant (WIPP) Seal System Performance Program*, SAND89-0386. Sandia National Laboratories, Albuquerque, NM.
- Nowak, E. J., D. F. McTigue, and R. Beraun, 1988. *Brine Inflow to WIPP Disposal Rooms: Data Modeling and Assessment*, SAND88-0112. Sandia National Laboratories, Albuquerque, NM.
- Nowak, E. J., J. R. Tillerson, and T. M. Torres, 1990 (in preparation). *Initial Reference Seal System Design: Waste Isolation Pilot Plant (WIPP)*, SAND90-0355. Sandia National Laboratories, Albuquerque, NM.
- Ozsisik, M. N., 1968. *Boundary Value Problems of Heat Conduction*. International Textbook Co., Scranton, PA.
- Palmer, A. R., 1983. *The Decade of North American Geology 1983 Geologic Time Scale*, Geological Society of America.
- Prausnitz, J. M., 1969. *Molecular Thermodynamics of Fluid-Phase Equilibria*, Prentice-Hall, Inc., Englewood Cliffs, NJ.
- Pub. L. 96-164, 1980. Department of Energy National Security and Military Applications of Nuclear Energy Authorization Act of 1980, Title II - General Provisions: Waste Isolation Pilot Plant, Delaware Basin, NM, Pub. L. No. 96-164, 93 Stat. 1259.

References

- Rechard, R. P. and K. W. Schuler, 1982. *Permeability Change Near Instrumentation Holes in Jointed Rock: Implications for the Tuff Radionuclide Migration Field Experiment*, SAND81-2584. Sandia National Laboratories, Albuquerque, NM.
- Rechard, R. P., 1989. *Review and Discussion of Code Linkage and Data Flow in Nuclear Waste Compliance Assessments*, SAND87-2833. Sandia National Laboratories, Albuquerque, NM.
- Rechard, R. P., H. J. Iuzzolino, J. S. Rath, A. P. Gilkey, R. D. McCurley, D. K. Rudeen, 1989. *User's Manual for CAMCON: Compliance Assessment Methodology Controller*, SAND88-1496. Sandia National Laboratories, Albuquerque, NM.
- Shakoor, A. and H. R. Hume, 1981. *Physical Properties Data for Rock Salt: Chapter 3, Mechanical Properties*, NBS Monograph 167. National Bureau of Standards, Washington DC, pp. 103-203.
- Silling, S. A., 1983. *Final Technical Position on Documentation of Computer Codes for High-Level Waste Management*, NUREG-0856. U.S. Nuclear Regulatory Commission, Washington, DC.
- Sjaardema, G. D., and R. D. Krieg, 1987. *A Constitutive Model for the Consolidation of WIPP Crushed Salt and Its Use in Analysis of Backfilled Shaft and Drift Configurations*, SAND87-1977. Sandia National Laboratories, Albuquerque, NM.
- Stein, C. L., and J. L. Krumhansl, 1986. *Chemistry of Brines in Salt from the Waste Isolation Pilot Plant (WIPP), Southeastern New Mexico: A Preliminary Investigation*, SAND85-0897. Sandia National Laboratories, Albuquerque, NM.
- Stormont, J. C., 1988. *Preliminary Seal Design Evaluation for the Waste Isolation Pilot Plant*, SAND87-3083. Sandia National Laboratories, Albuquerque, NM.
- Streeter, V. L., and E. B. Wylie, 1975. *Fluid Mechanics*. Sixth Edition, McGraw-Hill Book Co., New York, NY.
- Tyler, L. D., R. V. Matalucci, M. A. Molecke, D. E. Munson, E. J. Nowak, and J. C. Stormont, 1988. *Summary Report for the WIPP Technology Development Program for Isolation of Radioactive Waste*, SAND88-0844. Sandia National Laboratories, Albuquerque, NM.
- Voss, C. I., 1984. *SUTRA (Saturated-Unsaturated TRANsport): A Finite-Element Simulation Model for Saturated-Unsaturated, Fluid-Density-Dependent Ground-Water Flow with Energy Transport or Chemically Reactive Single-Species Solute Transport*. U.S. Geological Survey National Center, Reston, VA.
- Waste Management Technology Dept., 1987. *In Situ Testing at the Waste Isolation Pilot Plant*, SAND87-2382. Sandia National Laboratories, Albuquerque, NM.
- Wawersik, W. R., and C. M. Stone, 1985. *Application of Hydraulic Fracturing to Determine Virgin In Situ Stress Around Waste Isolation Pilot Plant--In Situ Measurements*, SAND85-1776. Sandia National Laboratories, Albuquerque, NM.
- Weast, R. C., ed., 1974. *Handbook of Chemistry and Physics*. 55th Edition, CRC Press, Cleveland, OH.
- WEC (Westinghouse Electric Corporation), 1985. *TRU Waste Acceptance Criteria for the Waste Isolation Pilot Plant*, Revision 2, WIPP-DOE-069-Rev. 2. Westinghouse Electric Corporation, Carlsbad, NM.

- WEC (Westinghouse Electric Corporation), 1989. *Waste Isolation Pilot Plant No-Migration Variance Petition, Vol. 1*, DOE/WIPP 89-003. Prepared for U.S. Department of Energy by Westinghouse Electric Corporation, Carlsbad, NM.
- 10 *CFR* 61. *Disposal of High-Level Radioactive Wastes in Geologic Repositories, Technical Criteria*. U.S. Nuclear Regulatory Commission (NRC), Title 10 Code of Federal Regulations Part 60 (*10 CFR 60*).
- 40 *CFR* 191. *Environmental Radiation Protection Standards for Management and Disposal of Spent Nuclear Fuel, High-Level, and Transuranic Radioactive Wastes*. U.S. Environmental Protection Agency (EPA), Title 40 Code of Federal Regulations Part 191 (*40 CFR 191*).

References

Distribution:

Federal and State Agencies

U.S. Department of Energy (5)
Office of Civilian Radioactive Waste
Management

Attn: Deputy Director, RW-2
Associate Director, RW-10
Associate Director, RW-20
Associate Director, RW-30
Associate Director, RW-40

Forrestal Building
Washington, DC 20585

Office of Geologic Repositories
Forrestal Building
Washington, DC 20585

U.S. Department of Energy (5)
Albuquerque Operations Office

Attn: B. G. Twining
J. E. Bickel
R. Marquez
D. Krenz
J. Arthur

P.O. Box 5400
Albuquerque, NM 87185

U.S. Department of Energy (9)
WIPP Project Office (Carlsbad)

Attn: A. Hunt (5)
T. Lukow
V. Daub (2)
B. Young

P.O. Box 3090
Carlsbad, NM 88221

U.S. Department of Energy
Research & Waste Management Division

Attn: W. R. Bibb, Director

P.O. Box E
Oak Ridge, TN 37830

U.S. Department of Energy
Richland Operations Office
Nuclear Fuel Cycle & Production
Division

Attn: R. E. Gerton
P.O. Box 500
Richland, WA 99352

U.S. Environmental Protection Agency
Office of High Level Waste (2)

Attn: D. Egan
M. Cotton
401 M Street, SW
Washington, DC 20460

U.S. Department of Energy (7)
Office of Defense Waste and
Transportation Management

Attn: J. E. Lytle, DP-10
T. B. Hindman, DP-12
M. Duff, DP-123
J. Mathur, DP-123
A. Follett, DP-122
C. H. George, DP-124
L. D. Tyler, DP

Washington, DC 20545

U.S. Department of Energy
Idaho Operations Office
Fuel Processing and Waste
Management Division

Attn: J. E. Solecki
785 DOE Place
Idaho Falls, ID 83402

U.S. Department of Energy
Savannah River Operations Office
Defense Waste Processing
Facility Project Office

Attn: W. D. Pearson
P.O. Box A
Aiken, SC 29802

U.S. Geological Survey
Branch of Regional Geology

Attn: R. Snyder
MS913, Box 25046
Denver Federal Center
Denver, CO 80225

U.S. Geological Survey
Conservation Division

Attn: W. Melton
P.O. Box 1857
Roswell, NM 88201

Distribution (Continued):

U.S. Geological Survey (2)
Water Resources Division
Attn: K. Peter
Suite 200
4501 Indian School, NE
Albuquerque, NM 87110

U.S. Department of Energy (2)
Rocky Flats Area Office
Attn: W. C. Rask
R. M. Ostmeyer
P.O. Box 928
Golden, CO 80402-0928

U.S. Department of Energy
Los Alamos Area Office
Attn: J. D. Tillman
528 35th St.
Los Alamos, NM 87544

U.S. Nuclear Regulatory
Commission (6)
Division of Waste Management
Attn: M. J. Bell
H. Miller
J. Philip
R. E. Browning
M. R. Knapp
NRC Library
Mail Stop 623SS
Washington, DC 20555

Environmental Evaluation Group (3)
Attn: Library
Suite F-2
7007 Wyoming Blvd., N.E.
Albuquerque, NM 87109

New Mexico Bureau of Mines
and Mineral Resources (2)
Attn: F. E. Kottolowski, Director
J. Hawley
Socorro, NM 87801

State of New Mexico
HEQ - Environmental Improvement Division
Attn: K. Jones
1190 St. Francis Dr.
Santa Fe, NM 87503

Laboratories/Corporations

Argonne National Laboratory (2)
Attn: D. Hambeley
D. Tomasko
9700 South Cass Avenue
Argonne, IL 60439

Battelle Pacific Northwest Laboratories (6)
Attn: D. J. Bradley
J. Relyea
R. E. Westerman
S. Bates
H. C. Burkholder
L. Pederson
Battelle Boulevard
Richland, WA 99352

Bechtel, Inc. (2)
Attn: E. Weber
H. Taylor
45-11-B34
P.O. Box 3965
San Francisco, CA 94119

Brookhaven National Laboratory
Associated Universities, Inc.
Attn: P.W. Levy
Upton, NY 11973

E. I. Dupont de Nemours Company (6)
Savannah River Laboratory
Attn: N. Bibleer
E. L. Albenisius
M. J. Plodinec
G. G. Wicks
C. Jantzen
J. A. Stone
Aiken, SC 29801

RE/SPEC, Inc.
Attn: W. E. Coons
P. F. Gnirk
P.O. Box 14984
Albuquerque NM 87191

RE/SPEC, Inc. (5)
Attn: L. L. Van Sambeek
D. B. Blankenship
G. Callahan
T. Pfeifle
J. L. Ratigan
P.O. Box 725
Rapid City, SD 57709

Distribution (Continued):

Rockwell International
Attn: C. E. Wickland
Rocky Flats Plant
Golden, CO 80401

Savannah River Plant
Attn: R. G. Baxter
Building 704-S
Aiken, SC 29808

INTERA Technologies, Inc. (4)
Attn: G. E. Grisak
J. F. Pickens
A. Haug
Suite 300
6850 Austin Center Blvd.
Austin, TX 78731

INTERA Technologies, Inc.
Attn: W. Stensrud
P.O. Box 2123
Carlsbad, NM 88221

IT Corporation (3)
Attn: R. F. McKinney
J. Myers
J. Hart
Suite 700
5301 Central Avenue, SE
Albuquerque, NM 87108

IT Corporation
Attn: D. E. Deal
P.O. Box 2078
Carlsbad, NM 88221

Los Alamos National Laboratory
Attn: B. Erdal, CNC-11
Los Alamos, NM 87545

Oak Ridge National Laboratory (4)
Attn: R. E. Blanko
E. Bondietti
C. Clairborne
G. H. Jenks

Box Y
Oak Ridge, TN 37830

Western Water Consultants
Attn: D. Fritz
P.O. Box 3042
Sheridan, WY 82801

In-Situ, Inc. (2)
Attn: S. C. Way
C. McKee
209 Grand Avenue
Laramie, WY 82070

Systems, Science and Software (2)
Attn: E. Peterson
P. Lagus
P.O. Box 1620
La Jolla, CA 92038

Rockwell International (3)
Atomics International Division
Rockwell Hanford Operations
Attn: J. Nelson (HWVP)
P. Salter
W. W. Schultz
P.O. Box 800
Richland, WA 99352

Westinghouse Electric Corporation (7)
Attn: Library
W. C. Moffitt
W. P. Poirer
W. R. Chiquelin
V. F. Likar
D. J. Moak
R. F. Kehrman
P.O. Box 2078
Carlsbad, NM 88221

SAIC
Attn: H.R. Pratt,
Senior Vice President
10260 Campus Point Drive
San Diego, CA 92121

SAIC
Attn: M.B. Gross
Asst. Vice President
Suite 1250
160 Spear Street
San Francisco, CA 94105

SAIC
Attn: G. Dymmel
101 Convention Center Drive
Las Vegas, NV 89109

Western Water Consultants
Attn: P. A. Rechard
P.O. Box 4128
Laramie, WY 82071

Distribution (Continued):

Dennis W. Powers
Star Route Box 87
Anthony, TX 79821

Ecodynamics Research Associates (2)
Attn: P. J. Roache
P. Knupp
P.O. Box 8172
Albuquerque, NM 87198

Deuel and Associates, Inc.
Attn: R. W. Prindle
208 Jefferson, NE
Albuquerque, NM 87109

Arthur D. Little, Inc.
Attn: C. R. Hadlock
Acorn Park
Cambridge, MA 02140-2390

Universities

University of Arizona
Department of Nuclear Engineering
Attn: J. G. McCray
Tucson, AZ 85721

University of Arizona
Department of Hydrology & Water Resources
Attn: S. P. Newman
Tucson, AZ 85721

Pennsylvania State University
Materials Research Laboratory
Attn: D. Roy
University Park, PA 16802

Texas A&M University
Center of Tectonophysics
College Station, TX 77840

University of Wyoming
Department of Civil Engineering (2)
Attn: V. R. Hasfurth
Laramie, WY 82071

University of Wyoming
Department of Geology
Attn: J. I. Drever
Laramie, WY 82071

University of Wyoming
Department of Mathematics
Attn: R. E. Ewing
Laramie, WY 82071

University of California, Los Angeles
Mechanical, Aerospace, and Nuclear
Engineering Department (2)
5532 Boelter Hall
Attn: W. E. Kastenberg
D. Browne
Los Angeles, CA 90024

Libraries

NM Department of Energy & Minerals
Attn: K. LaPlante, Librarian
P.O. Box 2770
Santa Fe, NM 87501

Thomas Brannigan Library
Attn: D. Dresp, Head Librarian
106 W. Hadley St.
Las Cruces, NM 88001

Hobbs Public Library
Attn: M. Lewis, Librarian
509 N. Ship Street
Hobbs, NM 88248

New Mexico State Library
Attn: I. Vollenhofer
P.O. Box 1629
Santa Fe, NM 87503

New Mexico Tech
Martin Speere Memorial Library
Campus Street
Socorro, NM 87810

New Mexico Junior College
Pannell Library
Attn: R. Hill
Lovington Highway
Hobbs, NM 88240

U.S. Department of Energy
Albuquerque Operations Office
Attn: National Atomic Museum Library
P.O. Box 5400
Albuquerque, NM 87185

University of New Mexico (2)
Geology Department
Attn: D. G. Brookins
Library
Albuquerque, NM 87131

Distribution (Continued):

Carlsbad Municipal Library
WIPP Public Reading Room
Attn: L. Hubbard, Head Librarian
101 S. Halagueno St.
Carlsbad, NM 88220

University of New Mexico
General Library
Government Publications Department
Albuquerque, NM 87131

National Academy of Sciences, WIPP Panel

Vanderbilt University
Department of Environmental and
Water Resources Engineering
Attn: F. L. Parker
Nashville, TN 37235

J. O. Blomeke
Route 3
Sandy Shore Drive
Lenoir City, TN 37771

U.S. Geological Survey
Water Resources Division
Attn: D. Bredehoeft, M/S 439
345 Middlefield Road
Menlo Park, CA 94025

K. P. Cohen
928 N. California Avenue
Palo Alto, CA 94303

F. M. Ernsberger
250 Old Mill Road
Pittsburgh, PA 15238

University of New Mexico
Department of Geology
Attn: R. C. Ewing
200 Yale, NE
Albuquerque, NM 87131

University of Minnesota
Department of Civil and
Mineral Engineering
Attn: C. Fairhurst
500 Pillsbury Dr. SE
Minneapolis, MN 55455

Dr. D'Arcy A. Shock
233 Virginia
Ponca City, OK 74601

National Academy of Sciences
Committee on Radioactive
Waste Management
Attn: P. B. Myers, Staff Director
2101 Constitution Avenue
Washington, DC 20418

Board on Radioactive Waste
Management
Attn: I. Alterman, GF462
2101 Constitution Avenue
Washington, DC 20418

University of Virginia
Department of Environmental Sciences
Attn: G. M. Hornberger
Clark Hall
Charlottesville, VA 22903

Electric Power Research Institute
Attn: C. G. Whipple
3412 Hillview Avenue
Palo Alto, CA 94303

DOE Blue Ribbon Panel

New Mexico State University
New Mexico Water Resources Research
Institute
Attn: T. Bahr, Director
Las Cruces, NM 88001

Nuclear Management Resources Council
Attn: R. Bishop
1776 I Street NW, Suite 300
Washington, DC 20006

BDM Corporation
Attn: A. Kubo
7915 Jones Branch Drive
McLean, VA 22102

Leonard Slosky
1675 Broadway, Suite 1400
Denver, CO 80202

Newal Squyres, Esq.
P.O. Box 1368
Boise, ID 83702

Distribution (Continued):

Performance Assessment Peer Review Panel

College of Ocean and Fishery Sciences
Attn: G. R. Heath
University of Washington
Seattle, WA 98195

University of California
Department of Nuclear Engineering
4153 Etcheverry Hall
Attn: T. H. Pigford
Berkeley, CA 94270

University of California
Mine Engineering Dept.
Rock Mechanics Engineering
Attn: N. Cook
Berkeley, CA 94270

T. A. Cotton
4429 Butterworth Place, NW
Washington, DC 20016

Future Resources Associates Inc.
Attn: R. J. Budnitz, President
2000 Center Street, Suite 418
Berkeley, CA 94704

University of Illinois
Department of Geology
245 Natural History Bldg.
Attn: C. J. Mann
1301 West Green Street
Urbana, IL 61801

Woods Hole Oceanographic Institute
Attn: C. D. Hollister, Dean for Studies
Woods Hole, MA 02543

Disposal Safety, Inc.
Attn: B. Ross
1629 K Street NW, Suite 600
Washington, DC 20006

Foreign Addresses

Studiecentrum Voor Kernenergie
Centre D'Energie Nucleaire
Attn: A. Bonne
SCK/CEN
Boeretang 200
B-2400 Mol
BELGIUM

Atomic Energy of Canada, Ltd. (2)
Whiteshell Research Estab.
Attn: P. Haywood
J. Tait
Pinewa, Manitoba, CANADA
ROE 1L0

Ontario Hydro Research Lab
Attn: D. K. Mukerjee
800 Kipling Avenue
Toronto, Ontario, CANADA
M8Z 5S4

ANDRA
Attn: D. Alexandre, Deputy Director
31, Rue de la Federation
75015 Paris, FRANCE

Lab Géologie Appliqué
Attn: G. deMarsily
Tour 26, 5 Étage
4 Place Jussieu
F-75242, Paris, Cedex 05 FRANCE

OECD Nuclear Energy Agency
Division of Radiation Protection
and Waste Management
Attn: Jean-Pierre Olivier
38, Boulevard Suchet
75016 Paris, FRANCE

Centre D'Estudes Nucleaires
De La Vallee Rhone
Attn: C. Sombret
CEN/VALRHO
S.D.H.A. BP 171
30205 Bagnols-Sur-Ceze
FRANCE

Bundesministerium fur Forschung und
Technologie
Postfach 200 706
5300 Bonn 2
FEDERAL REPUBLIC OF GERMANY

Bundesanstalt fur Geowissenschaften
und Rohstoffe
Attn: M. Langer
Postfach 510 153
3000 Hanover 51
FEDERAL REPUBLIC OF GERMANY

Distribution (Continued):

Hahn-Mietner-Institut fur Kernforschung
 Attn: W. Lutze
 Glienicker Strasse 100
 100 Berlin 39
 FEDERAL REPUBLIC OF GERMANY

Institut fur Tieflagerung (4)
 Attn: K. Kuhn
 Theodor-Heuss-Strasse 4
 D-3300 Braunschweig
 FEDERAL REPUBLIC OF GERMANY

Kernforschug Karlsruhe (1)
 Attn: K. D. Closs
 Postfach 3640
 7500 Karlsruhe
 FEDERAL REPUBLIC OF GERMANY

Physikalisch-Technische Bundesanstalt
 Attn: P. Brenneke
 Postfach 33 45
 D-3300 Braunschweig
 FEDERAL REPUBLIC OF GERMANY

British Nuclear Fuels, plc
 Attn: D. R. Knowles
 Risley, Warrington, Cheshire WA3 6AS
 1002607 GREAT BRITAIN

Japan Atomic Energy Research Institute
 Attn: S. Tashiro
 Tokai-Mura, Ibaraki-Ken
 319-11 JAPAN

Netherlands Energy Research Foundation
 ECN (2)
 Attn: Tuen Deboer, Mgr.
 L. H. Vons
 3 Westerduinweg
 P.O. Box 1
 1755 ZG Petten, THE NETHERLANDS

Svensk Karnbransleforsorjning AB
 Attn: F. Karlsson
 Project KBS
 Karnbranslesakerhet
 Box 5864
 10248 Stockholm, SWEDEN

British Geological Survey
 Attn: Neil Chapman
 Keyworth
 GBR-Nottingham NIZ 5GG
 UNITED KINGDOM

Sandia Internal

1511 D. K. Gartling
 1511 P. Hopkins
 1520 L. W. Davison
 1521 H. S. Morgan
 3141 S. A. Landenberger (5)
 3151 W. I. Klein (3)
 3154-1 C. L. Ward, for DOE/OSTI
 Unlimited Release, UC-721 (8)
 6000 D. L. Hartley
 6300 R. W. Lynch
 6310 T. O. Hunter
 6312 F. W. Bingham
 6312 G. E. Barr
 6313 T. E. Blejwas
 6315 L. E. Shephard
 6315 P. C. Kaplan
 6340 W. D. Weart
 6340 S. Pickering
 6341 R. C. Lincoln
 6341 D. Garber
 6341 R. L. Hunter
 6341 R. D. Klett
 6341 J. M. Hovan
 6342 D. R. Anderson (10)
 6342 B. L. Baker
 6342 J. E. Bean
 6342 J. Berglund
 6342 S. G. Bertram-Howery
 6342 K. F. Brinster
 6342 L. S. Gomez
 6342 A. P. Gilkey
 6342 R. V. Guzowski
 6342 H. J. Iuzzolino
 6342 M. G. Marietta (5)
 6342 R. D. McCurley
 6342 J. S. Rath
 6342 R. P. Rechar (25)
 6342 D. K. Rudeen
 6342 J. Sandha
 6342 J. D. Schreiber
 Sandia WIPP Central Files (25)
 6343 T. M. Schultheis
 6344 E. D. Gorham
 6344 R. L. Beauheim
 6344 P. B. Davies
 6344 S. J. Finley
 6344 A. M. LaVenue
 6344 M. D. Siegel
 6345 A. R. Lappin
 6345 R. Beraun
 6345 L. H. Brush
 6345 G. E. Bujewski
 6345 B. M. Butcher

Distribution (Continued):

6345 M. A. Molecke
6346 J. R. Tillerson
6346 D. J. Borns
6346 B. L. Ehgartner
6346 D. E. Munson
6346 E. J. Nowak
6346 T. M. Torres
6350 W. C. Luth
6400 D. J. McCloskey
6413 J. C. Helton
6415 R. M. Cranwell
6416 E. J. Bonano
8524 J. A. Wackerly (SNLL Library)



8232-2/070199



00000001 -



8232-2/070199



00000001 -



8232-2/070199



00000001 -

